Long-range Ocean Acoustic Propagation Experiment (LOAPEX): Preliminary analysis of source motion and tidal signals

Michael R. Zarnetske

A thesis
submitted in partial fulfillment of the
requirements for the degree of

Master of Science

University of Washington

2005

Program Authorized to Offer Degree:
School of Oceanography

University of Washington
Graduate School

This is to certify that I have examined this copy of a master's thesis by

Michael R. Zarnetske

and have found it is complete and satisfactory in all respects,
and that any and all revisions required by the
final examining committee have been made.

Committee Members:

____

Bruce Howe

____

Steven Riser

____

Kenneth Bube

Date: ________________

In presenting this thesis in partial fulfillment of the requirements for a master's degree at the University of Washington, I agree that the library shall make its copies freely available for inspection. I further agree that extensive copying of this thesis is allowable only for scholarly purposes, consistent with fair use as prescribed in the U.S. Copyright Law. Any other reproduction for any purposes or by any means shall not be allowed without my written permission.

Signature ______________________

Date __________________________

University of Washington

Abstract

Long-range Ocean Acoustic Propagation Experiment (LOAPEX):
Preliminary analysis of source motion and tidal signals

Michael R. Zarnetske

Chair of the Supervisory Committee:
Research Associate Professor Bruce Howe
School of Oceanography

In the Long-range Ocean Acoustic Propagation Experiment (LOAPEX), a ship suspended source transmitted to various receivers around the north Pacific. The position of the acoustic source was monitored precisely so that effects of its motion can be removed from the received signals. Acoustic receptions at one fixed bottom receiver ('r') were analyzed for ranges of 250 km to 3000 km to the source. Acoustic arrivals are identified using ray trace model predictions. The travel time variations of the identified arrivals over the one to two days of transmissions at each station have an obvious strong tidal component. The measured variability (5-10 ms amplitude) correlates very well with the predicted path-averaged tidal signal (correlation coefficient 0.2-0.97). These correlations provide confidence the source/receiver system is working as expected. Residual travel time fluctuations of 2-5 ms rms attributed to other high frequency ocean variability, such as internal waves, is present in the shorter range transmissions of distances 250-1000 km. Travel time fluctuations of 5-13 ms rms present for the longer ranges of 1000-3000 km are less than the expected values of 12-17 ms rms. The average horizontal source displacement during a typical 20-minute transmission is sufficiently small so it can be ignored over these time scales. The mean travel time offsets relative to the Levitus World Ocean Atlas are 0.09-0.265 s, implying a range and depth averaged ocean colder by 0.023-0.066 °C than the Levitus World Ocean Atlas for the particular LOAPEX paths and times of year.

Table of Contents

List of Figures iii

List of Tables v

1 Introduction 1

1.1 Acoustic tomography 1

1.2 Previous moving ship tomographic experiments 3

1.3 Tidally influenced travel times 4

2 LOAPEX 5

2.1 Scientific goals 5

2.2 Acoustic array overview 6

3 Source Navigation 11

3.1 Cable dynamics model 12

3.2 C-Nav 14

3.3 Acoustic Doppler current profiles 21

3.4 Drag coefficients 25

3.5 Source positioning comparison 27

3.5.1 Interrogator/transponder 27

3.5.2 Vertical source motion: MicroCAT 31

3.6 Source velocity comparison 32

4 Acoustic Receptions 37

4.1 Propagation predictions 37

4.1.1 MAP Program 39

4.1.2 Time front predictions 39

4.2 Measured receptions 42

4.2.1 Acoustic arrival pre-processing 42

4.2.2 Received time series 43

4.3 Comparison between measured and predicted arrivals – ray identification 44

4.4 Reception variability 48

4.5 Predicted and measured tidal signal 49

4.6 First-order temperature change estimates 59

5 Conclusions 61

5.1 Comparing measured and predicted tidal signals 61

5.2 Mean travel times 62

5.3 Source position and velocity estimates 62
5.4 Further studies 64
References 66
Appendix 1: Instrumentation data sheets 70
Appendix 2: WHOI Cable screen capture examples 80
Appendix 3: C-Nav LOAPEX station time series 84
Appendix 4: ADCP time series for all LOAPEX stations 91
Appendix 5: Plan-view of ship and source position during source deployments. 98
Appendix 6: Position comparison: Ship (C-Nav), Source (WHOI Cable and Interrogator/Transponder) 111
Appendix 7: S4 current meter time series for all LOAPEX stations 124
Appendix 8: Source velocity comparison time series: S4-ADCP and WHOI Cable 131
Appendix 9: LOAPEX stations to 'r' path sound velocity profiles 144
Appendix 10: Predicted eigenrays, time fronts and arrival angles for the paths between all LOAPEX stations and 'r'. 151
Appendix 11: Predicted time front and measured reception alignments for all receptions at 'r' from the LOAPEX stations 164
Appendix 12. Receptions at 'r' for all LOAPEX transmissions shown in a waterfall format 177
Appendix 13: Comparison of first four tracked raw acoustic arrivals and test tidal travel time offsets 184
Appendix 14: Comparison of first four tracked and corrected acoustic arrivals and test tidal travel time offsets 191

List of Figures

Figure 2.1. Overview of LOAPEX array. 7
Figure 2.2. LOAPEX acoustic source. 9
Figure 2.3. Ship position over 12 hours during source deployment at T250. 10
Figure 3.1. Source deployment instrumentation. 12
Figure 3.2. C-Nav receiver antenna. 15
Figure 3.3 Global C-Nav satellite coverage. 16
Figure 3.4. C-Nav position quality parameters for 31 hours at T250. 17
Figure 3.5. R/V Melville on-board GPS system comparison. 19
Figure 3.6a. Vertical and horizontal comparison of on-board GPS systems. 20
Figure 3.6b. Expanded vertical comparison of on-board GPS systems. 20
Figure 3.7a. Acoustic Doppler current profile at station T250. 21
Figure 3.7b. Acoustic Doppler current profile for station T250. 22
Figure 3.8. Depth averaged current during source deployment to 800 m at T250. 24
Figure 3.9. Plan-view of source and ship position during the 800 m source deployment at ship station T250. 25
Figure 3.10. Source and cable drag coefficient sensitivity study results. 26
Figure 3.11. Position comparison: station T250. 29
Figure 3.12. East/west position comparison: station T250. 29
Figure 3.13. Measured and predicted vertical source position and vertical ship position for the 800-m deployment at station T250. 31
Figure 3.14. S4 current meter measurements at T250. 33
Figure 3.15. Expanded S4-ADCP vs. WHOI Cable source velocity comparison for T250. 34
Figure 3.16. Correlation between modeled and measured (S4-ADCP) source velocity. 36
Figure 4.1. Sound speed profile transect between T250 (1) and ‘r’ (2). 38
Figure 4.2. Eigenray predictions between 800 m transmissions at T250 and ‘r’ 40
Figure 4.3. Eigenray predictions between 350 m transmissions at T250 and ‘r’ 41
Figure 4.4. All station receptions at ‘r’ shown as a function of azimuth angle, where zero degrees is due east and increases counterclockwise. 42
Figure 4.5. Processing steps performed on the received signals at ‘r’. 43
Figure 4.6a. Processed beamformed data received at ‘r’ from T250 800m transmissions. 44
Figure 4.6b. A slice through the beamformed intensity plot in (a). 44
Figure 4.7a. Predicted time front and measured receptions with corresponding ray identifier of 800-m transmissions from T250 to ‘r’. 45
Figure 4.7b. Predicted time front and measured receptions with corresponding ray identifier of 350-m transmissions from T250 to ‘r’. 46
Figure 4.8. Waterfall plot of the receptions at ‘r’ from station T250. Ray identifiers determined from the acoustic predictions have been included. 47
Figure 4.9. Barotropic tidal elevation (color scale) and co-tidal lines. 51

Figure 4.10. Path-average travel time offsets from all LOAPEX stations to ‘r’. 52
Figure 4.11a. Tide test signal (blue) overlaid with time series of four uncorrected tracked arrivals at ‘r’ from the transmissions at T250. 53
Figure 4.11b. Tide test signal (blue) overlaid with average of four uncorrected arrivals at ‘r’ from the 800-m deep transmissions at T250. 54
Figure 4.12a. Tide test signal (blue) overlaid with time series of four tracked arrivals with source position corrections at ‘r’ from the 800-m deep transmissions at T250. 55
Figure 4.12b. Tide test signal (blue) overlaid with average of four tracked arrivals with source corrections at ‘r’ from the 800-m deep transmissions at T250...............55
Figure 4.13. Path averaged tidal predictions and acoustically measured, source motion corrected, travel time perturbations. 57
Figure 4.14a. Comparison between tidal model predicted offset and uncorrected acoustically measured offsets for all LOAPEX stations to receiver ‘r’. 58
Figure 4.14b. Comparison between tidal model predicted offset and corrected acoustically measured offsets for all LOAPEX stations to receiver ‘r’. 59

List of Tables

Table 2.1. LOAPEX stations, transmission time windows (ref. yearday 2004), and distance to receiver ‘r’. 8
Table 3.1. Input parameters to WHOI Cable. 14
Table 3.2. Time windows of questionable C-Nav receptions. 18
Table 3.3. *R/V Melville* on-board GPS system comparion. 19
Table 3.4. Comparison between measured and predicted source position using WHOI Cable and the interrogator/transponder pair....................30
Table 3.5. Measured and predicted source velocity comparison. 35
Table 4.1. Summary of nominal time delays introduced by the transmitter/receiver electronics and processing. 48
Table 4.2. Summary of time shifts needed to align acoustic receptions at ‘r’ with predictions....................48
Table 4.3. Predicted tidal travel time signals and currents. 52
Table 4.4. Comparison between averaged tracked path arrivals and the predicted tidal signal between the LOAPEX stations and ‘r’. 56
Table 4.5. Perturbations between LOAPEX measured and from 50 year September World Ocean Atlas average. 60

ACKNOWLEDGMENTS

This work was supported by the Office of Naval Research grants N00014-04-1-0416 and N00014-03-1-0181. The Applied Physics Laboratory and the School of Oceanography helped to fund my first year at the University of Washington, during which the main design and organization of the LOAPEX experiment took place. Also during this time, my general knowledge of the science of acoustic tomography was expanded through many thoughtful discussions with my advisor, Dr. Bruce Howe, and others, including Dr. Brian Dushaw, Dr. James Mercer, and Dr. Rex Andrew. My other committee members: Professors Steve Riser and Kenneth Bube, helped to keep me on the 'straight and narrow' through their thoughtful suggestions. For my general knowledge of the hardware and data processing, Don Reddaway, Lyle Gullings, Joe Wigton, and Linda Buck offered immeasurable support. I would also like to thank Drs. John Colosi and Peter Worcester and the rest of the R/V *Revelle* science party and crew for allowing me to assist in the SPICEX cruise.

On a personal note, I would very much like to thank my mother, father and sister for their support while I attempted to acquire this degree. Of course, I also would like to thank everyone else whom I confided in while running through the gauntlet known as the Physical Oceanography program at the University of Washington. Your names are too numerous to mention but you helped me out in ways words cannot describe.

1 Introduction

The purpose of the Long-rang Ocean Acoustic Propagation EXperiment (LOAPEX) is to provide range-varying acoustic data to better understand the basic physics of low-frequency, long range, broadband propagation, specifically: the effects of environmental variability on signal stability and coherence; the fundamental limits to signal processing at long range imposed by the ocean processes and the ambient noise environment; and to provide multiple acoustic paths at many angles from which to calculate nearly-synoptic sound speed (temperature) fields of the North Pacific Ocean using acoustic thermometry.

The field component of the experiment consisted of suspending a low-frequency acoustic source from a ship and transmitting to receivers at various ranges. A prerequisite to using the received acoustic data for the above purposes is to know the source position precisely and accurately; a major part of this thesis is devoted to quantifying this. To obtain a preliminary measure of the overall quality of the data, tidal signals in the measured travel time data are compared with the predicted tidal signal, with favorable results. Also, the average absolute travel times are compared with those computed using historical data as a first step to tomography.

In the balance of this section, a brief review is given of acoustic tomography, including moving ship tomography and tidal measurements using tomography. This is followed by a more detailed introduction to the LOAPEX experiment (section 2) and a discussion of the source navigation (section 3). The acoustic receptions at one receiver 'r' are presented with the tidal analysis and estimates of mean travel time (section 4). Section 5 has concluding remarks.

1.1 Acoustic tomography

Tomography is a two step measurement process to image the interior of a volume. In the first step, energy propagates through the known volume along many source-receiver paths at many different angles and the effects of the medium on the energy are measured. The second step is the inversion of these effects to reconstruct an image of the volume.

In the case of ocean acoustic tomography, the energy is sound and the usual measured datum is travel time between sources and receivers. Given the travel time and the known distances, the speed of sound (proportional to ocean temperature) is obtained. Many such measurements along many paths at many angles are inverted for the sound speed field, hence temperature. Because warm water has a higher sound speed than cold water, a relative increase in travel time implies a cooling, and vice versa. Also, because sound travels faster with a current than against, the difference in travel times in each direction along a path is a measure of the current along the path (here sound speed effects are canceled).

Tomography also takes advantage of the ocean being nearly transparent to low frequency sound, thus enabling acoustic energy to travel great distances with little attenuation. In the vertical, as depth increases beneath the surface, sound speed decreases with decreasing temperature and increases with increasing pressure forming the "sound channel," a waveguide that traps energy and permits efficient propagation removed from scattering boundaries (e.g., the surface and the bottom). Where the competing effects of temperature and pressure balance, there is a sound speed minimum, at approximately 800-m in the case of the Long-range Ocean Acoustic Propagation Experiment. Acoustic energy propagates through this waveguide and can be represented by modes or quasi-sinusoidal rays. In the later case, sound energy travels along (nearly) deterministic "eigenrays" between a source and a receiver. This has the benefit of sampling the ocean over depth, but with an "up-down ambiguity."

The first description of ocean acoustic tomography appears in Munk and Wunsch (1979). The authors put forth a design for a sampling system, and the algorithms necessary to process the data. The monograph by Munk, Worcester and Wunsch (1995) describes the technique and subsequent developments in detail.

One way travel time signals measured between the ship-deployed source and one receiver over a day or two at each ship station are interpreted in two ways in this thesis. In the first, the variation of travel time at tidal frequencies is interpreted as the path averaged tidal current. In the second, the average measured travel time gives a measure of average temperature along each path.

1.2 Previous moving ship tomographic experiments

Of the numerous long-range acoustic experiments performed, only a few have used a ship-deployed source or receiving array. Four notable experiments were:

(1) Applied Tomography Experiment 1990 (ATE90, Walter, 1993). Here, a ship-deployed hydrophone array was towed north of the Gulf Stream and received signals from a bottom mounted source on the north slope of Bermuda. The received transmissions traversed the Gulf Stream. From the receptions, the position of the Gulf Stream and smaller-scale features, such as warm-core and cold-core eddies, were determined.

(2) Acoustic Mid-Ocean Dynamics Experiment – Moving Ship Tomography, 1991 (AMODE-MST Group, 1994). In this experiment a 700-km diameter array of six moored sources transmitted every 3 hours for 50 days to a vertical line array deployed by a ship circumnavigating the source array on a 1000-km diameter circle. Data were processed to produce a high-resolution map of sound speed (temperature).

(3) ATOC Engineering Test (AET), 1994 (Colosi et al., 1999). Here, an ATOC source (the same as used here in LOAPEX) was deployed from R/V *Flip* and its transmissions were received on vertical arrays of hydrophones. Much of what is now known about long-range, low-frequency propagation comes from this experiment.

(4) Alternate Source Test (AST), 1996 (Worcester et al., 1999). Here, an HLF-6 source transmitted simultaneous coherent 28- and 84-Hz signals. The lower

frequency 28-Hz receptions showed more stability and coherence than the higher frequency ones.

The experiment described and analyzed here is the reciprocal of what was reported by Walter (1993) such that LOAPEX has fixed receivers and deployed a source from a ship.

1.3 Tidally influenced travel times

Due to the averaging nature inherent in long range acoustic propagation, tomography offers a natural method with which to measure large scale ocean processes. Travel times of reciprocal 1000 km range acoustic transmissions from the 1987 Reciprocal Tomography Experiment were used to determine the barotropic tidal currents with exceptional accuracy as well as detect a large-scale, phase coherent baroclinic tidal current in the central North Pacific (Dushaw et al., 1995). The difference in the reciprocal travel times that determined the sound speed change which was interpreted as baroclinic tide displacement. As a result, ocean acoustic tomography offers perhaps the only in-situ method to accurately measure tidal currents because tomography inherently averages over depth and large horizontal scales. Historical or available current meter measurements are too sparse and noisy to provide sufficient accuracy to test tidal models, as was shown in Dushaw et al. (1999). Such critical tests are useful because of the wide range of applications of the global tidal models, e.g., estimates of barotropic tidal dissipation at topographic features, or measurements of the effect of tidal currents on the rotation rate of the earth. Direct solutions to the astronomically forced Laplace tidal equations are available in a global model by Egbert et al. (1994). This model is used here to predict the tidally-related one-way travel time signal, which is compared with the measured equivalent along the selected set of paths between LOAPEX source stations and a fixed receiver, ‘r’.

2 LOAPEX

LOAPEX (Long range Ocean Acoustic Propagation Experiment) is one part of three coupled experiments, all contributing to the overall scientific goal of the North Pacific Acoustic Laboratory (NPAL), which is to investigate the ultimate coherence limits of long-range acoustic propagation imposed by ocean variability and the ambient sound field. NPAL evolved from the Acoustic Thermometry of Ocean Climate (ATOC) program, which used long-range acoustic travel time perturbations to measure basin-scale heat content from tomographic inversions.

2.1 Scientific goals

LOAPEX has four main scientific goals:

First, LOAPEX is aimed at understanding the types of small-scale ocean variability important in causing acoustic scattering both within the acoustic waveguide (sound channel), and into and out of the acoustic waveguide. The scattering observed in previous experiments was greater than the predicted amount from internal wave models. LOAPEX aims to determine physical reasons to account for this increased scattered acoustic energy.

Second, LOAPEX is designed with multiple transmission stations to provide a systematic way to explore the evolution with range of both the highly scattered finale, and of the fluctuation statistics of resolved ray and mode arrivals. Typically, an acoustic signal arriving at a fixed receiver at distances of one hundred kilometers or more, has three different reception sections. In the mid-latitudes, the early-arriving acoustic energy is associated with steep arrival angles and is considered ray-like which means the arrivals can be efficiently represented by frequency independent ray tracing. The mid-section of the arrival is a transition from early ray-like arrivals to mode-like arrivals. The final section is a completely mode-like arrival structure, which is highly scattered and difficult to interpret. The entire structure can be explained by the wave equation, but rays are used for simplicity. The distinct differences in the arrival sections are due mainly to the resolvability and stability of rays or modes depending on the scattering by the ocean between the source and the receiver. The transition from ray- to mode-like arrivals depends on the frequency of the transmitted signal.

Third, LOAPEX is aimed at investigating the possible causes of extensive scattering into predicted shadow zones. The scattering could be caused by internal waves, or spiciness, for example. It is with the multiple transmissions at various ranges, providing numerous realizations of deep acoustic arrival structures at the various receivers, which is a major thrust of on-going data analysis and research.

Fourth, LOAPEX is using both moored sources (as described below) and the ship suspended source to augment basin-scale observations of temperature made using the bottom mounted Kauai source and receivers, thus providing a denser network of acoustic paths and more data to assimilate into and improve existing numerical models. Only the ship deployed source transmissions are discussed here, with the work described laying the foundation to use the acoustic data in a tomographic sense.

2.2 Acoustic array overview

In LOAPEX, an acoustic source was suspended from an oceanographic research vessel at various points in the North Pacific over the span of 30 days (Mercer et al., 2005). The source deployment stations and the locations of fixed receivers in the North Pacific are shown in Figure 2.1. Table 2.1 contains the list of ship stop positions. The moored vertical line array (VLA) is shown as a yellow dot (Figure 2.1) at the approximate position of 34°N, 138°E. There were actually two vertical arrays positioned very closely, the shallow (SVLA) and the deep (DVLA). The LOAPEX stations are shown along the black line extending westward from the position of the VLA. Traveling along this black line, subsequent LOAPEX stations are 50 km, 250 km, 500 km, 1000 km, 1600 km, 2300 km and 3200 km from the VLA, respectively. These stations are referred to in shorthand as T50, T250, T500, T1000, T1600, T2300, and T3200, respectively. This notation is followed throughout the text. In addition to these 'T' stations, the source was also deployed 40 km ENE of the position of the bottom-mounted transmitter north of Kauai (TKauai). Transmissions from the later source position will be compared to the transmissions made by the bottom mounted source in another study. This comparison helps to characterize and quantify the bottom interaction occurring near the bottom-mounted source.

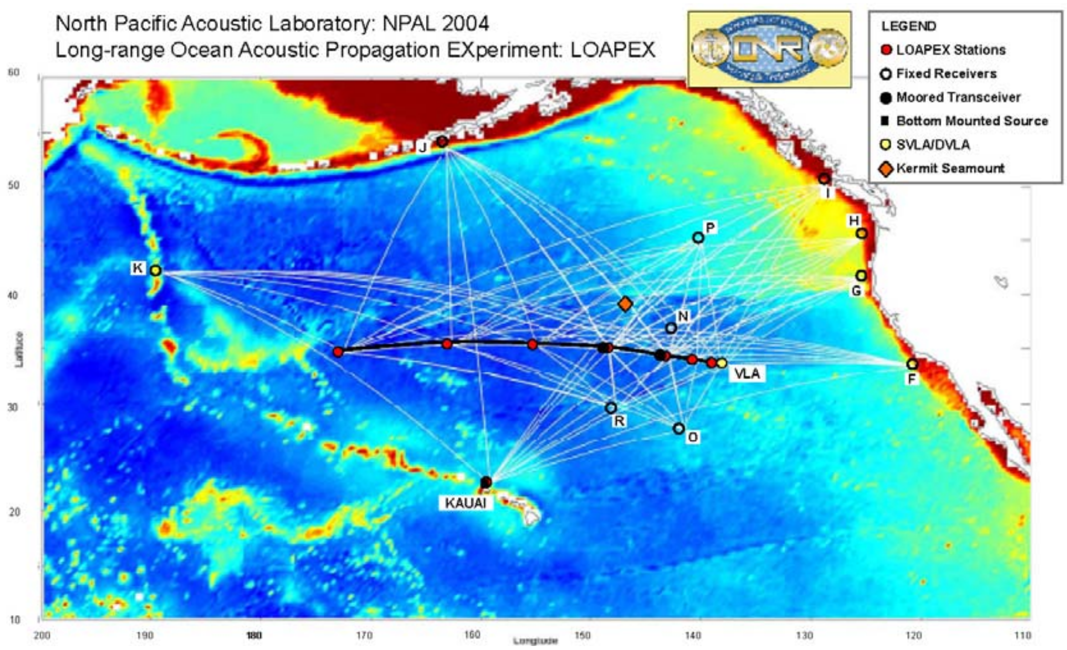

Figure 2.1. Overview of LOAPEX array.

Table 2.1. LOAPEX stations, transmission time windows (ref. yearday 2004), and distance to receiver ‘r’.

Station	**Depth**	**Start time**	**Stop Time**	**Position**		**Distance to 'r'**
	(m)	decimal yearday		Lat (°N)	Lon (°E)	(km)
T50	800	259.70833	260.12500	33.51359	-138.208350	1002.3578
	350	259.00000	259.70832			
T250	800	261.35833	261.99028	33.86978	-140.32299	847.3381
	350	260.74804	261.35832			
T500	800	263.60022	264.25994	34.24884	142.88250	691.8316
	350	262.76689	263.60020			
T1000	800	265.77198	267.25591	34.86417	-148.28013	588.9539
	350	265.40867	265.76039			
T1600	350	268.65413	269.99788	35.28561	-154.94997	749.4577
T2300	500	273.41667	273.97569	35.31273	-162.64797	1533.6231
	350	272.73194	273.41666			
T3200	500	277.50066	278.15342	34.63182	-172.47287	2387.7021
	350	276.83397	277.49716			
R	1320			29.5835	-147.7429	

At each station the source (Figure 2.2) was lowered to two depths, either 350 m and 800 m, or 350 m and 500 m, where it transmitted m-sequence signals with one of two center frequencies: 68.5 Hz for the shallower depths or 75 Hz for the deeper depths. Other signal types were transmitted but are not used in this analysis. The transmissions were received at numerous fixed receivers (Figure 2.1). The receptions at receiver ‘r’ are analyzed here to provide an early indication of what should be possible using data collected on the other receivers. The pertinent characteristics of this source are its low-frequency, high-bandwidth, high-power level and its consistent output independent of depth.

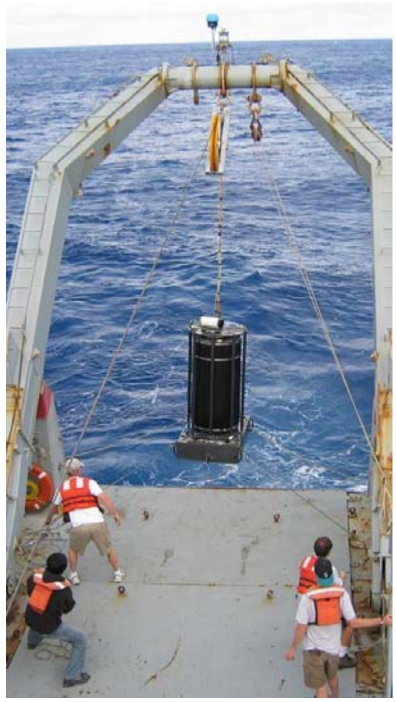

Figure 2.2. LOAPEX acoustic source**.**

Many tomography and acoustic propagation experiments use combinations of fixed and/or moored instruments, often arranged on vertical arrays that slowly “swayed in the breeze” due to tidal and other currents. These weak currents offset the source or receiver array and affect the phase and the travel time of signals. LOAPEX used a ship-suspended source arrangement, which showed more high-frequency movement than a moored vertical hydrophone array. However, the multiple source positions provided the acoustic path multiplication advantage. As each source station is introduced, the number of acoustic paths increases as the product of the number of receivers and the number of source stations. Therefore, although the source motion might complicate the initial travel time accuracy, once it is accounted for, the multiple paths between the known position of the source and the multiple receivers offers very good coverage of the North Pacific.

To perform precise acoustic travel time calculations, account of the source movement must be taken. During LOAPEX, the position of the source remained nearly beneath the support vessel during the deployments. At deployment stations, the ship was in dynamic positioning mode to remain within a few meters of the desired latitude and longitude.

Typically, while on station, the ship remained within 6 m of the desired position. The positioning of the ship during one such deployment is shown in Figure 2.3. The figure shows the time series of the ship's position acquired by a globally corrected differential global positioning system, C-Nav, which will be discussed in detail below.

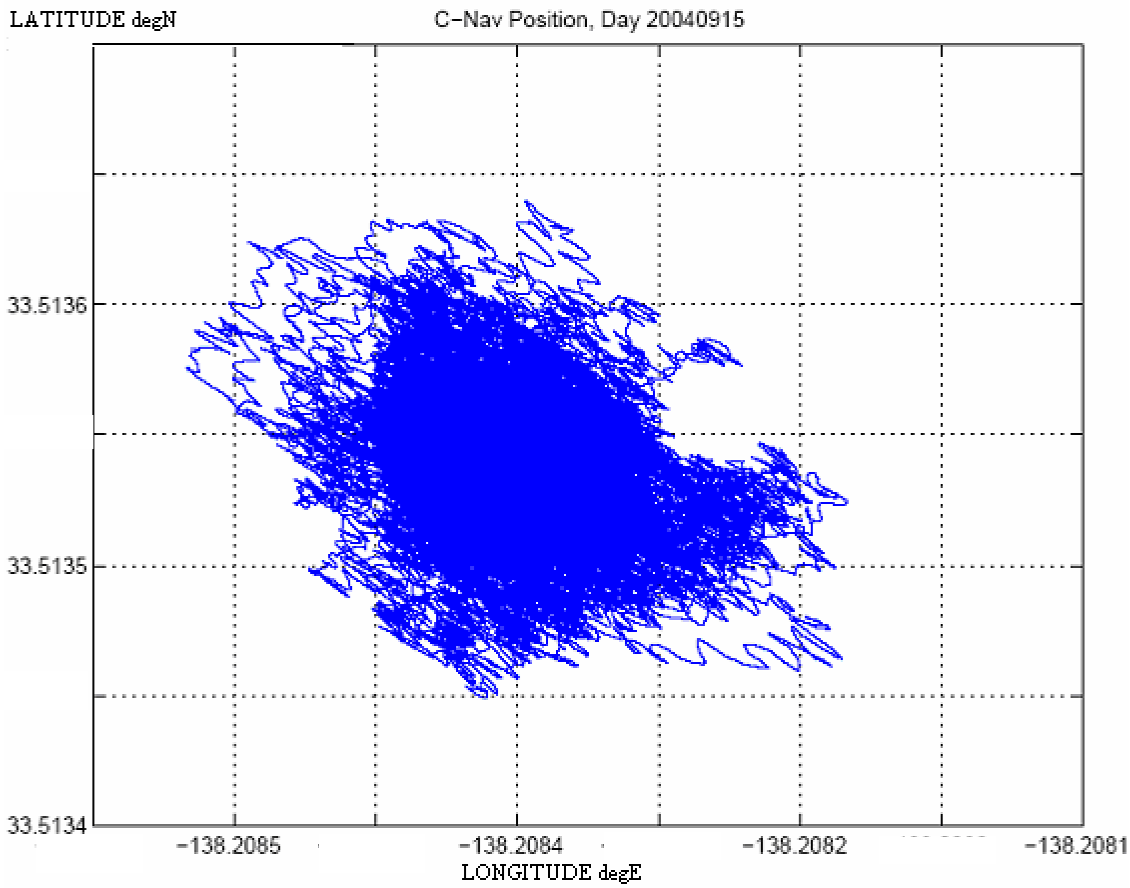

Figure 2.3. Ship position over 12 hours during source deployment at T250.

3 Source Navigation

Knowledge of the absolute position of the acoustic source is required to correct the receptions and to use them in the tomographic and acoustic propagation/ocean fluctuation studies. To determine the position of the source during the LOAPEX transmissions, several instruments were deployed with the source at each ship stop (Figure 3.1). Data sheets for each instrument package can be found in Appendix 1. At each ship stop (i.e., 'T' station), the acoustic source was deployed with the following instruments:

- SBE 37-SM MicroCAT: Pressure sensor. This sensor was placed approximately 20 m above source on deployment cable. This was used to measure pressure (i.e. depth) of the source during its deployments.
- Interrogator/transponder pair. The 'Woods Hole interrogator' was placed 6 m above the source on the deployment cable. It measured round-trip travel time, ranging off of a bottom mounted transponder to provide horizontal position of the source relative to the geodesic path to the VLA. The sample interval was 6 sec for all but one station, T3200, where the sample rate of 3 sec.
- S4 current meter. The S4 was deployed 6 m beneath the source to measure the velocity of the source relative to the water surrounding it. It sampled every 30 sec.
- Acoustic Doppler Current Profiler (ADCP). The ADCP collected data continuously for the entire cruise. It was used during each deployment to measure the absolute water velocity profile beneath the ship to 800 m water depth in 16 m bins, each averaged over 5 minutes.
- C-Nav. With its global positioning system receiver on the A-frame, directly above the deployment of the source, C-Nav provided position estimates once per second at decimeter accuracy.

A dynamic prediction software package, WHOI Cable v2.2 (Gobat et al., 2000), was used to estimate source position. The forcing input data to the model were the ADCP and the C-Nav time series. The steps in the source localization modeling are outlined in the following sections. The source position and velocity predicted by the model are compared to the position and velocity estimated using the in-situ instrumentation packages deployed with the source at each ship stop. These comparisons produced high confidence in the dynamic modeling software to accurately predict the position and velocity of the source during each deployment, and thus the ability to measure travel times for source motion correctly.

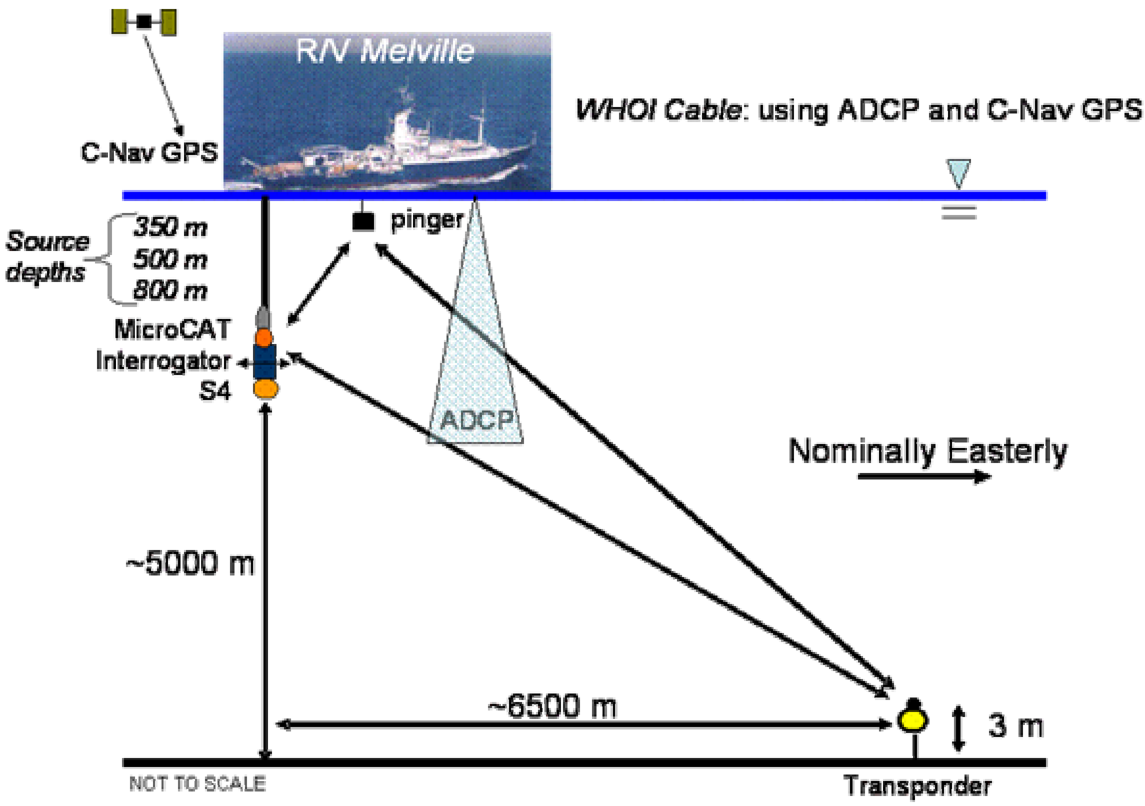

Figure 3.1. Source deployment instrumentation.
At each ship stop the acoustic source was instrumented as shown to estimate its motion during the transmissions.

3.1 Cable dynamics model

WHOI Cable v2.0 (Gobat et al., 2000) is a time domain numerical simulation tool for moored and towed oceanographic systems. It is used for mooring system design and allows the inclusion of typical ocean conditions and oceanographic mooring instruments and components. In the case of LOAPEX, the software is used in a 'towing' mode, forced by the position of the ship and the velocity of the water below the ship. During all source deployments, the ship was dynamically positioned.

The WHOI Cable solver is based on the governing differential equations for two- and three-dimensional static and dynamic problems (Gobat, 2000, and Tjavaras, 1996). These equations include parameters of bending stiffness, material nonlinearities, transverse and longitudinal drag, and Eularian coordinate transformations.

For both static and dynamic solutions, the mathematical problem is set up as a collection of coupled, nonlinear partial differential equations. The system of equations is solved numerically by discretizing the continuous forms of the governing equations using spatial finite differences centered on grid points defined by the user. This is known as the generalized-α algorithm which offers superior accuracy and stability when compared to the box method, trapezoidal rule and backward differences (Chung et al., 1993, and Gobat et al., 2002).

At each step of the solution, the system of nonlinear equations is discretized and solved by an iterative, implicit, adaptive relaxation technique (Gobat, 2000, and Press et al., 1989). The initial guess for the solution in the static problems is calculated using a shooting method. For the dynamic solution the initial guess at each time step is the solution from the previous time step. For each iteration the equations are solved using a sparse Gaussian elimination algorithm for which the computational effort scales linearly with the number of nodes (Sherman, 1978).

The input parameters for the software are shown in Table 3.1. For reference, Appendix 2 provides screen captures of the WHOI Cable model on a PC platform.

Table 3.1. Input parameters to WHOI Cable.

Ship/Platform	
ADCP Profiles	Timeseries
GPS position (C-Nav)	Timeseries (converted to velocity by model)
Cylindrical Source	
Diameter:	1.1 m
Height:	2 m
Buoyancy:	5976 N
Mass:	2409 kg
UNOLS 0.680" Cable	
Horizontal Drag coefficient	1.5
Vertical Drag coefficient:	0.01
Bulk modulus:	11.1 MPa
Diameter:	17 mm
Wet mass:	8.1 kg/m
Static Elongation:	1.6 m (800m with 2400 kg)
Medium (Seawater)	
Density:	1025 kg/m^3
Gravity:	9.81 m/s^2

3.2 C-Nav

Throughout the duration of the LOAPEX cruise, the position of the ship was continuously monitored and recorded by C-Nav. The C-Nav system was rented for the LOAPEX cruise aboard the R/V *Melville* from C&C Technologies, in Lafayette, LA. The C-Nav antenna was placed on the A-frame of the R/V *Melville*, directly above the deployment point for the acoustic source (Figure 2.2). C-Nav provides world-wide dual-frequency corrected GPS coverage. The dual frequency corrects for ionospheric errors, while data from globally distributed ground stations are used to correct for GPS satellite ephemeris errors, GPS clock error, and other atmospheric effects in real time via a geostationary satellite downlink. Position is sampled at 1 Hz. The position accuracy is sub-decimeter. Figure 3.3 shows the regions of coverage for the globally corrected global positioning system. A rectangle indicates the area of the LOAPEX ship stations. At stations T2300 and T3200, the satellite receptions were intermittent due to low declination of the satellite orbit combined with interference with the ship's superstructure. These two stations, at the western end of the boxed region, lie in the transition zone between two satellite coverage zones.

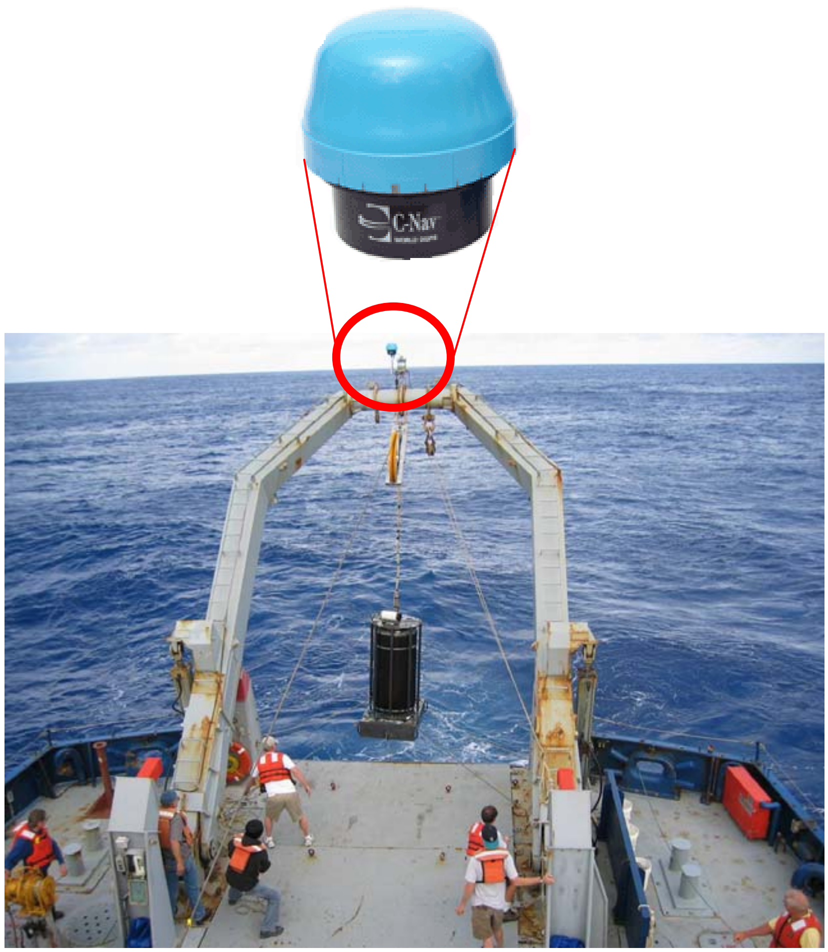

Figure 3.2. C-Nav receiver antenna.

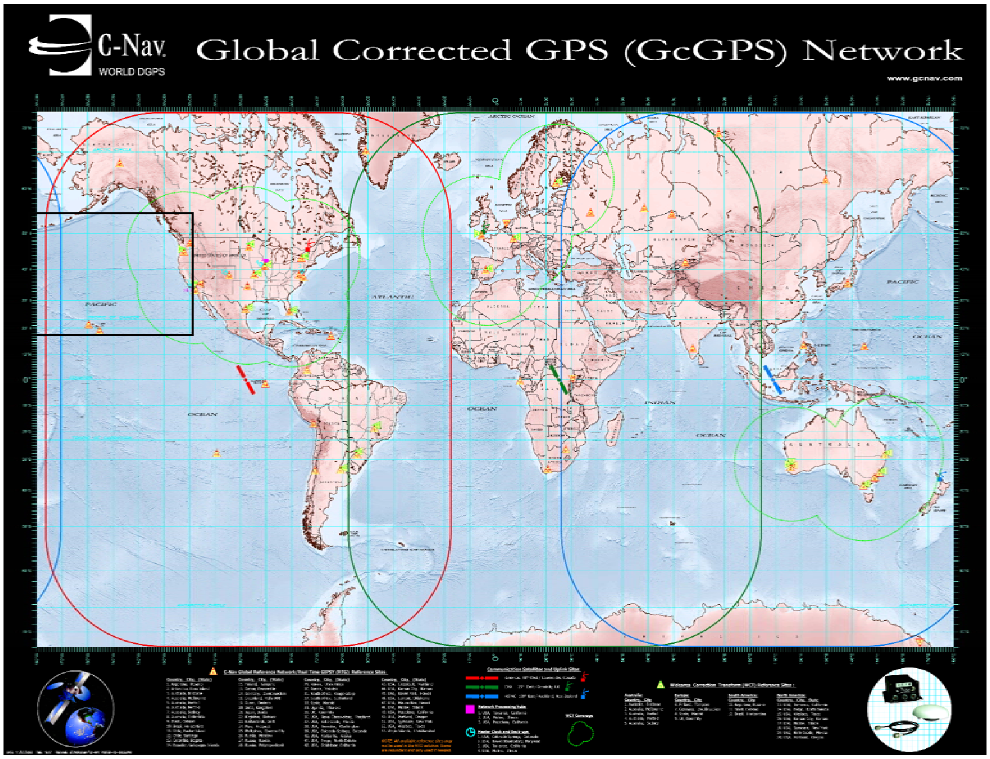

Figure 3.3 Global C-Nav satellite coverage.

In addition to time, latitude, longitude and altitude, the C-Nav records other parameters that help indicate the quality of the received signals and accuracy of the position estimates. An example of these ancillary parameters is shown in Figure 3.4. All of the LOAPEX station C-Nav data are plotted and presented in Appendix 3. The top plot in Figure 3.4 is the number of satellites in view. For the GPS receiver to unambiguously determine its position it needs data from a minimum of four satellites so it can triangulate its position, as well as determine its own clock offset. Receiving additional satellite-receiver ranges creates an over-determined problem and improves the accuracy of the position estimation. The second plot shows the age of correction (CornAge), or how long in seconds since the last correction reception from the geostationary satellite. The correction age was almost always about 10 sec. Higher numbers, growing to 1000 sec on occasion, indicate low accuracy, and possible drifting of the position estimate. The third and fourth plots show the vertical and horizontal dilutions of precision (VDOP and HDOP), respectively, which are measures of how well the position is estimated based on the quality of GPS position estimate. The final plot shows the figure of merit (FOM), which is the overall quality of the position estimate. It is calculated using the values of the number of satellites in view, dilutions of precision and correction age.

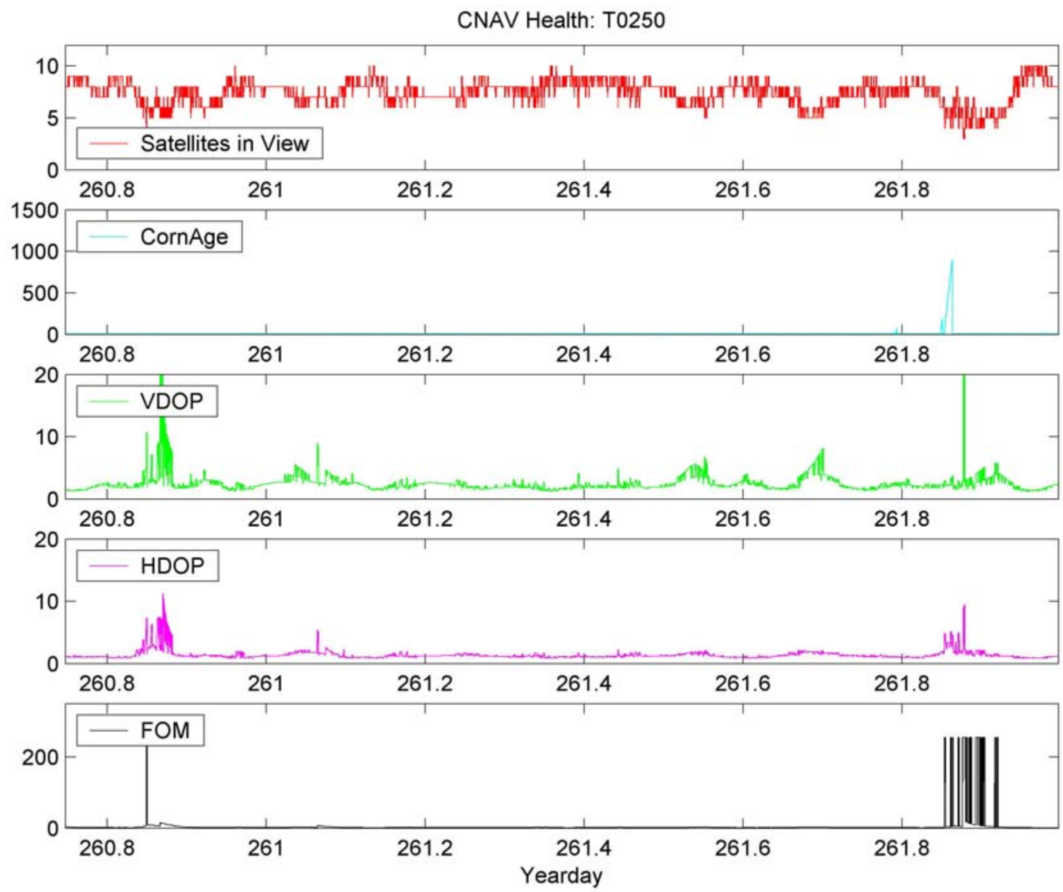

Figure 3.4. C-Nav position quality parameters for 31 hours at T250.

Through postprocessing, times of a low number of satellites in view, or high FOMs, or high DOPs can be flagged in the C-Nav output as having low accuracy, thus indicating a lower confidence in the resultant source position prediction. For example, in Figure 3.4, during the time window of 261.85 and 261.90, the CornAge was greater than 500 s, thus requiring adjustment prior to inputting the position information into WHOI Cable. The adjustment of the data included high-pass filtering with a 30-s cutoff to remove any potential of position drift due to the long correction ages. Table 3.2 shows all of the times during LOAPEX where the data was processed with this high-pass filtering. As shown, this occurred during less than 2% of the duration of the LOAPEX cruise, and the length of time of poor data (i.e. times of very high FOM values) remained short. Station T3200 is unique in that it has periods of good and bad data are grouped together. To simplify the processing the entire window shown was filtered, although there were periods of good data included. The filtering effectively smoothes the position data and removes any long-term drifts due to low number of satellites in view and high dilutions of precision. The data may have been poor in these regions because of low declination angle of the available satellites, and/or blocking of the satellite reception by the superstructure of the R/V *Melville* to the C-Nav antenna.

Table 3.2. Time windows of questionable C-Nav receptions.

Station	**Windows of Poor Data** (yearday of 2004)		**Duration** (days)
	start	end	
T50	---	---	---
T250	261.9000	261.9050	0.0050
T500	---	---	---
T1000	---	---	---
T1600	269.5900	269.5950	0.0050
T2300	273.8100	273.9600	0.1500
T3200	276.9500	276.9800	0.0300
	277.1500	277.5600	0.4100

Measurements made near the pier in San Diego prior to the departure for the LOAPEX cruise confirm the ability of C-Nav to provide high precision with no bias over longer term measurements on the order of source deployment stations. The R/V *Melville* is outfitted with two other GPS systems, a Trimble dual frequency P-code receiver and a Furuno single frequency GP-90 receiver. The pierside quantitative comparison showed the C-Nav to be superior in precision. The quantitative comparison is shown in Table 3.3. Approximately 9.5 hours of data are shown in Figures 3.5 and 3.6a. The C-Nav data are uniformly smooth and the deviations about the mean position shown in Table 3.3 are an order of magnitude lower than for the other two GPS systems. Also, both the P-Code and the C/A Code data showed significant jumps and a wide range of variability. The small motion of the ship is also included in the statistics. The sinusoidal variation in the C-Nav vertical motion corresponds to the tidal signal of San Diego. The tide tables for the harbor predict a 1.12-m peak-peak tide change between a low at 0838 and a high at 1528 UTC (during yearday 253). This 1.12-m signal is nearly exactly measured by the C-Nav system (Figure 3.6).

Table 3.3. *R/V Melville* on-board GPS system comparion.

	C-Nav	Trimble	Furuno GP-90
RMS/Pk-Pk (m)	RTG-Dual	P code	C/A code
East/West	**0.11/0.86**	**0.66/5.14**	**0.88/9.8**
North/South	**0.12/0.97**	**1.20/6.67**	**1.1/8.33**
Vertical	**0.40/1.39**	**2.36/17.3**	**2.1/16**

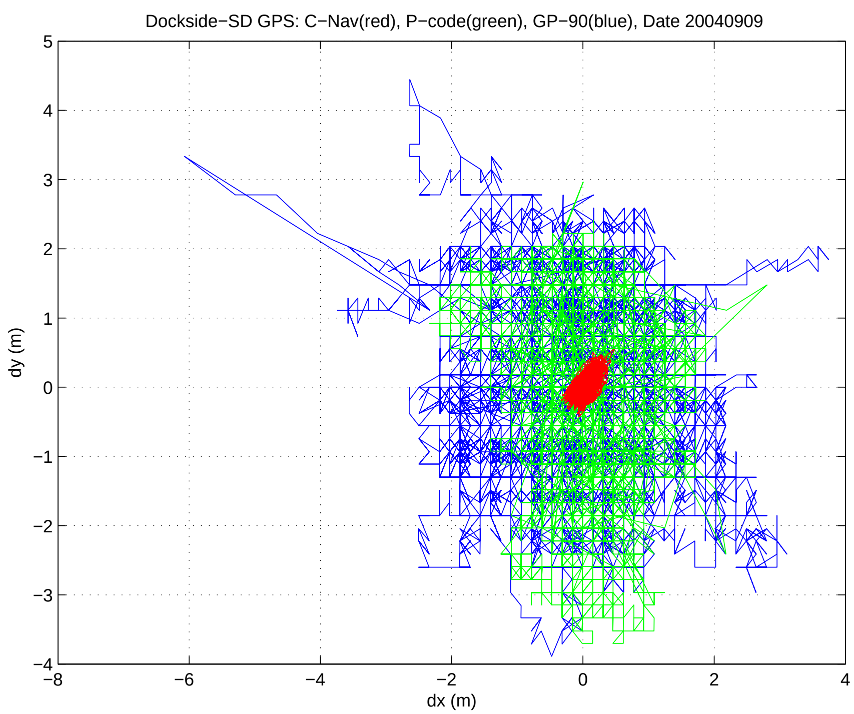

Figure 3.5. R/V Melville on-board GPS system comparison.

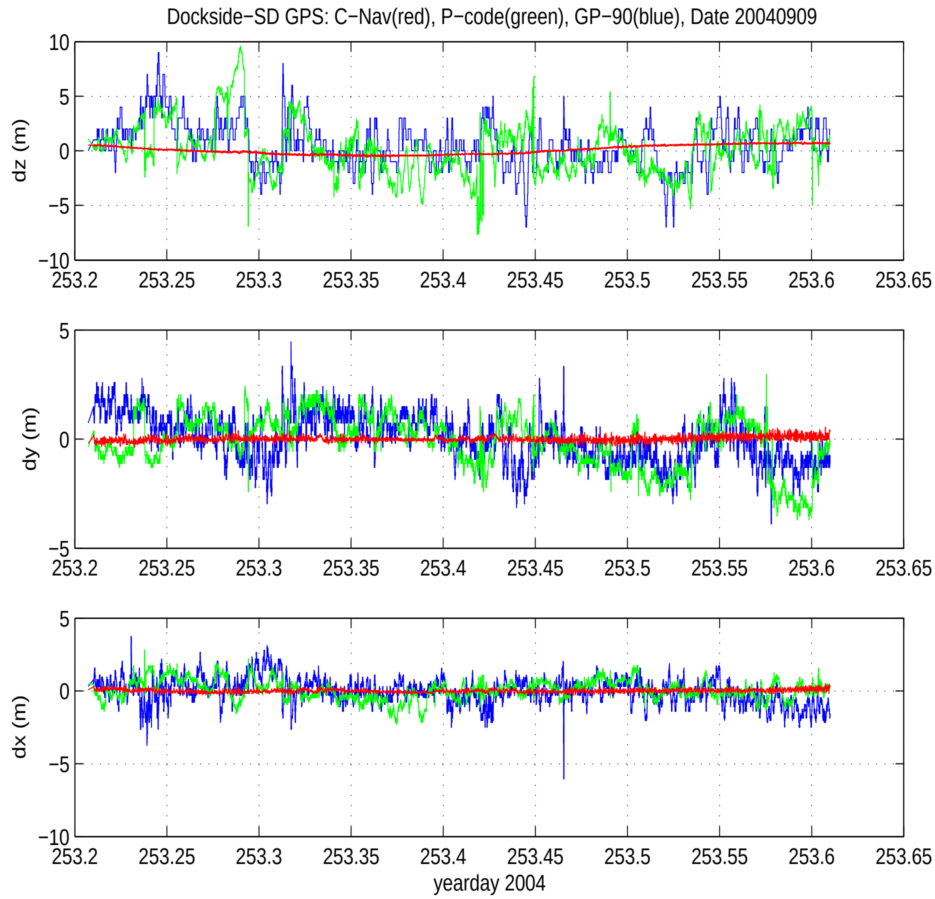

Figure 3.6a. Vertical and horizontal comparison of on-board GPS systems.

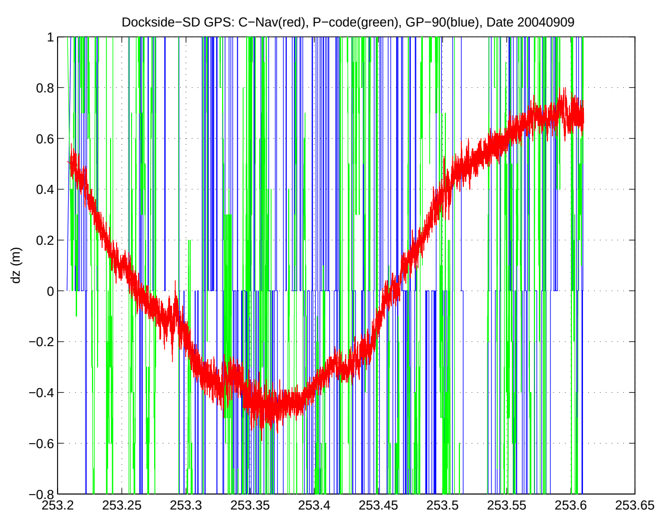

Figure 3.6b. Expanded vertical comparison of on-board GPS systems.

3.3 Acoustic Doppler current profiles

The RD Instruments Ocean Surveyor 75-kHz ADCP time series from each transmission station are shown in their entirety in Appendix 4. Figure 3.7 shows the data from LOAPEX station T250, which is representative of all the LOAPEX stations. In Appendix 4 the plots are arranged in paired pages, with the first page showing the time series of the absolute horizontal velocity magnitude and direction, in m/s and degrees, respectively. The second page shows the absolute horizontal velocity north and east components and the absolute vertical velocity, both in m/s. The horizontal axes for each plot are the year days during which the source was suspended at the specific station. The vertical axes are depth. As one can see, no measurements are shown below 800m, which is the approximate depth limit of the ADCP because of the weak return signal from the few scatterers at this depth. According to the manufacturer, the depth range, with the 16-m depth bin used during the cruise, is 560-700 m with the ship stationary. The data received down to 800 m is a windfall for the application for the source modeling. For velocity the manufacturer specifies an accuracy of ±0.5 cm/s for the deepest bin and the 5-minute averaging used.

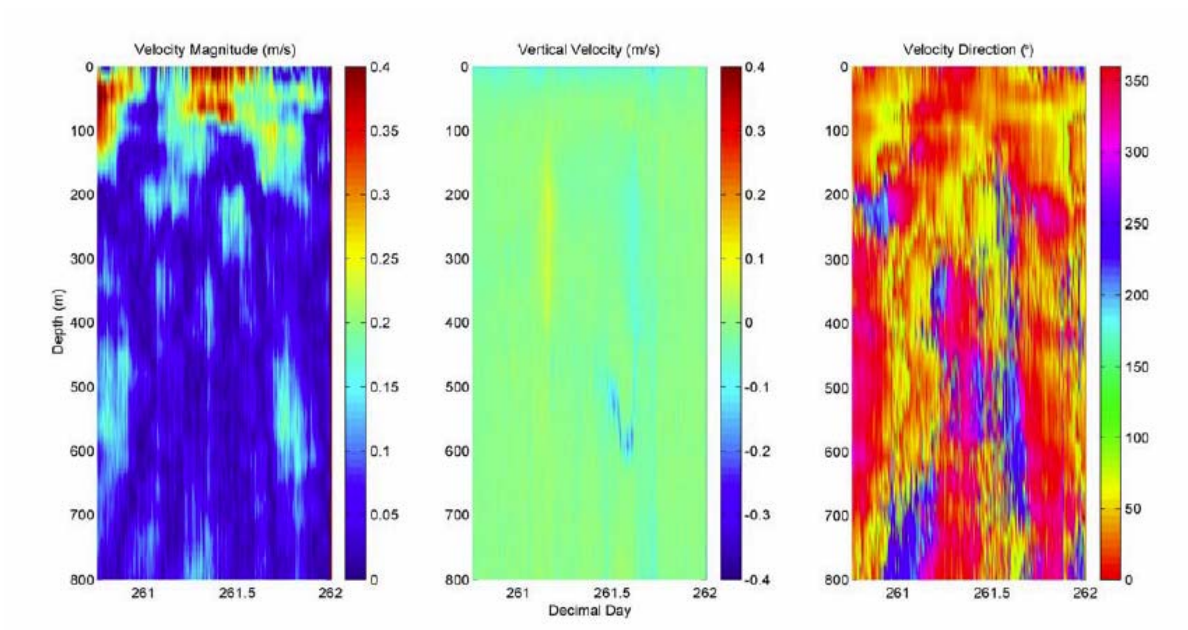

Figure 3.7a. Acoustic Doppler current profile at station T250.

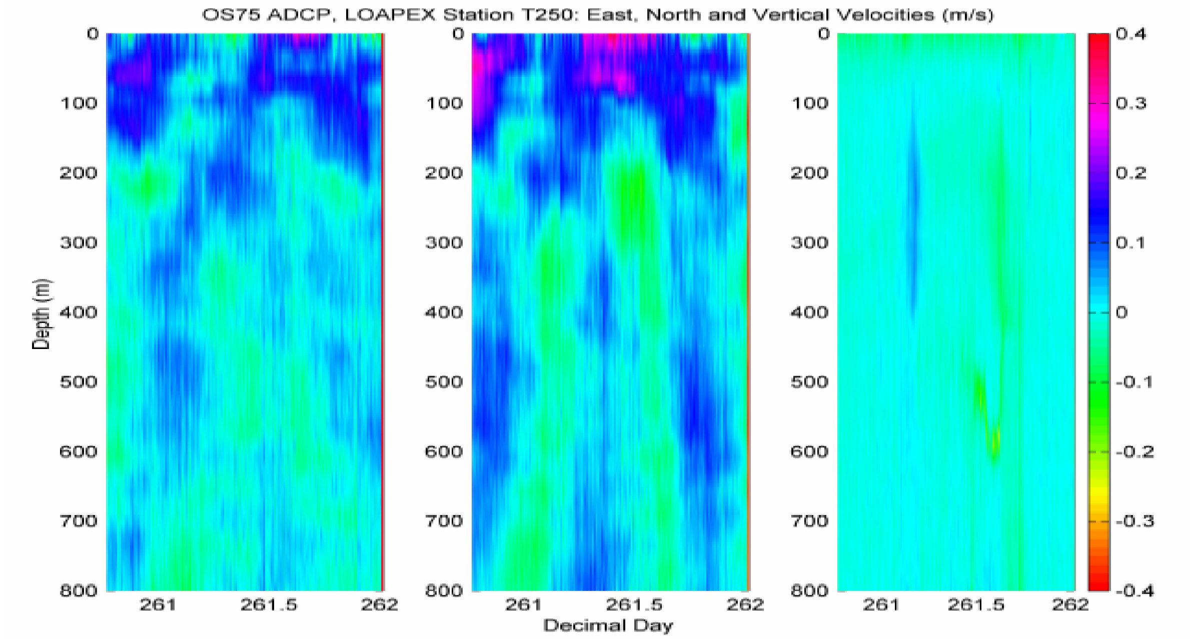

Figure 3.7b. Acoustic Doppler current profile for station T250.

To create the absolute velocity components of the current beneath the ship, the movement of the ship was removed using the P-Code GPS signal from the on-board Ashtech GPS receiver. The C-Nav was not integrated into the ADCP due to the short time available to network the systems prior to departure.

The ADCP collected data averaged over depth bins and time ensembles. Depth bins, or cells, are windows along the entire profiling depth that are each individually averaged. This averaging reduces the effects of spatial aliasing and noisy data. The depth bins used started at 24 m and continued downward at 16 m intervals to 800 m total.

The ADCP measured and recorded a velocity profile every minute. These measurements were then combined so as to create 5-minute (0.003472 year day) averages, or ensembles. By collecting five minutes worth of current data and averaging, the measurement uncertainty and random errors introduced by the positioning systems are reduced, producing more consistent absolute velocity averages.

To quantify the effect the local currents have on source displacements, the depth-averaged current velocity was determined for station T250 when the source was at 800 m depth (Figure 3.8). Clearly, the currents are small. Over the time series shown, the mean current has a magnitude of 3.9 cm/s and a direction of 62.4°. The position of the source and the ship during this deployment is shown in Figure 3.9. The plot shows 31 hours of data. The ship position was determined by C-Nav, and the source position was determined from WHOI Cable model, which used the ADCP and the C-Nav GPS ship position as forcing data. The mean current of 3.9 cm/s towards 62.4° caused a 2-3 m shift of the source position over the duration of the deployment in the general northeast direction. Values similar to this 3.9 cm/s were recorded the other stations. WHOI Cable uses the initial position given by ship position, and the initial ADCP profile to determine a zero position for the source. As the model progresses forward in time, the source position is estimated from these forcing functions. A complete set of the plan-view plots of the ship/source positions during each source deployment (Figure 3.9) are shown in Appendix 5.

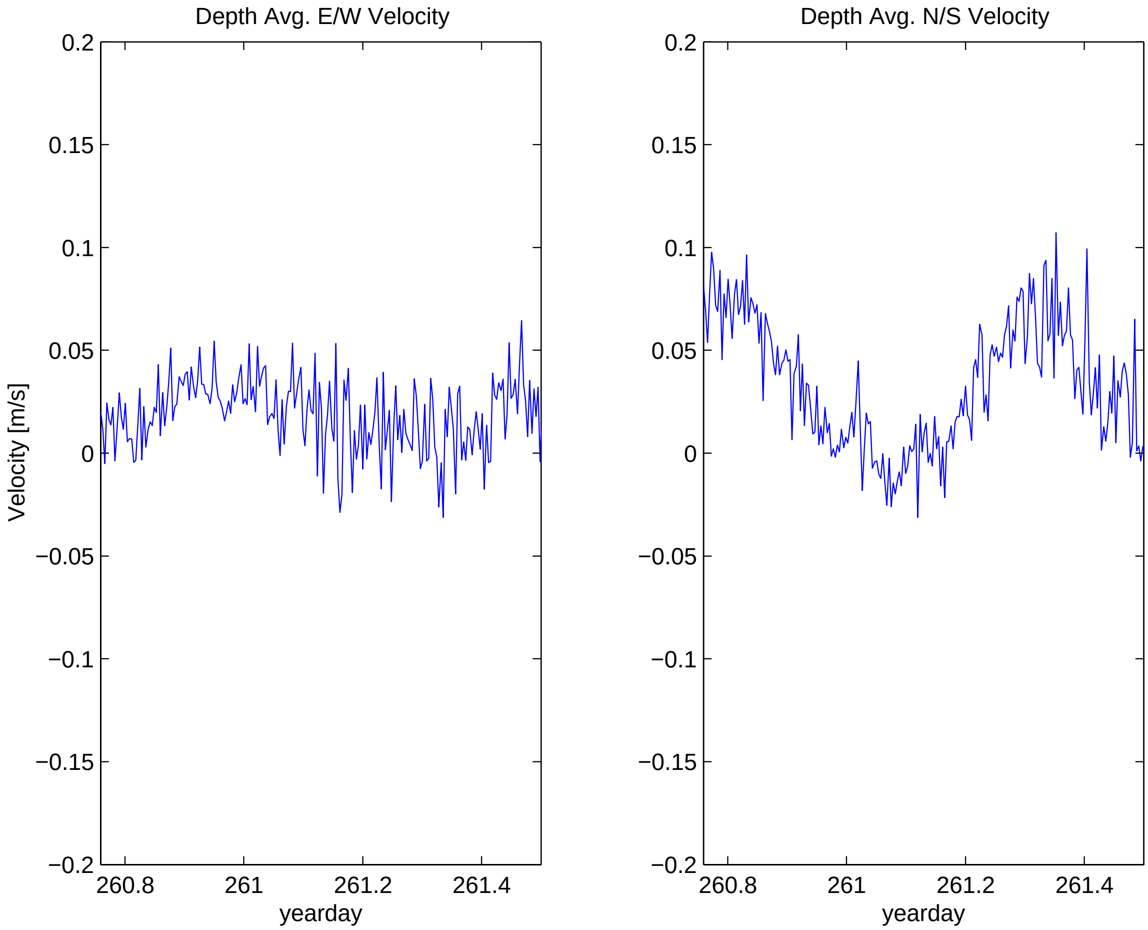

Figure 3.8. Depth averaged current during source deployment to 800 m at T250.

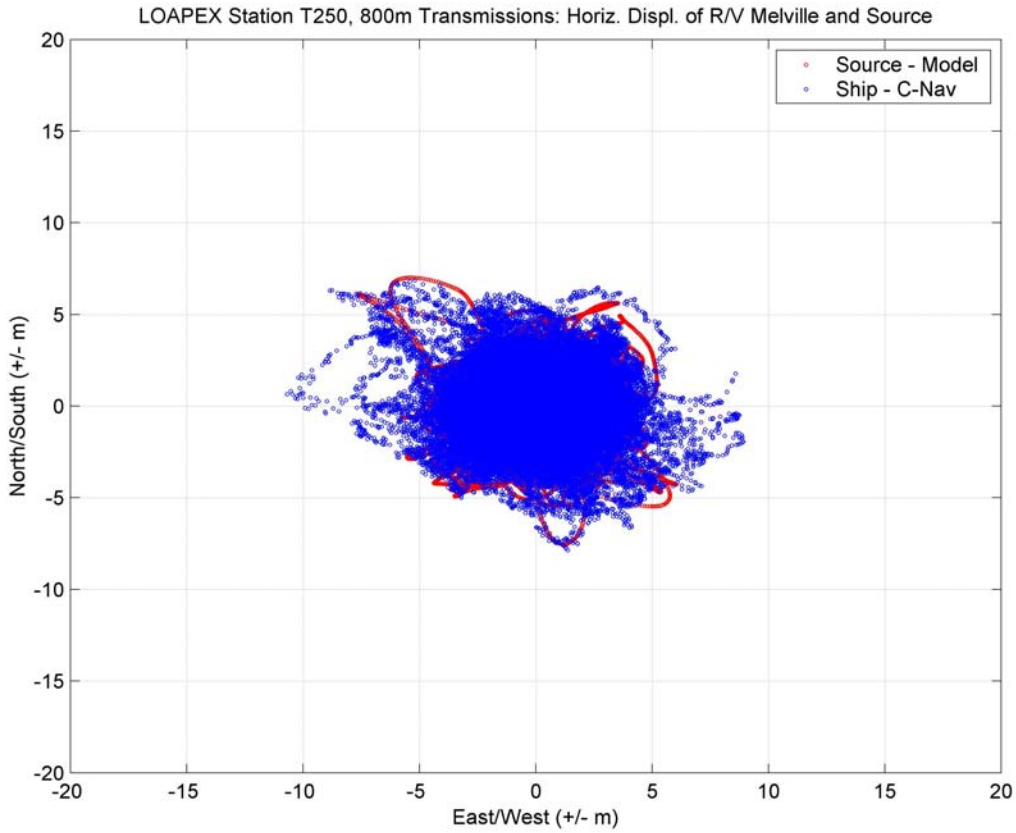

Figure 3.9. Plan-view of source and ship position during the 800 m source deployment at ship station T250.

3.4 Drag coefficients

WHOI Cable has not been used previously to model a ship-deployed source configuration. To determine what values to use for the cable and source drag coefficients, a sensitivity study was performed. A representative 30-minute portion of source position data from station T3200 was used for this study because T3200 was the most dynamically active station with rougher seas and higher winds affecting the ship's ability to station keep using dynamic positioning. The cable model was run with the same C-Nav position and ADCP data series as input for each trial. Estimates of the initial drag coefficients were based on previous similar studies of Yoerger et al. (1991); Grosenbaugh et al. (1991); and Alexander, (1981). For the cable, values of 1.5 for the transverse, and 0.01 for the longitudinal coefficients were used. For the source, it was modeled as a cylinder with an initial transverse coefficient of 0.6. WHOI cable does not require a longitudinal coefficient for the source. For the sensitivity study the transverse drag coefficients were halved and doubled for the cable and for the source, in independent trials. A plot showing all trials is shown in Figure 3.10. The effect of the source drag coefficient on the positioning of the source by WHOI Cable was negligible, thus the cable transverse drag coefficient dominates. The large range of cable drag coefficient values changed the source position by less than one meter. Therefore, the literature-based cable transverse and longitudinal coefficients of 1.5 and 0.01 were used for all source position time series. The source transverse coefficient of 0.6 was held constant as well.

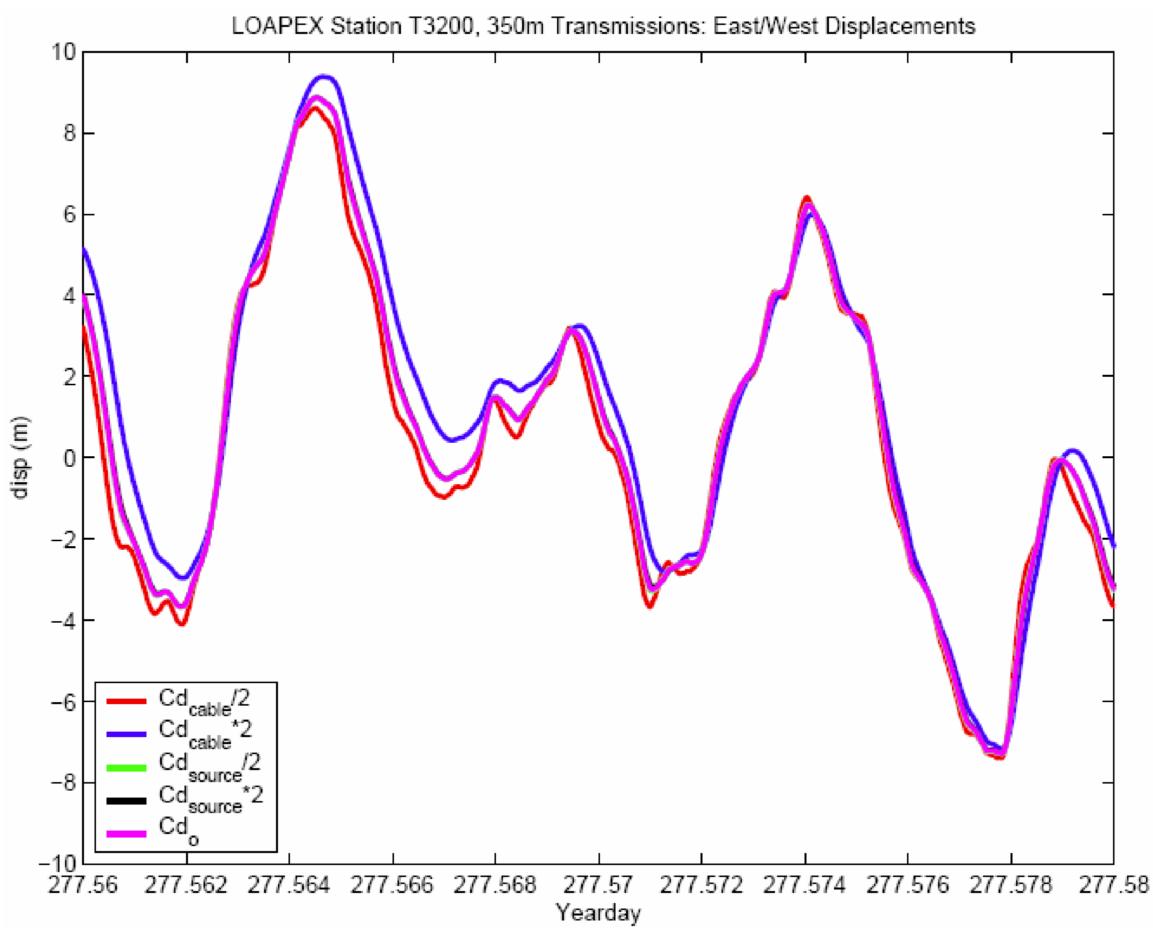

Figure 3.10. Source and cable drag coefficient sensitivity study results.

3.5 Source positioning comparison

In-situ measurements were used during each ship-stop to independently measure the position and velocity of the source (Figure 3.1). Results from these measurements compared with the WHOI Cable estimates are very similar, thus giving high confidence that the cable model can accurately predict the dynamics of the source from the C-Nav and ADCP forcing.

3.5.1 Interrogator/transponder

To provide the best direct measure of the horizontal position of the source while deployed and transmitting, a 'skeleton' long baseline acoustic navigation system was deployed using an interrogator/transponder pair. The interrogator was installed 20 m above the nominal acoustic center of the source on the deployment cable. The transponder was pre-deployed approximately 6 km in the direction along the geodesic towards the VLA from the source deployment position. The deployments resulted in source position measurements along the nominally eastward direction. Because of constraints on available ship time, the positions of the transponders were not surveyed: their positions were approximated using the known surface drop position and the depth of the water as measured by the ship's echosounder.

The source motion along the geodesic to the VLA is determined by the interrogator/transponder pair from

[1] $$\delta x = \frac{-C_o}{\cos\theta_o}\delta t$$

where C_o is the nominal sound speed (1480 m/s), θ_o is the ray angle from the source to the transponder using the approximate (straight-line) geometry, and $\delta t = (tt\text{-}tt_o)/2$ is the perturbation travel time, where tt and tt_o are the measured and average round trip travel times, respectively. The interrogator sampled every 3 s for station T3200, but sampled every 6 s at the earlier stations.

The estimated δx, the C-Nav ship position, and the WHOI Cable model output for 30 minutes of deployment time at station T250 are shown in the top panel of Figure 3.11. These interrogator, ship and modeled source comparisons are included in their entirety in Appendix 6. Interrogator/transponder time series for stations T50, T1000, and T2300 were not included in the appendix due to incorrect interrogator initialization causing short, intermittent data to be recorded. The lower panel of Figure 3.11 shows a comparison of the north/south ship position and the source position estimated using WHOI Cable. The offset between the ship and the source is thought to be caused by currents. During this time window, a nominally southward current of approximately 2 cm/s is evident in the ADCP time series.

The interrogator/transponder time series was highly variable because of a low signal-to-noise ratio. To reduce the variability of the time series, the data was windowed between a manually specified start and stop time, and then median filtered using a 30-s window. Also, a known 66ms/hr increase, or time shortening, internal clock error was removed. The result of these processing steps is shown in Figure 3.12. The interrogator/ transponder time series very nearly overlays the source position, except for the beginning of the data set. The difference between the interrogator/transponder time series and the source position time series after yearday 260.97 is likely caused by the limited number of clean samples for the interrogator/transponder. For instance, eliminating the five points lying between 260.965 and 260.968 and below -3.5 m would show a higher correlation of the compared time series. Another feature of the curve shown in Figure 3.12 is the approximate 6-minute oscillation. The longer ship position record for this station reveals this east/west oscillation for periods of about one hour. The ship was dynamically positioned for all stations and the reaction of this system to correct the position of the ship nominally followed a five to ten minute cycle.

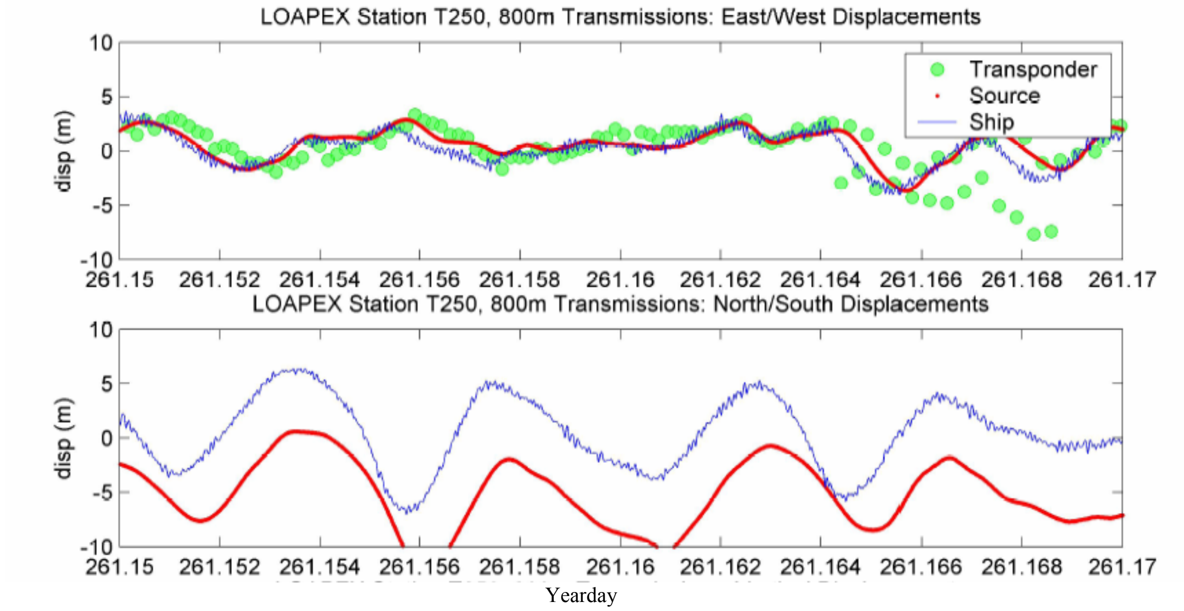

Figure 3.11. Position comparison: station T250.

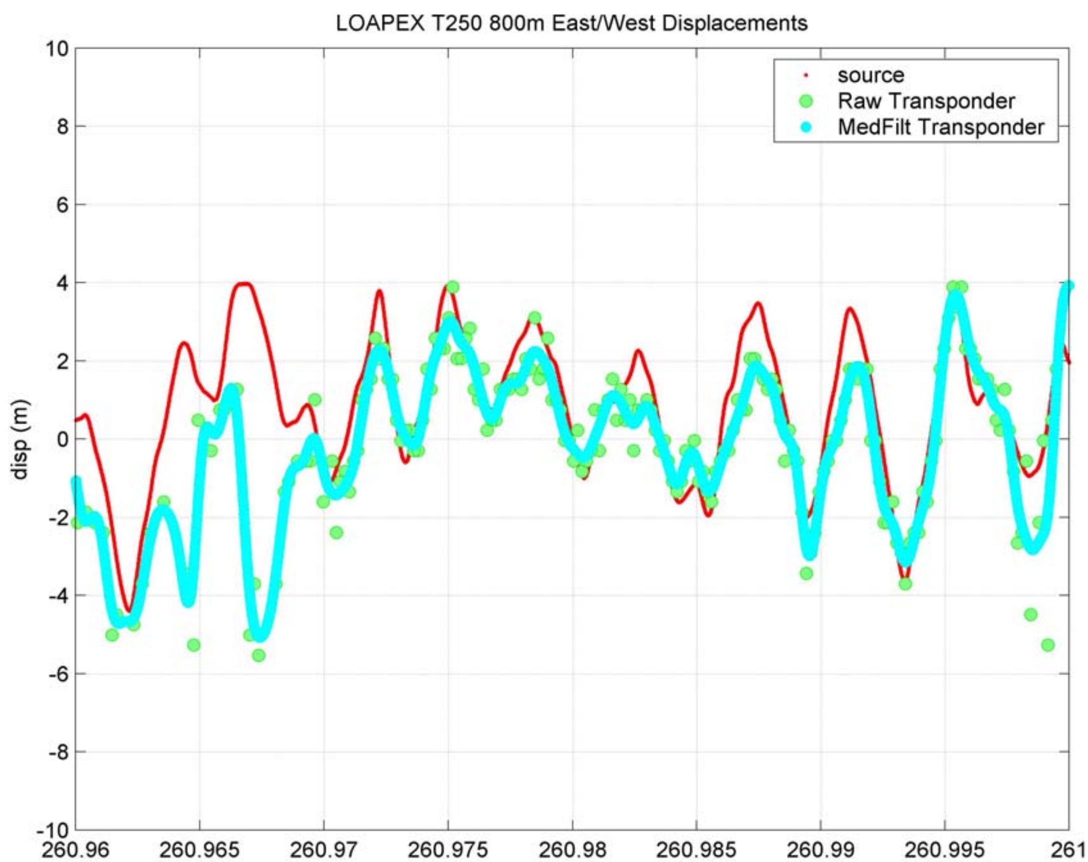

Figure 3.12. East/west position comparison: station T250.

A summary of all of the source position comparisons between the interrogator/ transponder and WHOI Cable model is shown in Table 3.4. The root-mean-square difference between the source position predictions from WHOI cable and the interrogator time series averaged 1.5 m over all ship stops. This value is considered good because the source position during the LOAPEX deployments varied roughly between ±10 m. The correlation coefficient R_{xy} remained acceptably high with a value of 0.84 averaged over the values at each ship stop. For station T3200 large temporal lags between the time series were measured when the source was at 500 m depth. These values are likely due to an offset introduced to the time series when the instrument pair was initialized, and also reset during the source deployment time series. In summary, the average correlation coefficient between the model and the interrogator was a relatively high 0.84, with a maximum of 0.96 and a minimum of 0.71.

Table 3.4. Comparison between measured and predicted source position using WHOI Cable and the interrogator/transponder pair.

Station	Depth (m)	R_{xy}	Lag (sec)	rms diff (m)	Lag (corrected) (sec)
T50	350 800	n/a n/a	n/a n/a	n/a n/a	n/a n/a
T250	350 800	0.82 0.77	-5.0 -7.0	1.5 1.7	-1.7 -3.2
T500	350 800	0.93 0.96	-2.7 -2.7	1.6 1.4	-0.5 0.1
T1000	350 800	n/a n/a	n/a n/a	n/a n/a	n/a n/a
T1600	350	0.82	-1.3	0.6	2.3
T2300	350 500	n/a n/a	n/a n/a	n/a n/a	n/a n/a
T3200	350 500	0.85 0.71	-8.0 -27.3	1.50 2.2	-4.70 -24.4

3.5.2 Vertical source motion: MicroCAT

A Seabird MicroCAT was deployed to measure pressure approximately 20 m below the acoustic center of the source. The MicroCAT also measured temperature, but the temperature time series was not used here. Initial comparisons between the measured MicroCAT depth versus time and the C-Nav GPS vertical motion showed the amplitude of the MicroCAT was approximately 60% of the amplitude measured by the shipboard C-Nav GPS. The MicroCAT acquired 6-second averages logged every 15 seconds, thus smoothing the averaging and aliasing the time series by only taking one sample in 15 seconds; this explains the estimated 60% reduction in amplitude. Figure 3.13 shows a comparison of the MicroCAT measurements overlaid with the source position prediction from WHOI Cable, and the vertical motion of the ship, as recorded by C-Nav. As one can see, the envelope of the MicroCAT time series is noticeably smaller in amplitude. Alternately, one may consider the dynamic stretch of the cable. This parameter is taken into account in WHOI Cable based on the effective modulus of the cable. However, the predicted tension of the cable was not measured during the source deployment, nor was it recorded from the WHOI Cable model predictions so its effects cannot be compared nor quantified. The effect of the stretch of the cable on the source position is estimated as negligible (approx. 1 m). Vertical time series for the LOAPEX stations when MicroCAT data were available is shown in Appendix 6.

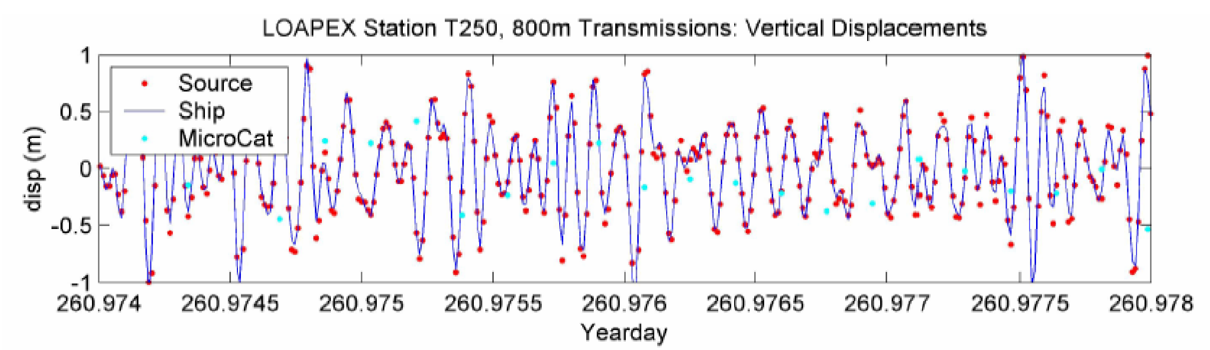

Figure 3.13. Measured and predicted vertical source position and vertical ship position for the 800-m deployment at station T250.

3.6 Source velocity comparison

Independent sensors were used during each ship-stop to measure the position and velocity of the source (Figure 3.1). The velocity sensor data for each station show similar trends and statistics as those predicted by WHOI Cable.

The InterOcean Systems, Inc. S4 current meter measures the voltage resulting from the motion of a conductor (i.e., seawater) through a magnetic field generated by the instrument. Faraday's law of electromagnetic induction defines the voltage produced in a conductor as the product of the speed of the conductor (seawater velocity) times the magnitude of the magnetic field times the length of the conductor. For the S4 the conductor length is the effective path between the sensing electrodes. The magnetic field intensity is generated by a circular coil, internal to the S4, driven by a precisely regulated alternating current. The use of an alternating magnetic field and synchronous detection techniques to measure the voltage at the sensing electrodes, provides an extremely stable, low noise current measurement. Two orthogonal pairs of electrodes and an internal flux gate compass provide the current vector (InterOcean Systems, 2005).

The S4 was deployed 10 m below the source to measure the velocity of the water relative to the source. The S4 sampled instantaneously every 30 seconds. Figure 3.14 shows the full time series captured by the S4 during deployment at T250 and Appendix 7 shows the recorded data from the S4 for all the LOAPEX stations. The spikes and steps at the beginning and the end of the time series are the result of deployment and recovery transients.

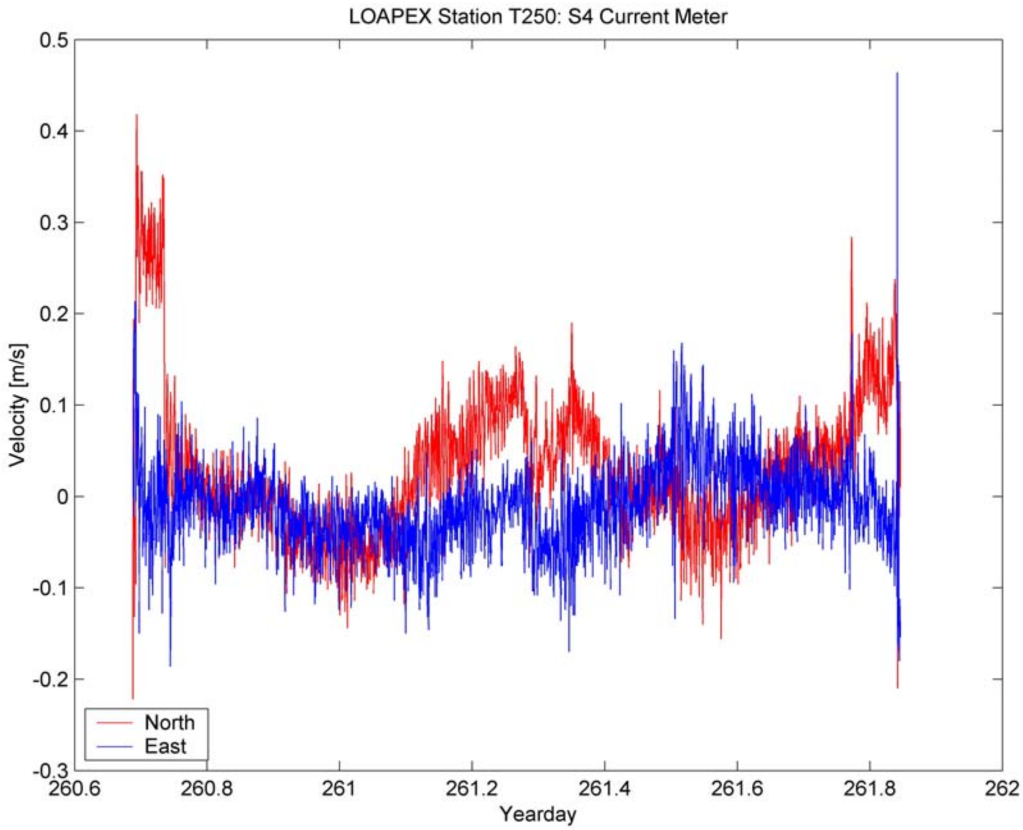

Figure 3.14. S4 current meter measurements at T250.

Combining the measurements made by the S4 and the absolute velocity of the water measured by the ADCP at the source depth results in an absolute velocity of the source. Figure 3.15 shows an expanded comparison of the velocity of the source, predicted from WHOI Cable, and source velocity estimated from the difference S4-ADCP from station T250 at 800 m depth. The predicted and measured low-frequency trends in the east/west and north/south source velocities compare well.

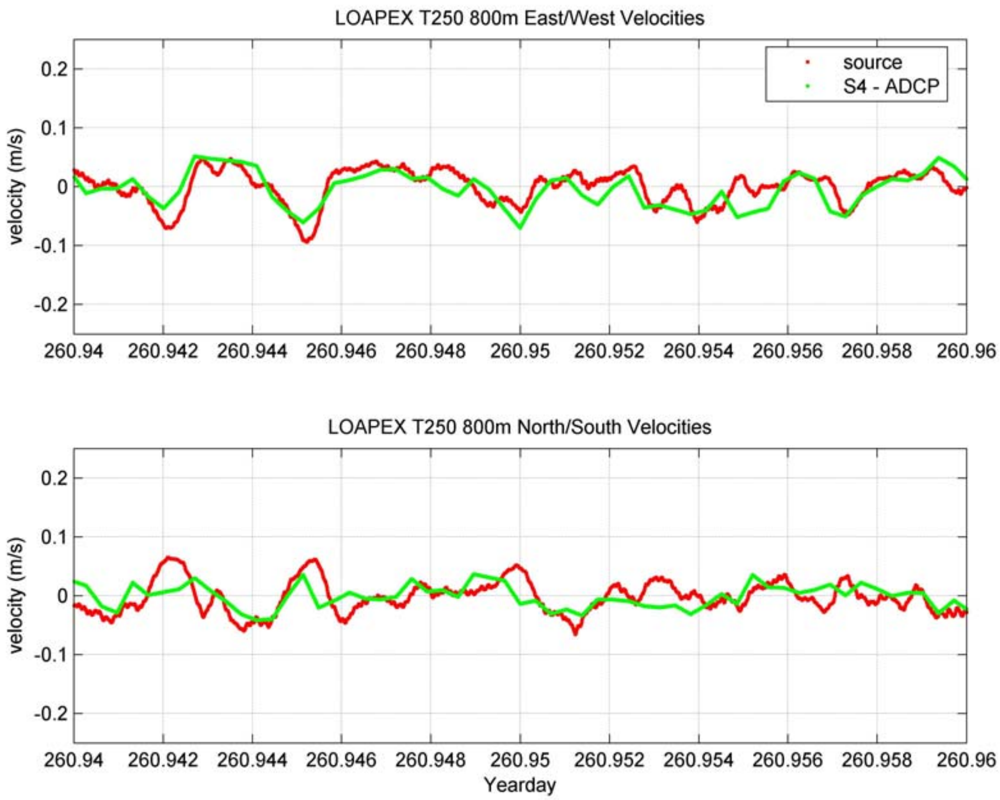

Figure 3.15. Expanded S4-ADCP vs. WHOI Cable source velocity comparison for T250.

Table 3.6 shows a quantitative comparison for all of the LOAPEX stations, based on the predicted WHOI Cable velocity, and the S4-ADCP difference calculation. Ideally, a higher correlation coefficient, and a shorter lag time are expected, but one must consider the ADCP is sampling deeper than its specified depth (<700m) and the mismatch in sampling frequencies between the S4 (30 s) and the ADCP (5 minute averages). During the LOAPEX cruise, the ADCP read data well to approximately 400 m. Velocity measurements below 400 m became increasingly unreliable with deeper depths based on the higher variability existing in the deeper measurements, which is not inherent to this region of the North Pacific. Also, the manufacturer specification states higher errors are present in time series deeper than 400 m. However, no spikes were present in the data due to the 5-minute averaging. To determine the absolute source velocity, the ADCP 5-minute bin averages to 800 m were subtracted from each of the 30-second readings of the S4 occurring within that five minutes. Certain stations, such as T250, T1000, T2300, have high lag times between the model and the measurements of 16, 13, 13 and 11 s, respectively. It is unclear what caused large lag times; an overly noisy time series resulting from the S4-ADCP calculation is possible. At station T3200, the correlation coefficients are small and the rms difference is large. The higher sea state present at this station, combined with the sample frequency difference between the S4 and the ADCP contributed to the poor comparison. All of the figures showing the data presented in Table 3.6 are in Appendix 8. Figure 3.16 shows a graphical correlation between the S4-ADCP subtraction and the predicted source velocity at station T250. In summary, over all stations, the average rms difference was 0.052 m/s, while the average rms source velocity from WHOI Cable was 0.54 m/s, and the average correlation was 0.5.

Table 3.5. Measured and predicted source velocity comparison.

Station	Depth (m)	Direction	R_{xy}	Lag (sec)	rms diff (m/s)	Window (hrs)	Yearday start	Yearday end
T50	350	E/W	0.670	2	0.042	11.6808	259.7083	260.1
		N/S	0.780	-1	0.039			
	800	E/W	0.270	-1	0.07	14.6472	259.1	259.7083
		N/S	0.320	-4	0.072			
T250	350	E/W	0.560	0	0.04	9.4008	261.3583	261.845
		N/S	0.450	1	0.048			
	800	E/W	0.467	16	0.042	14.5992	260.748	261.3583
		N/S	0.562	8	0.0312			
T500	350	E/W	0.570	2	0.036	15.8328	263.6002	264.2599
		N/S	0.690	-3	0.033			
	800	E/W	0.430	-2	0.042	19.9992	262.7669	263.6002
		N/S	0.590	-7	0.04			
T1000	350	E/W	0.654	6	0.0278	35.6136	265.772	267.2559
		N/S	0.632	13	0.0378			
	800	E/W	0.490	9	0.0448	7.44	265.45	265.76
		N/S	0.470	6	0.0438			
T1600	350	E/W	0.450	4	0.054	25.872	268.92	269.998
		N/S	0.640	-3	0.044			
T2300	350	E/W	0.351	13	0.0724	13.4088	273.4167	273.9754
		N/S	0.428	11	0.0566			
	500	E/W	0.365	2	0.0577	14.8008	272.8	273.4167
		N/S	0.439	2	0.0624			
T3200	350	E/W	0.603	3	0.0428	15.4896	277.507	278.1524
		N/S	0.505	4	0.0617			
	500	E/W	0.245	4	0.0886	15.9168	276.834	277.4972
		N/S	0.169	4	0.1152			

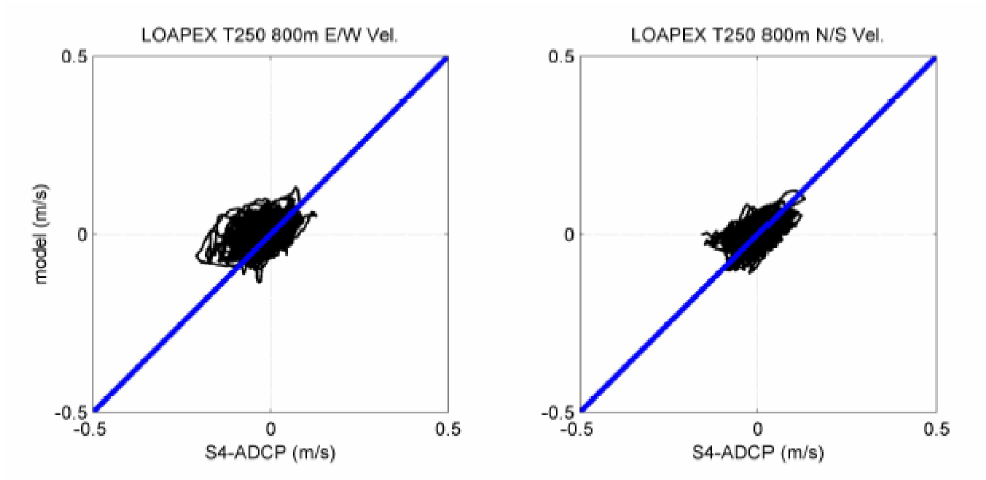

Figure 3.16. Correlation between modeled and measured (S4-ADCP) source velocity.

4 Acoustic Receptions

To extract scientific data from the acoustic signals provided by the LOAPEX transmissions, acoustic propagation analyses were preformed from all of the ship-stop locations to fixed receiver ‘r’. These analyses first involved propagation predictions made using ray theory where each eigenray is identified. These eigenrays are then matched with measured receptions based on the predicted and measured arrival times. These identified receptions are then tracked through each transmission in order to identify travel time perturbations. These travel time perturbations are then be analyzed for ocean variability along the identified path.

4.1 Propagation predictions

Over much of the world’s temperate oceans, the sound channel axis is characterized by a sound speed profile with a minimum at 800-1200 m depth. This sound speed minimum is caused by the strong dependence of sound speed on temperature and pressure. Sound speed increases with increasing temperature and with increasing pressure. In the upper ocean, as the temperature decreases with increasing depth, the sound speed decreases. As depth increases, the pressure increases. These two competing effects produce a wave guide or sound channel with an axis of minimum sound speed that focuses the acoustic energy and allows it to travel for great distances.

During LOAPEX, the sound speed minimum was at approximately 800 m. Figure 4.1 shows the sound velocity profiles between the position of T250 and the position of receiver ‘r’. These are based on temperature and salinity fields in the World Ocean Atlas as compiled by Levitus and colleagues (Levitus et al., 1994). The blue curve at the bottom of the figure represents the bathymetry between T250 and ‘r’ based on the database provided by Smith et al. (1994). The sound speed transects for all of the LOAPEX stations to ‘r’ are included in Appendix 9.

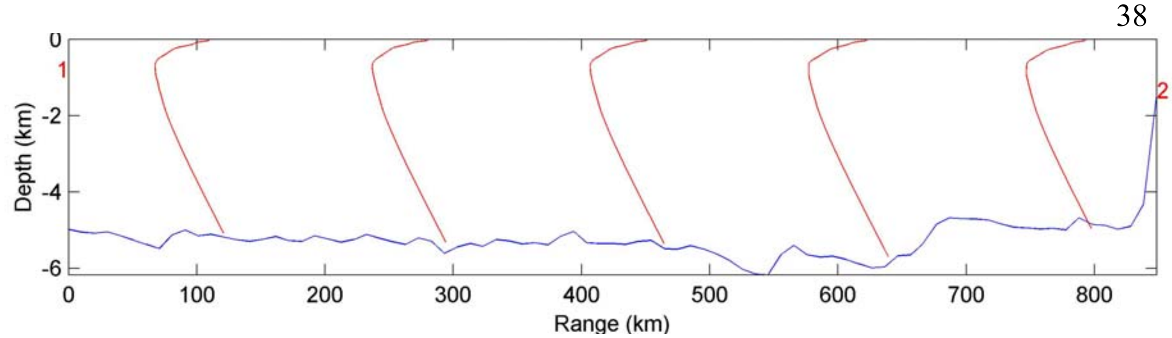

Figure 4.1. Sound speed profile transect between T250 (1) and ‘r’ (2).

Propagation modeling based on ray theory is used to predict the acoustic paths (eigenrays) between the LOAPEX source locations and the fixed receiver ‘r’. Rays travel perpendicular to the acoustic wavefronts and in the sound channel follow quasi-sinusoidal paths as they refract towards the depth of the sound speed minimum, and away from high sound speed regions.

Four different forms of raypaths occur in long-range acoustic propagation. The first type is a refracted-refracted (RR) ray. These rays never touch the surface, nor the bottom, but are refracted at their upper and lower turning points. The second type of ray is a refracted-surface reflected (RSR) ray, which refracts at its lower turning points, but reflects off of the surface at its upper turning (reflection) points. The third type of ray is a refracted-bottom reflected (RBR) ray, which is refracted at its upper turning point and is reflected off of the bottom at its lower turning point. The last type of ray reflects at both its upper and lower turning points and is called a surface reflected-bottom reflected (SRBR) ray. For the propagation modeling done here, only RSR and RR rays are considered. Bottom reflected rays are not considered due to their increased complexity once they have encountered the bottom. The launch angle (either positive or negative) and the number of turning points each ray passes through are both used to identify the rays. For example, a +23 ray has an upward launched ray at the source and 23 turning points before reaching the receiver. This ray is downward going at the receiver.

4.1.1 MAP Program

MAP is a Matlab graphical user interface (GUI) incorporating an extensive database using Levitus (1982) and Levitus et al. (1994) has been developed by Eggen (2005) and Dushaw (2003). MAP calls EIGENRAY, which is a Fortran code originally developed by Bowlin et al. (1992), and streamlined by Dushaw (2003). The bathymetry is extracted from the database along geodesics using the WGS-84 (1984) ellipsoid parameters. Horizontal refraction of the rays is not considered as this is negligible in the case (Dushaw et al., 1993). As in the examples shown above with the navigation and source position measurements, the acoustic propagation between station T250 and receiver 'r' are used as examples in the text.

4.1.2 Time front predictions

The acoustic predictions for the deep and the shallow source depths from T250 to 'r' are shown in Figure 4.2 and Figure 4.3, respectively. Three thousand acoustic rays were launched between ±15°. Removing the SRBR and the RBR rays results in only RR and RSR eigenrays, as shown in the top panel of the two figures. The rays are color coded by the receive angle, either positive or negative. The middle panels of Figure 4.2 and Figure 4.3 show the time front receptions for the T250 to 'r' path. These plots show the arrival depth (ordinate) and time (abscissa) of all 3000 rays launched from the acoustic source at the range of the receiver. The position where the time front intersects the receiver depth corresponds to the expected arrival time of that particular RR or RSR eigenray. The major difference between the deep and the shallow transmission predictions is the width of the doublets.

In the bottom panels of Figure 4.2 and Figure 4.3, the arrival time and arrival angle (an upward going ray has a positive receive angle) of each eigenray is plotted, along with the ray-loop identifier (i.e., number of turning points). The receiver is bottom mounted, therefore it is expected the upward going receptions will be heavily attenuated. Aligning the position of the identified arrivals with the time front plot show the downward going rays are represented by the negative slopes on the accordion plot. This pattern assists in the identification of the measured receptions (below). The eigenray predictions between all of the LOAPEX stations and ‘r’ are shown in Appendix 10.

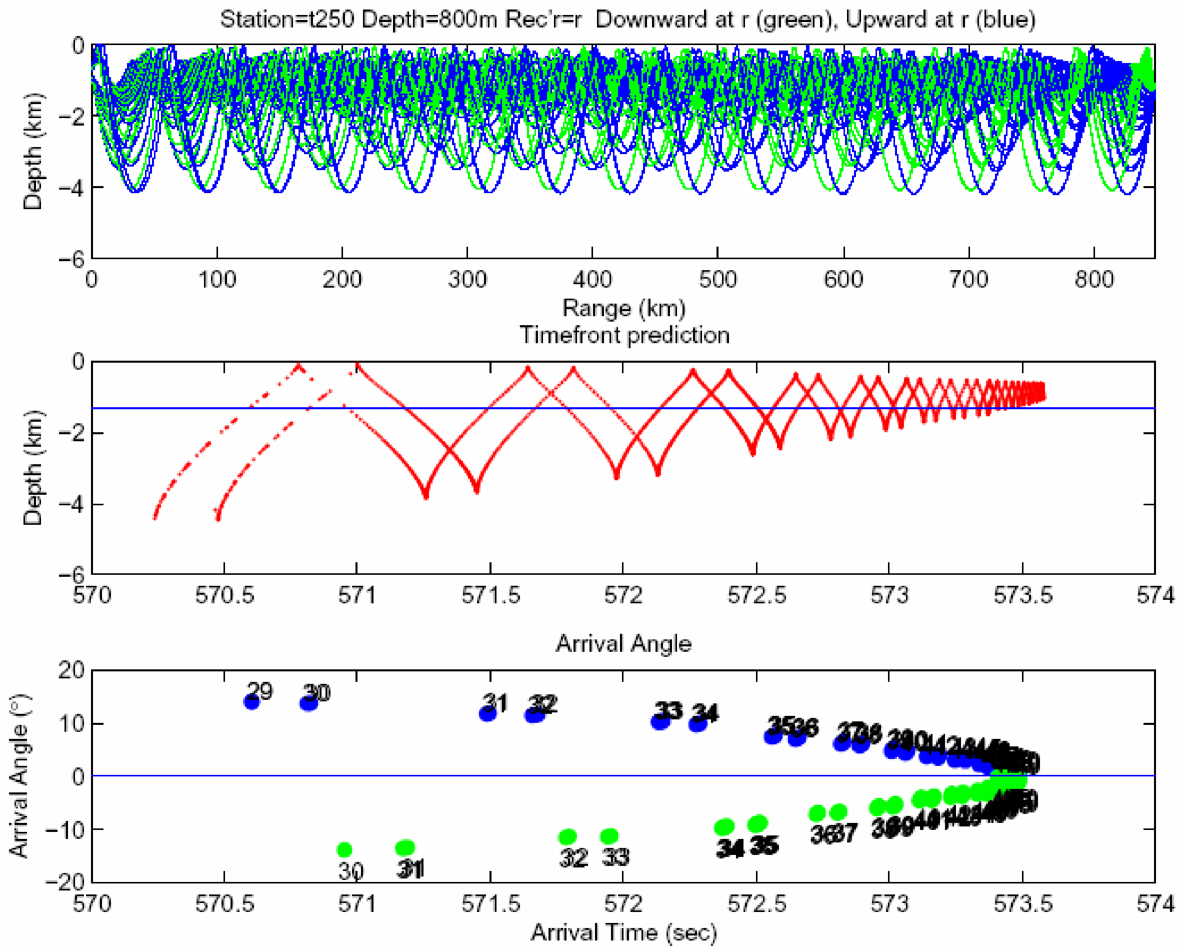

Figure 4.2. Eigenray predictions between 800 m transmissions at T250 and ‘r’.

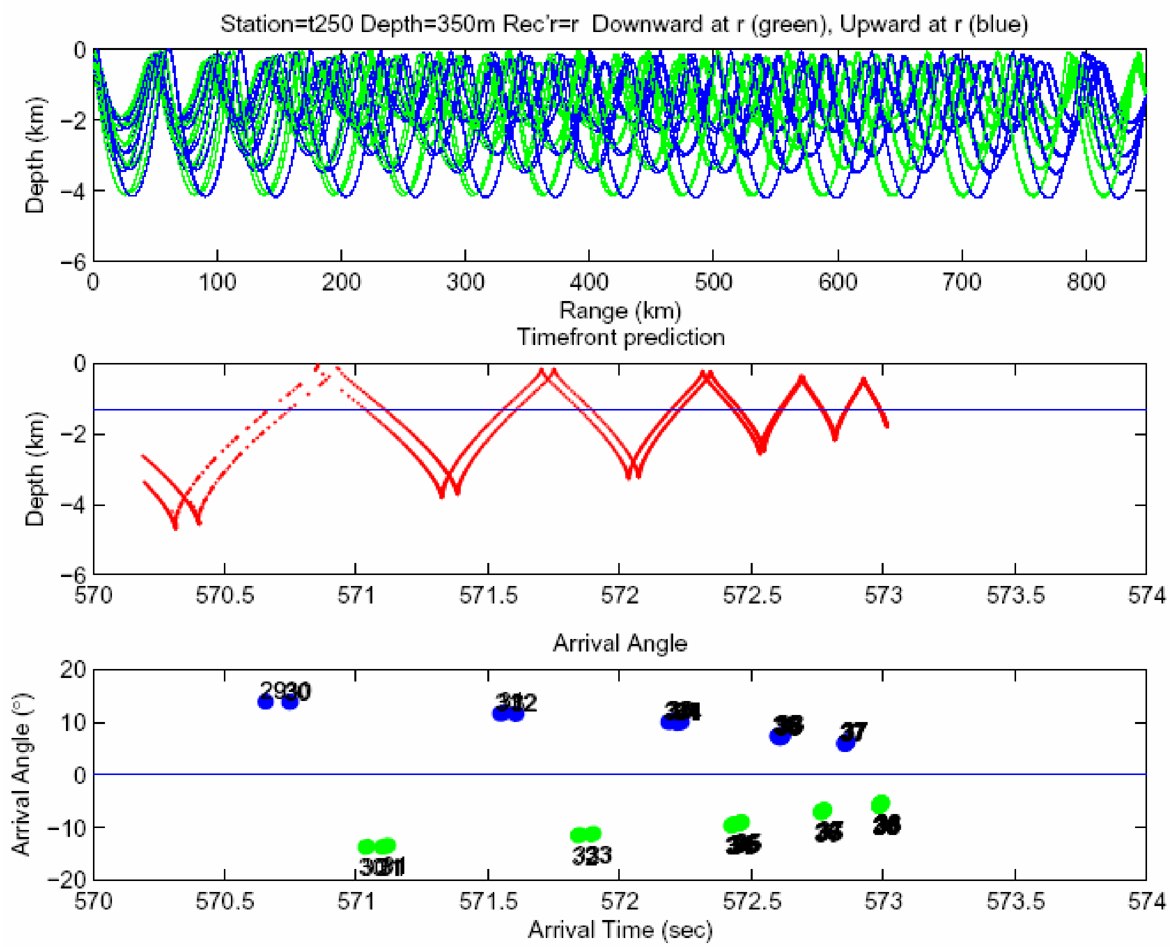

Figure 4.3. Eigenray predictions between 350 m transmissions at T250 and ‘r’.

Figure 4.4 combines all the predicted acoustic arrival patterns into one figure as a function of azimuth relative to receiver ‘r’, where 0° is due east from ‘r’ and increases counterclockwise. The reception lengths tend to shorten with shorter ranges because it was the northward stations from ‘r’ that had the closest proximity to ‘r’.

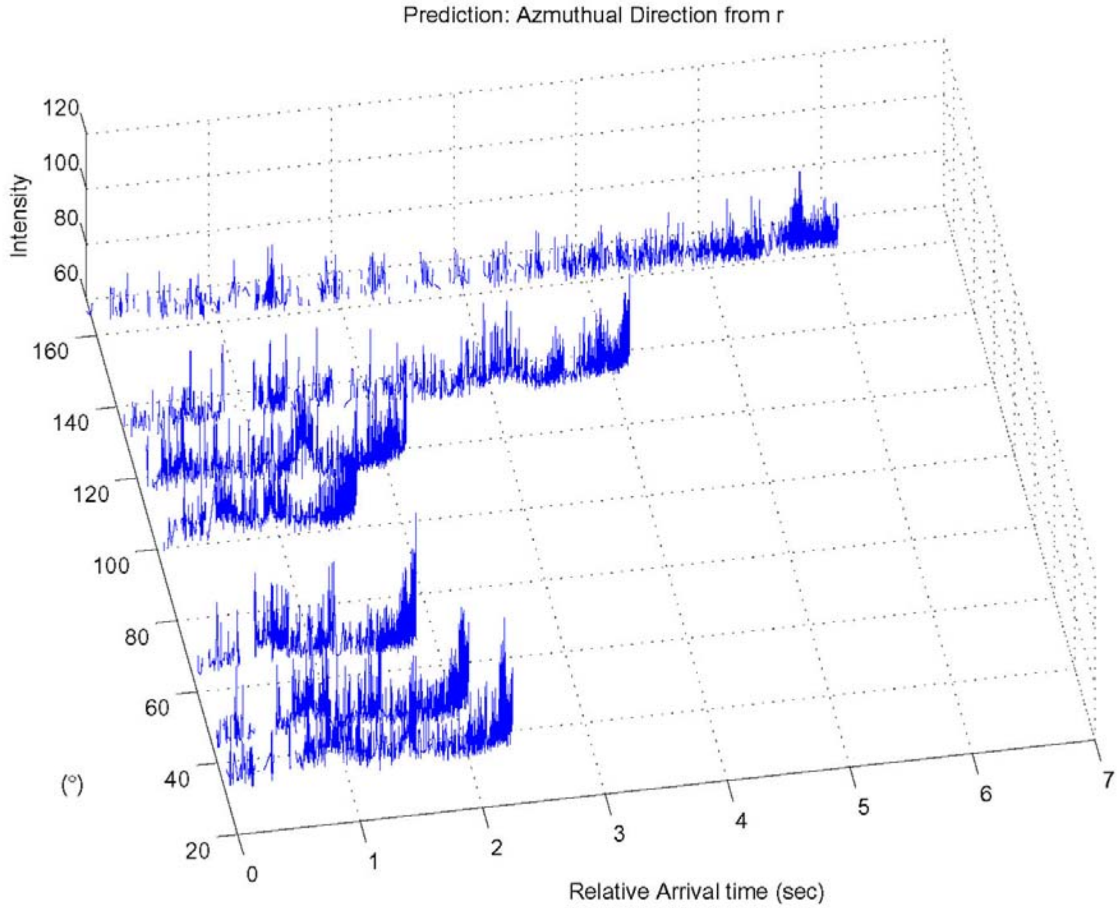

Figure 4.4. All station receptions at 'r' shown as a function of azimuth angle, where zero degrees is due east and increases counterclockwise.

4.2 Measured receptions

The receptions received at 'r' from stations T50 through T3200 are presented and discussed here. As before, station T250 has been used as an example when detail is called for. The predictions shown above were aligned with raw arrivals and each measured arrival peak was matched with a specific predicted ray (i.e., identified). Then the identified arrivals were tracked over time to produce a time series. These time series of tracked and identified arrival peaks are the data used in the subsequent analysis.

4.2.1 Acoustic arrival pre-processing

The signals received at 'r' from the LOAPEX deployed source transmissions required numerous processing steps to put them into a usable form. The processing included the following steps in order: circular coherent averaging of consecutive m-sequence transmissions, replica correlation processing, beamforming based on the orientation of the receiver, a second averaging to obtain further receive signal gain, and picking peaks as a function of arrival time and angle. Here, peaks only higher than a certain signal-to-noise threshold were retained; typical threshold values were approximately 12-14 dB. Figure 4.5 shows the individual steps of the signal processing in order to transform the initial hydrophone receptions to received time series. The process shown in Figure 4.5 is the same that has been used for the last 10 years with related ATOC and NPAL data.

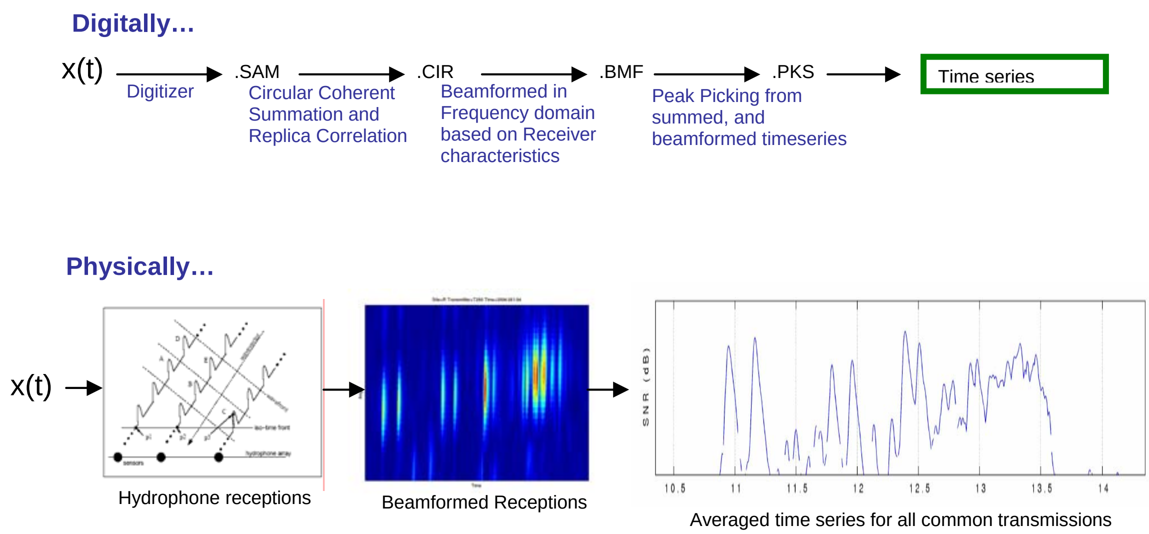

Figure 4.5. Processing steps performed on the received signals at ‘r’.

4.2.2 Received time series

For the T250 to ‘r’ receptions, the output of the beamformer is represented in Figure 3.6a. Extracting amplitude above a minimum SNR level versus time along a horizontal line across the middle of the plot gives the result shown in Figure 4.6b. Distinct peaks are evident. These peaks are used to compare with the predicted receptions (below).

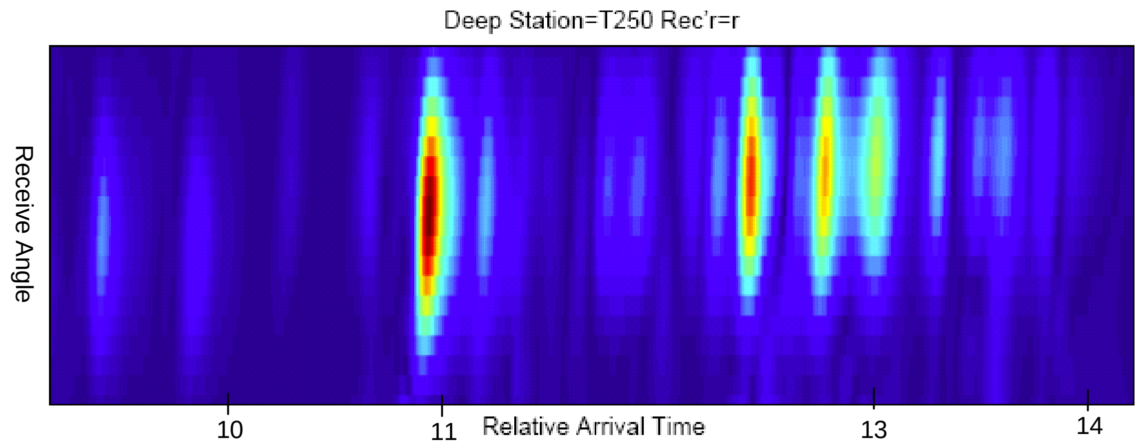

Figure 4.6a. Processed beamformed data received at 'r' from T250 800m transmissions.

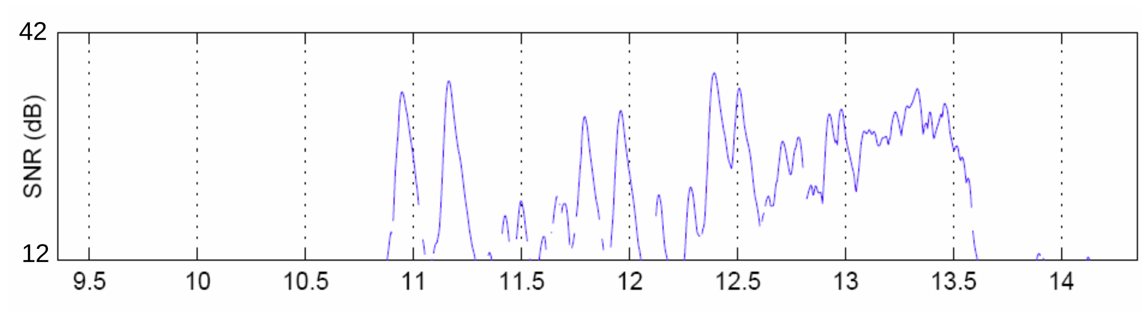

Figure 4.6b. A slice through the beamformed intensity plot in (a).

4.3 Comparison between measured and predicted arrivals – ray identification

To determine the difference caused by the ocean between the sources and receiver 'r', the prediction of the acoustic propagations were compared with the measured receptions. The World Ocean Atlas (Levitus et al., 1994) was used to perform the acoustic ray propagation modeling, and differences in the measured receptions reflect a change relative to the WOA.

Once the receptions have been processed, they are in a form that can be related and compared to the propagation predictions. An alignment of the receptions at 'r' from the 800 m and 350 m transmissions from T250 are shown in Figure 4.7a and Figure 4.7b, respectively. The top panel of each figure shows the predicted time front. The center panel shows the received time series as a cut through the beamformed plot shown above.

The bottom panel shows the arrival time and SNR level of each of the highest coherently summed m-sequence peak. The receptions after 573.5 sec are jumbled and likely contain energy scattered by the bottom in the vicinity of the receiver. It is the more distinct, early arrivals that are used for alignment purposes and subsequent analyses. Figure 4.8 shows all of the transmission receptions from T250 at ‘r’. This waterfall plot shows the deep transmission in blue and the shallow transmissions in red. The middle panels in Figure 4.7 show representative curves extracted from the beamformed plot for the reception. Figure 4.8 shows the doublet narrowing from the deep transmissions to the shallow transmissions, as also shown in the predictions. A complete set of LOAPEX receptions in this three panel format is shown in Appendix 11. Appendix 12 contains the corresponding complete set of the three-dimensional waterfall plots shown in Figure 4.8.

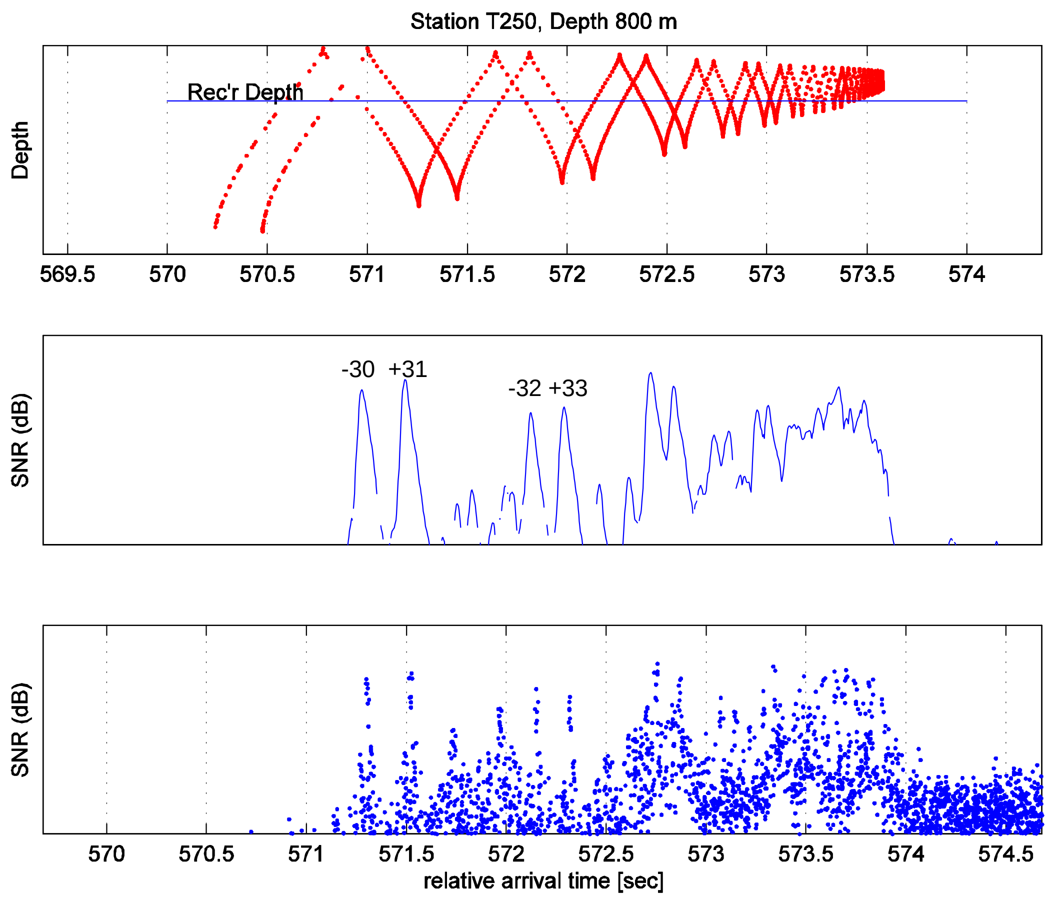

Figure 4.7a. Predicted time front and measured receptions with corresponding ray identifier of 800-m transmissions from T250 to ‘r’.

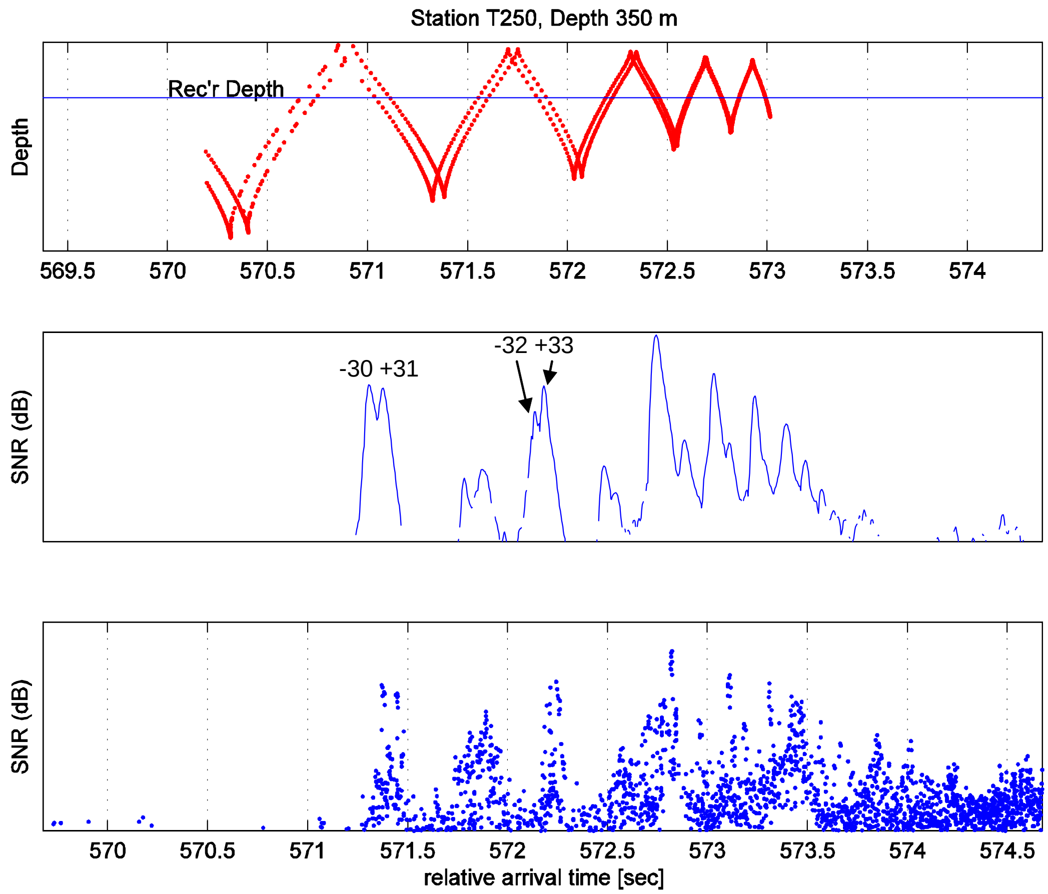

Figure 4.7b. Predicted time front and measured receptions with corresponding ray identifier of 350-m transmissions from T250 to ‘r’.

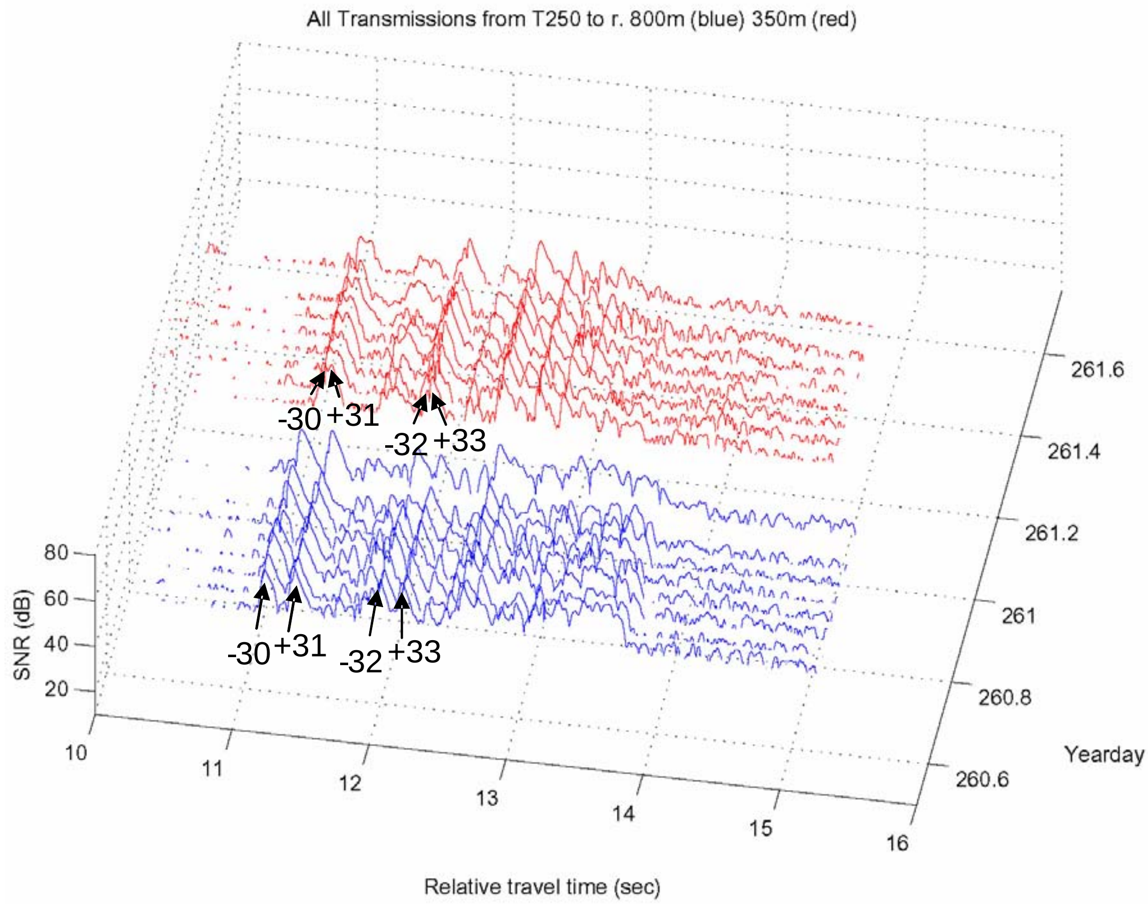

Figure 4.8. Waterfall plot of the receptions at 'r' from station T250. Ray identifiers determined from the acoustic predictions have been included.

To align the predictions with the measured data shown in Figure 4.7a and Figure 4.7b, 305 ms were added to the predicted travel times. This offset reflects ocean variability as well as hardware and software offsets. The hardware and software offsets are estimated from both the transmitter and the receiver, however, these values only amount to approximately 60 ms of lag time. Table 4.1 contains a summary of these estimated offsets. The source transmissions were processed through a CPU and amplifier prior to the actual transmission through the transducer into the water, where a majority of this delay is the transducer itself. This delay is estimated as 30 ±10 ms (Andrew, 2005). Once the signal is received at 'r', it travels along a bottom laid cable to a shore side data acquisition computer in Hawaii. This delay is estimated as 10 ±2 ms, based on electrical travel time along the cable of 2/3 the speed of light. The receiver electronics include filtering, which adds an estimated 20 ±5 ms delay (Andrew, 2005). These delays combine to yield a total estimated signal delay of 60 ±17 ms, assuming a random distribution. Taking 60 ms of nominal delay into account, leaves a total delay of 245 ms, which is the "ocean signal": the difference between the WOA and the actual measurements. Table 4.2 summarizes all of the time shifts required to align all LOAPEX measured receptions with their corresponding predictions. As noted in the table, the time corrections are all delays (lags), meaning the signal was arriving later than predicted, even after applying the adjustments. What this means for the temperature difference from WOA will be discussed below.

Table 4.1. Summary of nominal time delays introduced by the transmitter/receiver electronics and processing.

Measurement timing adjustments (ms)	
Transmitter Xdcr/Filter	20
Cable Delay	10
Receiver Digitizer/Filter	30
Total	**60**

Table 4.2. Summary of time shifts needed to align acoustic receptions at 'r' with predictions. All time lag values have been corrected with the engineering time lags mentioned in the text.

Time lag for allignment	
Station	**Lag** (ms)
T50	265
T250	245
T500	225
T1000	115
T1600	90
T2300	145
T3200	140

4.4 Reception variability

Referring to the initial predictions of the acoustic receptions, it was shown that time front segments with negative slopes in the accordion plot correspond to the downward going rays at the receiver. The alignments shown in Figure 4.7a and Figure 4.7b show the higher peaks of the received time series corresponding to the predicted downward going eigenray arrivals, confirming the assumption of very little received acoustic energy from upward going rays. However, there are measurable peaks corresponding to the positive slopes of the time front. For the purpose here, the higher, earlier identified peaks were tracked and analyzed.

At each station, the source was deployed 16-24 hours. During this time the source was held at two different depths. The source continuously transmitted 20-minute transmissions every hour during each deployment, therefore providing hourly transmissions over 16-24 hours from which the variations in the transmission travel time were made. Eighty-minute transmissions were also conducted, as well as modified m-sequence signals. These other types of signals were not analyzed in this thesis. The variations in the travel time from the analyzed 20-minute transmissions were then tracked through this 16-24 hour time window using the identified eigenray arrival peaks from the receptions. The major signal which contributing to the inter-transmission travel time variability was the multi-harmonic barotropic tidal oscillation. Because of the large influence of the tidal currents on the travel time (sound travels faster with a current than against), the tide offers a very good signal from which to investigate the robustness of the LOAPEX receptions. In the following sections the measured travel time data is compared with predicted tidal signals.

4.5 Predicted and measured tidal signal

In the ocean, as acoustic energy propagates through tidal currents it speeds up or slows down because it is either traveling with or against the current. The following defines the applicable travel time path integral:

[2] $$\tau = \int_{\Gamma} \frac{dx}{C(z)U(r,z)\cos(\theta)}$$

where τ is travel time, Γ is the path x, $C(z)$ is the sound speed and $U(r,z)$ is the flow velocity magnitude, in this case, the tidal current, and is modified by its azumith existing between the source and receiver.

Figure 4.9 shows a global view of the barotropic tidal elevation resulting from astronomical forcing; the area sampled by the LOAPEX transmissions is boxed. A tidal model, such as the one developed by Egbert et al. (2001), can be used to provide tidal velocity components. A software package by Dushaw (2002) extracts these tidal velocity components along the path between a source and a receiver and determines the travel time perturbation due to the tidal currents. The tidal influence to travel time varies between ±5 ms at T50 to ±12 ms at T3200. Relating these measurements to a path-averaged (along r, and z) current magnitude yields:

[3] $$\delta t = \frac{R}{C_o^{\ 2}} u_{avg}$$

where δt is the travel time offset τ, R is the range between transmitter and receiver, C_o is the nominal sound speed along the path given by r and z, and u_{avg} is the path averaged tidal current velocity. The paths investigated here vary in length and in orientation relative to the local tidal current direction and magnitude. The breaks in the station tidal signals represent specific times when the source was not transmitting, either due to the lowering or raising of the source, or due to ship transit.

Figure 4.10 shows the predicted tidal travel time signals for each of the LOAPEX transmissions to receiver ‘r’. Peak-to-peak travel time variability and resultant path averaged tidal currents from Figure 4.10 are shown in Table 4.3. The tidal current causes larger offsets over longer distances partly because of the range factor in equation [4] as well as the possibility of a contribution by the fortnightly tidal constituent.

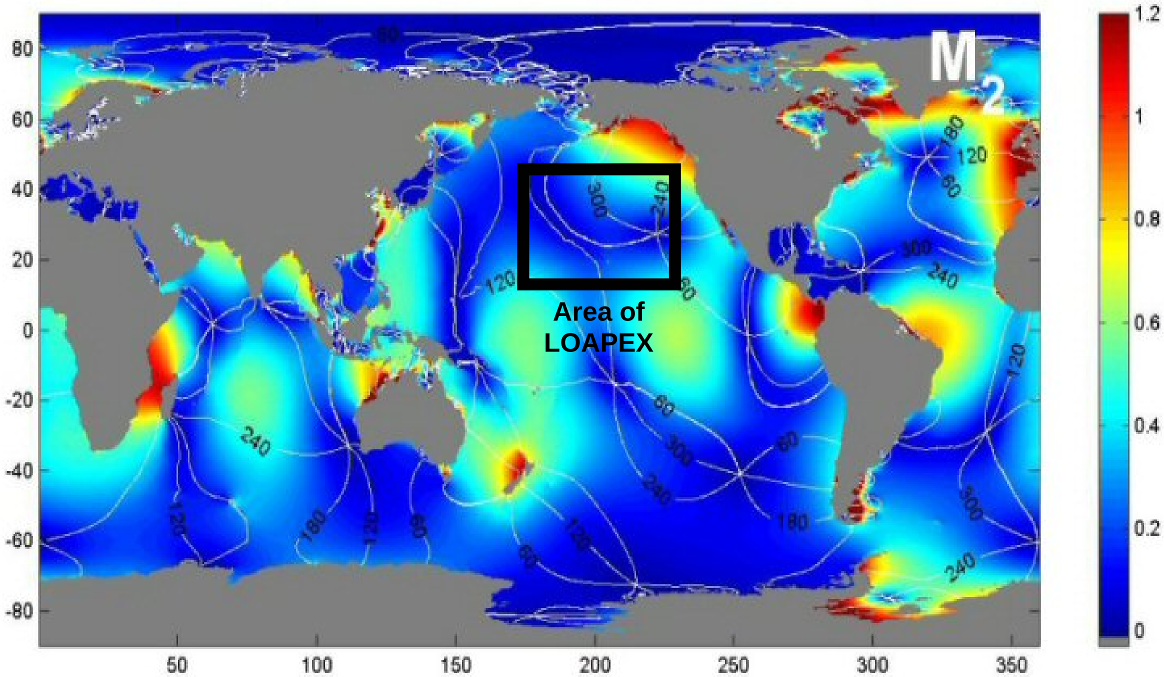

Figure 4.9. Barotropic tidal elevation (color scale) and co-tidal lines.

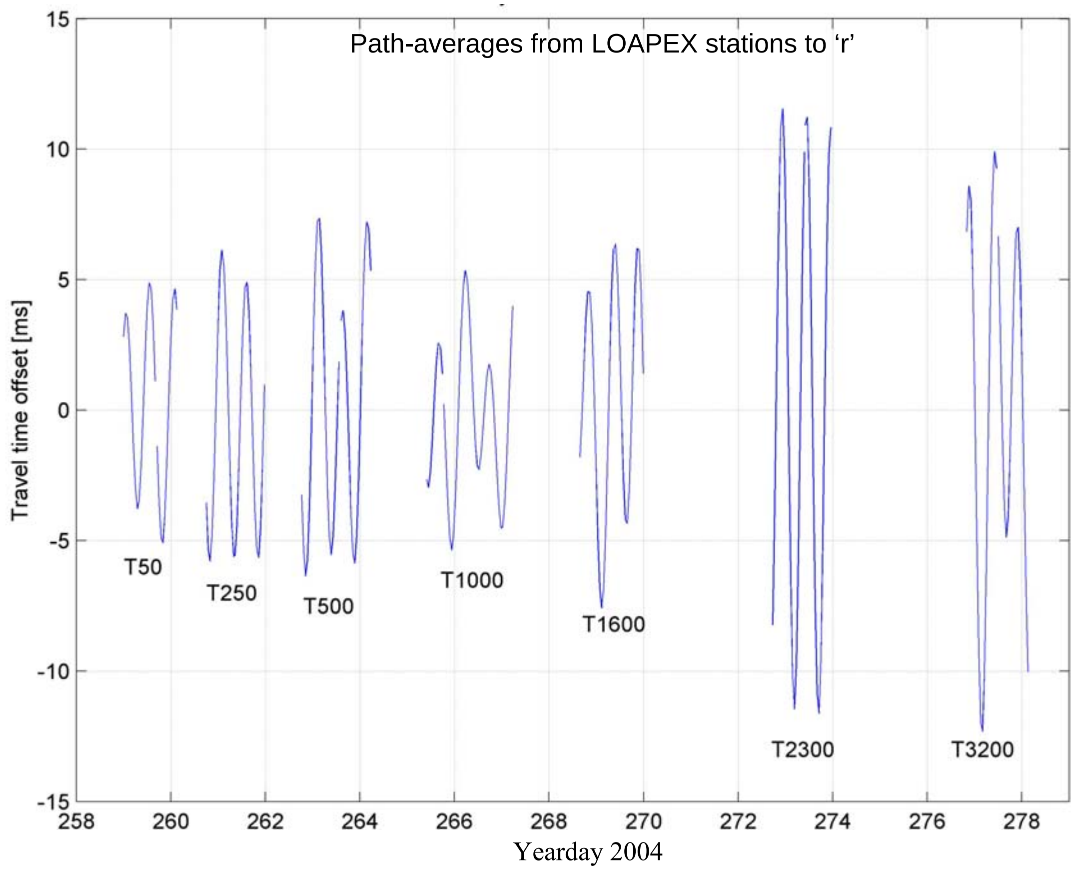

Figure 4.10. Path-average travel time offsets from all LOAPEX stations to 'r'.

Table 4.3. Predicted tidal travel time signals and currents.

Station	Range to 'r' (km)	Peak Value (ms)	U_{Peak} (cm/s)	RMS Value (ms)	U_{RMS} (cm/s)
T50	1002	5	1.09	3.54	0.77
T250	847	6	1.55	3.68	0.95
T500	692	7	2.22	4.81	1.52
T1000	589	5	1.86	3.61	1.34
T1600	749	6	1.75	3.68	1.07
T2300	1534	12	1.71	8.48	1.21
T3200	2388	11	1.01	6.79	0.62

The first four most distinct arrivals of the downward going rays at the receiver were tracked through all of the transmissions from each ship stop. Overlaying these four tracked path arrivals with the predicted path averaged tidal signal yields a distinct similarity. Figure 4.11a shows the tidal signal in blue overlaid with the tracked receptions at 'r' from T250. Both the deep and shallow transmissions are included in the time series. These four tracked receptions are plotted as different colors using linear interpolation between points. The magenta curve is the most jagged with outliers shown at yearday 261.38 and 261.62. These values are likely due to a low signal-to-noise level in the tracked reception; these data points were kept as part of the raw time series, but were eliminated later. Figure 4.11b shows the average of the four time series with the predicted signal. The average time series were calculated from finding the mean travel time perturbation for every consecutive arrival from the four tracked series. At this stage, the measured travel times are not corrected for the motion of the source during the transmissions. The shallow transmissions exhibit noisier time series due to the tighter arrival and the greater difficulty in determining between individual arrivals which might only be separated by 5 ms. The four individual and averaged reception time series overlaid with the tidal signal for all of the stations is shown in Appendix 13.

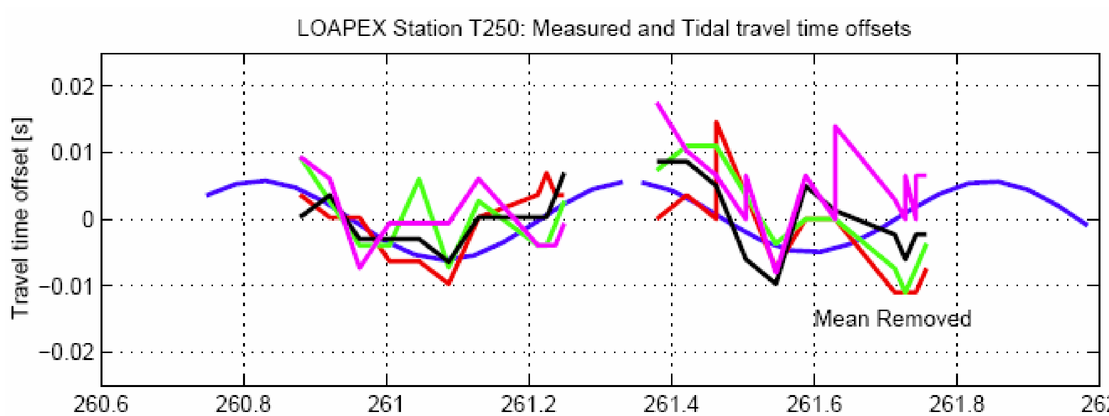

Figure 4.11a. Tide test signal (blue) overlaid with time series of four uncorrected tracked arrivals at 'r' from the transmissions at T250.

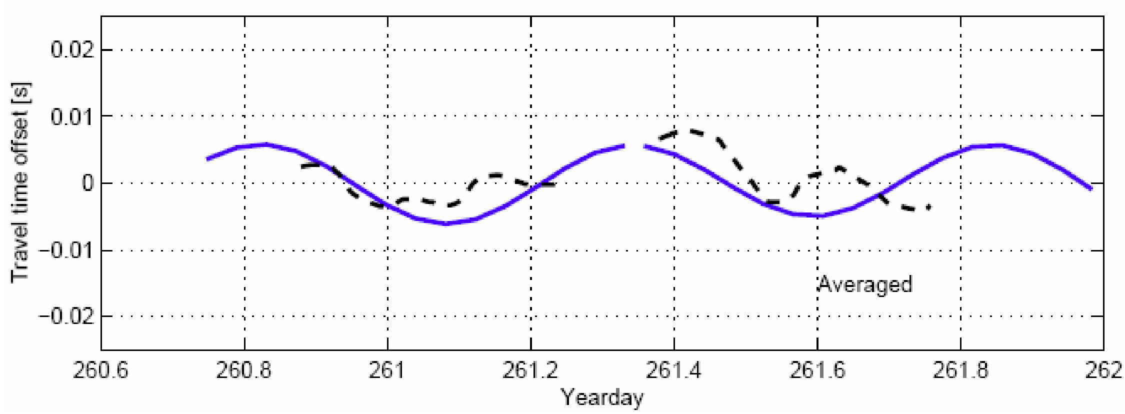

Figure 4.11b. Tide test signal (blue) overlaid with average of four uncorrected arrivals at ‘r’ from the 800-m deep transmissions at T250.

The source position estimates from section 2 were used to correct the tracked path time series. The average source position relative to the nominal station coordinates over the 20-minute duration of the transmissions was determined. The shift in position in the direction to receiver ‘r’ was converted to a travel time offset and added to each of the four tracked arrivals. The maximum position shift was 10.1 m, relating to a time shift of 6.8 ms, using a nominal sound speed of 1490 m/s. This correction occurs for T3200, which was the station with the highest sea state during the duration of the source deployment. Figure 4.12a shows the same tracked arrivals from T250 at ‘r’ as shown in Figure 4.11, but with the source position corrections included and obvious outliers removed. The tidal signal is included. Similarly, Figure 4.12b shows the average of the four tracked arrivals overlaid with the tidal signal. Overall, the source position corrections did not shift the tracked arrivals significantly, nor was there a mean offset introduced. Again, the shallower transmissions exhibited noisier time series because of the tightness of the doublet and the difficulty involved in separating the specific arrivals. Appendix 14 shows all of the corrected tracked and averaged arrivals from all of the stations.

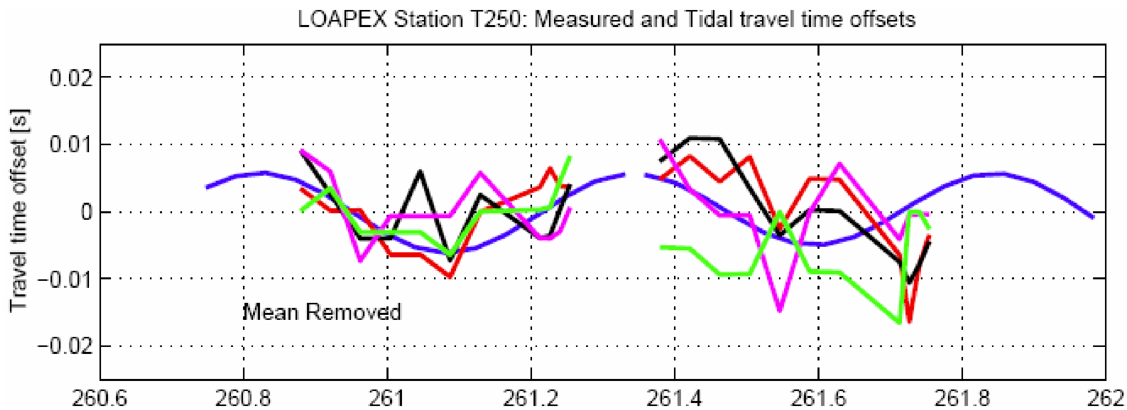

Figure 4.12a. Tide test signal (blue) overlaid with time series of four tracked arrivals with source position corrections at 'r' from the 800-m deep transmissions at T250.

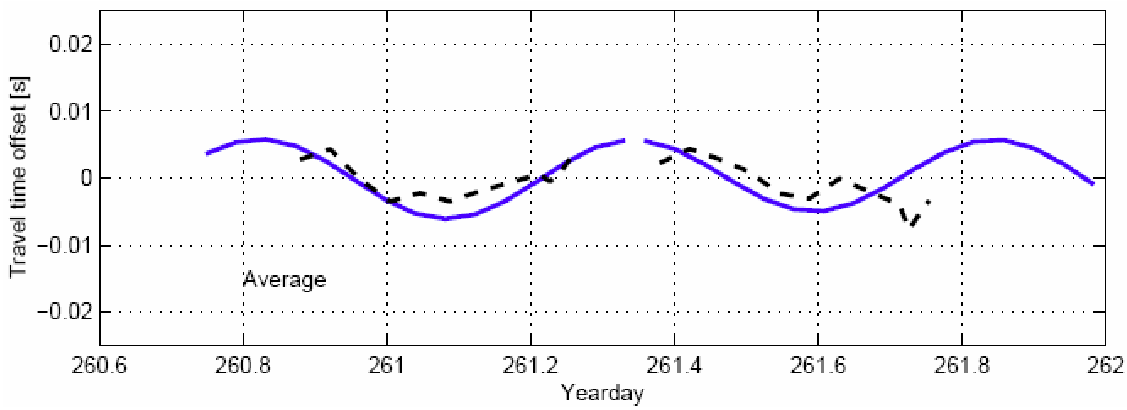

Figure 4.12b. Tide test signal (blue) overlaid with average of four tracked arrivals with source corrections at 'r' from the 800-m deep transmissions at T250.

Table 4.4 shows the quantitative comparison between the averaged uncorrected and corrected tracked reception signal and the predicted tidal signal. The table shows a comparison between the root-mean-square difference between the two time series, separating deeper and shallower transmissions. There is increase in the rms difference and a decrease in the correlation coefficient between the uncorrected and corrected deep transmissions. The shallow uncorrected and corrected transmission comparison shows a decrease in the rms difference and an increase in the correlation coefficients in three out of the seven transmissions, including T50, T1000, and T1600. The other stations showed decreased correlation coefficient values and increased rms differences. All of these comparative statistics suggest there are causes beyond the source motion contributing to the accuracy of acoustics to measure the tide test signal. These alternate causes could include sound channel scattering, internal wave effects, and possibly a baroclinic tidal constituent in addition to the barotropic tidal signal considered here.

Table 4.4. Comparison between averaged tracked path arrivals and the predicted tidal signal between the LOAPEX stations and 'r'.

	UNCORRECTED rms (measured - predicted)				**CORRECTED** rms (measured - predicted)			
Station	Deep (ms)	Rxy	Shallow (ms)	Rxy	Deep (ms)	Rxy	Shallow (ms)	Rxy
T50	2.8	0.87	4.2	0.23	3.0	0.84	3.3	0.91
T250	2.0	0.93	3.4	0.40	3.8	0.43	5.3	0.37
T500	1.7	0.97	2.7	0.95	4.6	0.80	4.3	0.76
T1000	1.9	0.87	4.0	0.61	4.5	0.20	3.4	0.70
T1600			3.0	0.78			2.3	0.87
T2300	5.2	0.89	5.1	0.90	7.9	0.76	6.8	0.61
T3200	8.3	0.91	6.5	0.26	8.8	0.68	13.3	0.57

An overlay of the predicted tidal signal from Figure 4.10 with the acoustically measured, corrected signal is shown in Figure 4.13. Generally, the comparison is good, though there are clearly times when the comparison is poor. The predictions are plotted against the uncorrected and corrected acoustic measurements in Figures 4.14a and b, respectively. This representation shows little difference between the uncorrected and the corrected data. Therefore, the conclusion is that source motion does not have a significant effect on the tracked receptions for the typical 20-minute time scales of the signal and the time scales of ship motion over the duration of a station stop.

The tidal signal and the acoustic receptions at station T3200 (black dots) do not compare well in either case. A baroclinic tidal component is speculated as the source for the large difference shown (Dushaw, 2005). This baroclinic signal could be propagating northward from the Hawaiian Ridge with a crest parallel to the path between T3200 and 'r'. The other tracked receptions from the other stations also show differences from the tidal signal, which could also be due to baroclinic tides, as well as by internal waves (at higher frequency). Analyzing these data in this context is beyond the scope of this thesis.

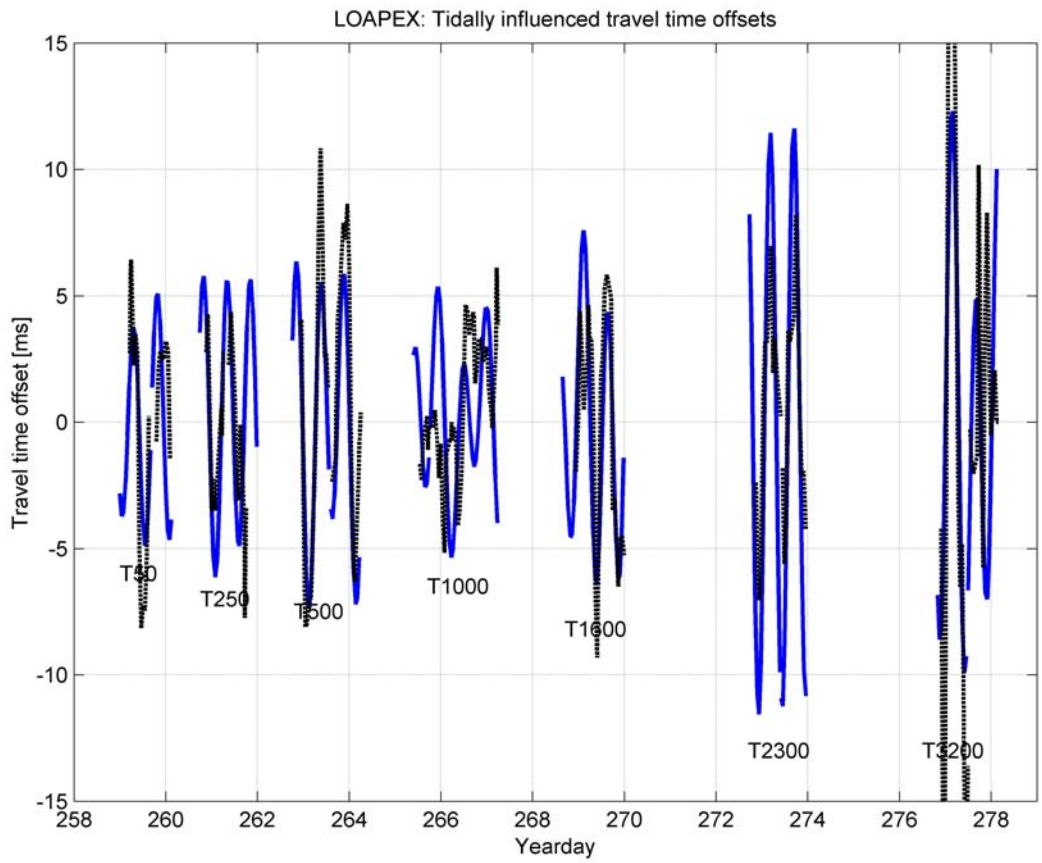

Figure 4.13. Path averaged tidal predictions and acoustically measured, source motion corrected, travel time perturbations.

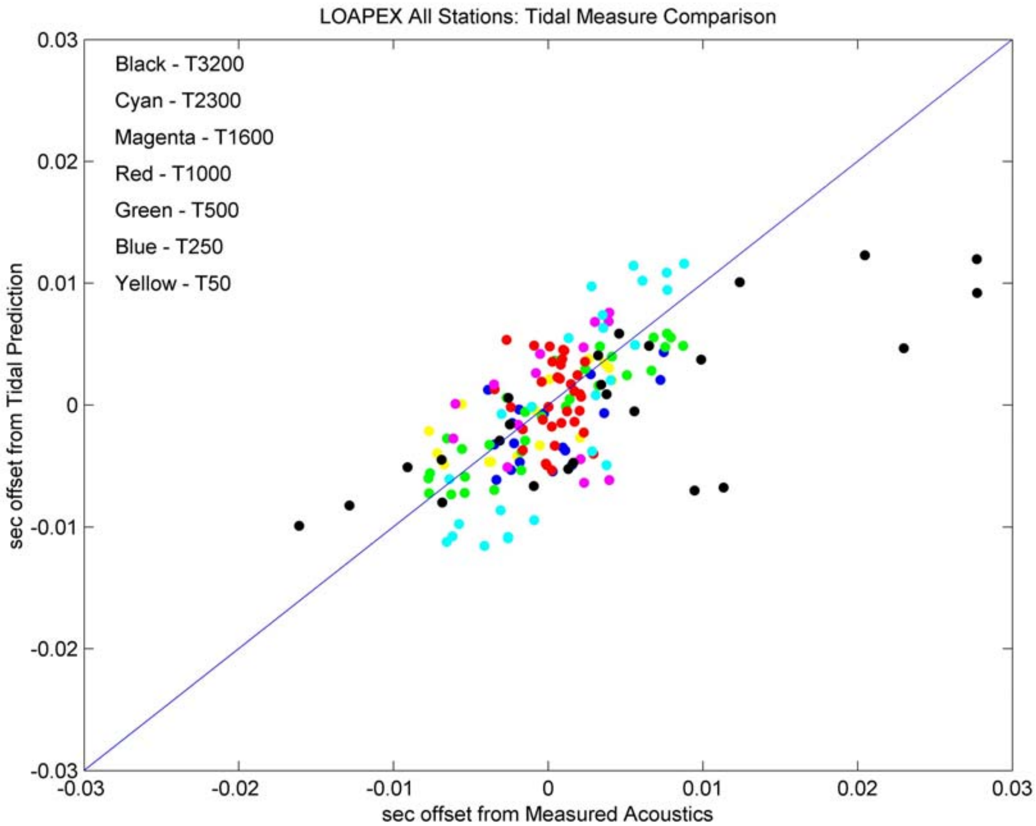

Figure 4.14a. Comparison between tidal model predicted offset and uncorrected acoustically measured offsets for all LOAPEX stations to receiver ‘r’.

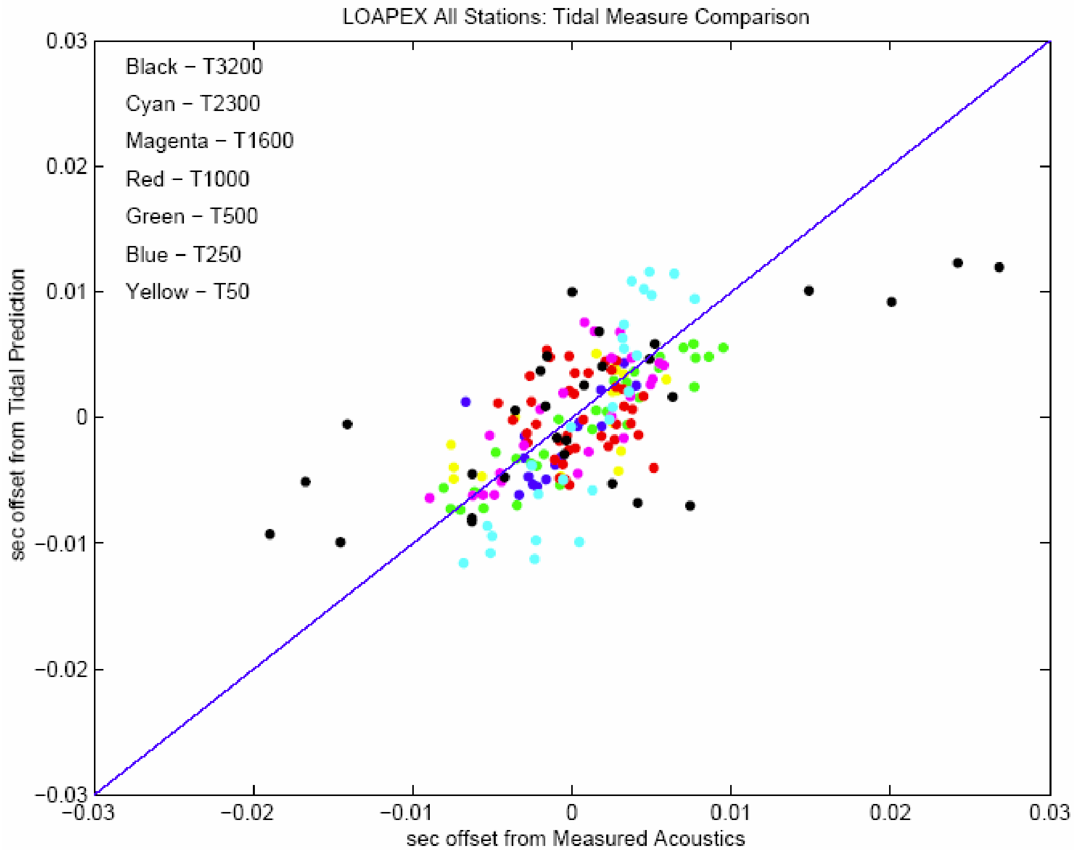

Figure 4.14b. Comparison between tidal model predicted offset and corrected acoustically measured offsets for all LOAPEX stations to receiver 'r'.

4.6 First-order temperature change estimates

The time shifts given in Table 4.3 can be used to determine the change in sound speed and temperature from the measured ocean during LOAPEX to the ocean in which the propagation modeling was performed (i.e., World Ocean Atlas). These travel time perturbations are related to sound speed perturbations through:

$$[4] \qquad \delta t = \frac{R}{C_o^{\,2}} \delta C$$

where R is the range between the source and receiver, C_o is the nominal sound speed, δt is the time shift, and δC is the perturbation in sound speed. The sound speed perturbation is then converted to nominal temperature perturbation δT through

$$[5] \qquad \delta T = \frac{1}{4} T \delta C$$

where the factor of ¼, with units of °C /(m/s), comes from the equation for the sound speed in seawater.

From the average perturbation travel time for each station, which is the averaged and measured World Ocean Atlas value, the perturbation sound speed and temperature is calculated using the above simple formulae and is shown in Table 4.5. All the perturbation temperatures are positive: the ocean during LOAPEX was warmer than for the September average World Ocean Atlas ocean, which was used to calculate the predicted travel time series. These comparisons show specific measurement differences along distinct acoustic paths during the time period between mid-September and mid-October of 2004 and the 50 year September average from the World Ocean Atlas; using longer term acoustic measurements would provide a more accurate comparison with longer World Ocean Atlas averages for each individual path, which are varying independently in position. Each path is a spatial sample of that region of the ocean based on its range and specific azimuth slice though the North Pacific. The left column in Table 4.5 represents estimated source position ambiguities and unresolved error estimate in the receiver position.

Table 4.5. Perturbations between LOAPEX measured and from 50 year September World Ocean Atlas average.

Station	**$\delta\tau$** (ms)	**δC** (m/s)	**δT (add to WOA)** (°C)	**±10ms Error** (±ºC)
T50	265	0.579	0.145	0.0055
T250	245	0.633	0.158	0.0065
T500	225	0.712	0.178	0.0080
T1000	115	0.428	0.107	0.0090
T1600	90	0.263	0.066	0.0070
T2300	145	0.207	0.052	0.0036
T3200	140	0.128	0.032	0.0023

5 Conclusions

The results of this preliminary analysis indicate the Long-range Ocean Acoustic Propagation EXperiment has produced a data set of high quality. Measured travel time perturbations agree well with predicted tidal current signals. Mean travel times show plausible, smooth changes with respect to azimuth/range along the path analyzed. Also, source motion is understood and well measured.

There is reasonable expectation that future, more detailed analyses directed at coherence studies and mapping the large scale ocean will be very productive.

5.1 Comparing measured and predicted tidal signals

Measured and predicted tidal signals have correlations of 0.20 to 0.97. There are some indications (along longer correlation times) that baroclinic tides may be influencing the longer paths which lie more parallel to the Hawaiian Ridge, an area known to contain such tidal signals. More detailed analysis of the residual high-frequency travel time data will reveal whether this is true, and also address the contribution due to internal waves, spice, and other ocean processes.

The analysis showed it is not necessary to incorporate source motion corrections when using signals averaged over 20-minutes or longer. Over these time scales, the average source position was within10 m of the nominal location and the rms deviation for all the stations and transmissions was approximately 1 m. The deviations are inconsequential when studying tidal fluctuations.

It is important to note that any time invariant uncertainty in the source and receiver timing and position drops out when considering tidal and high-frequency fluctuations.

5.2 Mean travel times

The very crude path averaged temperature perturbations measured relative to the World Ocean Atlas appear plausible: 0.032 to 0.178 °C is well within the expected a priori uncertainty. The smooth variation with azimuth/range is qualitatively reassuring.

If the differences in measured temperature from one of the LOAPEX transmission statioons to ‘r’ paths to the next is of interest, all the time invariant clock uncertainty will cancel. The confidence is high that the ship and source position error is negligible. If the position of ‘r’ has an unknown error, it is highly likely it can be detected through an analysis of the receptions at ‘r’ as a function of their receive angle. In principle, if there is sufficient geometric diversity in the path geometry of the entire experiment, it may be able to solve for receiver position and clock offsets using the multiple transmission angles and ranges from the LOAPEX ship stop stations and ‘r’.

When absolute temperatures are being compared, any uncertainty in the clock and position could cause errors, but there is high confidence in the shipboard timing and positioning, thereby alleviating these error possibilities.

5.3 Source position and velocity estimates

A considerable amount of effort was invested in understanding the source motion because of its possible effect on the interpretation of the received acoustic signals.

The source position and velocity are accurately predicted using WHOI Cable, which utilizes inputs from the ADCP and the C-Nav time series. For the duration of the LOAPEX station deployments, the ADCP time series appeared good and valid with no obvious problems or spikes in the timeseries. C-Nav data was generally very good quality. When the number of satellites in view dropped below five, some smoothing was performed, but this occurred less than 2% of the total deployment time. The durations of these time periods were typically short, shorter than the horizontal time constant of the source motion. Table 2.2 outlines the periods of poor C-Nav data: the time periods noted contained numerous short (<30 s) spikes in the time series, but were noted as the stated time periods for continuous data smoothing transitions. The source follows the low-frequency dynamics of the ship horizontally, and in the vertical, the source follows the heave of the ship, very similar to the vertical heave of a forced damped oscillator, with very little damping.

The east/west horizontal position comparison between WHOI Cable and the interrogator/transponder data showed station root mean square differences of 0.6-2.2 m, with correlation coefficients between 0.71 (at the station with the highest sea state) and 0.96, for the entire experiment; the rms value of the source displacement envelope was approximately 1 m. Given the nominal 75-Hz frequency and the associated 20 m wavelength used for the transmissions, and taking into account the noisy dataset of the interrogator, these rms offsets are almost negligible because they are maintained below 0.1λ and are correctable through appropriate Doppler processing of the acoustic receptions.

The velocity measurements of the ADCP and the S4 current meter also agreed well with the WHOI Cable source velocity predictions. This comparison is not as robust or as independent as the east/west displacement comparison between the model and the interrogator/transponder, because the absolute velocity measurements and predictions of the source were both based on the measured ADCP profiles obtained at each station. A factor reducing the robustness of the comparison was the mismatch in sampling frequencies: 30 s for the S4 and 5 minutes for the ADCP. However, the velocity measurements and predictions had correlation coefficients greater than 0.5, which is considered good given the cited limitations.

The source positioning results from the LOAPEX experiment inform the measurement requirements for future experiments. If the goal is to obtain travel time data for low-frequency processes (tidal periods or longer), WHOI Cable with C-Nav and ADCP data would be adequate. For studies involving shorter time scales, a similar suite of in situ instrumentation is suggested, i.e., depth, source velocity, and acoustic long-baseline tracking measurements. All three of these could be improved with better temporal sampling for all and more robustness for the last.

5.4 Further studies

In the context of acoustic thermometry and tomography, the next steps involved with the data analysis follow rather systematically. First, the propagation predictions for all of the available acoustic paths, based on the number of sources and receivers would be generated. Then, the measured acoustic receptions would be compared to the predictions to determine ray identification and subsequently tracked over time. Similar tidal analyses and crude absolute inversions would be done for each path. A more rigorous inversion procedure (i.e., the usual stochastic inverse / objective mapping) for path-averaged, depth-dependent sound speed/temperature should be performed. Then, this should be expanded to a three-dimensional objective map inversion that includes (receiver) position uncertainties.

The travel time perturbations can also be combined with the other environmental data collected from the LOAPEX cruise, including the full ocean depth conductivity-temperature-depth (CTD) measurements, the expendable bathythermographs, the Seaglider sections, and the underway CTD. This composite data set (including concurrent NPAL, SPICEX, and BASSEX transmissions and Argo floats) could be objectively mapped to provide a composite, time dependent estimate of the ocean state. Ultimately, all these data types could be assimilated into an ocean general circulation model that will provide a dynamically consistent ocean state estimate.

A major goal of the LOAPEX experiment is to better understand the effects of internal waves and spice on ocean acoustic propagation. For instance, how does the signal coherence vary as a function of range, depth, frequency and time? How well do present models of internal waves (and acoustic propagation) predict the measured coherence? What causes shadow zone arrivals – internal waves, spice, and/or other processes?

The LOAPEX transmissions, with the source position dataset, can assist in answering these questions. The position dataset provides the means for correcting received signals for the Doppler shift of the source on time scales shorter than an m-sequence transmission period of 20 minutes.

With the numerous source transmissions, source motion signal processing methodologies can be developed to remove the position of the source as a factor in the receptions. By removing the ambiguity of the source position, more accurate coherence, internal wave, and other smaller-scale changes can be investigated.

The Long-range Ocean Acoustic Propagation Experiment was successful in providing a moving ship platform for multiple acoustic transmissions from which to perform a multitude of oceanographic studies over a very broad area of the North Pacific Ocean.

References

Alexander, C.M., 1981: The complex vibrations and implied drag of a long oceanographic wire in cross-flow. *Ocean Engng*, **8**(4), 379-406.

AMODE-MST Group: Birdsall, T.G., Boyd, J., Cornuelle, B.M., Howe, B.M., Knox, R., Mercer, J.A., Metzger, K., Spindel, R.C., and Worcester, P.F., 1994: Moving ship tomography in the northwest Atlantic Ocean. *Eos*, **75**, 17, 21, 23.

Bowlin, J.B., Spiesberger, J.L., Duda, T.F., and Freitag, L.F., 1992: Ocean acoustical ray-tracing software RAY. Tech. Report WHOI-93-10, Woods Hole Oceanographic Institute, Woods Hole, MA.

Chung, J., and Hulbert, G.M., 1993: A time integration algorithm for structural dynamics with improved numerical dissipation. *Journal of Applied Mechanics*, **60**, 371-375.

Colosi, J.A., personal communication, 2004.

Colosi, J.A., Scheer, E.K, Flatte, S.M., Cornuelle, B.D., Dzieciuch, M.A., Munk, W.H., Worcester, P.F., Howe, B.M., Mercer, J.A., Spindel, R.C., Metzger, K., Birdsall, T.G., Baggeroer, A.B., 1999: Comparisons of measured and predicted acoustic fluctuations for a 3250-km propagation experiment in the eastern North Pacific Ocean. *J. Acoust. Soc. Am*., **105**, 3202.

Dushaw, B.D., personal communication, 2005.

Dushaw, B.D., personal communication, 2003.

Dushaw, B.D., 2002: Ocean Tide Model GUI in MATLAB, Avail: http://staff.washington.edu/dushaw/. Accessed: 17 July, 2005.

Dushaw, B.D., Howe, B.M., Mercer, J.A., and Spindel, R.C., 1999: Multimegameter-range acoustic data obtained by bottom-mounted hydrophone arrays for measurement of ocean temperature. *IEEE Journal of Oceanic Engineering*, **24**(2), 202-212.

Dushaw, B.D., Cornuelle, B.D., Worcester, PF., Howe, B.M., and Luther, D.S., 1995: Barotropic and baroclinic tides in the central North Pacific Ocean determined from long-range reciprocal acoustic transmissions. Journal of Physical Oceanography, **25**(4), 631-647.

Dushaw, B.D., Worcester, PF., Cornuelle, B.D., and Howe, B.M., 1993: Variability of heat content in the central north Pacific in summer 1987 determined from long-range acoustic transmissions. *J. Phys. Oceanogr*., **23**, 2650-2666.

Egbert, G.D., Bennett, A.F., and Foreman, M.G., 1994: TOPEX/POSEIDON tides estimated using a global inverse model. *Journal of Geophysical Research*, 99(C12), 24,821-24, 852.

Eggen, C., personal communication, 2005.

Gobat, J.I., personal communication, 2005.

Gobat, J.I., 2000: The dynamics of geometrically compliant mooring systems. PhD Thesis, Massachusetts Institute of Technology and Woods Hole Oceanographic Institute Joint Program.

Gobat, J.I., and Grosenbaugh, M.A., 2000: WHOI Vable v2.0: Time domain Numerical Simulation of Moored and Towed Oceanographic Systems. Woods Hole Oceanographic Institution Technical Report: WHOI-2000-08.

Gobat, J.I., and Grosenbaugh, M.A., 2002: Application of the generalized-a method to the time integration of the cable dynamics equations. *Comput. Methods Appl. Mech. Engrg*., **190**, 4817-4829.

Grosenbaugh, M.A., Yoerger, D.R., Hover, F.S., and Triantafyllou, M.S., 1991: Drag forces and flow-induced vibrations of a long vertical tow cable – Part II: Unsteady tow conditions. Journal of Offshore Mechanics and Arctic Engineering, **113**, 199-204.

Howell, C.T., 1992: Investigation of the dynamics of low-tension cables. PhD Thesis, Massachusetts Institute of Technology and Woods Hole Oceanographic Institute Joint Program.

InterOcean Systems, 2005: Theory: S4 current meter family. Available: http://www.interoceansystems.com/s4theory.htm. Accessed: 17 July, 2005.

Levitus, S., 1982: Climatological atlas of the world ocean. NOAA Prof. Paper, 13.

Levitus, S., Burgett, R., and Boyer, T., 1994: *World Ocean Atlas 1994, Vol. 3: Salinity*, NOAA Atlas NESDIS 3. Washington, DC., United States Government Printing Office.

Levitus, S., Burgett, R., and Boyer, T., 1994: *World Ocean Atlas 1994, Vol. 3: Temperature*, NOAA Atlas NESDIS 3. Washington, DC., United States Government Printing Office.

Liaw, C.Y., Shankar, N.J., and Chua, K.S., 1989: Large motion analysis of compliant structures using Euler parameters. *Ocean Engineering*. **16**, 545-557.

Mercer, J., Andrew, R., Howe, B., and Colosi, J., 2005: Cruise Report: Long-range Ocean Acoustic Propagation Experiment (LOAPEX). Applied Physics Labatory Technical Report: APL-UW TR 0501.

Munk, W., Worcester, P., and Wunsch, C., 1995: *Ocean Acoustic Tomography*. Cambridge University Press.

National Imagery and Mapping Agency, 1984: *World Geodetic System 1984 (WGS-84) – Its definition and relationships with local geodetic systems*, 3rd. ed., Washington, DC., National Imagery and Mapping Agency.

The NPAL Group (Colosi, J.A., Cornuelle, B.D., Dushaw, B.D., Dzieciuch, M.B., Howe, B.M., Mercer, J.A., Spindel, R.C., and Worcester, P.F., 2001: The North Pacific Acoustic Laboratory (NPAL) experiment. *J. Acoust. Soc. Am*., **109**, 2384.

Press, W.H., Flannery, B.P., Teukolsky, S.A., and Vetterling, W.T., 1989: *Numerical Recipies in C: The art of scientific computing*. Cambridge University Press, 2e.

Sherman, A.H., 1978: Algorithms for sparse Gaussian elimination with partial pivoting. *ACM Transactions on Mathematical Software*, **4**, 330-338.

Smith, W.H.F. and Sandwell, D.T., 1994: Bathymetric prediction from dense satellite altimetry and sparse shipboard bathymetry, *J. Geophys. Res*., **99**, 21803-21824.

Spiesberger, J.L., 1994: Successful ray modeling of acoustic multipaths over a 3000-km section of the Pacific. *J. Acoust. Soc. Amer.*, **95**, 3654-3657.

Tjavaras, A.A., 1996: Dynamics of highly extendable cables. PhD Thesis, Massachusetts Institute of Technology.

Urick, R.J., 1983: *Principles of Underwater Sound*. McGraw-Hill, New York.

Walter, C.G., 1993: Towed array tomography data of the Gulf Stream. MS Thesis, University of Washington.

Webster, W.C., 1995: Mooring induced damping. *Ocean Engineering*, **22**, 570-591.

Wendroff, B., 1960: On centered finite difference equations for hyperbolic systems. *Journal of the Society of Industrial and Applied Mathematics*, **8**, 549-555.

Worcester, P.F., Howe, B.M., Mercer, J.A., Dzieciuch, M.A., and the Alternate Source Test (AST) Group (Birdsall, T.A., Howe, B.M., Mercer, J.A., Metzger, K., Spindel, R.C., and Worcester, P.F., 1999: A comparison of long-range acoustic propagation at ultra-low (28 Hz) and very low (84 Hz) frequencies. Proceedings, U.S.-Russian Workshop on

Experimental Underwater Acoustics, November 18-19, Nyzhny Novgorod, Russia, 93-104.

Yoerger, D.R., Grosenbaugh, M.A., Triantafyllou, M.S., and Burgess, J.J., 1991: Drag forces and flow-induced vibrations of a long vertical tow cable – Part II: Unsteady tow conditions. Journal of Offshore Mechanics and Arctic Engineering, **113**, 117-127.

Appendix 1: Instrumentation data sheets

MicroCAT C-T Recorder (Serial Interface & Memory)

SBE 37-SM

The SBE 37-SM MicroCAT is a high-accuracy conductivity and temperature (pressure optional) recorder with internal battery and memory. Designed for moorings or other long duration, fixed-site deployments, the MicroCAT includes a standard serial interface and non-volatile FLASH memory. Construction is of titanium and other non-corroding materials to ensure long life with minimum maintenance, and depth capability is 7000 meters (23,000 feet).

Calibration coefficients are stored in EEPROM, and uploaded data is presented in ASCII engineering units. The data always includes Conductivity, Temperature, and Pressure (if optional pressure sensor is installed); time can be added to each scan if desired. The MicroCAT retains the temperature and conductivity sensors used in our time-proven SEACAT products; however, new acquisition techniques provide increased accuracy and resolution while reducing power consumption. Electrical isolation of the conductivity electronics eliminates any possibility of ground-loop noise.

The MicroCAT's unique internal-field conductivity cell is completely unaffected by external fouling, permitting the use of expendable anti-fouling devices to inhibit internal fouling and ensure stability. The aged and pressure-protected thermistor has a long history of exceptional accuracy and stability.

The MicroCAT's optional pressure sensor, developed by Druck, Inc., has a superior new design that is entirely different from conventional 'silicon' types in which the deflection of a metallic diaphragm is detected by epoxy-bonded silicon strain gauges. The Druck sensor employs a micro-machined *silicon diaphragm* into which the strain elements are implanted using semiconductor fabrication techniques. Unlike metal diaphragms, silicon's crystal structure is perfectly elastic, so the sensor is essentially free of pressure hysteresis. Compensation of the temperature influence on pressure offset and scale is performed by the MicroCAT's CPU.

SENSOR INTERFACE ELECTRONICS

Temperature is acquired by applying an AC excitation to a hermetically-sealed VISHAY reference resistor and an ultra-stable aged thermistor (drift rate typically less than 0.002 °C per year). The ratio of thermistor resistance to reference resistance is determined by a 24-bit A/D converter; this A/D also processes the pressure sensor signal. Conductivity is acquired using an ultra-precision Wien-Bridge oscillator. A high-stability reference crystal with a drift rate of less than 2 ppm/year is used to count the frequency from the oscillator.

COMMUNICATIONS AND INTERFACING

The MicroCAT communicates directly with a computer via standard RS-232 interface. Data can be uploaded at up to 38.4K baud. Real-time data can be transmitted at distances of up to 1000 meters (3300 feet) at 600 baud, simultaneously with recording. An optional RS-485 interface allows multiple MicroCATs to share a common 2-wire cable, minimizing cable complexity for C-T chains.

User-selectable operating modes include:

- **Autonomous Sampling** – allows sampling at pre-programmed intervals of 5 seconds to 9.1 hours, with the MicroCAT going to sleep between samples.
- **Polled Sampling** – allows sampling and data transmission to be triggered by a command from a computer or satellite, radio, or wire telemetry equipment.
- **Serial Line Sync** – allows sampling and data transmission to be triggered by a pulse on the serial line, which causes a sleeping MicroCAT to wake up, sample, record, and power off automatically.

OPTIONAL PUMP

The submersible pump comes on for 1/2 second each time the MicroCAT samples, providing the following advantages:

- **Improved conductivity response** – The pump flushes the previously sampled water from the conductivity cell and brings a new water sample quickly into the cell.
- **Improved anti-foul protection** – Water does not freely flow through the conductivity cell between samples, allowing the anti-foul concentration inside the cell to build up.

SOFTWARE

The MicroCAT is supplied with a powerful software package that includes:

- SEATERM© — Win 95/98/NT terminal program for easy communication and data retrieval.
- SEASOFT© — programs for calculation, display, and plotting of conductivity, temperature, pressure (optional), and derived variables such as salinity and sound velocity.

Sea-Bird Electronics, Inc.
1808 136th Place NE, Bellevue, Washington 98005 USA
Website: http://www.seabird.com

Fax: (425) 643-9954
Tel: (425) 643-9866
Email: seabird@seabird.com

Figure A1.1. Data sheet for MicrCAT, page 1.

MicroCAT C-T Recorder (Serial Interface and Memory) SBE 37-SM

DATA STORAGE AND BATTERY ENDURANCE

Converted temperature and conductivity are stored 5 bytes per sample, time 4 bytes per sample, and optional pressure 2 bytes per sample; memory capacity is in excess of 185,000 samples. The MicroCAT is powered by a 7.2 Ampere-Hour (nominal) battery pack consisting of six 9-volt lithium batteries which, when removed from the MicroCAT, can be shipped without hazardous material restrictions. The pack provides sufficient internal battery capacity for more than 175,000 samples (80,000 with optional pump).

SPECIFICATIONS

Measurement Range

Conductivity:	0 - 7 S/m (0 - 70 mS/cm)
Temperature:	-5 to 35 °C
Optional Pressure:*	20/100/350/1000/2000/3500/7000 m

*Expressed in meters of deployment depth capability.

Initial Accuracy

Conductivity:	0.0003 S/m (0.003 mS/cm)
Temperature:	0.002 °C
Optional Pressure:	0.1% of full scale range

Typical Stability *(per month)*

Conductivity:	0.0003 S/m (0.003 mS/cm)
Temperature:	0.0002 °C
Optional Pressure:	0.004% of full scale range

Resolution

Conductivity:	0.00001 S/m (0.0001 mS/cm)
Temperature:	0.0001 °C
Optional Pressure:	0.002% of full scale range
Time Resolution	1 second
Clock Accuracy	13 seconds/month
Quiescent Current	10 microamps
Current consumption per sample	0.1 amp-second
Acquisition Time	3 seconds per sample
Optional External Input Power	40 ma @ 9-24 VDC
Housing	Titanium
Depth Capability	7000 m (23,000 feet)

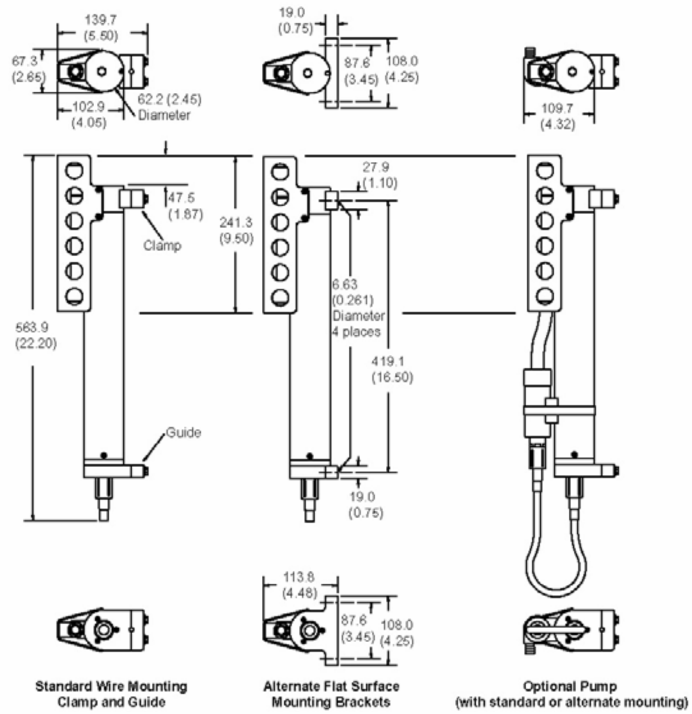

Dimensions in millimeters
(inches)

Weight (without pump)
in air: 3.8 kg (8.3 lbs)
in water: 2.3 kg (5.1 lbs)

Sea-Bird Electronics, Inc.
1808 136th Place NE, Bellevue, Washington 98005 USA
Website: http://www.seabird.com
Fax: (425) 643-9954
Tel: (425) 643-9866
Email: seabird@seabird.com

Figure A1.1. Data sheet for MicrCAT, page 2.

Figure A1.2. S4 Current Meter family. S4 was the unit used in LOAPEX.

Engineering Data & Specifications

Current Speed

Range	0-350 cm/sec (standard) 0-50, 0-100, 0-600, 0-750 cm/sec	
Accuracy:	2% of reading +/- 1 cm/sec	
Sampling Rate:	S4/S4A	2 Hz
	S4AH	5 Hz
Resolution:	2 Hz	0.03 to 0.35 cm/sec depending on range
	5 Hz	0.037 to 0.43 cm/sec depending on range
Noise:	Less than the resolution for averages of 1 minute or longer 0.05 cm/sec rms for 10 second averages 0.25 cm/sec rms for 2 second averages 0.75 cm/sec rms for burst sampling (0.5 second rate)	
Threshold:	Equal to resolution	
Vertical Response:	True cosine response (internally software corrected with Tilt option)	

Figure A1.3a. S4 Current Meter operational data.

Direction	
Type:	Flux-gate compass
Range:	0-360
Resolution:	0.5 deg
Accuracy:	+/- 2 deg within tilt angles of 5 deg
Tilt:	+/- 4 deg for tilt angles between 15 and 25 deg

Figure A1.3b. S4 Current Meter operational data.

Memory		
Type:	S4	CMOS static RAM (Non-restricted Lithium battery protected)
	S4A	Non-volatile flash memory
Battery Life:	S4	5 years
	S4A	No battery required
Capacity:	S4	64K bytes standard (128K, 256K, 512K, or 1M optional) 348,000 vector averages may be stored with 1M bytes
	S4A	5, 10, and 20 megabytes 7 million vector averages stored with 20 megabytes

Figure A1.3c. S4 Current Meter operational data.

Timekeeping	
Type:	Temperature stable quartz oscillator
Accuracy:	+/- 12 minutes/year
Power:	Temperature stable non-restricted Lithium battery (3 years)

Figure A1.3d. S4 Current Meter operational data.

Power Supply	
Type:	Internal batteries (6 Alkaline "D" cells), (Lithium optional)
Endurance:	Alkaline cells: 440 hours continuous logging. One year deployment with total on-time less than 440 hours. Lithium option: 1,600 hours continuous logging. Five years deployment with total on-time less than 1,200 hours.

Figure A1.3e. S4 Current Meter operational data.

Tilt Option	
Angle Range:	+/- 45 deg
Resolution:	0.06 deg
Accuracy:	(Angle Output) +/- 0.25 deg (Speed Correction) +/- 1% of reading at 45 deg tilt

Figure A1.3f. S4 Current Meter operational data.

Mechanical		
Size:	S4	25 cm (10 in) diameter
	S4 Deep	35.5 cm (14 in) diameter
Weight:	S4	Air: 11 kg (24 lb.), Water: 1.5 kg (4 lb.)
	S4 Deep	Air: 34.5 kg (76 lb.), Water: 10.5 kg (23 lb.)
Mooring:	In-line	
Through Load:	4,500 kg (10,000 lb.) working	
Pad Eyes:	Insulating liner, accepts 1.6 cm (5/8 in.) shackle pin	
Material:	Sphere, glass-filled cycloaliphatic epoxy. Mooring rod, Titanium 6 AL-4V	
Drag:	S4	4 kg (9 lb.) at 250 cm/sec (8 ft/sec)
	S4 Deep	0.63 kg (1.4 lb.) at 50 cm/sec 15.68 kg (34.57 lb.) at 250 cm/sec
Depth:	S4	1,000 m (3,200 ft) maximum
	S4 Deep	6,000 m (19,200 ft) maximum
Temperature:	Storage: -40 to +50 deg C Operating: -5 to +45 deg C	

Figure A1.3g. S4 Current Meter operational data.

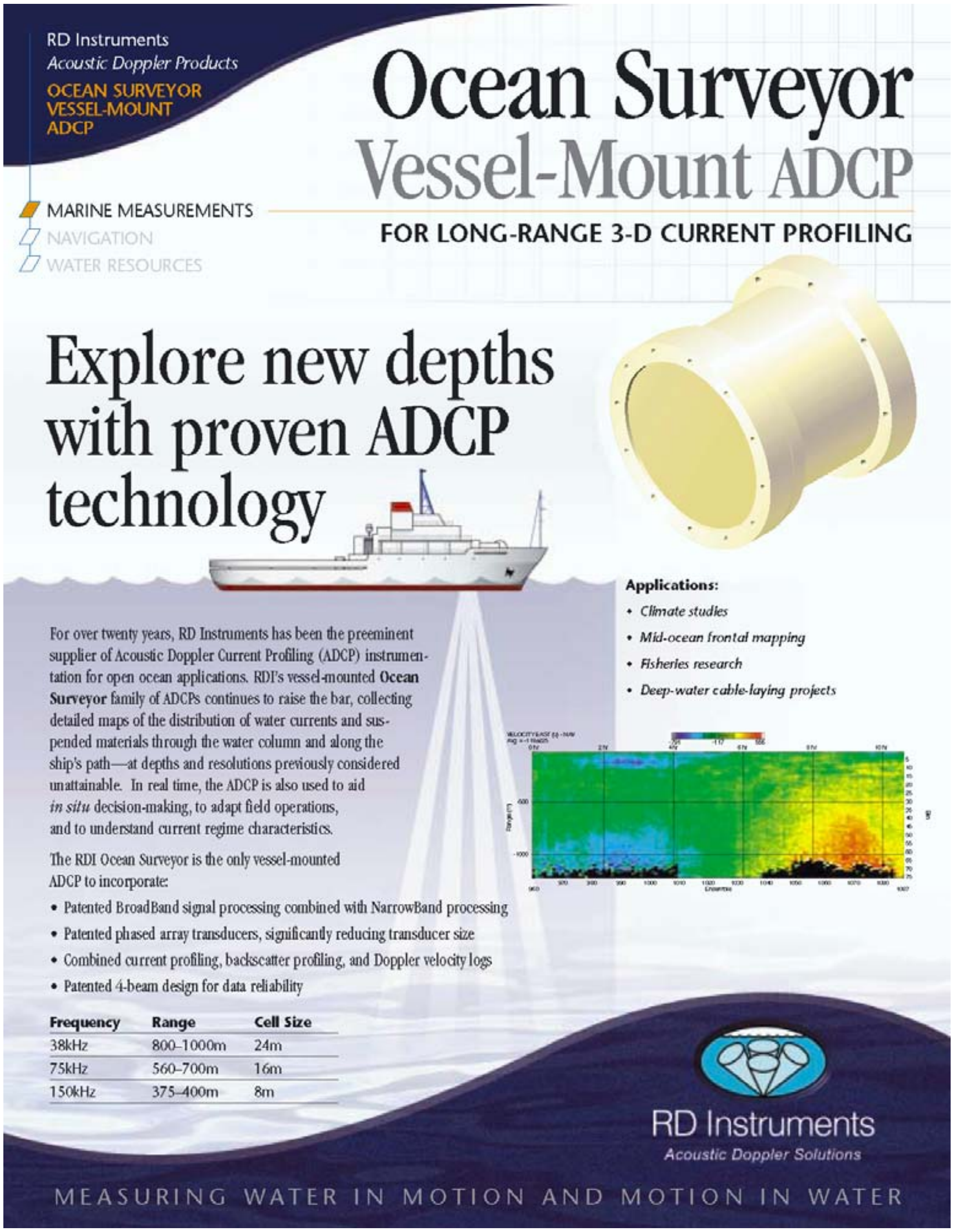

RD Instruments
Acoustic Doppler Products
OCEAN SURVEYOR VESSEL-MOUNT ADCP

MARINE MEASUREMENTS
NAVIGATION
WATER RESOURCES

Ocean Surveyor
Vessel-Mount ADCP

FOR LONG-RANGE 3-D CURRENT PROFILING

Explore new depths with proven ADCP technology

Applications:

- *Climate studies*
- *Mid-ocean frontal mapping*
- *Fisheries research*
- *Deep-water cable-laying projects*

For over twenty years, RD Instruments has been the preeminent supplier of Acoustic Doppler Current Profiling (ADCP) instrumentation for open ocean applications. RDI's vessel-mounted **Ocean Surveyor** family of ADCPs continues to raise the bar, collecting detailed maps of the distribution of water currents and suspended materials through the water column and along the ship's path—at depths and resolutions previously considered unattainable. In real time, the ADCP is also used to aid *in situ* decision-making, to adapt field operations, and to understand current regime characteristics.

The RDI Ocean Surveyor is the only vessel-mounted ADCP to incorporate:

- Patented BroadBand signal processing combined with NarrowBand processing
- Patented phased array transducers, significantly reducing transducer size
- Combined current profiling, backscatter profiling, and Doppler velocity logs
- Patented 4-beam design for data reliability

Frequency	Range	Cell Size
38kHz	800–1000m	24m
75kHz	560–700m	16m
150kHz	375–400m	8m

RD Instruments
Acoustic Doppler Solutions

MEASURING WATER IN MOTION AND MOTION IN WATER

Figure A1.4. ADCP data sheet, page 1.

Ocean Surveyor Vessel-Mount ADCP

FOR LONG-RANGE 3-D CURRENT PROFILING

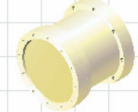

Technical Specifications

Water Profiling

Long-Range Mode	38kHz		75kHz		150kHz	
Vertical Resolution Cell Size[3]	Max. Range (m)[1]	Precision (cm/s)[2]	Max. Range (m)[1]	Precision (cm/s)[2]	Max. Range (m)[1]	Precision (cm/s)[2]
4m					*325–350*	*30*
8m			*520–650*	*30*	*375–400*	*19*
16m	*800–1000*	*30*	*560–700*	*17*		
24m	*800–1000*	*23*				

High-Precision Mode	38kHz		75kHz		150kHz	
Vertical Resolution Cell Size[3]	Max. Range (m)[1]	Precision (cm/s)[2]	Max. Range (m)[1]	Precision (cm/s)[2]	Max. Range (m)[1]	Precision (cm/s)[2]
4m					*200–250*	*12*
8m			*310–430*	*12*	*220–275*	*9*
16m	*520–730*	*12*	*350–450*	*9*		
24m	*730–780*	*9*				

[1] Ranges at 1 to 5 knots ship speed are typical and vary with situation.
[2] Single-ping standard deviation.
[3] User's choice of depth cell size is not limited to the typical values specified.

Profile Parameters

Velocity long-term accuracy (typical): ±1.0%, ±0.5cm/s
Velocity range: -5 to 9m/s
# of depth cells: 1–128
Max ping rate:
38kHz: 0.4 75kHz: 0.7 150kHz: 1.5

Bottom Track

Maximum altitude (precision <2cm/s):

38kHz	75kHz	150kHz
1700m	950m	600m

Echo Intensity Profile

Dynamic range: 80dB
Precision: ±1.5dB

Transducer & Hardware

Beam angle: 30°
Configuration: 4-beam phased array
Communications: RS-232 or RS-422 hex-ASCII or binary output at 1200–115,200 baud
Output power: 1000W

Standard Sensors

Temperature (mounted on transducer)
- Range: -5° to 45°C
- Precision: ±0.1°C
- Resolution: 0.03°

System Power

AC input: 90–250VAC, 47–63Hz
Power: 1400W

Environmental

Operating temperature: -5° to 40°C
Storage temperature: -30° to 50°C

Software

Use RDI's Windows-based software for the best results:
- **VMDAS**—Vessel-mount data acquisition system
- **WinADCP**—Data display and export

System Components

- 38, 75, or 150kHz transducer
- 19" rack-mount electronic chassis
- All-purpose deck box
- Gyrocompass interface board
- LCD gyro offset control display

User to supply compass input or GPS navigation data and NMEA tilt information.

Dimensions

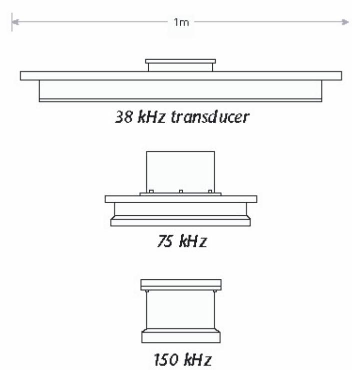

RD Instruments
Acoustic Doppler Solutions
www.rdinstruments.com

RD Instruments
9855 Businesspark Avenue, San Diego, CA 92131 USA
Tel. +1-858-693-1178 • Fax +1-858-695-1459 • E-mail: sales@rdinstruments.com
RDI Europe, Les Nertières, 5 allée Hector Pintus, 06610 La Gaude, France
Tel. +33-49-211-0930 • Fax +33-49-211-0931 • E-mail: rdi@rdieurope.com

Specifications subject to change without notice. Rev. 0104

Figure A1.4. ADCP data sheet, page 2

C-Nav WORLD DGPS

C-NAV2000

C-NAV DGPS

The C-Nav2000 sensor consists of a 10-channel dual-frequency precision GPS receiver, two additional channels for receiving Satellite Based Augmentation System (SBAS) signals and an L-band demodulator for reception of C-Nav correction service. The sensor can output raw data as fast as 50Hz and Position Velocity Time (PVT) data as fast as 25Hz through two 115kbps serial ports.

THE C-NAV 2000 RECEIVER:

- The **C-Nav2000** GPS receiver unit provides performance of several decimeters at either 1 or 5 updates per second. The receiver is ideally suited for positioning of dynamic and static vessels or vehicles on a global basis.
- The **C-Nav2000** receivers feature 10 channels of continuous GPS satellite tracking contained within a compact, rugged, weatherproof housing. For ease of operation and system integration, the C-Nav GPS unit has a single, rugged, waterproof 8-pin connector that provides RS-232 serial ports, a CAN BUS and DC power. During operation, the C-Nav GPS System can output a subset of NMEA-0183 messages, including QA/QC data. It is also capable of outputting RAW GPS measurement binary data for archiving and post-mission kinematic post-processing analysis.
- The **C-Nav2000** receiver is a single integrated package combining: antenna, geodetic quality dual-frequency GPS receiver, communications link, data demodulator, and control processor, which is rugged, reliable, and able to withstand the offshore environment.

C-NAV GPS GIVES YOU THE WORLD. ONE DECIMETER AT A TIME.

Figure A1.5. C-Nav data sheet, page 1

C-NAV2000

TECH SPECS

FEATURES

- "All-in-view" tracking
- Global decimeter-level accuracy using RTG corrections
- Fully automatic acquisition of satellite broadcast corrections
- Configurable for global L-band satellite coverage – StarFire, WAAS, EGNOS
- Single, integrated package - simple installation
- Rugged, waterproof, and dust-resistant housing and connector
- Wide-range (10-40 VDC) power supply
- L1 & L2 full wavelength carrier tracking
- C/A, P1, and P2 code tracking
- User programmable output rates
- Minimal data latency
- 2 separate SBAS (WAAS/EGNOS) channels
- Superior interference suppression
- Patented multipath rejection
- Supports NMEA 0183 v3.01 messages
- Self-survey mode (position averaging)
- CAN bus interface

PHYSICAL/ENVIRONMENTAL

- Size: D x H: 9.8 x 7.25 in (24.8 x 18.7 cm)
- Weight: 5.5 lbs (2.4 kg)
- Power
  - Input Voltage: 10-40 VDC
  - Consumption: <10 W (normal operating conditions)
1.2 A max @ 12 VDC
- I/O Connector: Rugged, weather-resistant, and waterproof
8-Pin connector design
- Temperature
  - Operating: -20° C to +70° C
  - Storage: -40° C to +85° C
- Humidity: 100% non-condensing

PERFORMANCE

- L-band receiver frequency
  - Automatically selected: 1525 to 1560MHz
- Real-time StarFire DGPS Accuracy
  - Position (H): 10 cm
  - Position (V): <30 cm
  - Velocity: 0.02 m/s
- Time-to-first-fix
  - Cold Start: 90 sec (typical)
- Reacquisition
  - "Coast" for 30 seconds with GPS lock: < 2 sec
  - L-band loss for more than 30 seconds with GPS lock: < 30 sec

I/O CONNECTOR ASSIGNMENTS

INPUT/OUTPUT DATA MESSAGES

- NCT Proprietary Data: PVT
Raw Measurement
Satellite Messages
Nav Quality
- NMEA Messages (Output): GGA, GLL, GSA, GST, RMC, VTG, ZDA, NAVQ, RXQ, SATS
- Code Corrections:
  - RTG (proprietary) – Internal LBM
  - WCT (proprietary) – Internal LBM
  - SBAS (WAAS/EGNOS) – Internal GPS
- Diagnostic Data/Command Serial port data rate is selectable: 4.8, 9.6, 19.2, 38.4 kbaud
- RAW GPS 'Binary' data port is fixed at 38.4 kbaud

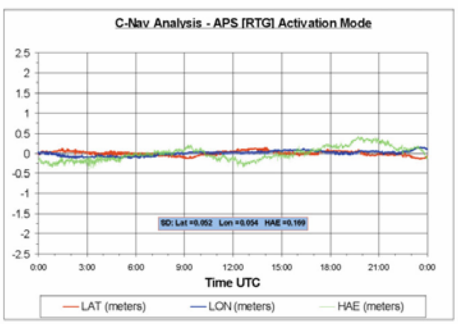

LAFAYETTE | 730 E. KALISTE SALOOM RD. | LAFAYETTE, LOUISIANA 70508 | TEL: (+1) 337.261.0660 | FAX: (+1) 337.261.0192
HOUSTON | 10615 SHADOW WOOD DR., STE. 100 | HOUSTON, TEXAS 77043 | TEL: (+1) 713.468.1536 | FAX: (+1) 713.468.1115
SOUTH AFRICA | #5 MELODIE ROAD | KIRSTENHOF 7945, SOUTH AFRICA | TEL: (+27) 21.702.1870 | FAX: (+27) 21.702.1870
BRASIL | AV. CHURCHILL, 109, 11°ANDAR, CEP 20020-050 | RIO DE JANEIRO – BRASIL | TEL: (+55) 21.22102555 | FAX: (+55) 21.22102557
SINGAPORE | 39 CHANGI SOUTH AVE2, APICO INDUSTRIAL BUILDING #04-05 | SINGAPORE 486352 | TEL: (+65) 62.95.9738 | FAX: (+65) 62.96.0098

WWW.CCTECHNOL.COM

Figure A1.5. C-Nav data sheet, page 2.

Appendix 2: WHOI Cable screen capture examples

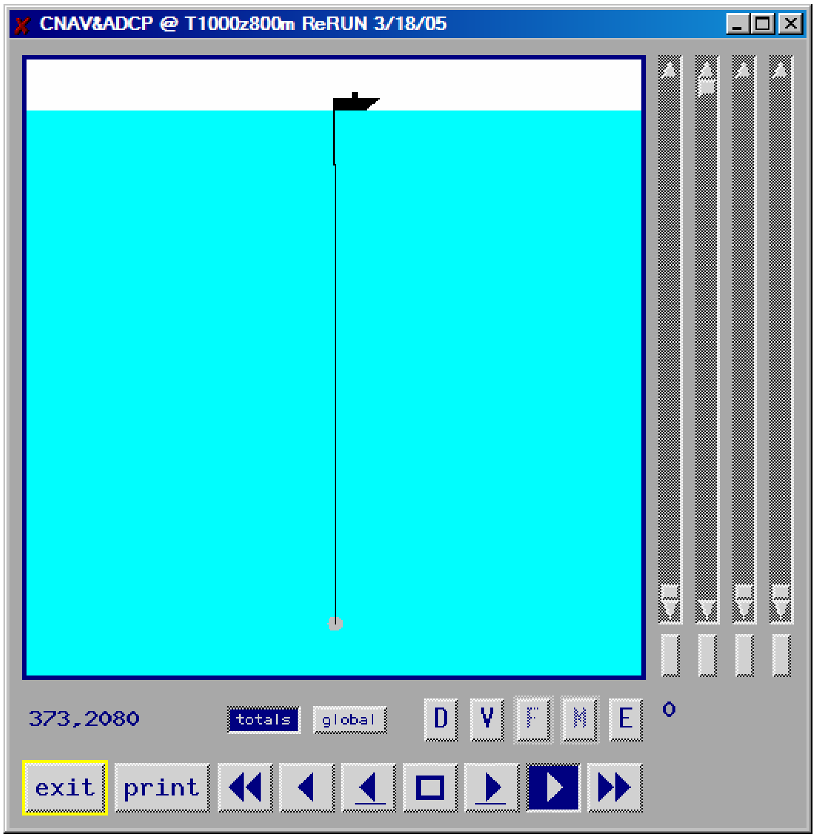

Figure A2.1. Screen capture of WHOI Cable solution animation.
The figure shows the ship on the surface, while the source is deployed 800 m below. The various buttons shown allow the user to play, rewind, fast-forward, stop and pause the playback of the time series position solution.

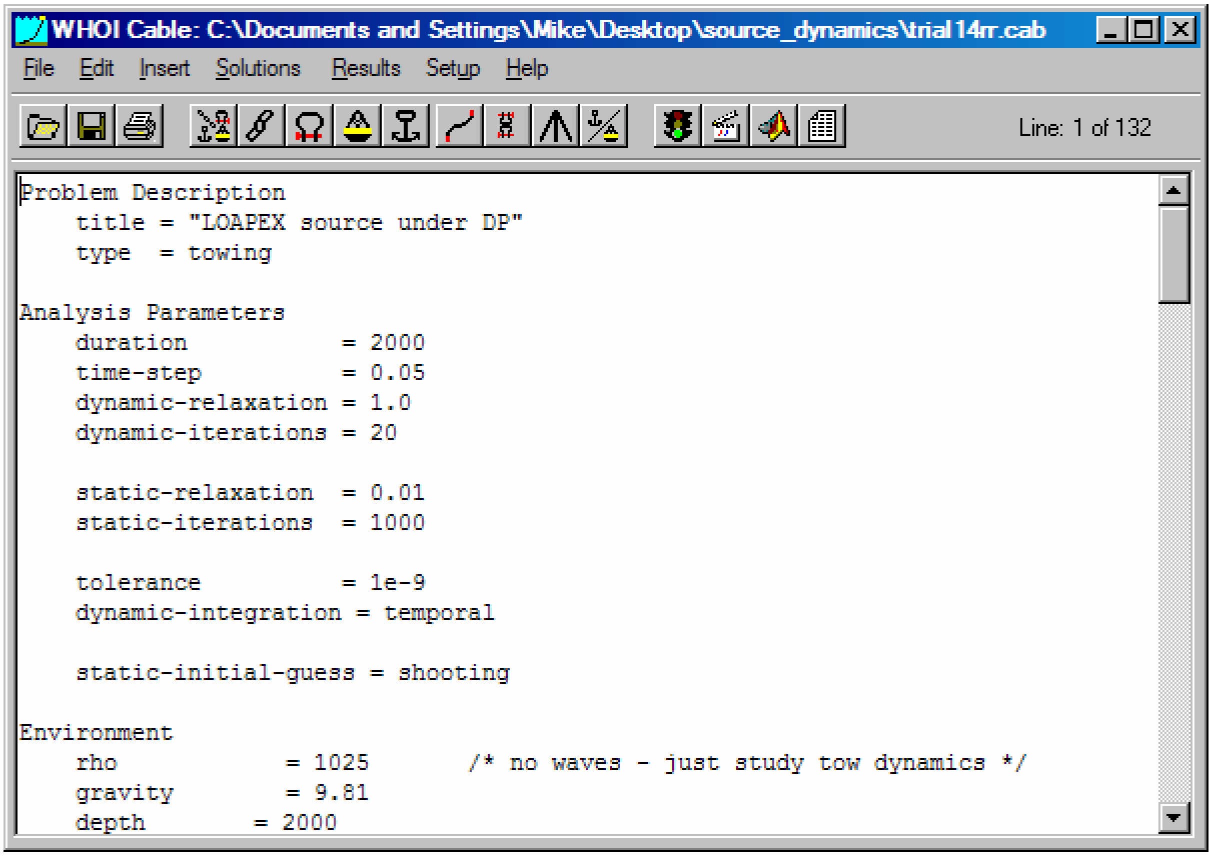

Figure A2.2. WHOI Cable initial set-up screen.

The figure shows the general text initialization of the WHOI Cable solver. Shown are the variables: solution duration in seconds; the time-step of the solver (not necessarily the solver output frequency); the dynamic and static relaxation and iteration variables, which define the solver solution technique; the tolerance, the global convergence error between iterations; the dynamic integration setting of time based solving; the static initial guess algorithm; and the environment variables of density (rho) in kg/m^3, gravity in m/s^2 and total depth in meters.

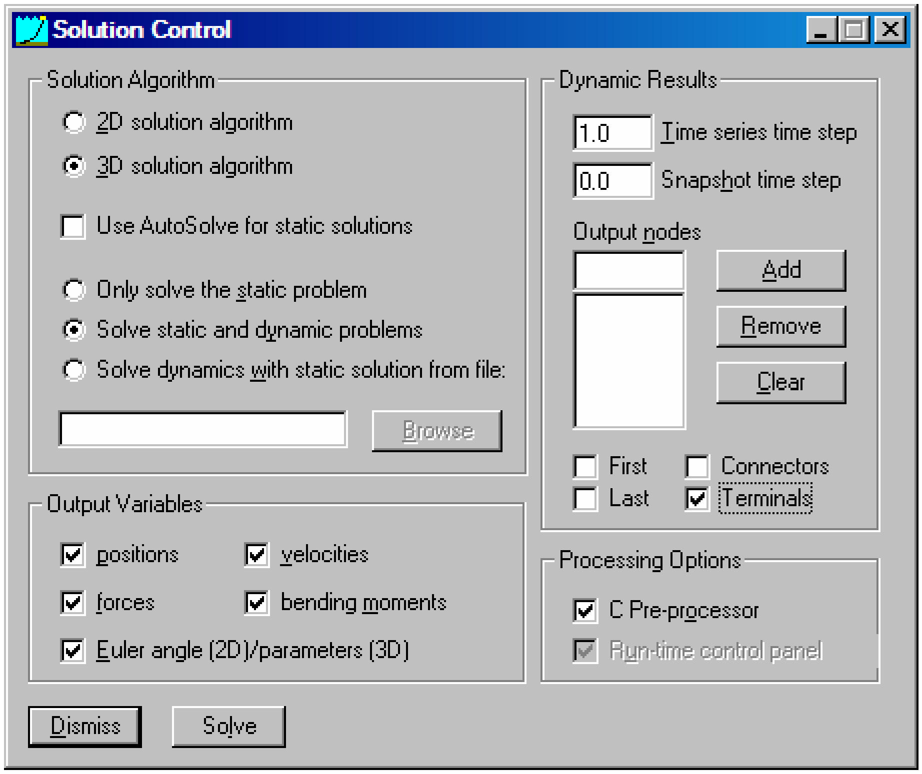

Figure A2.3. WHOI Cable solution initialization screen.
Shown are the initial solver settings which must be initialized prior to any solver run. These settings include the spatial solution dimensions, the solution outcome of static and/or dynamic, the output variables dumped to a data file, the output file time step of 1 s, the output location, in this case the two ends of the cable (ship and source) and the pre-processor, as written in C.

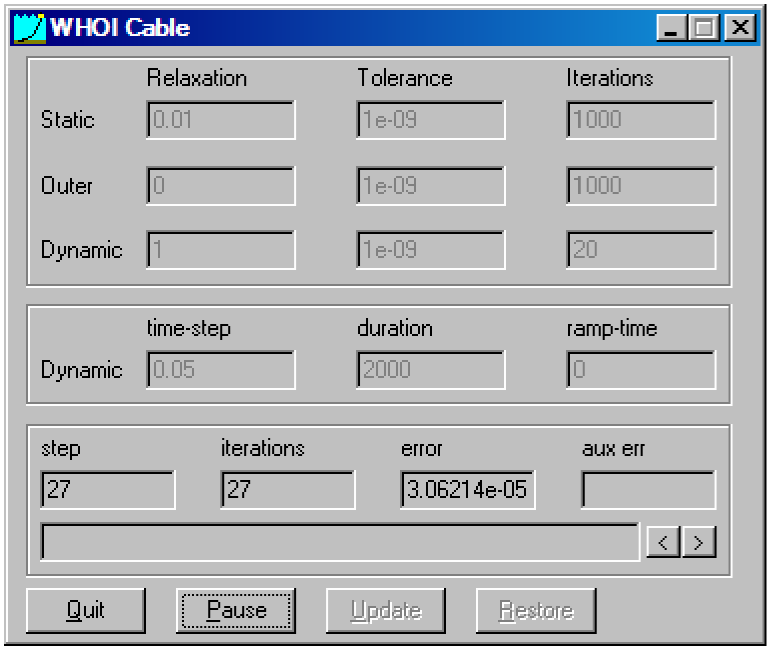

Figure A2.4. WHOI Cable solver screen.
Shown is the solver output screen which displays the relaxation, tolerance, iteration settings, the temporal settings, the step number, number of iterations performed at that step, and the related error to that iteration.

Appendix 3: C-Nav LOAPEX station time series

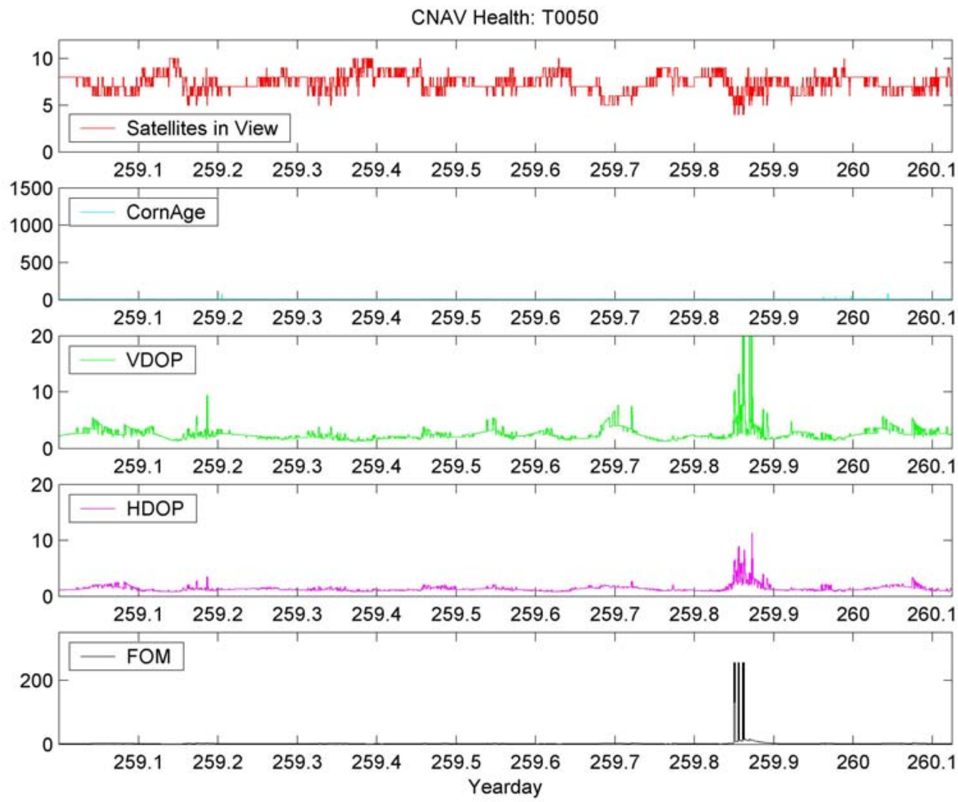

Figure A3.1. Station T50 C-Nav 'health' data. Note the time of high FOM corresponding to times of high HDOP, VDOP and low satellites in view.

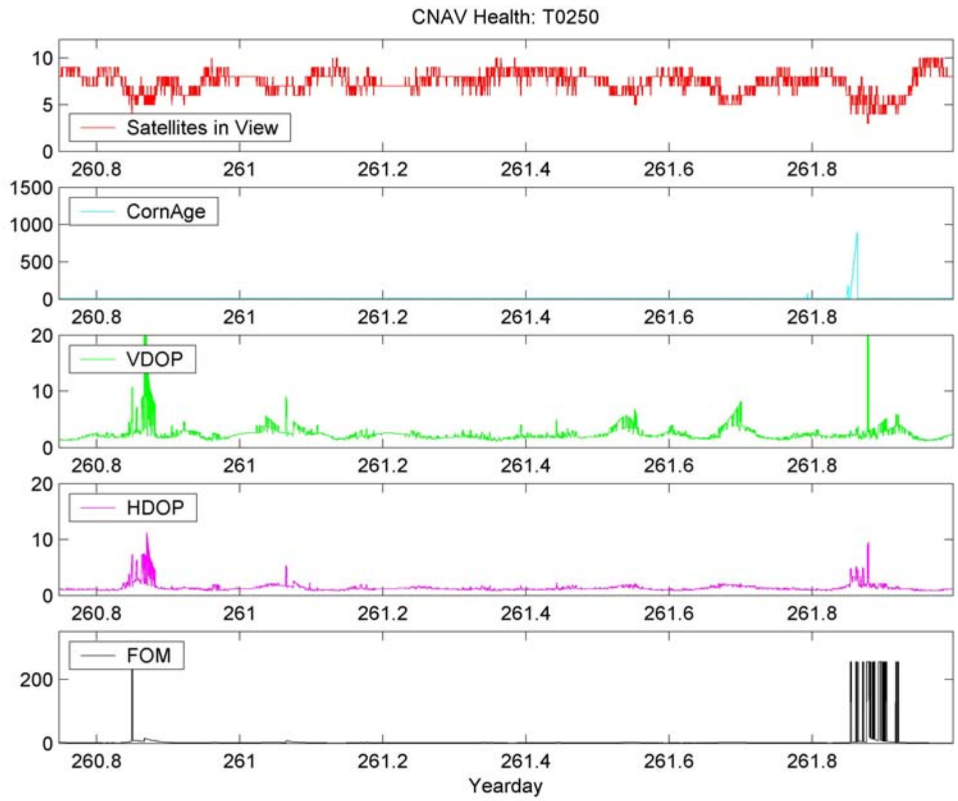

Figure A3.2. Station T250 C-Nav 'health' data. Note the time of high FOM corresponding to times of high HDOP, VDOP and low satellites in view.

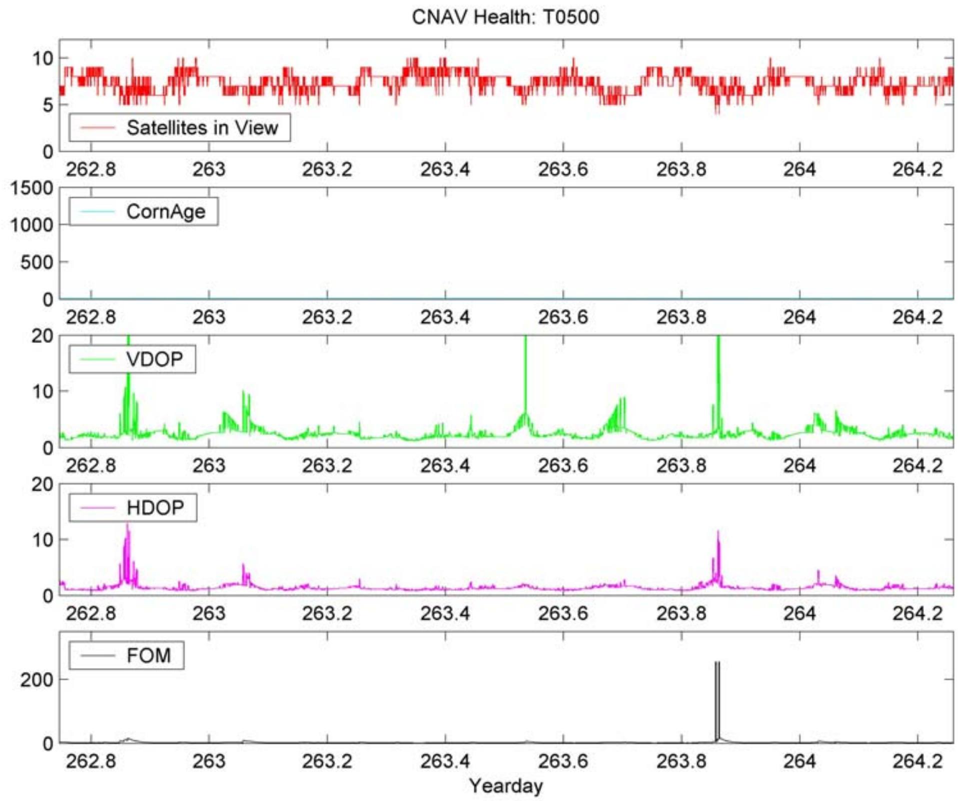

Figure A3.3. Station T500 C-Nav ‘health’ data. Note the time of high FOM corresponding to times of high HDOP, VDOP and low satellites in view, but the correction time remained very short.

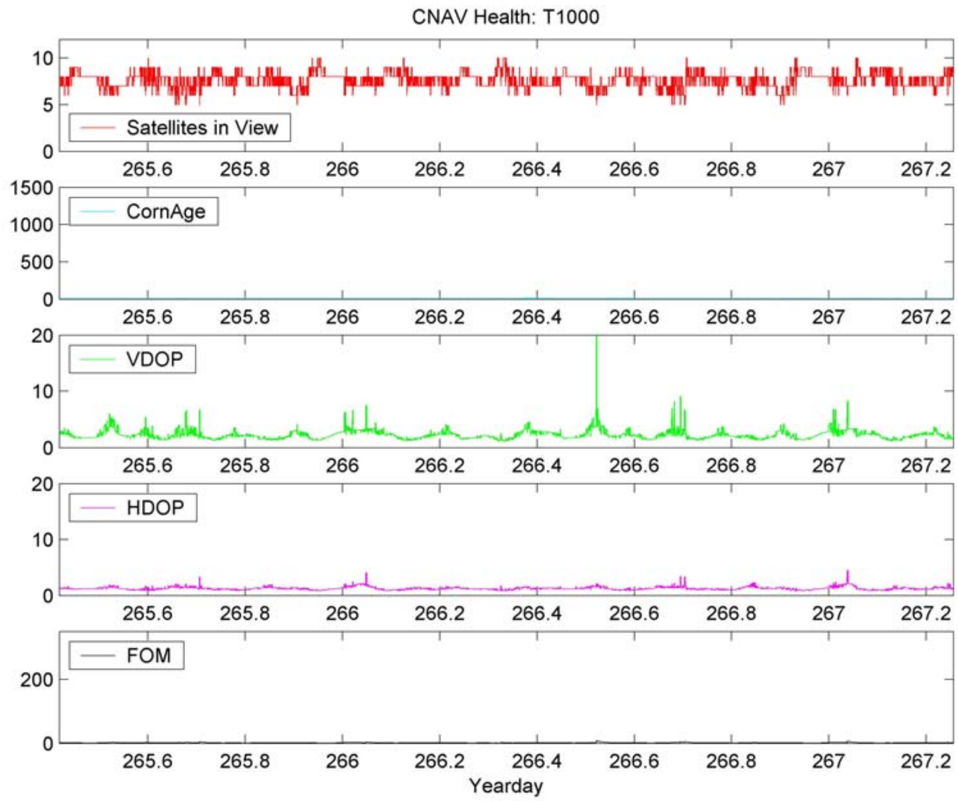

Figure A3.4. Station T1000 C-Nav ‘health’ data.

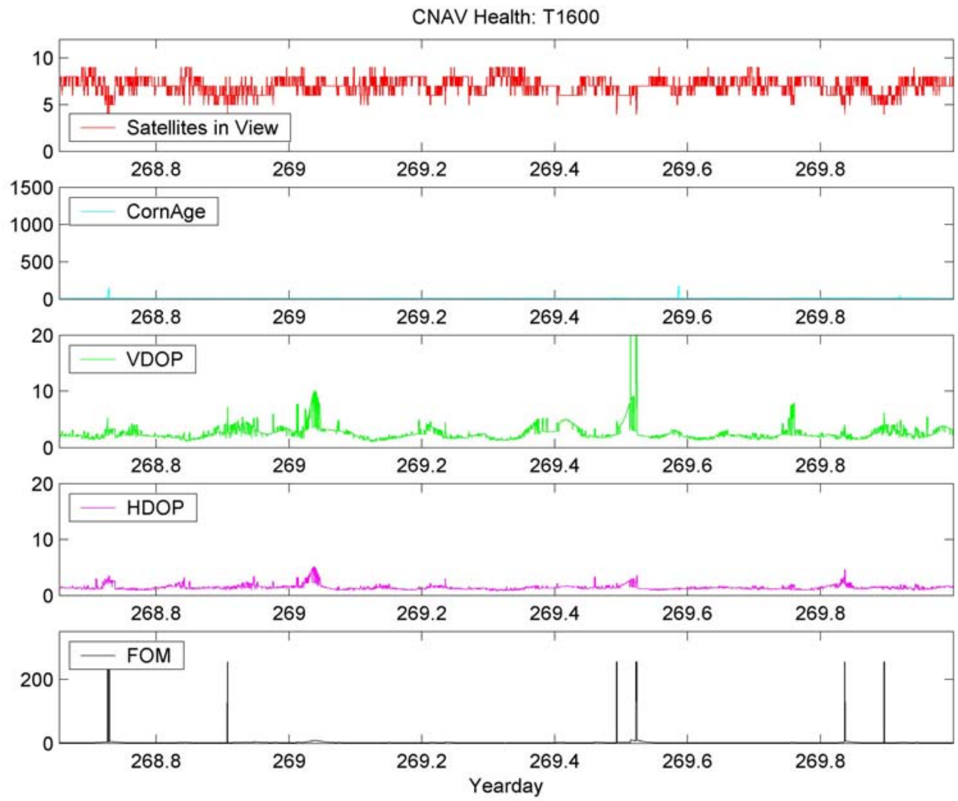

Figure A3.5. Station T1600 C-Nav 'health' data. Note the times of high FOM corresponding to times of high VDOP, but the HDOP remained low and the number of satellites in view remained high.

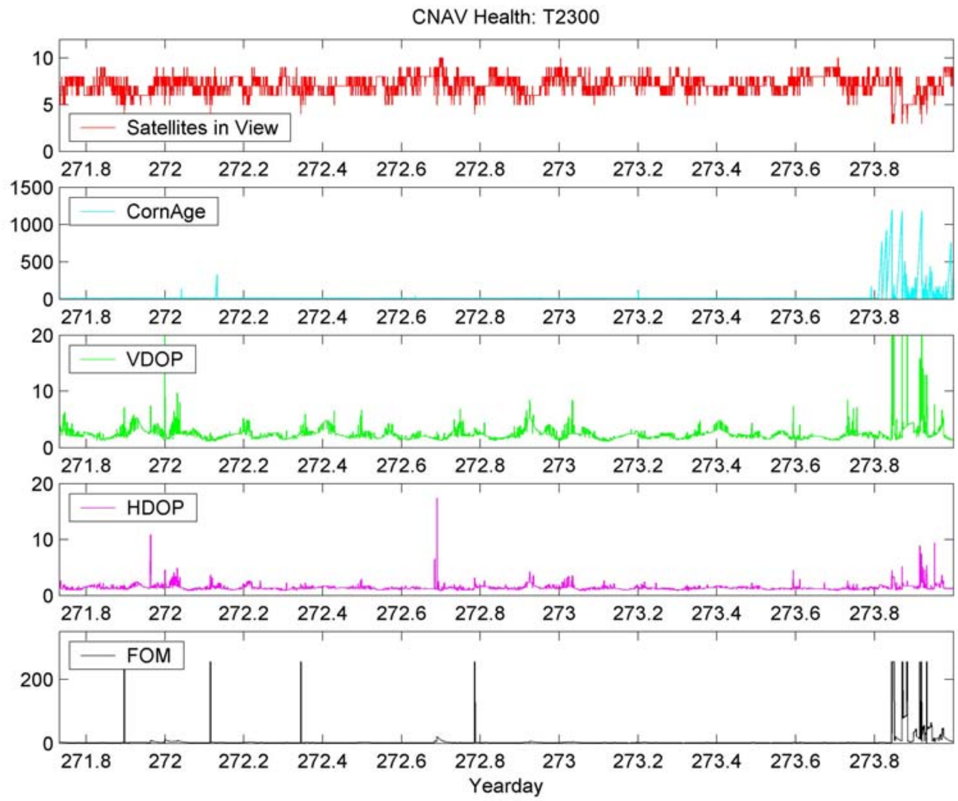

Figure A3.6. Station T2300 C-Nav ‘health’ data. Note the times of high FOM corresponding to times of high HDOP, VDOP, correction times and low satellites in view. These times contributed to excursions in the C-Nav data.

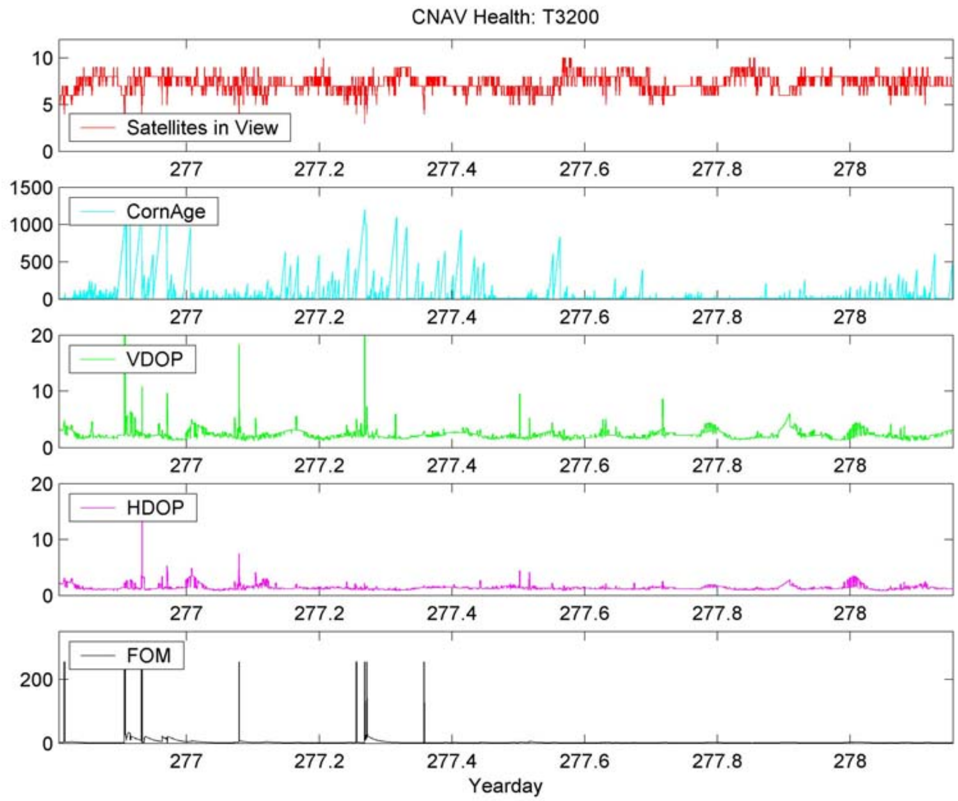

Figure A3.7. Station T3200 C-Nav ‘health’ data. Note the times of high FOM corresponding to times of high HDOP, VDOP, correction times and low satellites in view. These times contributed to excursions in the C-Nav data.

Appendix 4: ADCP time series for all LOAPEX stations

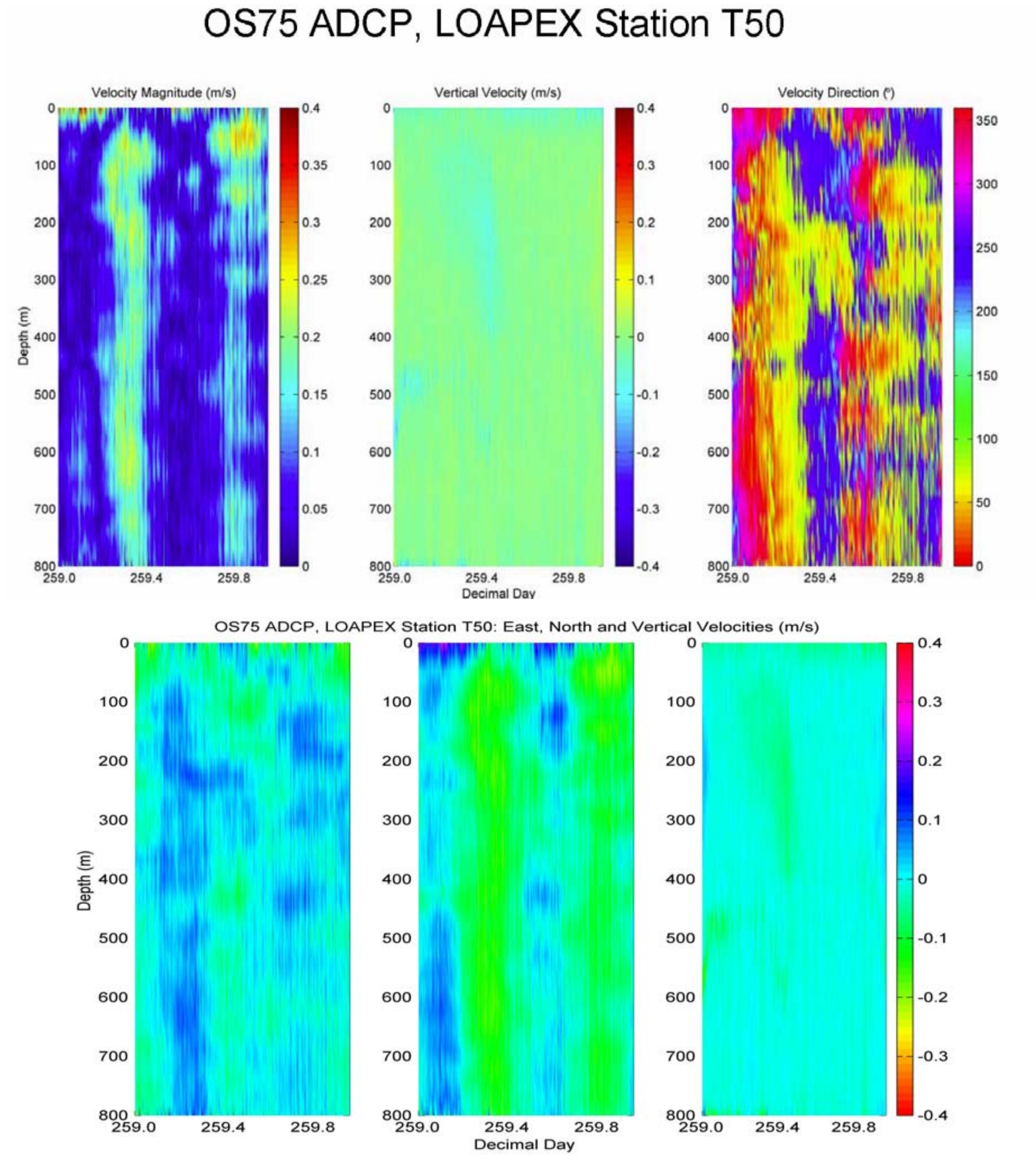

Figure A4.1. Station T50 ADCP time series.

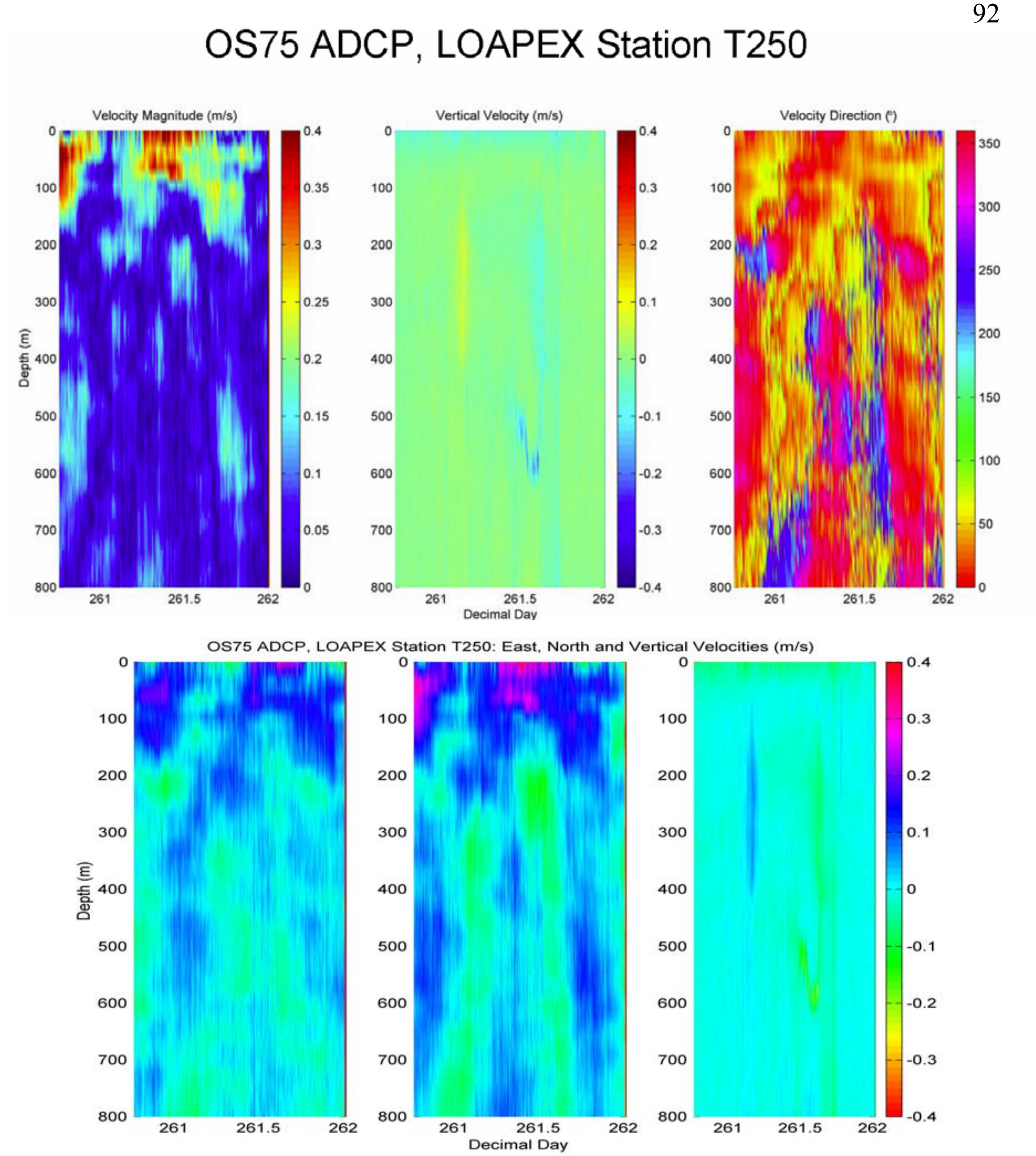

Figure A4.2. Station T250 ADCP time series.

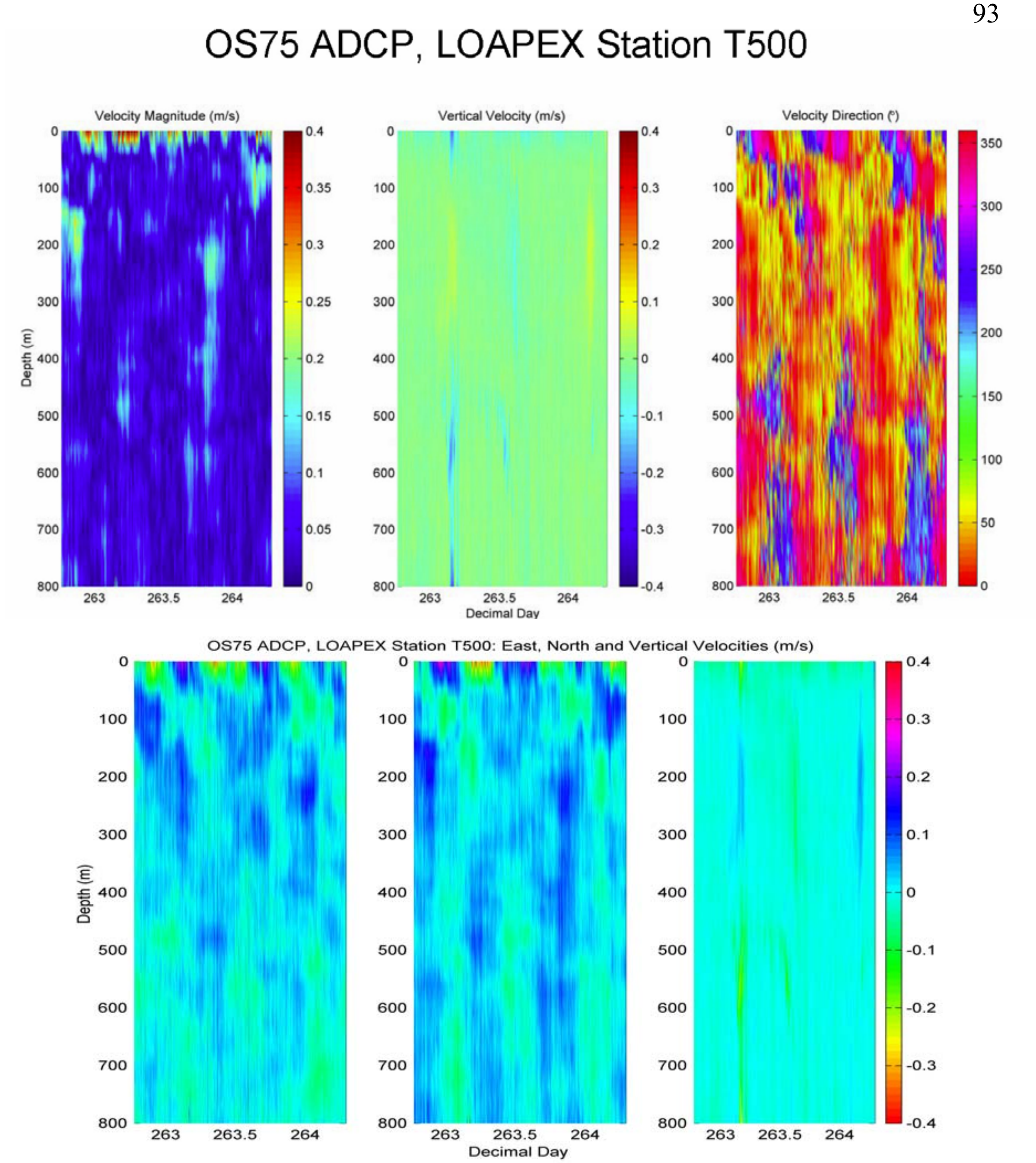

Figure A4.3. Station T500 ADCP time series

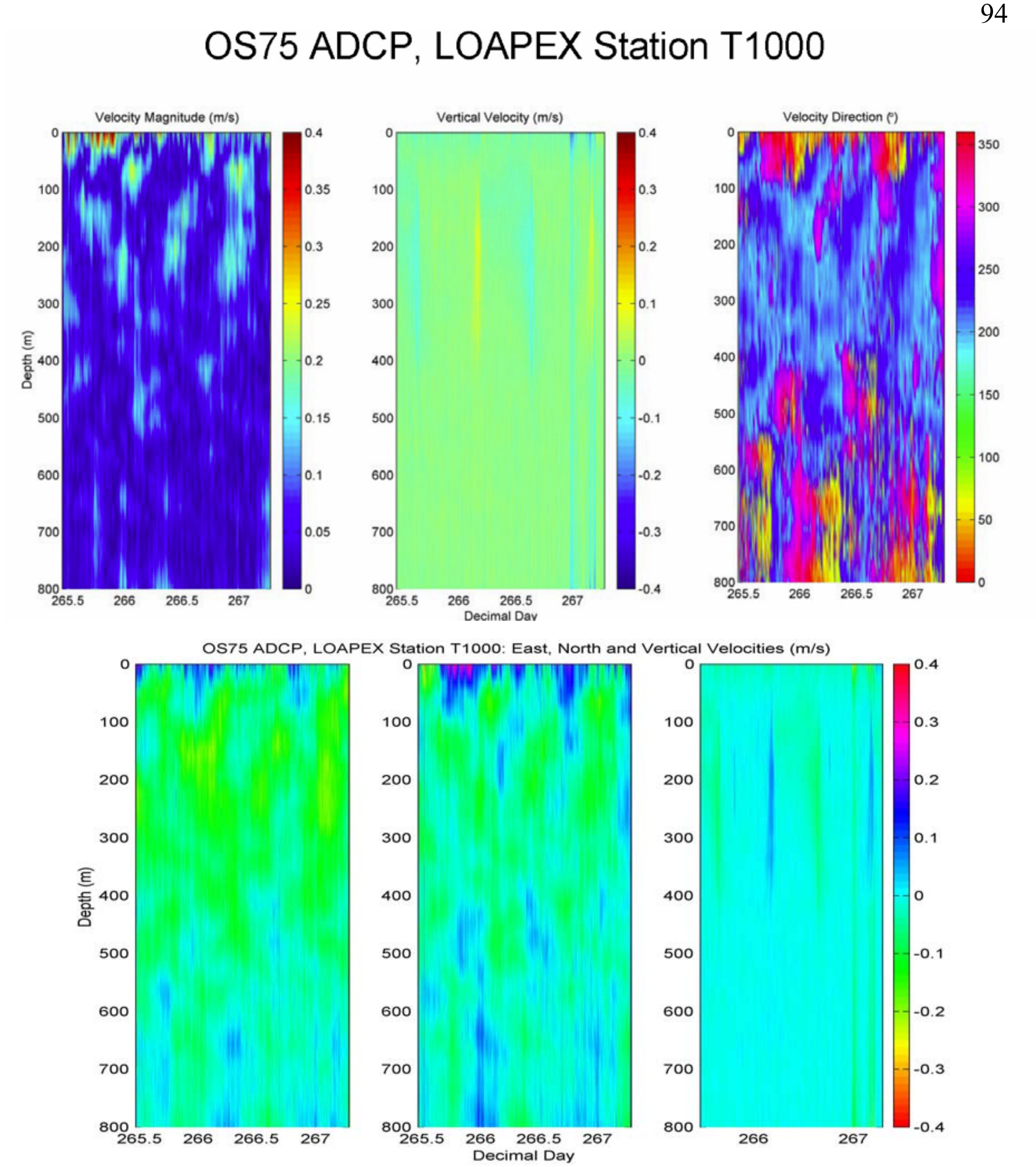

Figure A4.4. Station T1000 ADCP time series

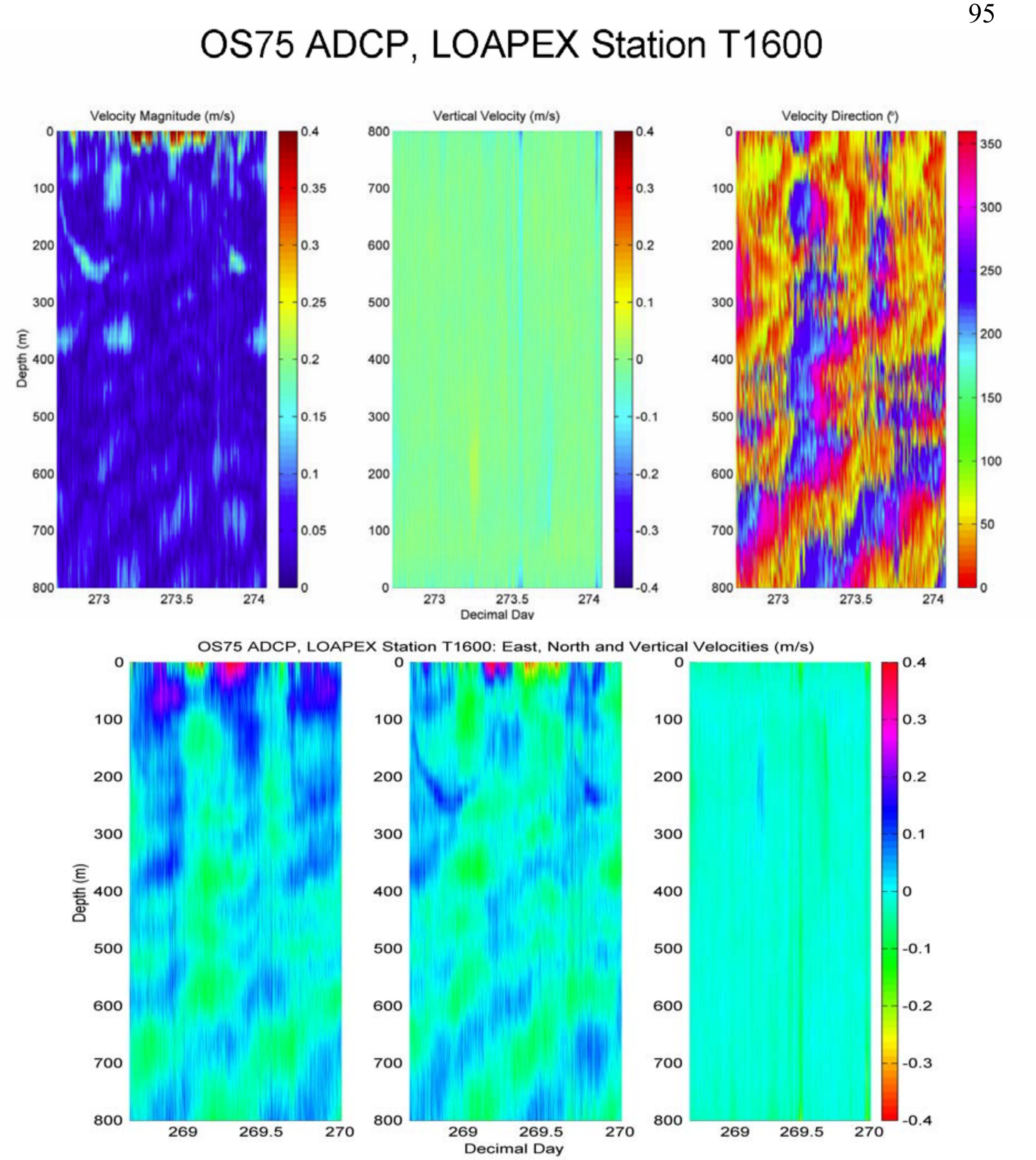

Figure A4.5. Station T1600 ADCP time series

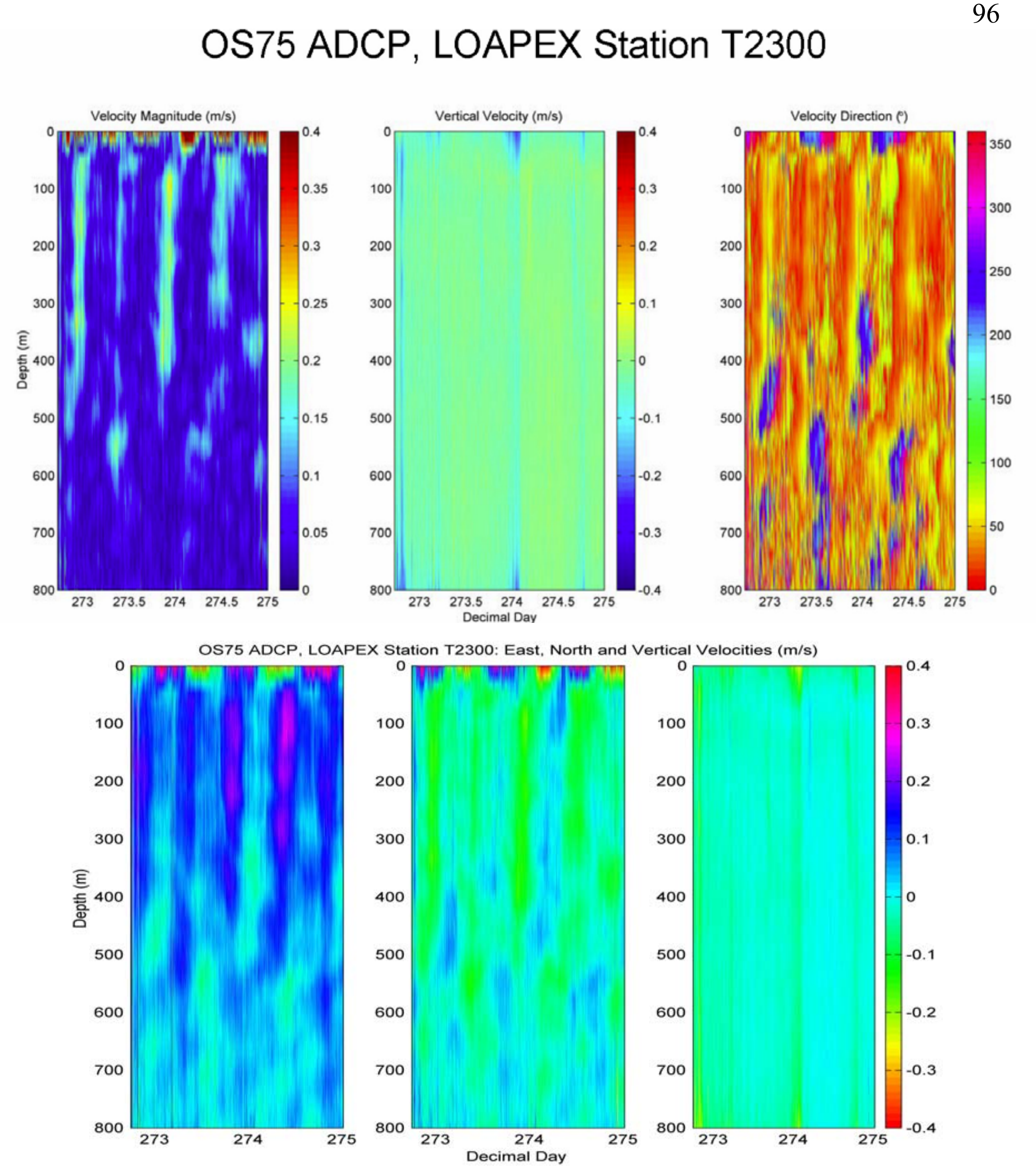

Figure A4.6. Station T2300 ADCP time series.

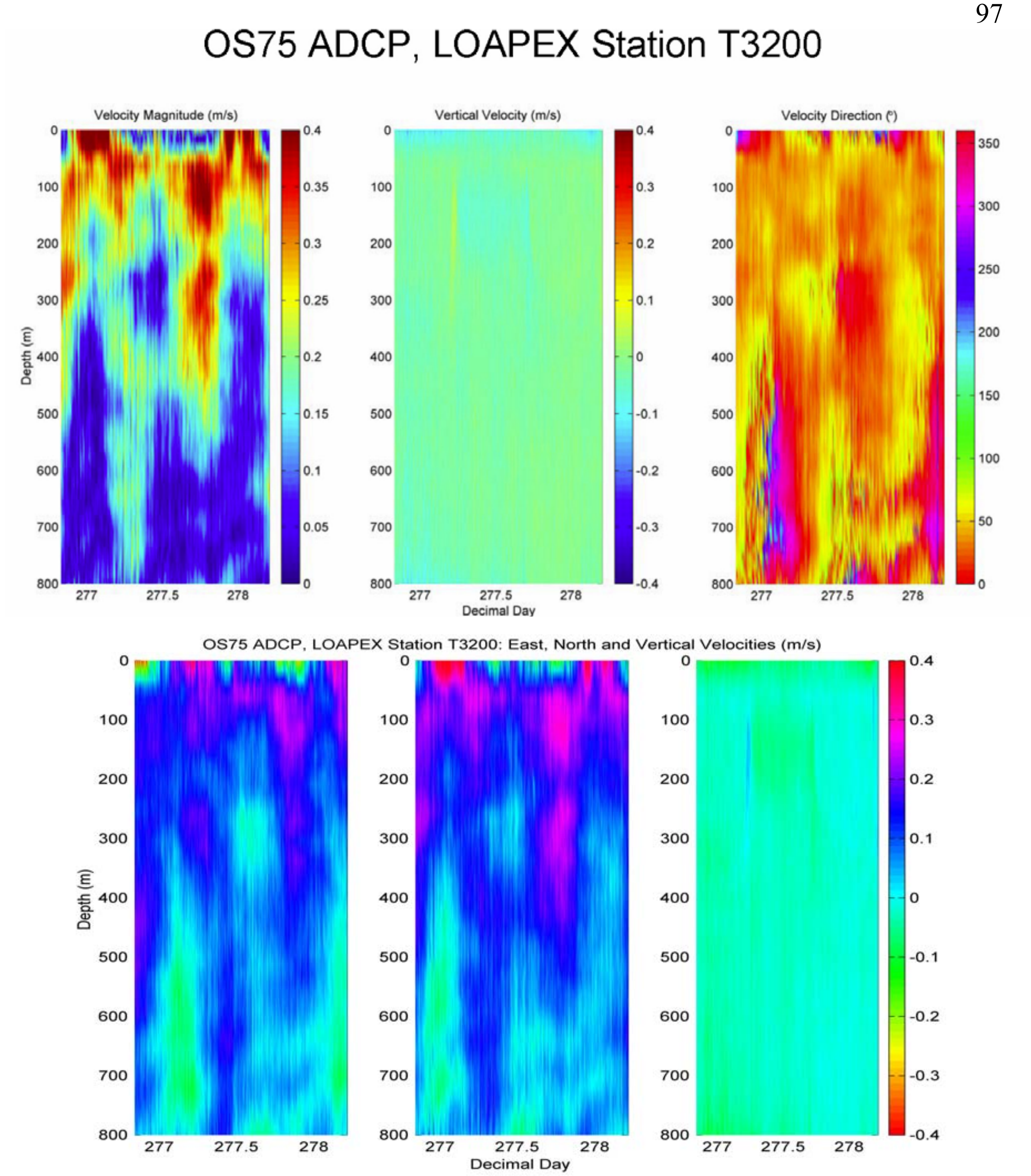

Figure A4.7. Station T3200 ADCP time series.

Appendix 5: Plan-view of ship and source position during source deployments.

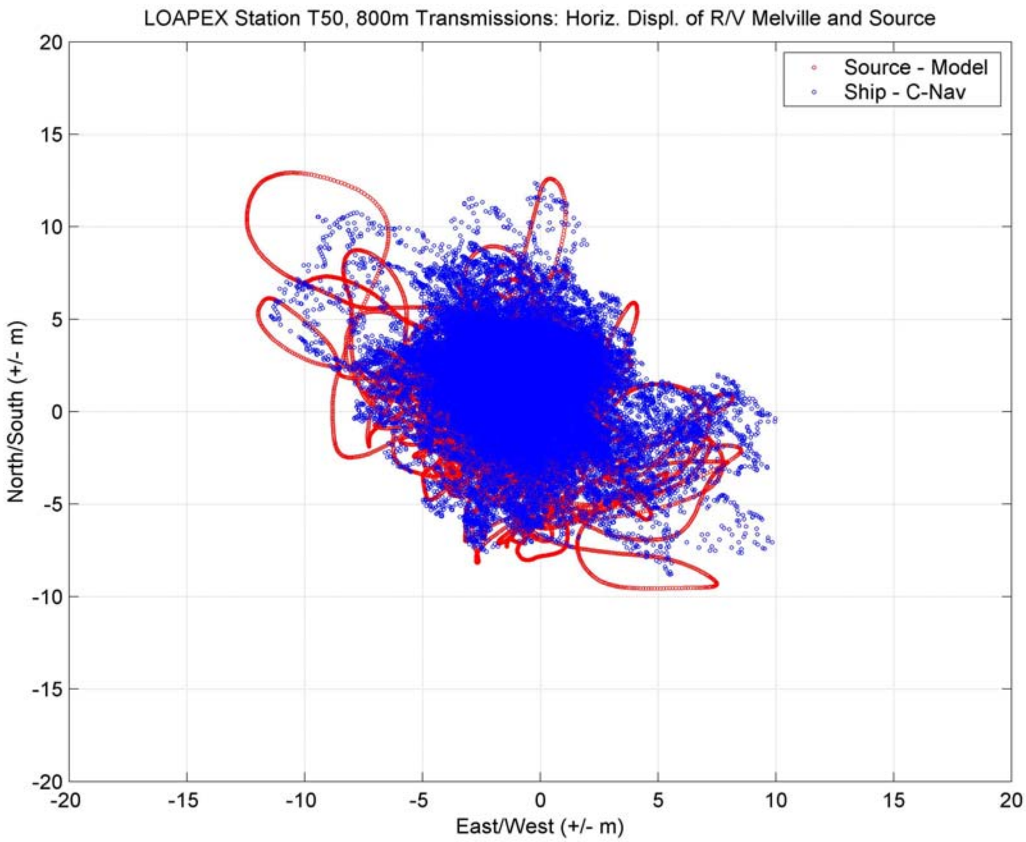

Figure A5.1. Station T50 ship and 800 m source position during deployment.

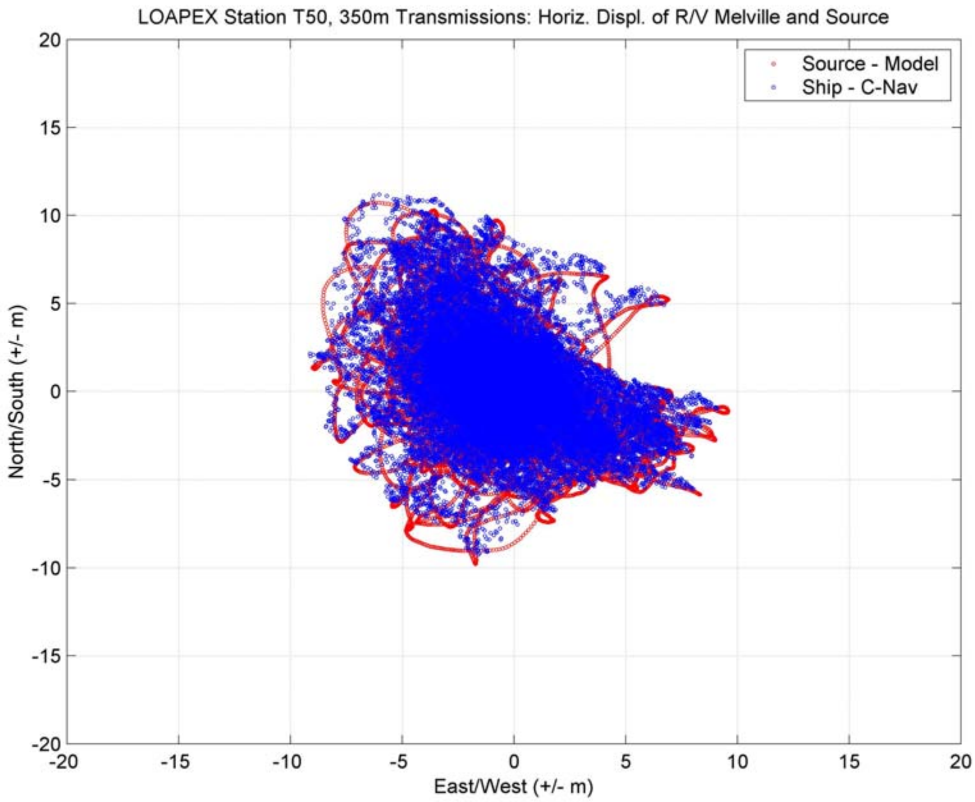

Figure A5.2. Station T50 ship and 350 m source position during deployment.

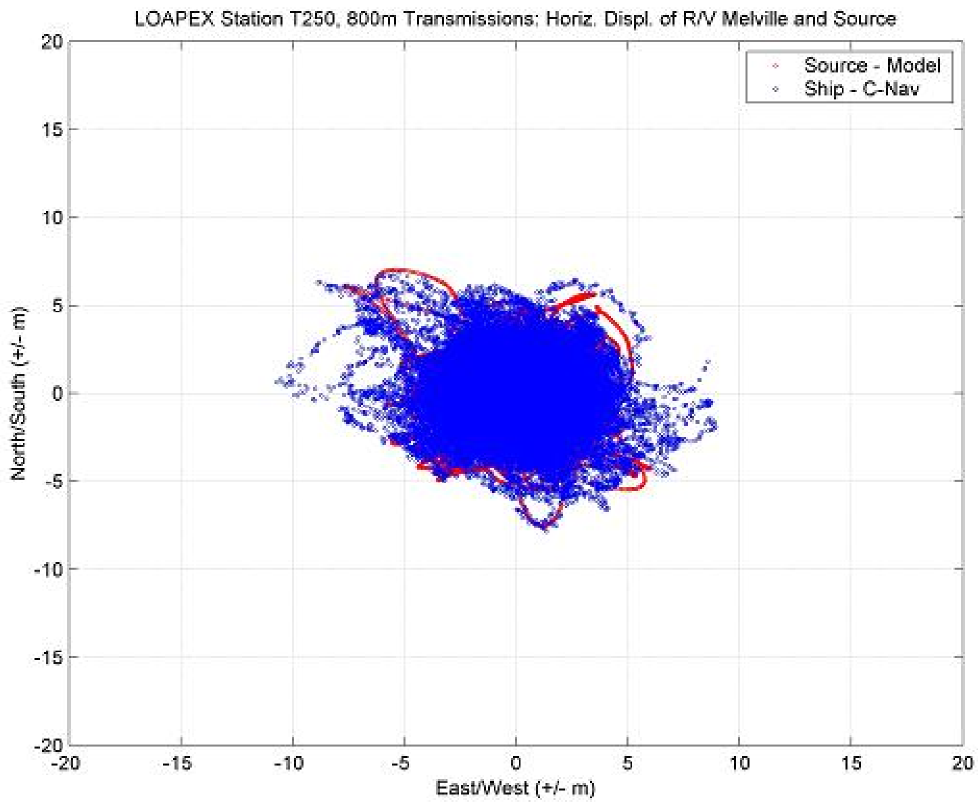

Figure A5.3. Station T250 ship and 800 m source position during deployment

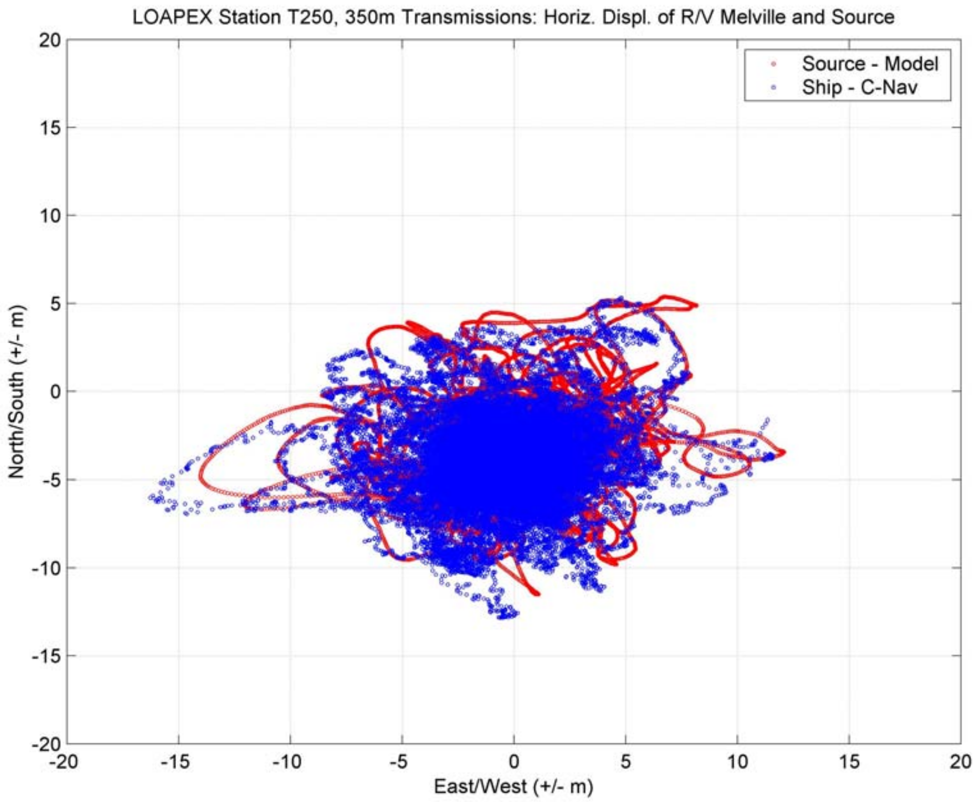

Figure A5.4. Station T250 ship and 350 m source position during deployment

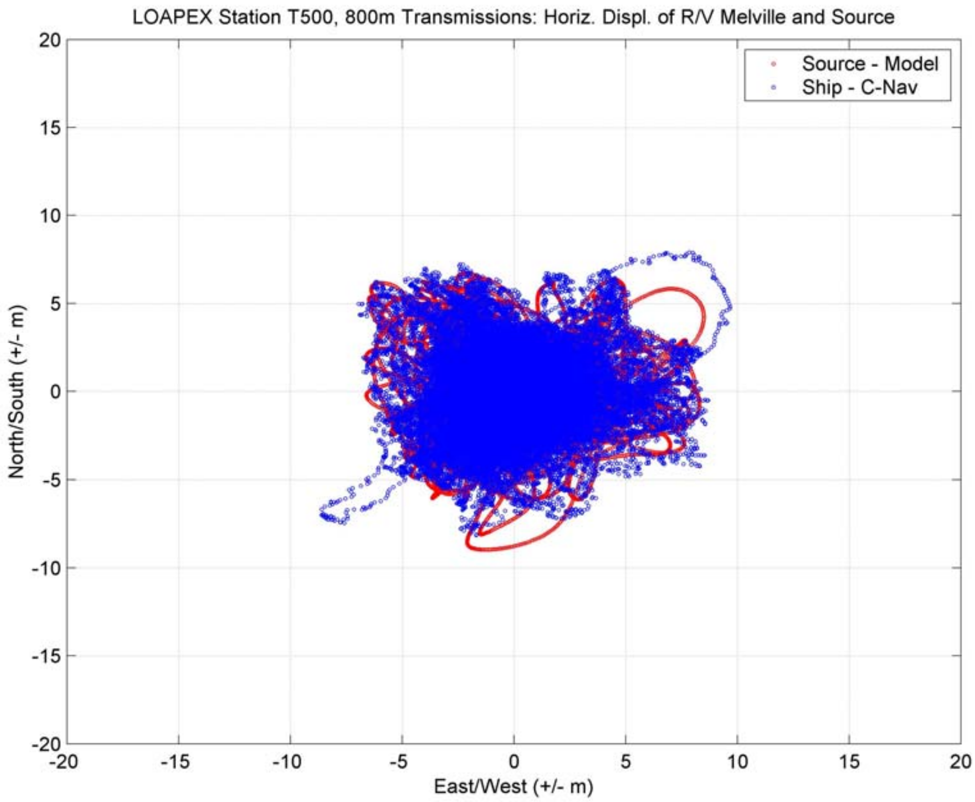

Figure A5.5. Station T500 ship and 800 m source position during deployment

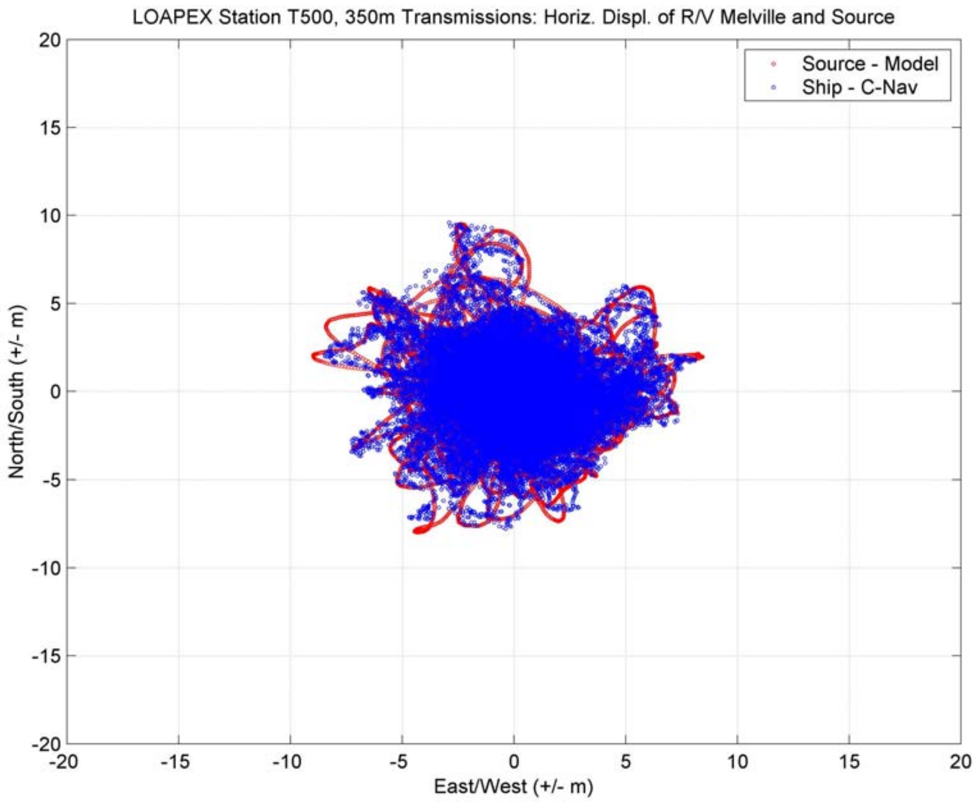

Figure A5.6. Station T500 ship and 350 m source position during deployment

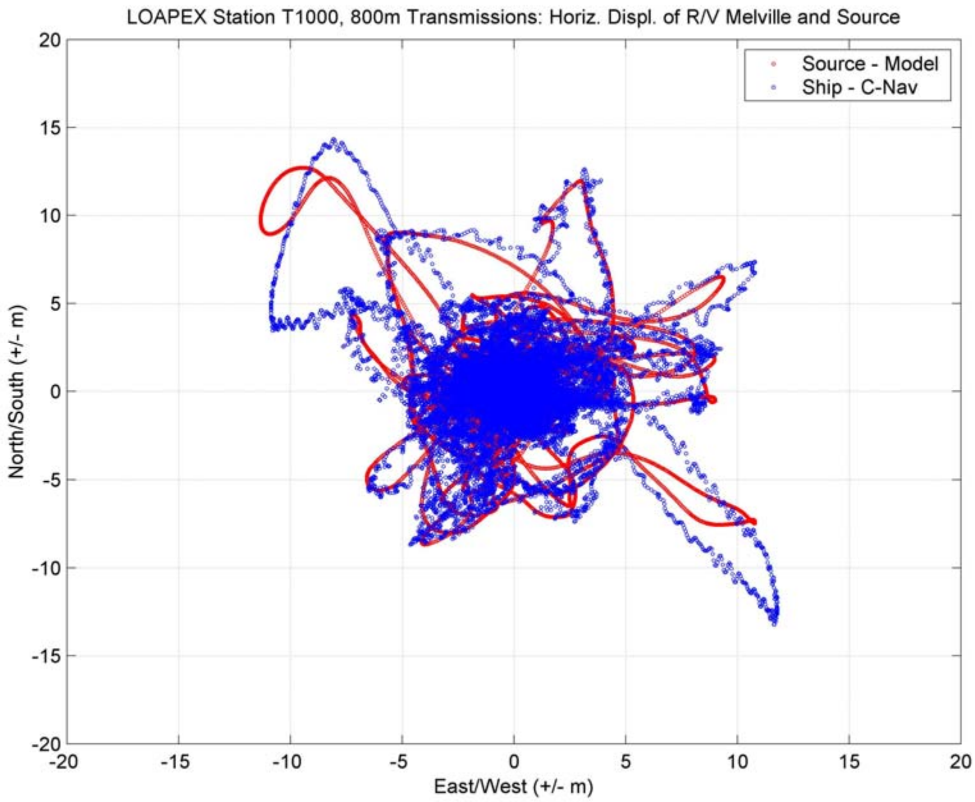

Figure A5.7. Station T1000 ship and 800 m source position during deployment

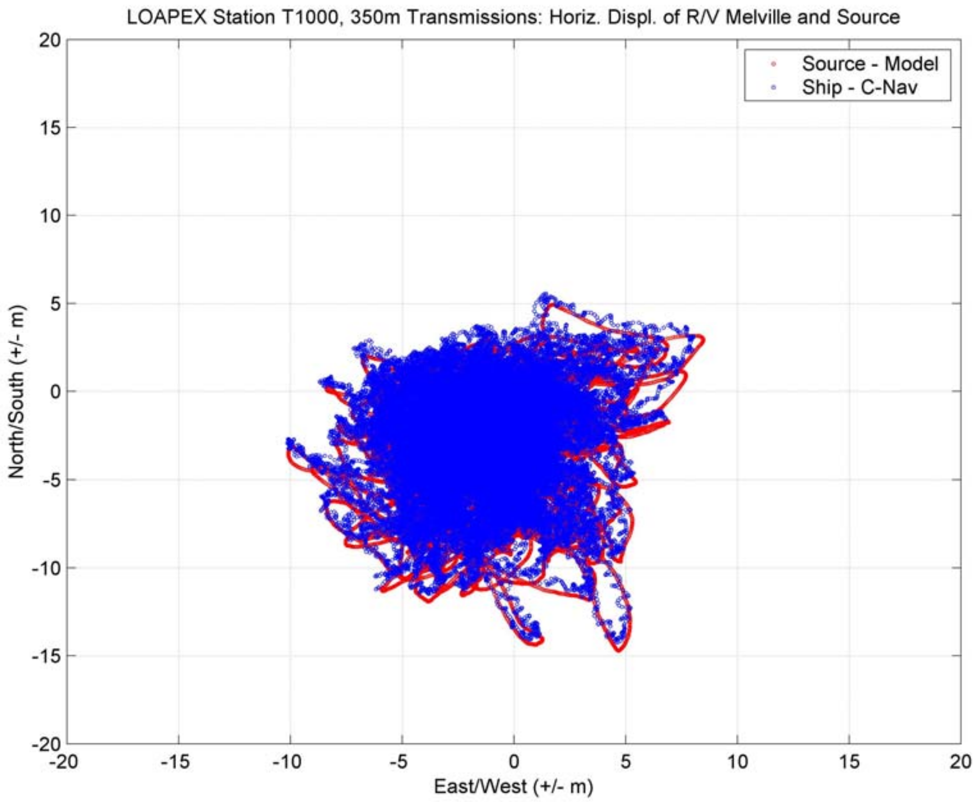

Figure A5.8. Station T1000 ship and 350 m source position during deployment

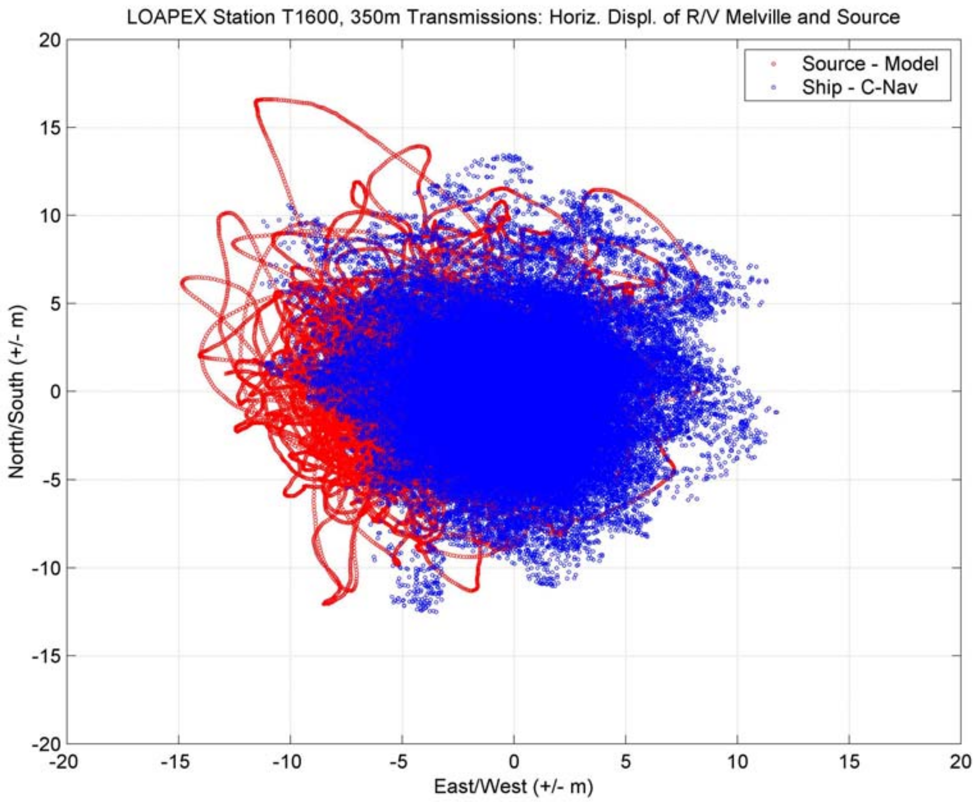

Figure A5.9. Station T1600 ship and 350 m source position during deployment

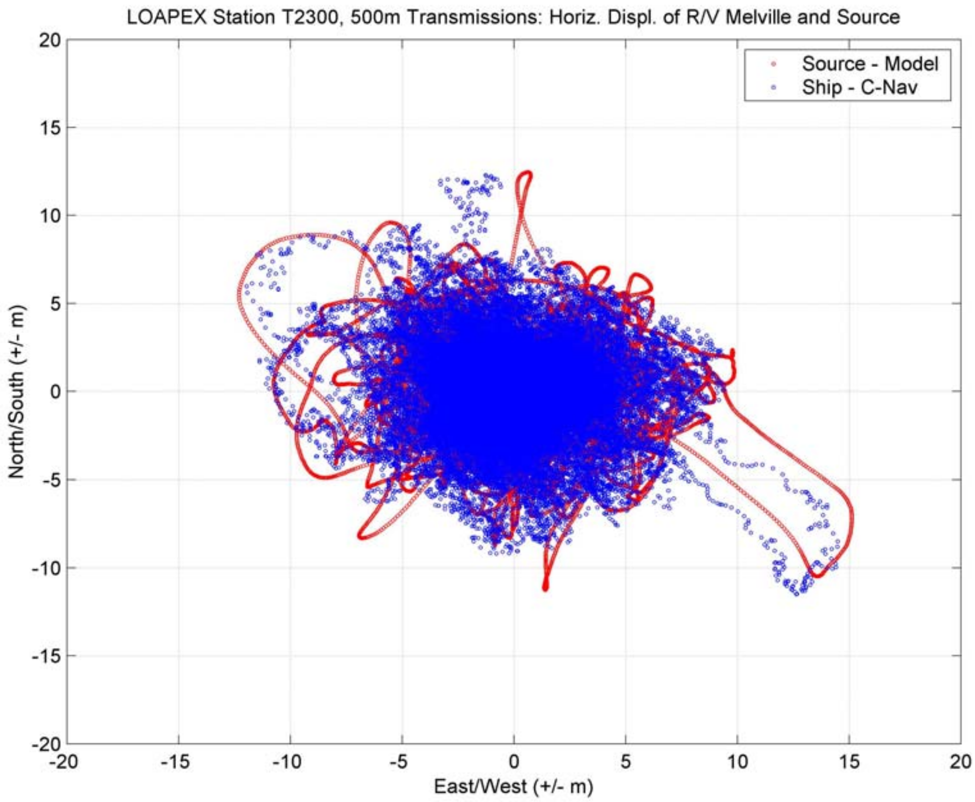

Figure A5.10. Station T2300 ship and 500 m source position during deployment

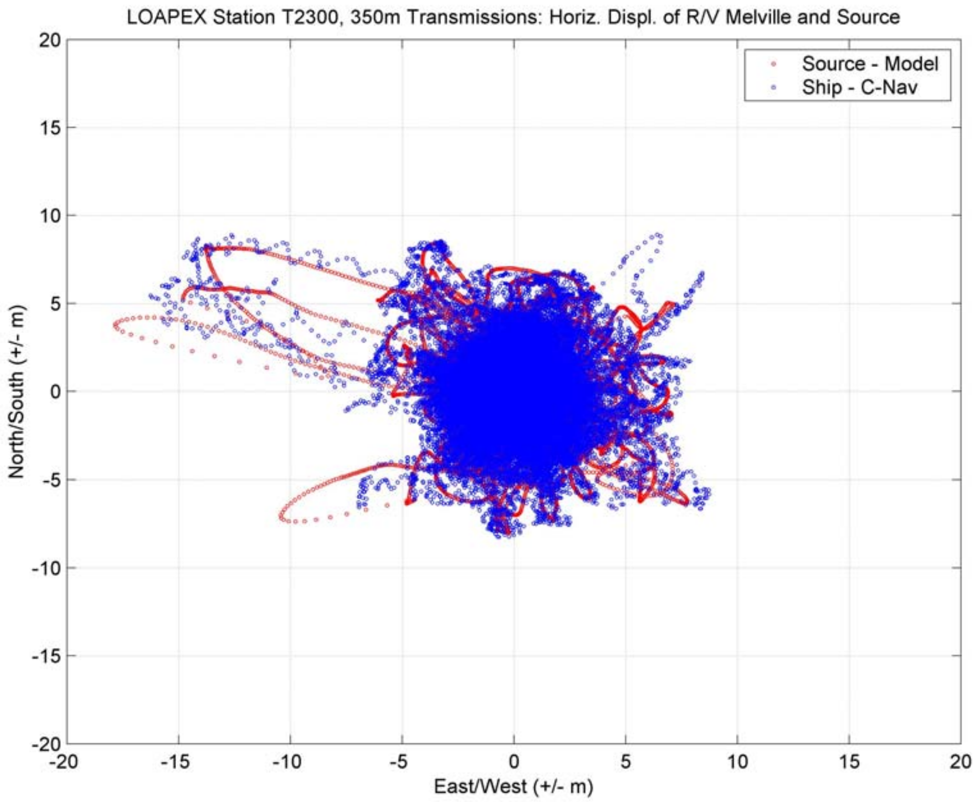

Figure A5.11. Station T2300 ship and 350 m source position during deployment

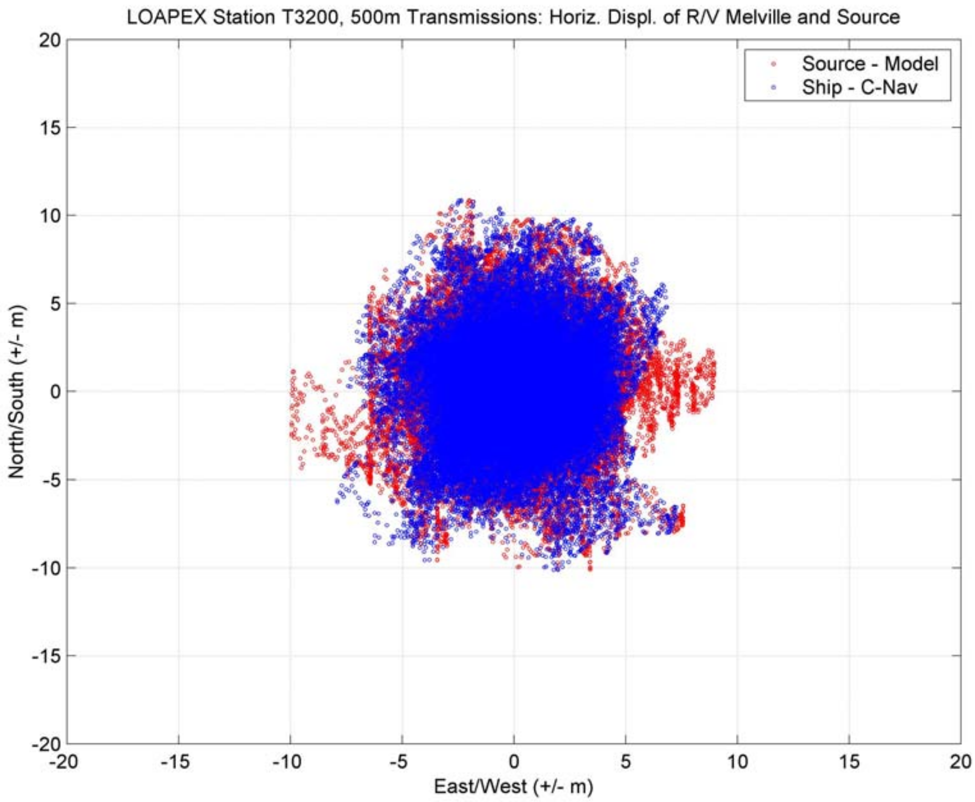

Figure A5.12. Station T3200 ship and 500 m source position during deployment

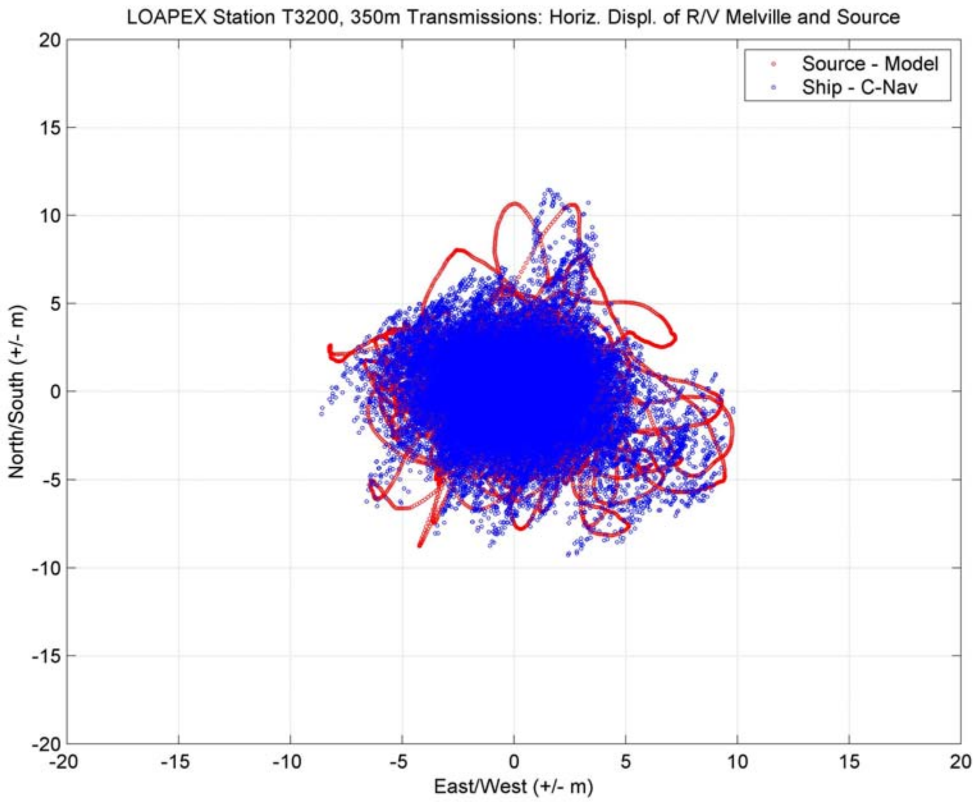

Figure A5.13. Station T3200 ship and 350 m source position during deployment

Appendix 6: Position comparison: Ship (C-Nav), Source (WHOI Cable and Interrogator/Transponder)

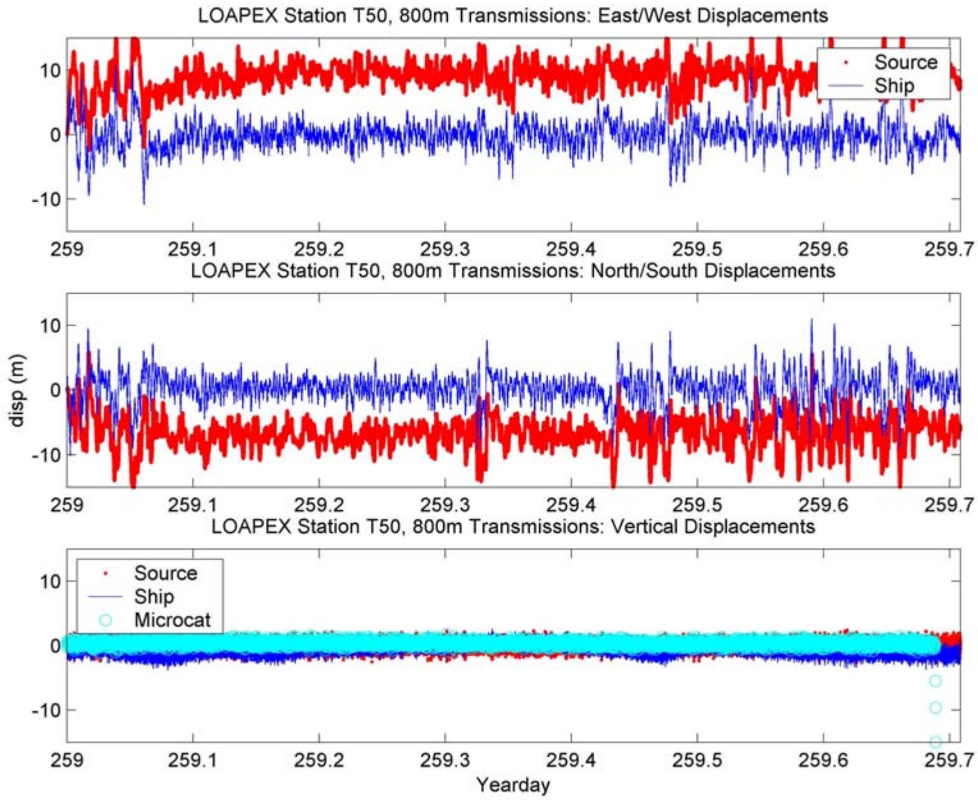

Figure A6.1. Station T50 ship and 800 m source position during deployment

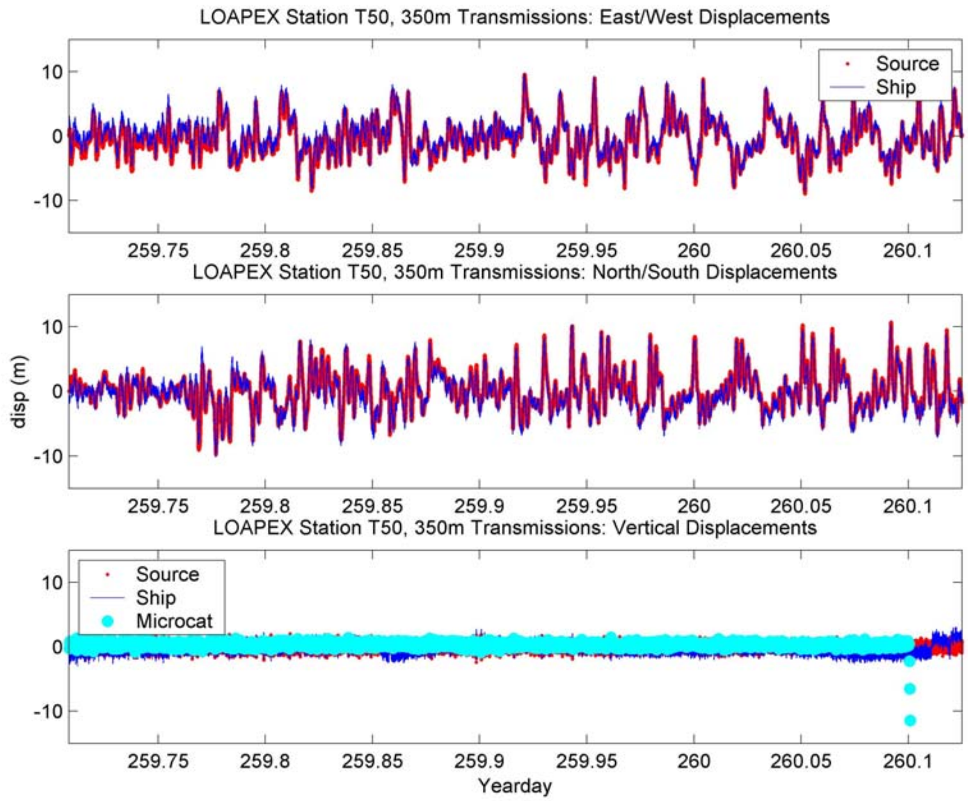

Figure A6.2. Station T50 ship and 350 m source position during deployment

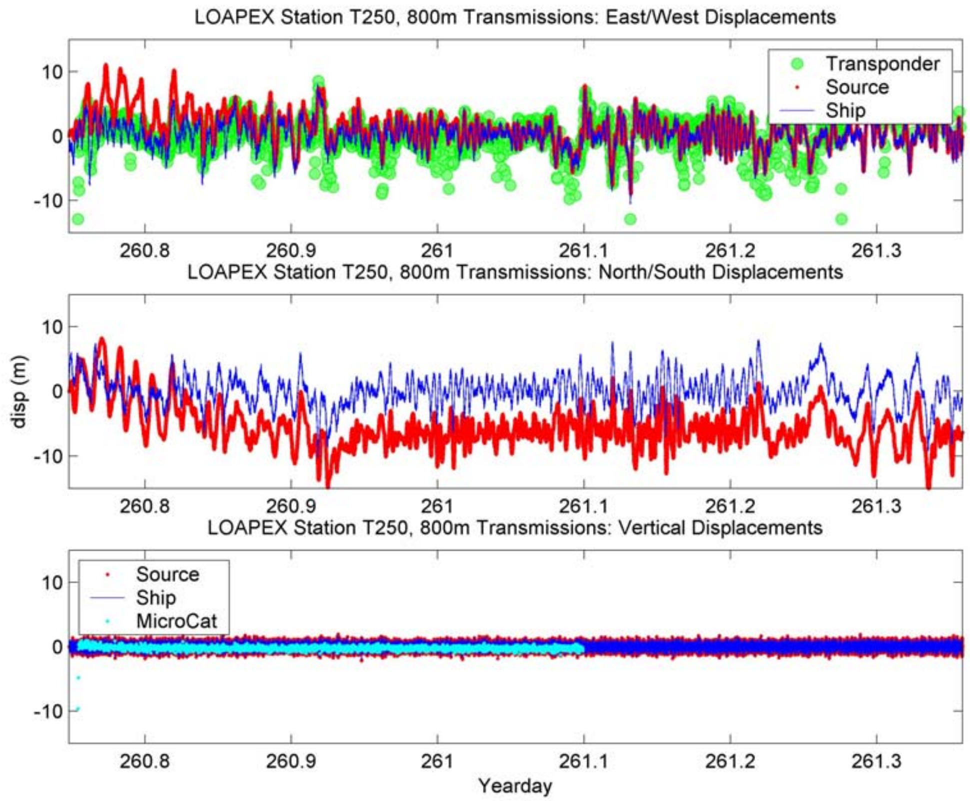

Figure A6.3. Station T250 ship and 800 m source position during deployment

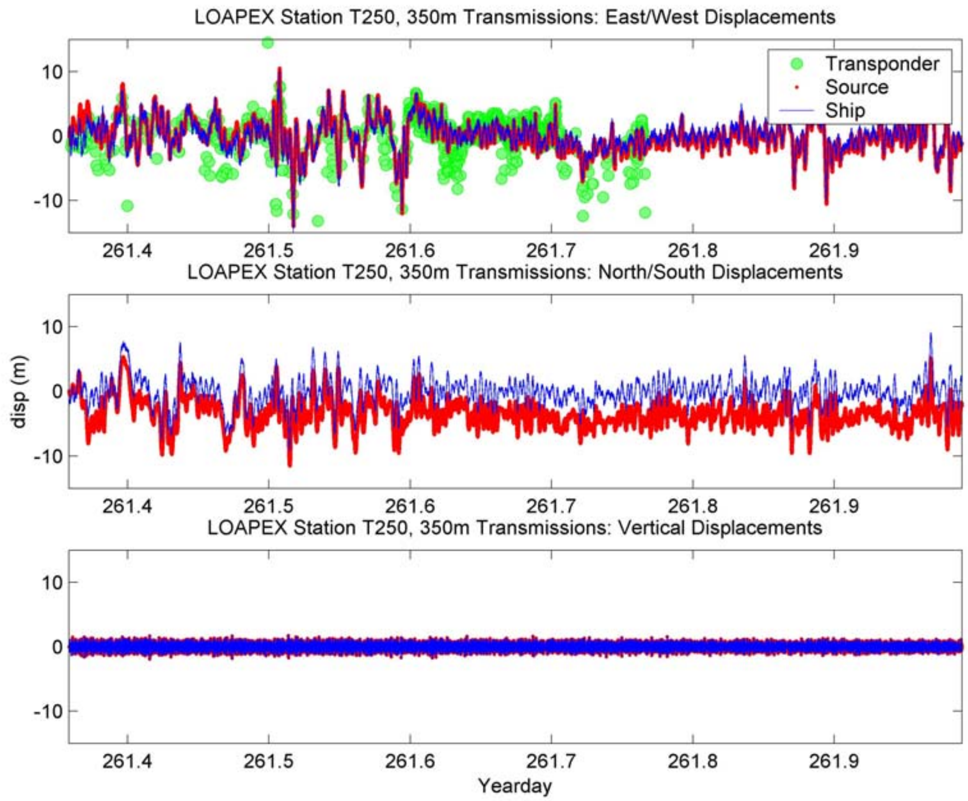

Figure A6.4. Station T250 ship and 350 m source position during deployment

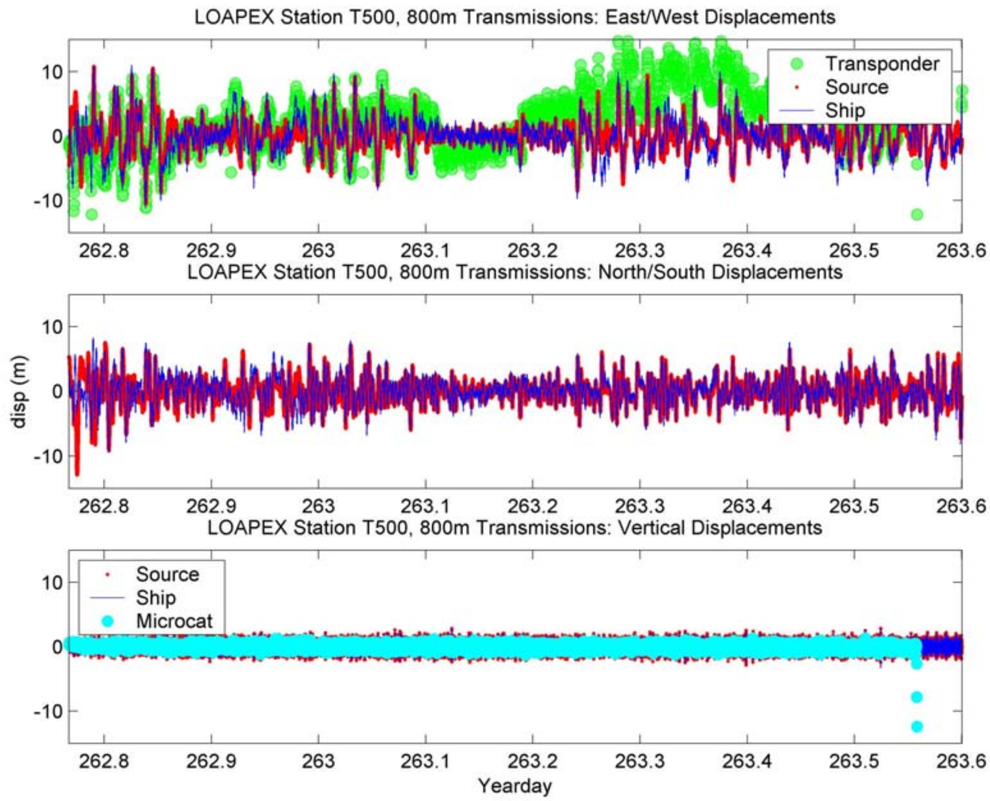

Figure A6.5. Station T500 ship and 800 m source position during deployment

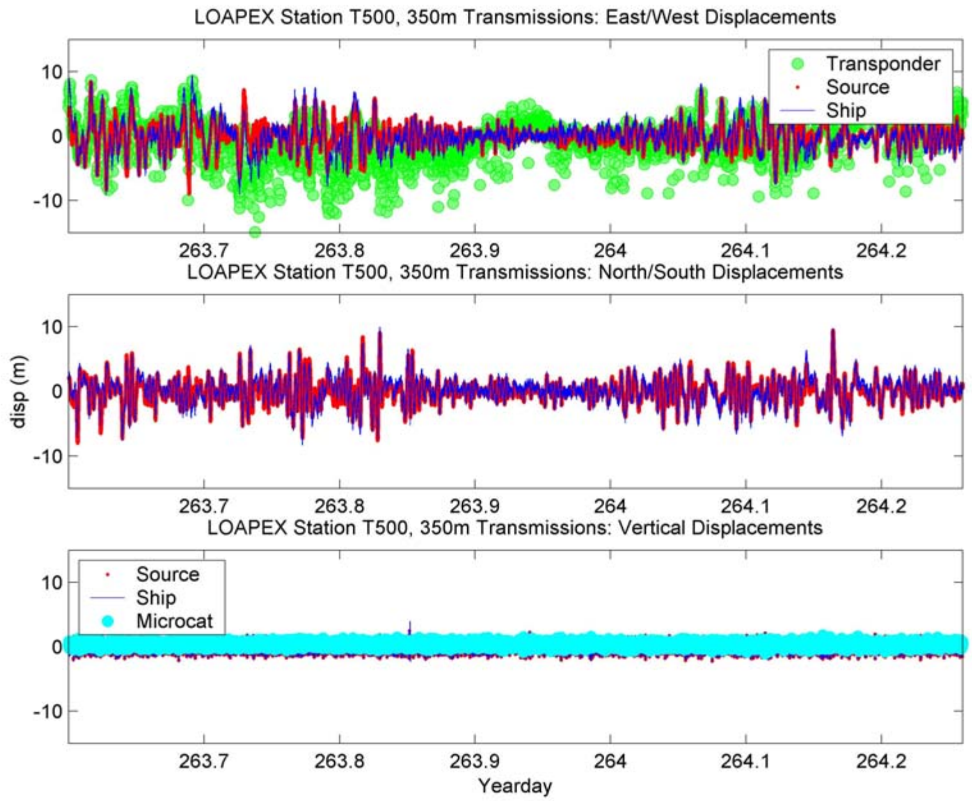

Figure A6.6. Station T500 ship and 350 m source position during deployment

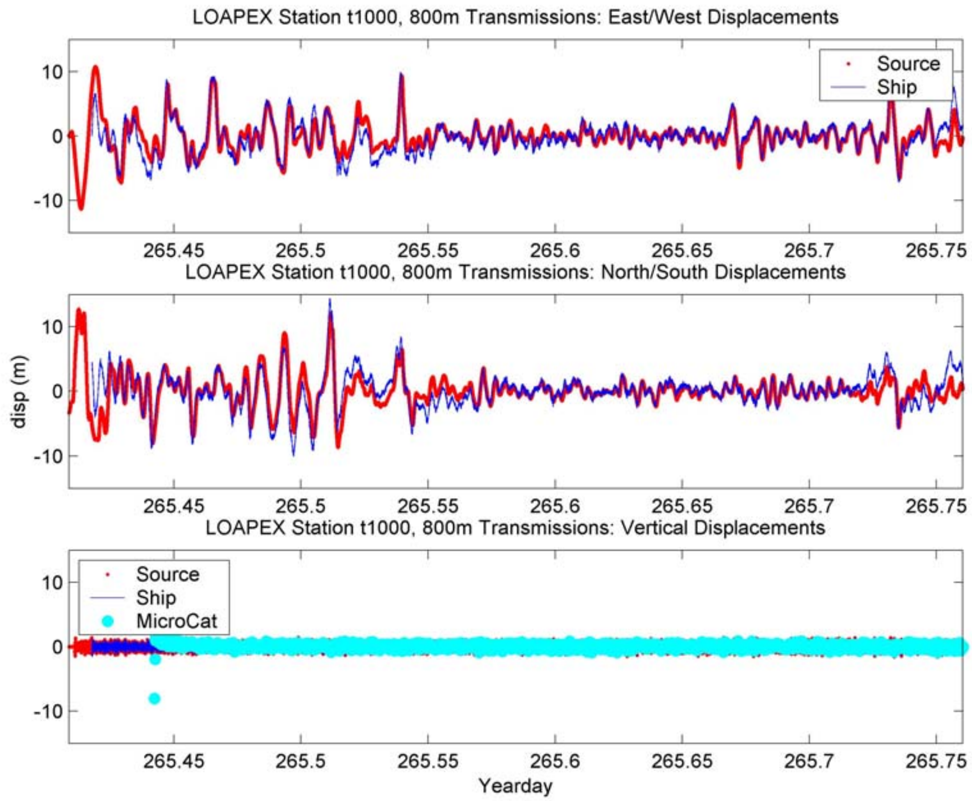

Figure A6.7. Station T1000 ship and 800 m source position during deployment

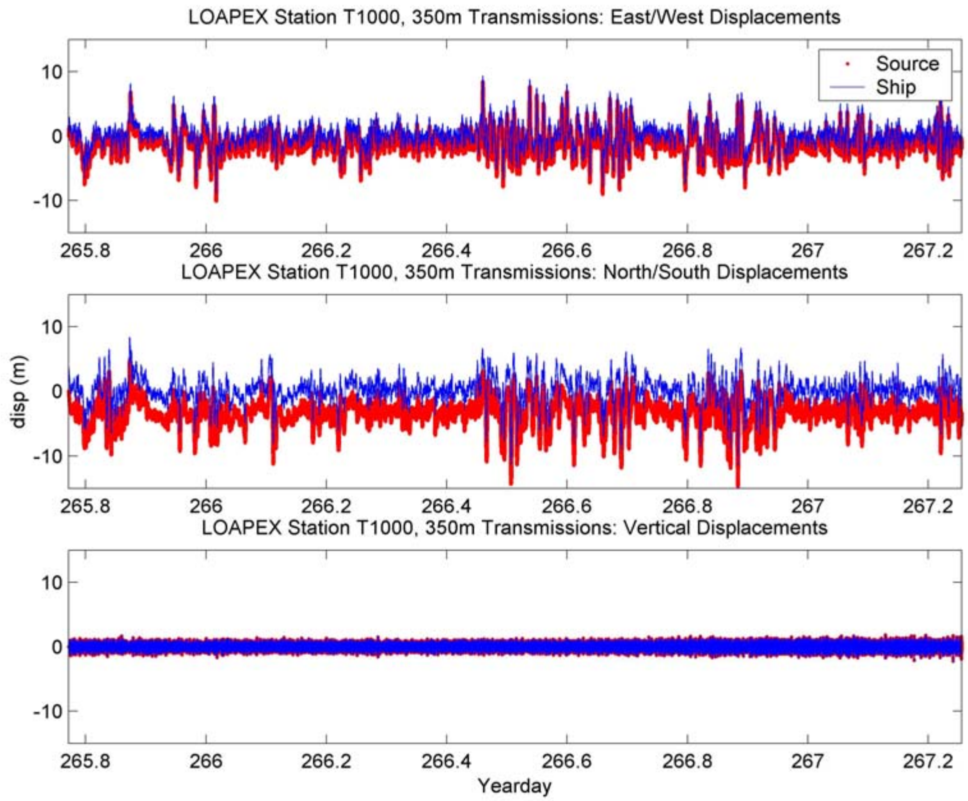

Figure A6.8. Station T1000 ship and 350 m source position during deployment

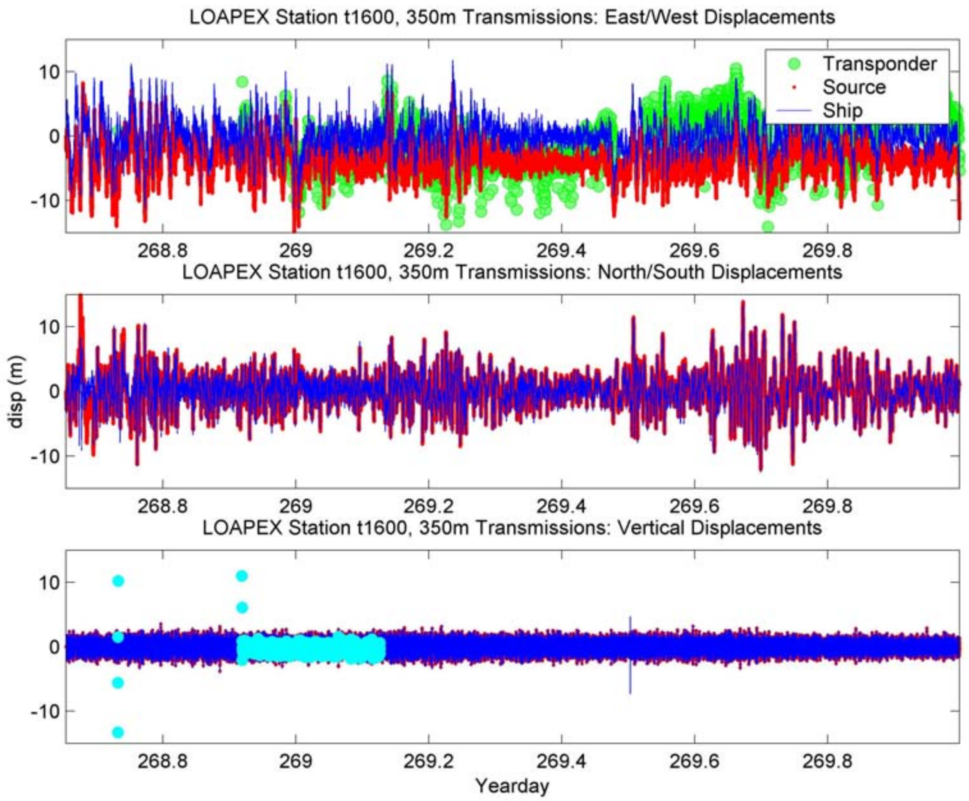

Figure A6.9. Station T1600 ship and 350 m source position during deployment

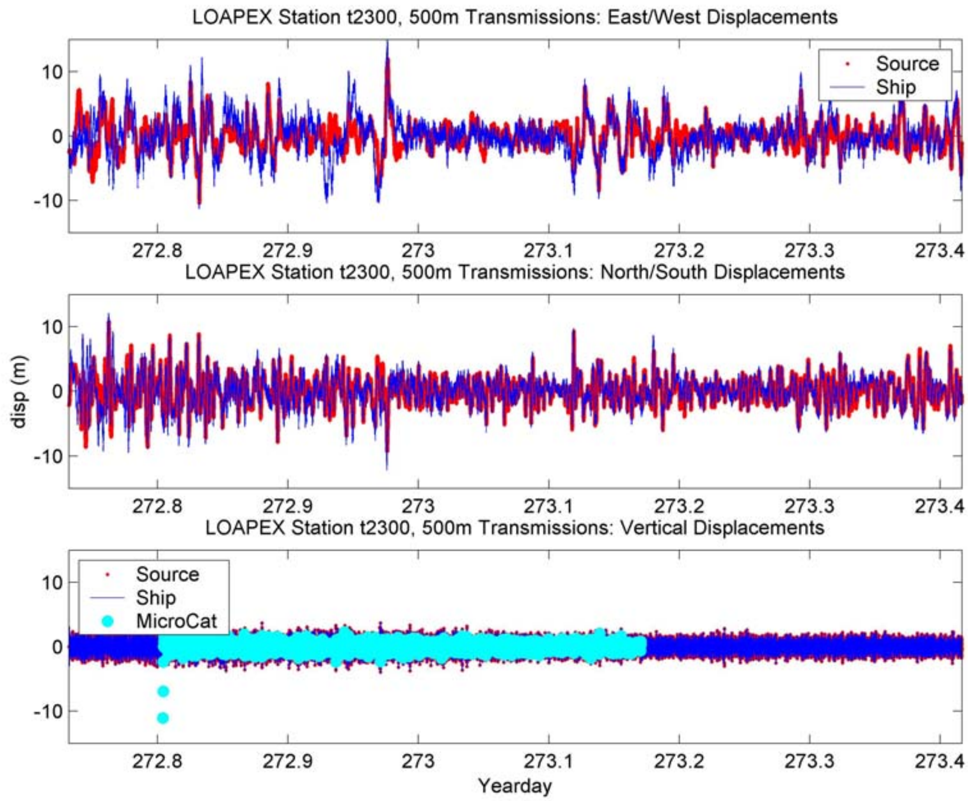

Figure A6.10. Station T2300 ship and 500 m source position during deployment

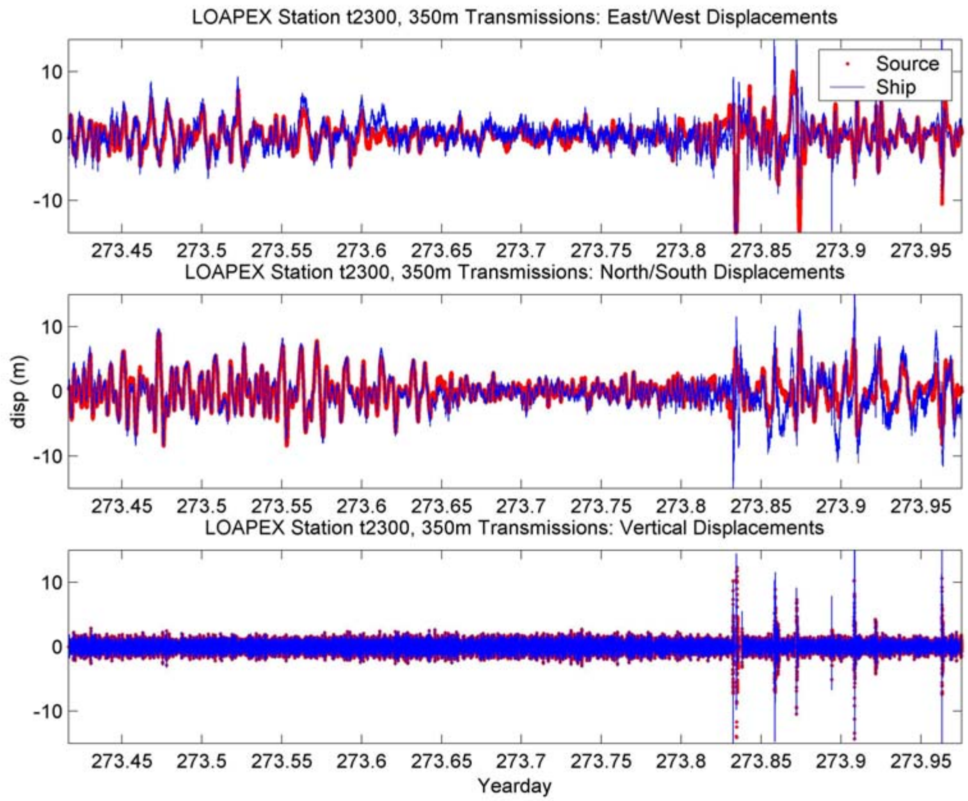

Figure A6.11. Station T2300 ship and 350 m source position during deployment. Note the times of high excursions. These times correlate to high values of FOM from the C-Nav time series.

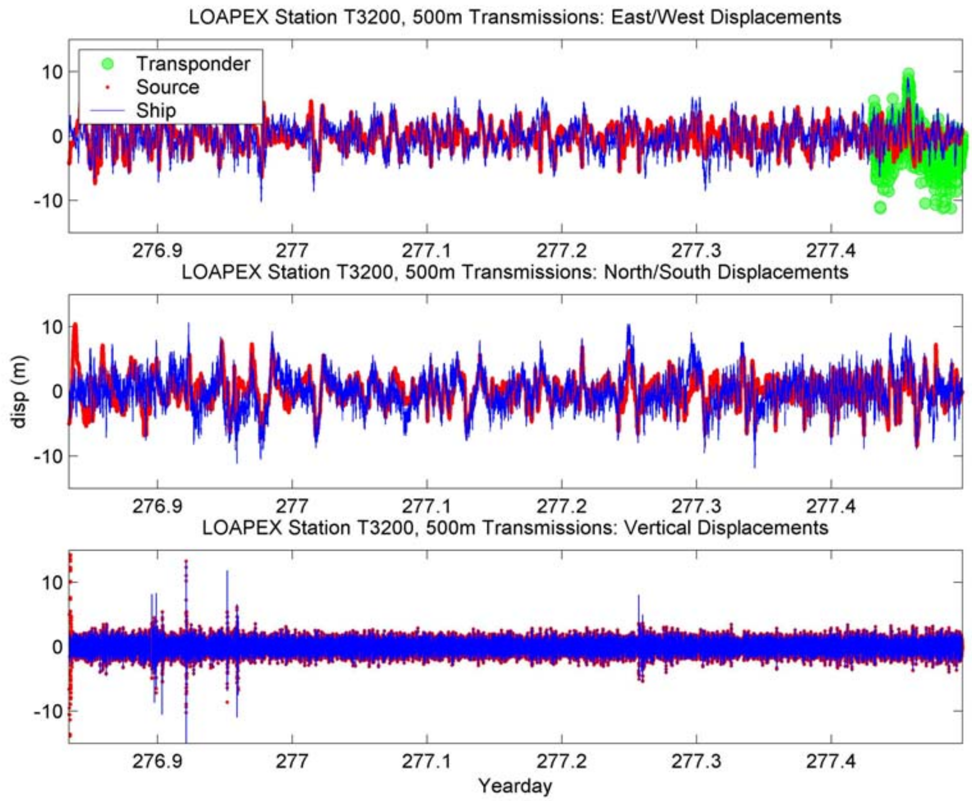

Figure A6.12. Station T3200 ship and 500 m source position during deployment. Note the times of high vertical excursions during the early part of the time series. These times correlate to high values of FOM from the C-Nav time series.

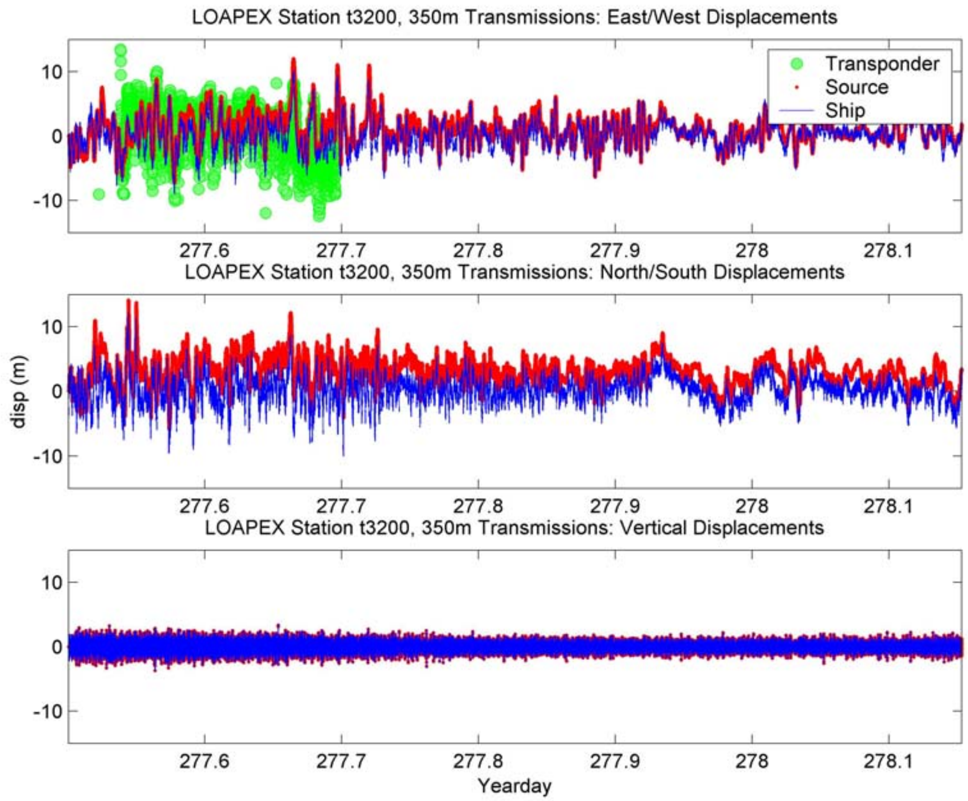

Figure A6.13. Station T3200 ship and 350 m source position during deployment

Appendix 7: S4 current meter time series for all LOAPEX stations

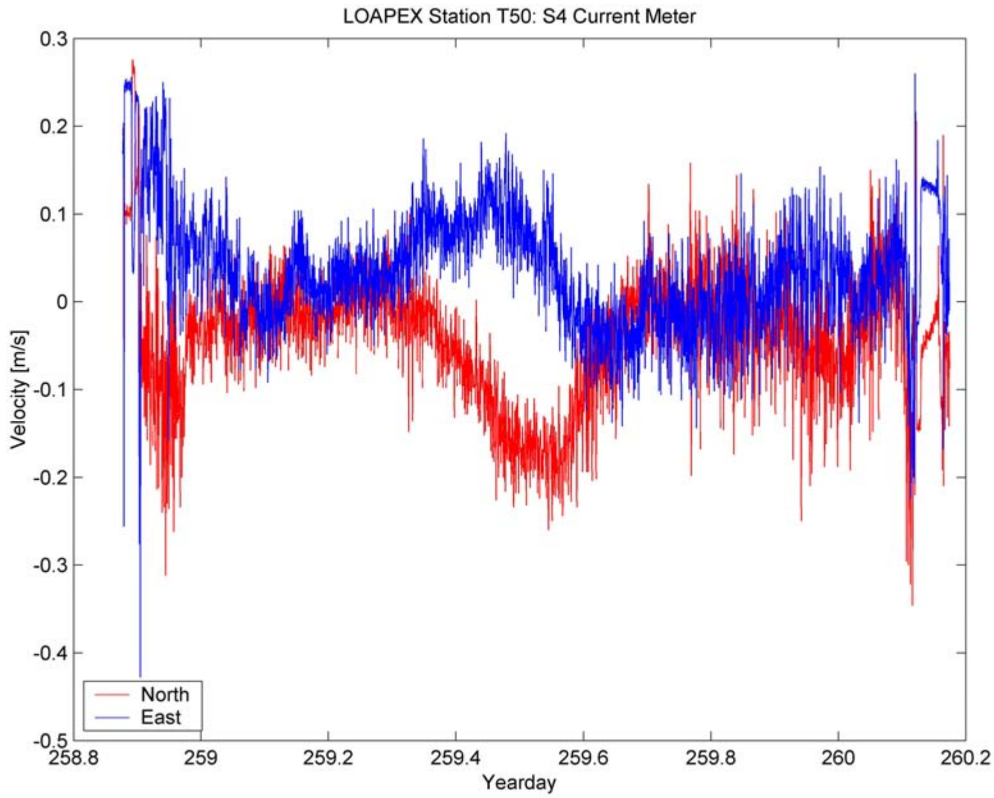

Figure A7.1. Station T50 S4 current meter time series. The high excursions shown at the beginning and end of the time series relate to deployment and recovery transients.

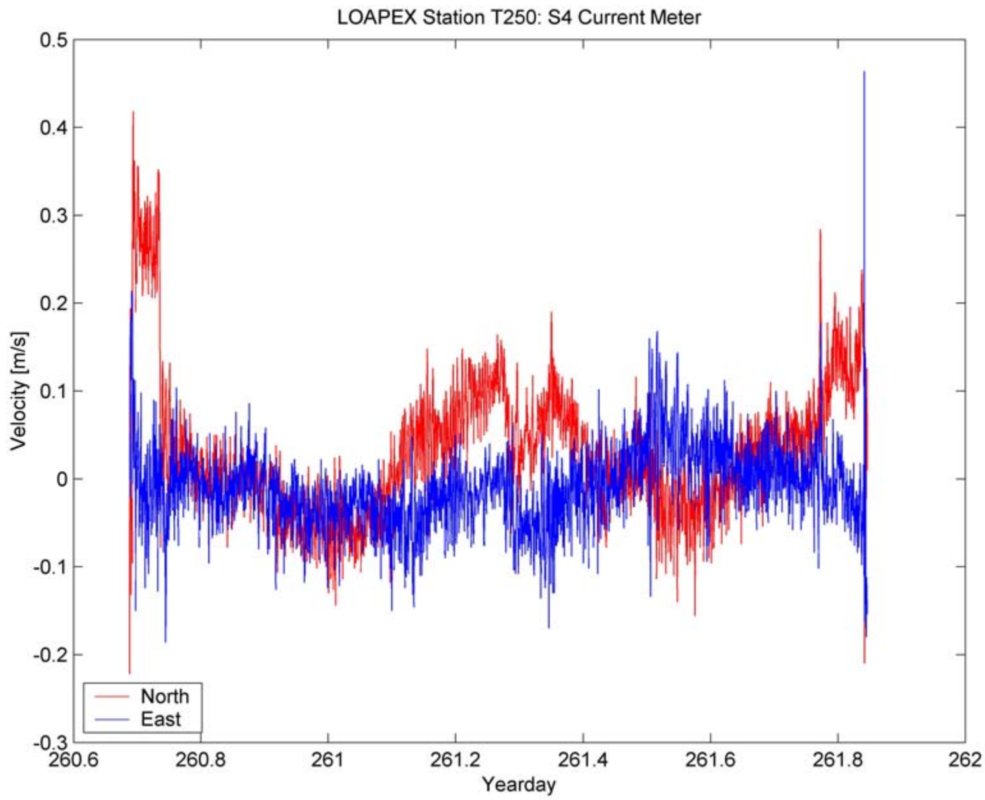

Figure A7.2. Station T250 S4 current meter time series. The high excursions shown at the beginning and end of the time series relate to deployment and recovery transients.

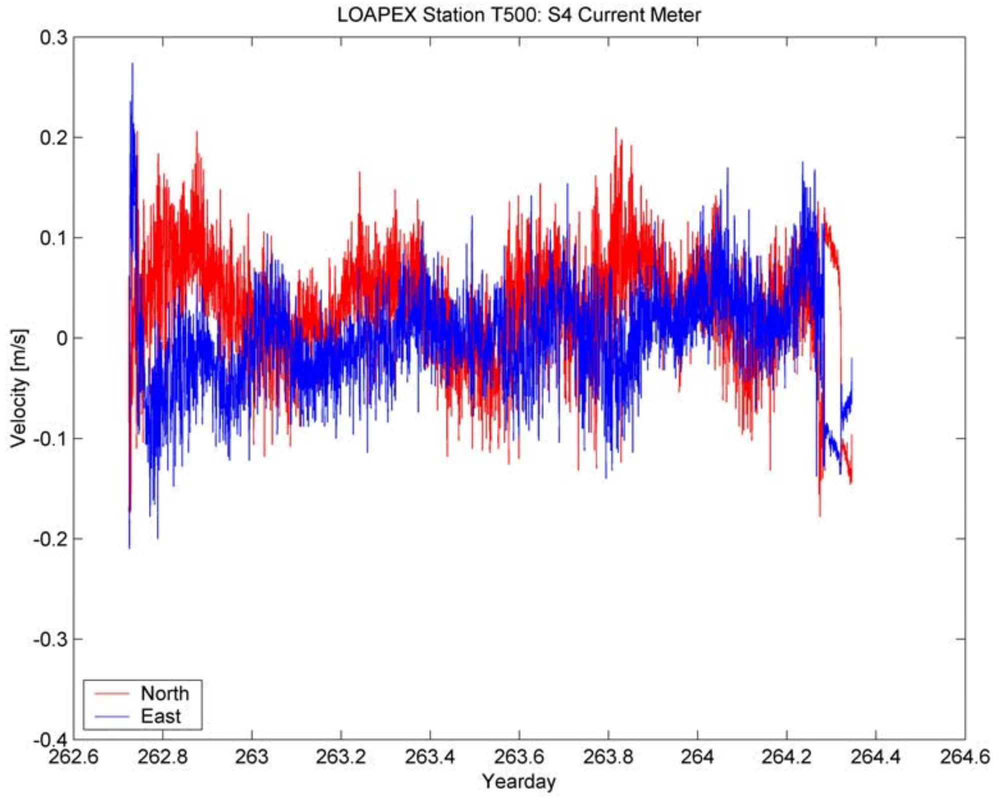

Figure A7.3. Station T500 S4 current meter time series. The high excursions shown at the beginning and end of the time series relate to deployment and recovery transients.

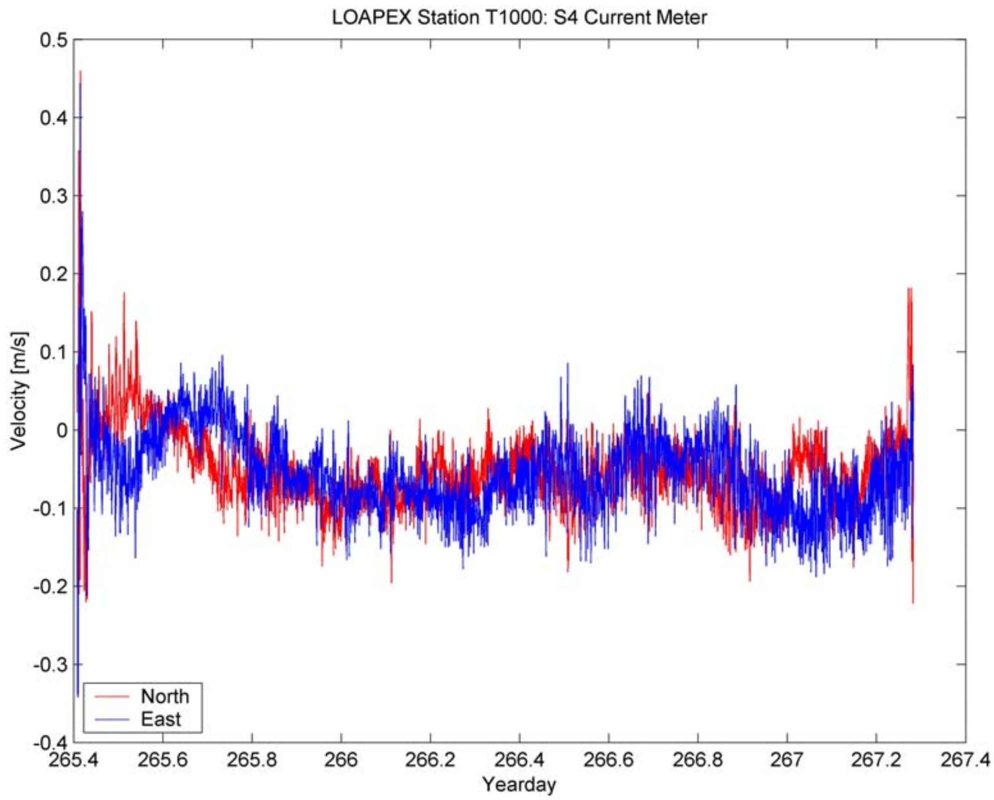

Figure A7.4. Station T1000 S4 current meter time series. The high excursions shown at the beginning and end of the time series relate to deployment and recovery transients.

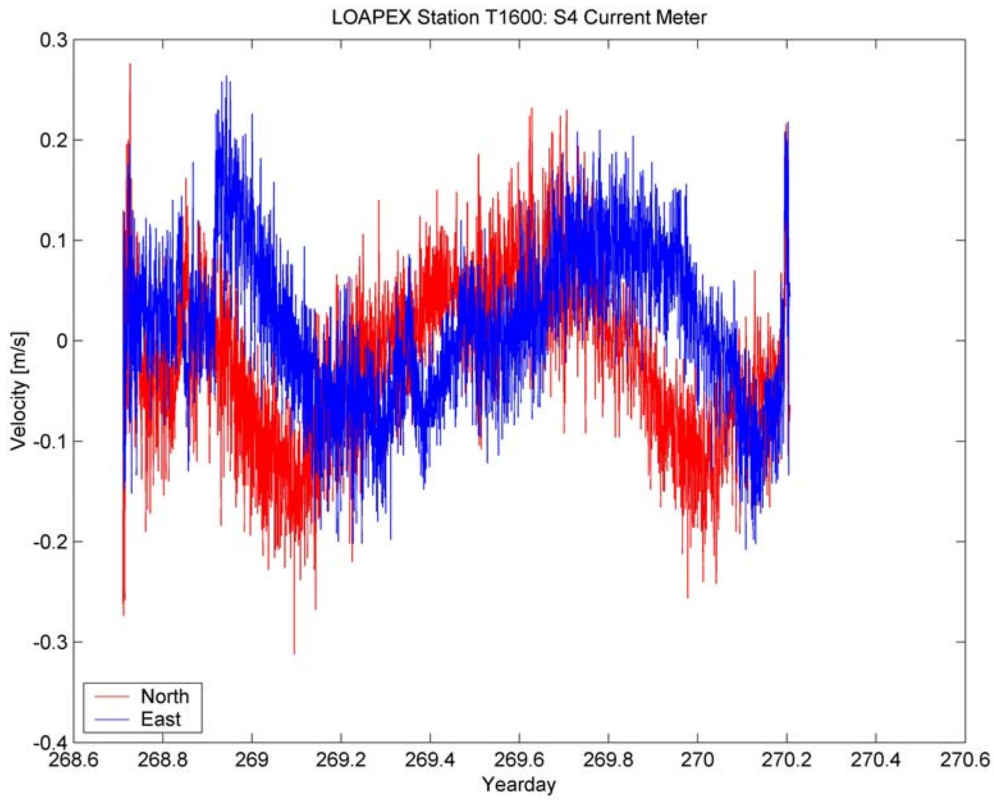

Figure A7.5. Station T1600 S4 current meter time series. The high excursions shown at the beginning and end of the time series relate to deployment and recovery transients.

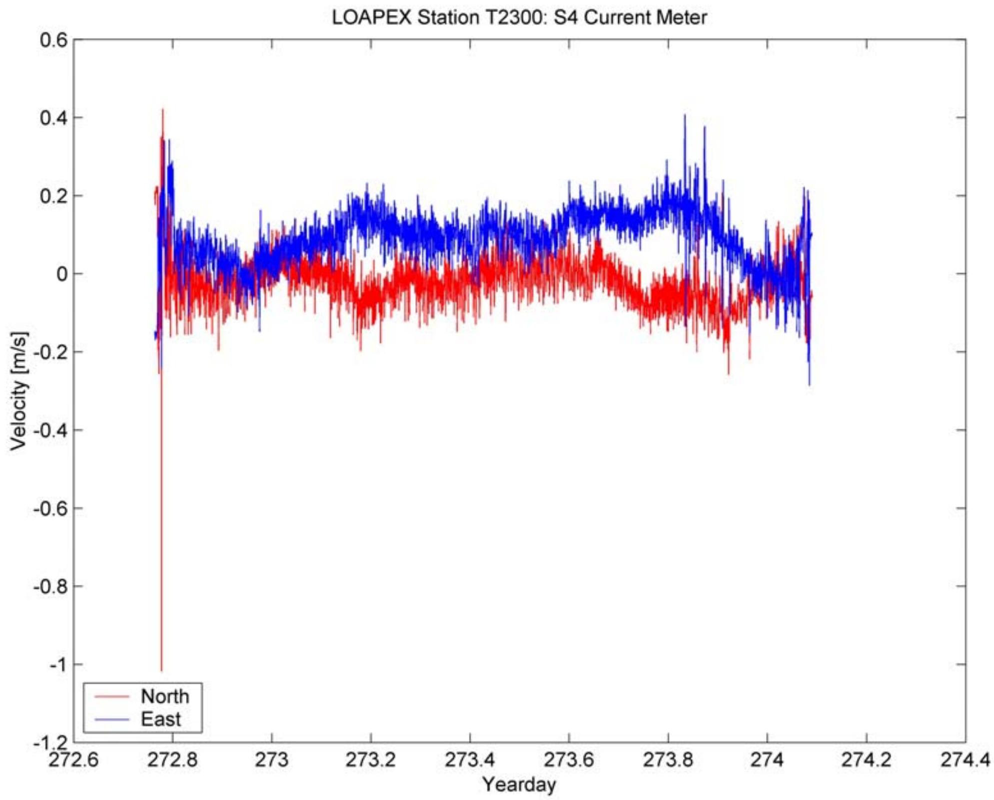

Figure A7.6. Station T2300 S4 current meter time series. The high excursions shown at the beginning and end of the time series relate to deployment and recovery transients.

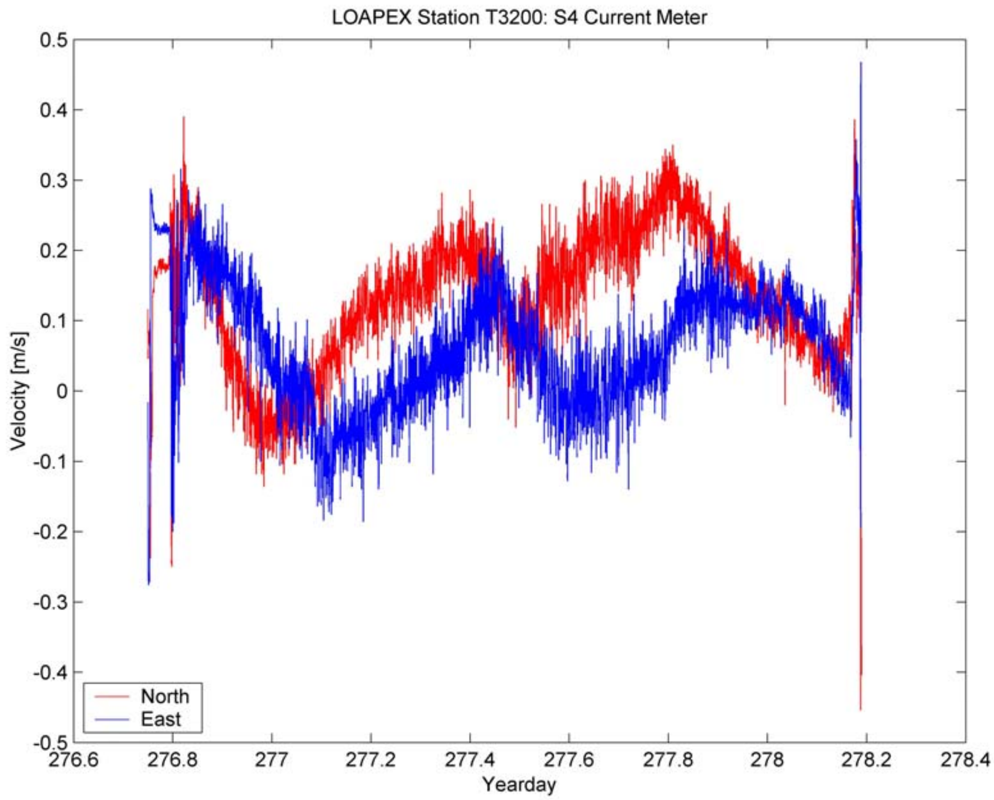

Figure A7.7. Station T3200 S4 current meter time series. The high excursions shown at the beginning and end of the time series relate to deployment and recovery transients.

Appendix 8: Source velocity comparison time series: S4-ADCP and WHOI Cable

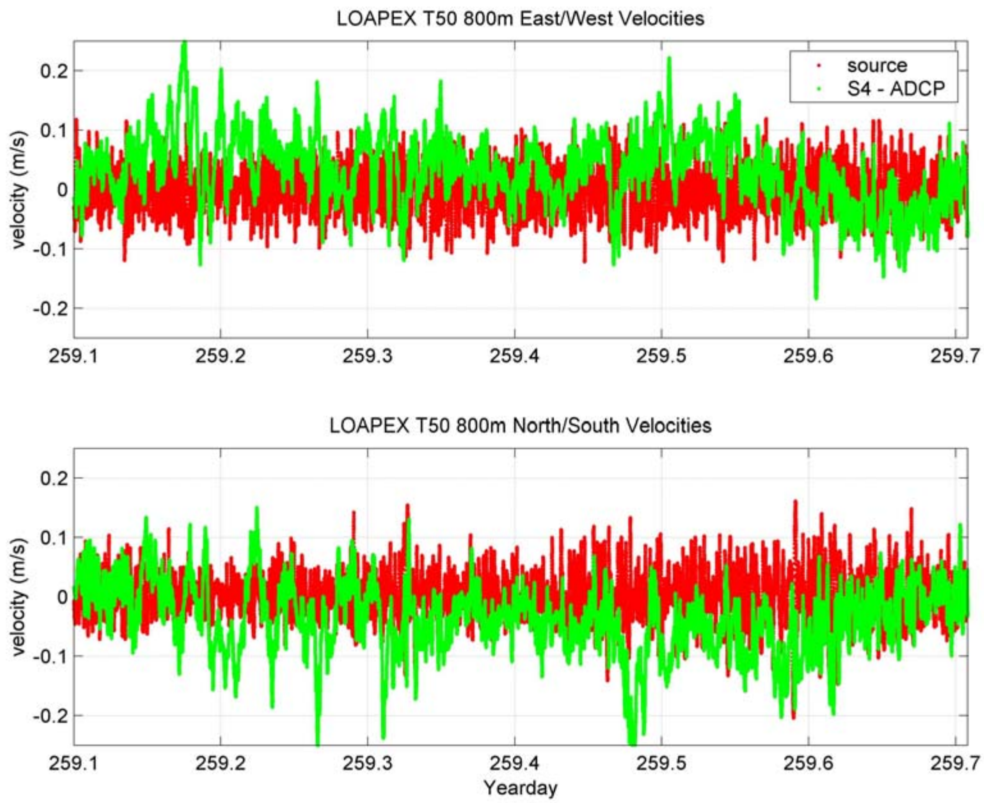

Figure A8.1. Station T50 800 m source deployment S4-ADCP and source prediction velocity comparison

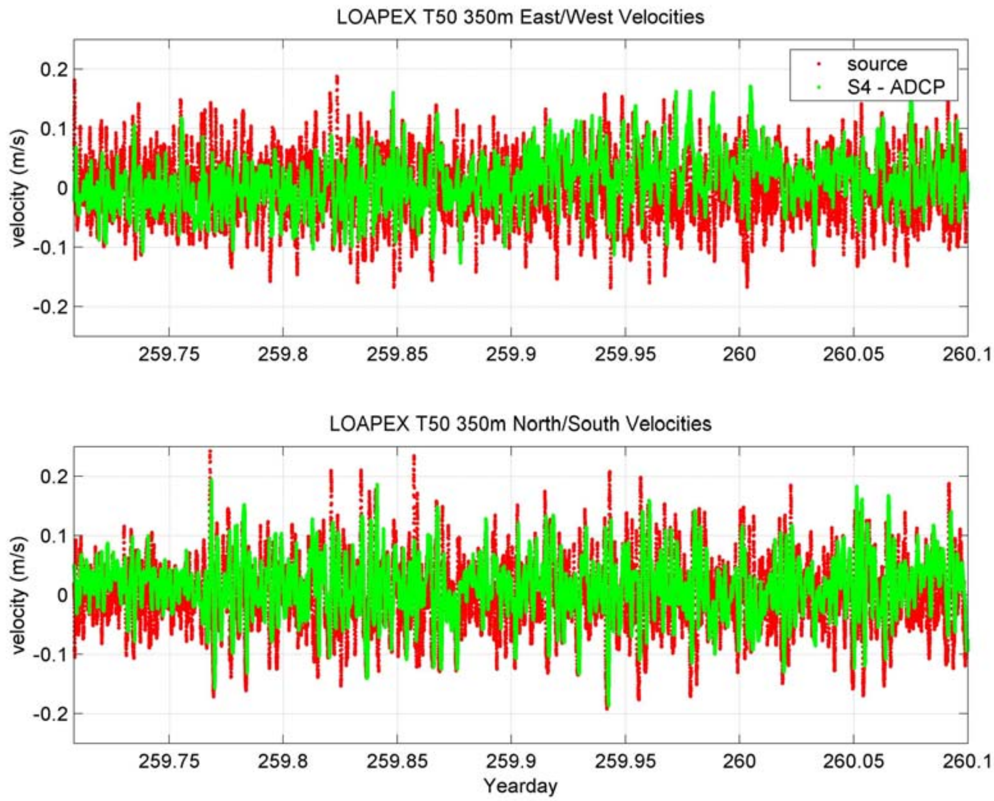

Figure A8.2. Station T50 350 m source deployment S4-ADCP and source prediction velocity comparison

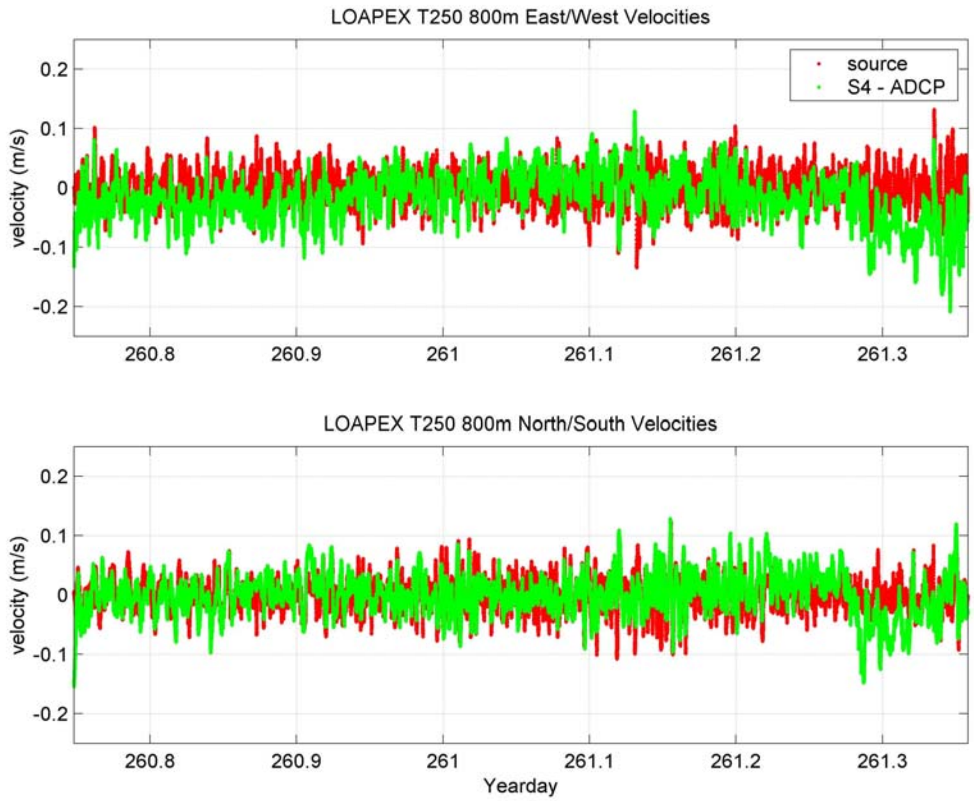

Figure A8.3. Station T250 800 m source deployment S4-ADCP and source prediction velocity comparison

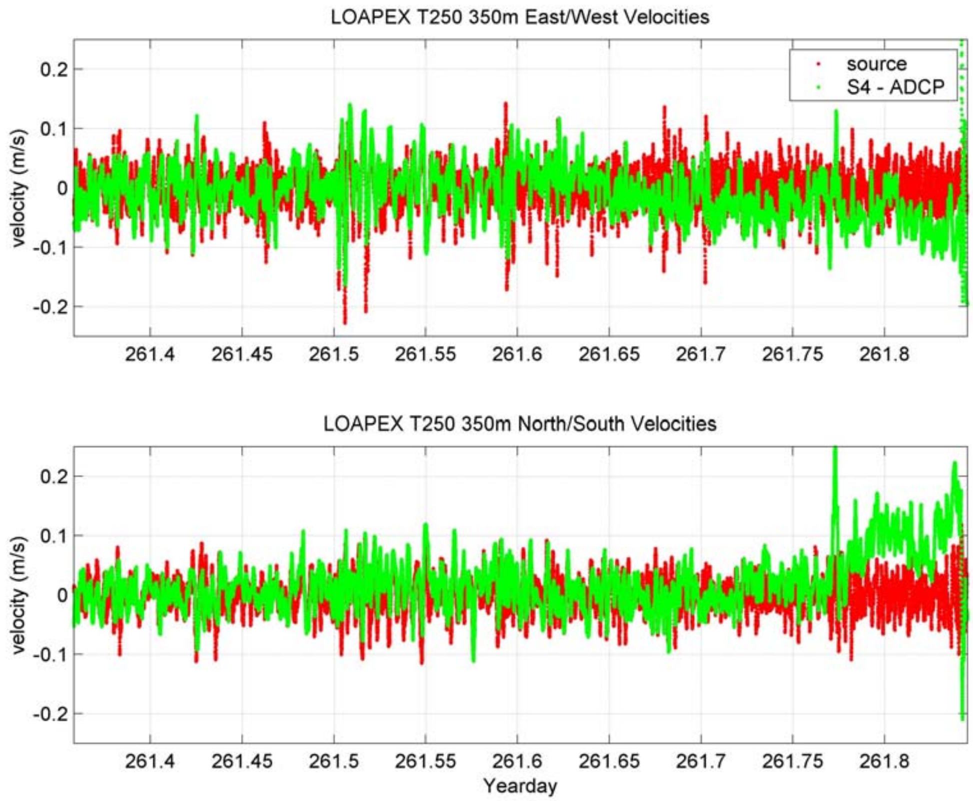

Figure A8.4. Station T250 350 m source deployment S4-ADCP and source prediction velocity comparison

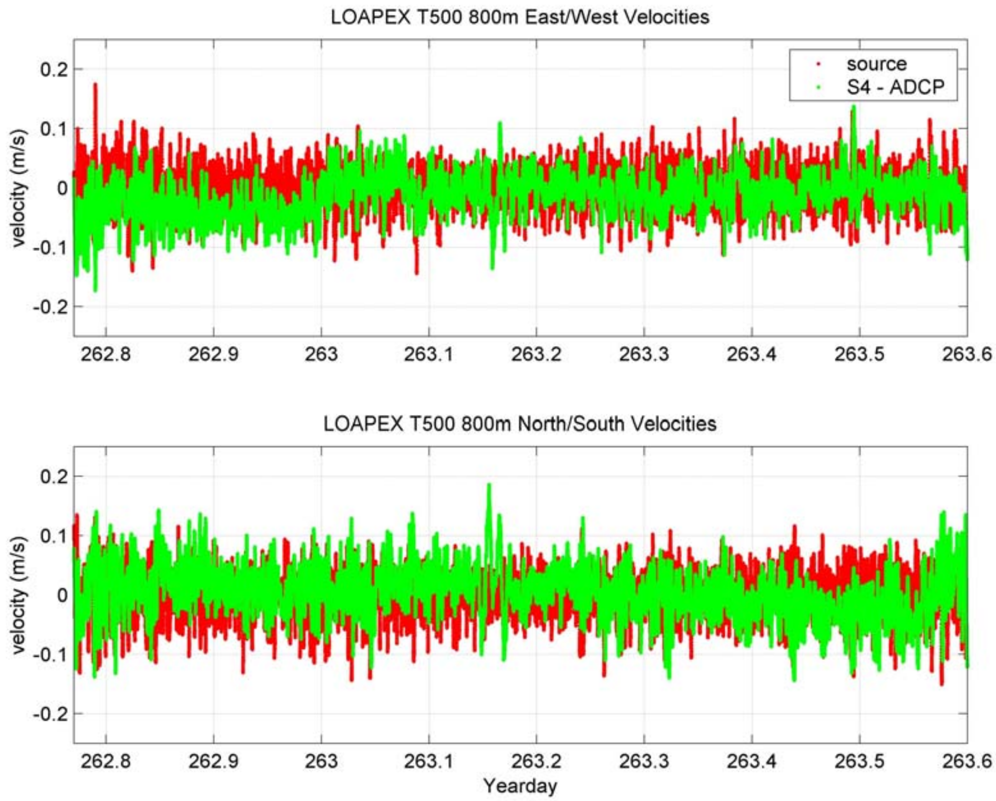

Figure A8.5. Station T500 800 m source deployment S4-ADCP and source prediction velocity comparison

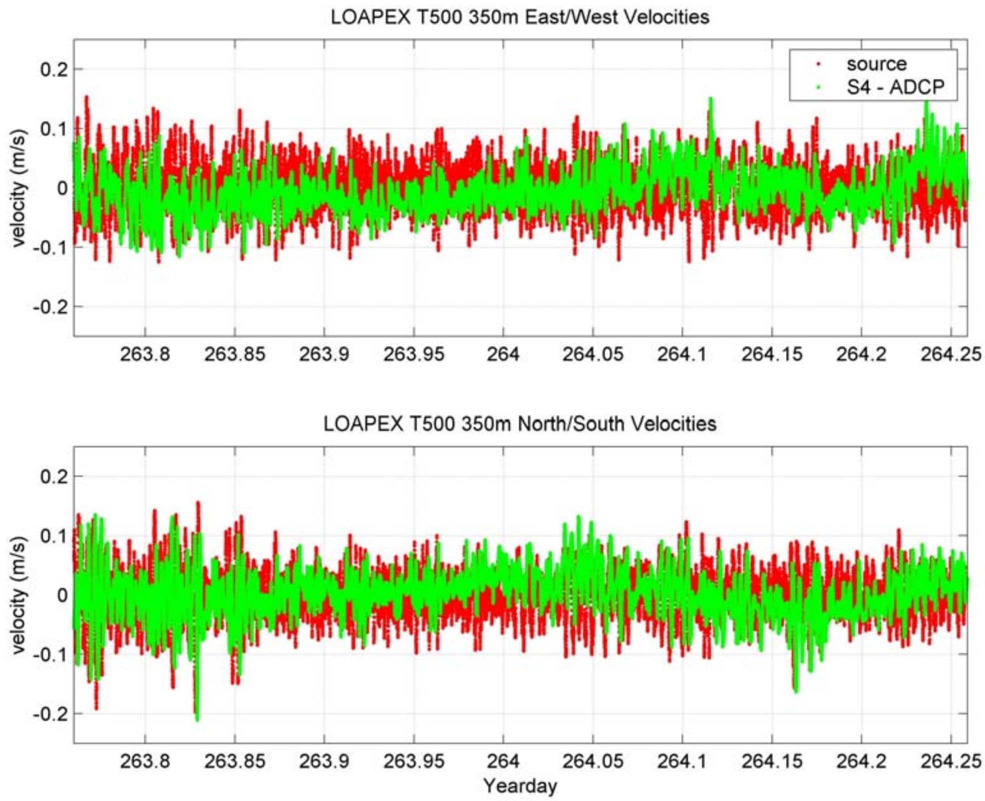

Figure A8.6. Station T500 350 m source deployment S4-ADCP and source prediction velocity comparison

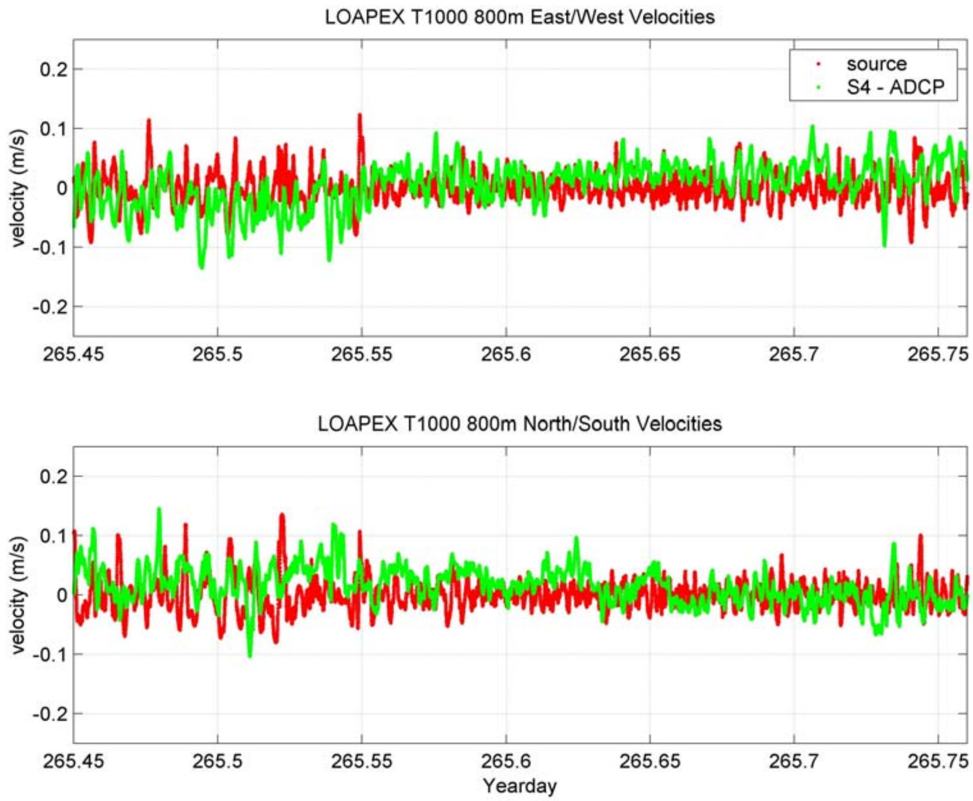

Figure A8.7. Station T1000 800 m source deployment S4-ADCP and source prediction velocity comparison

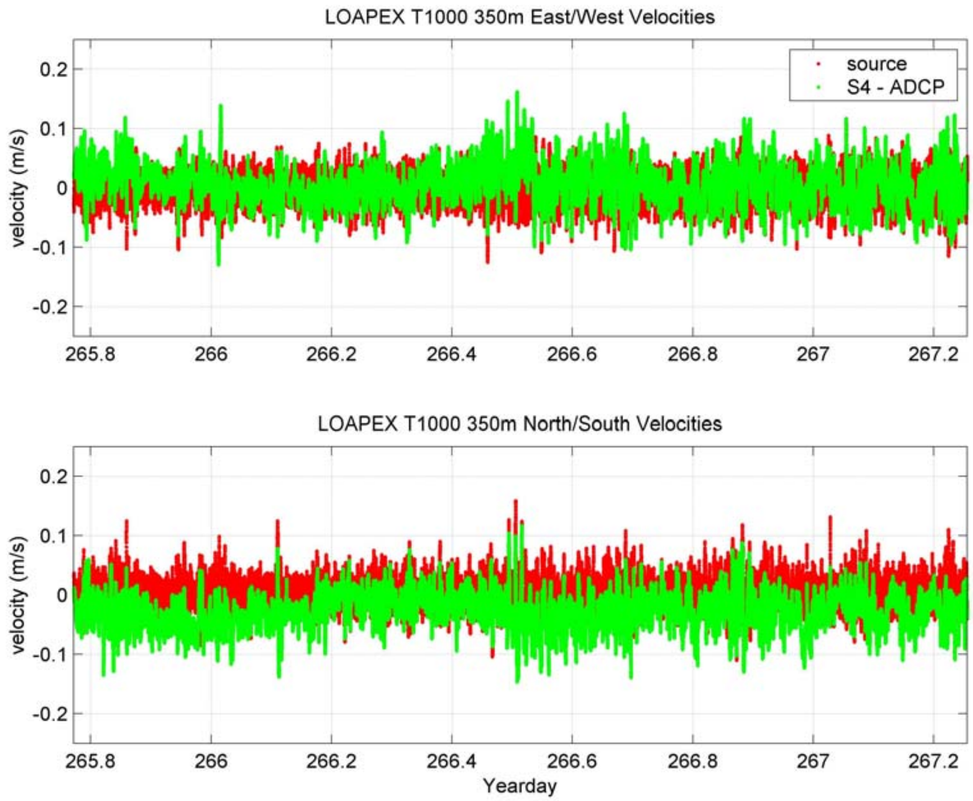

Figure A8.8. Station T1000 350 m source deployment S4-ADCP and source prediction velocity comparison

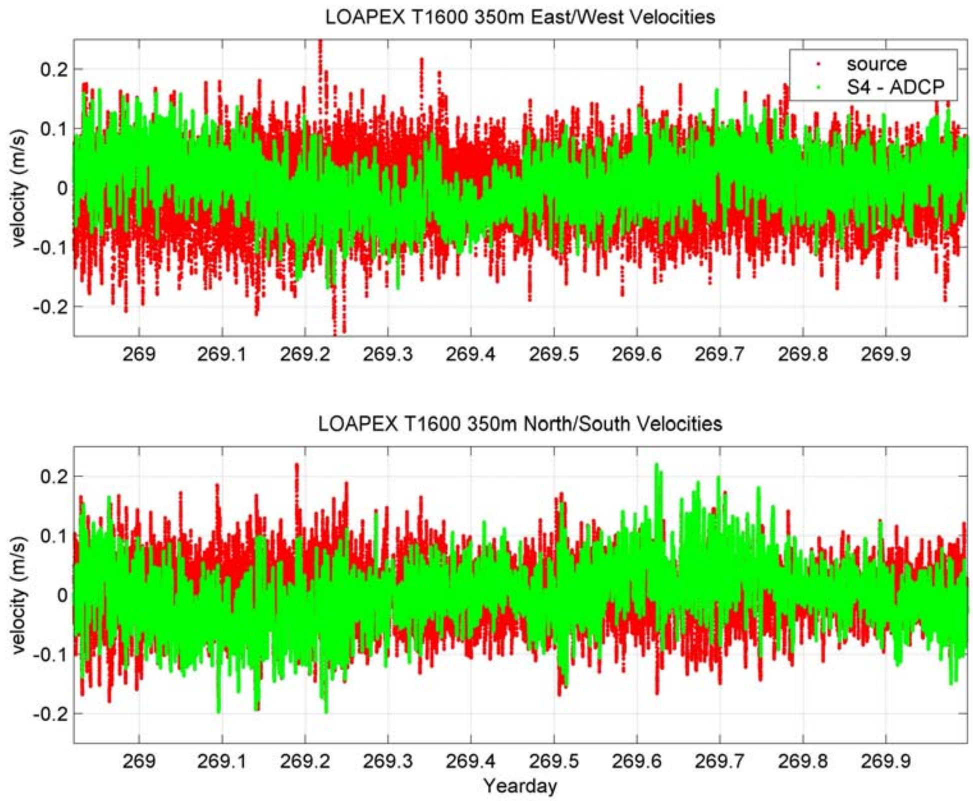

Figure A8.9. Station T1600 350 m source deployment S4-ADCP and source prediction velocity comparison

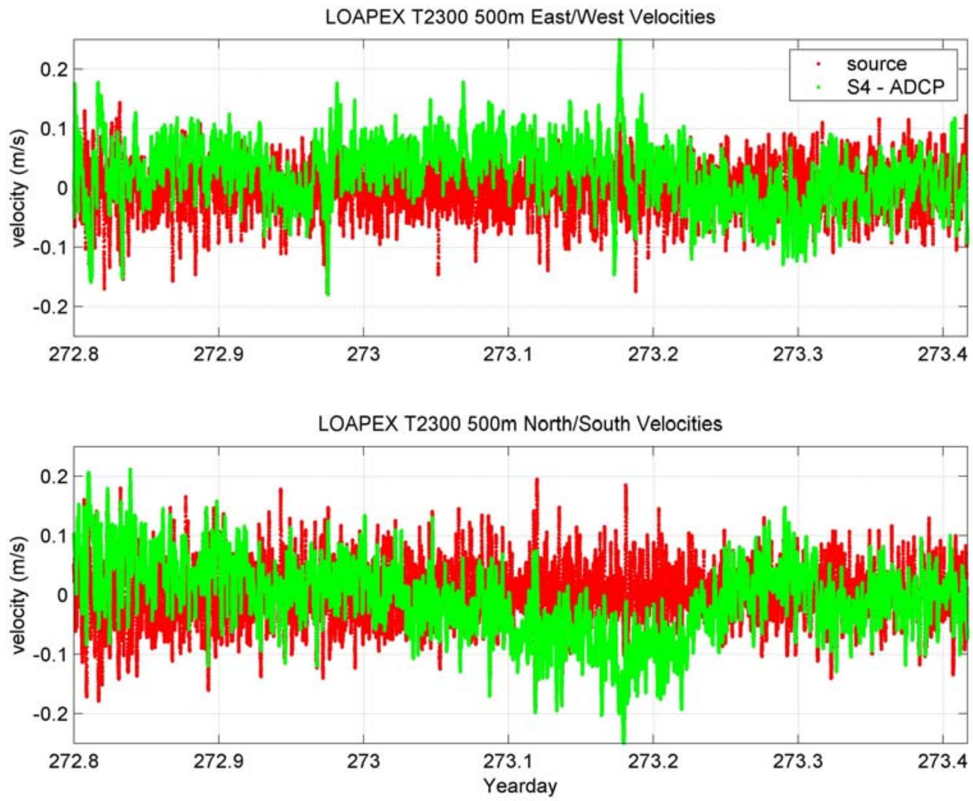

Figure A8.10. Station T2300 500 m source deployment S4-ADCP and source prediction velocity comparison

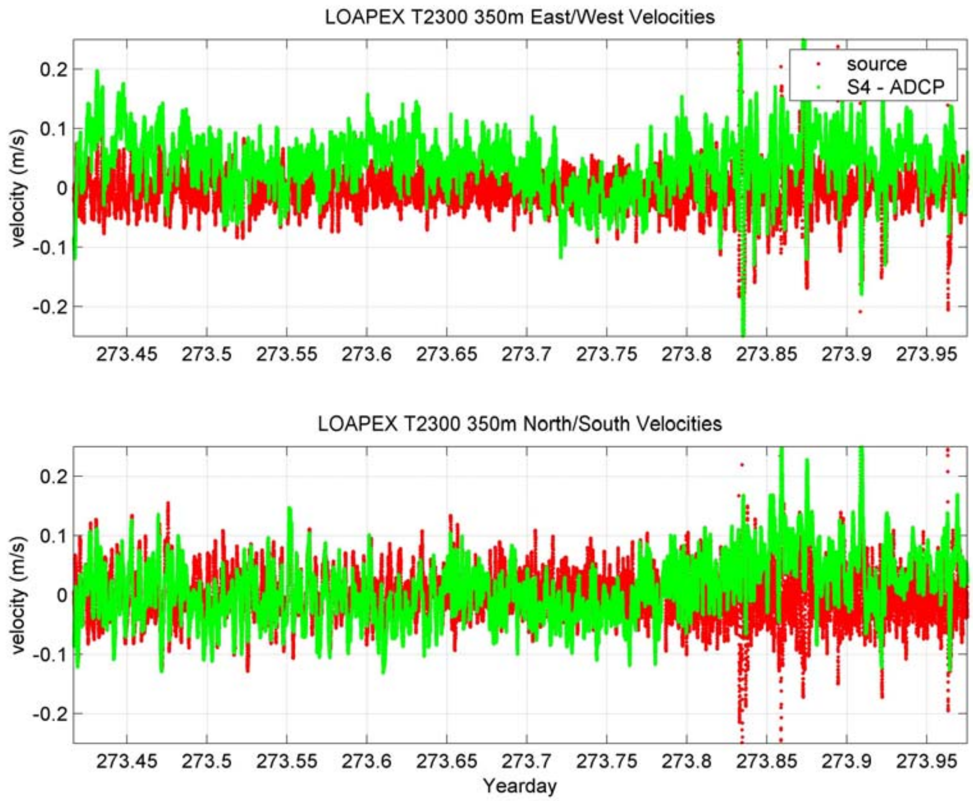

Figure A8.11. Station T2300 350 m source deployment S4-ADCP and source prediction velocity comparison. The high excursions shown at the end of the time series relate to source position predictions based on less reliable C-Nav data.

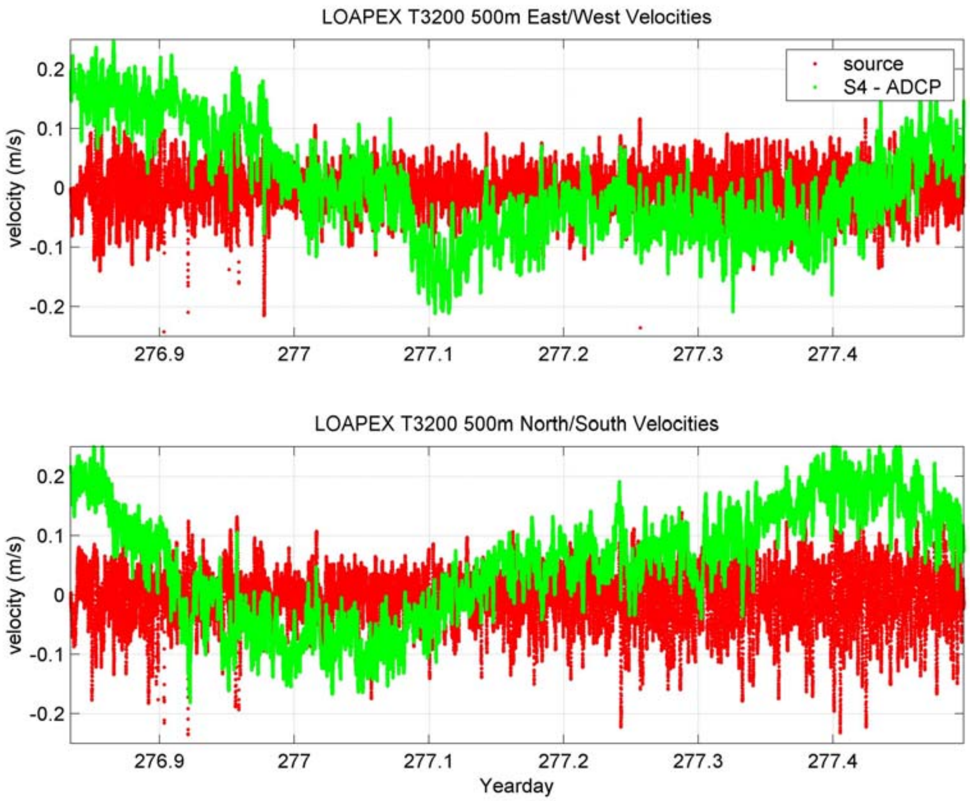

Figure A8.12. Station T3200 500 m source deployment S4-ADCP and source prediction velocity comparison

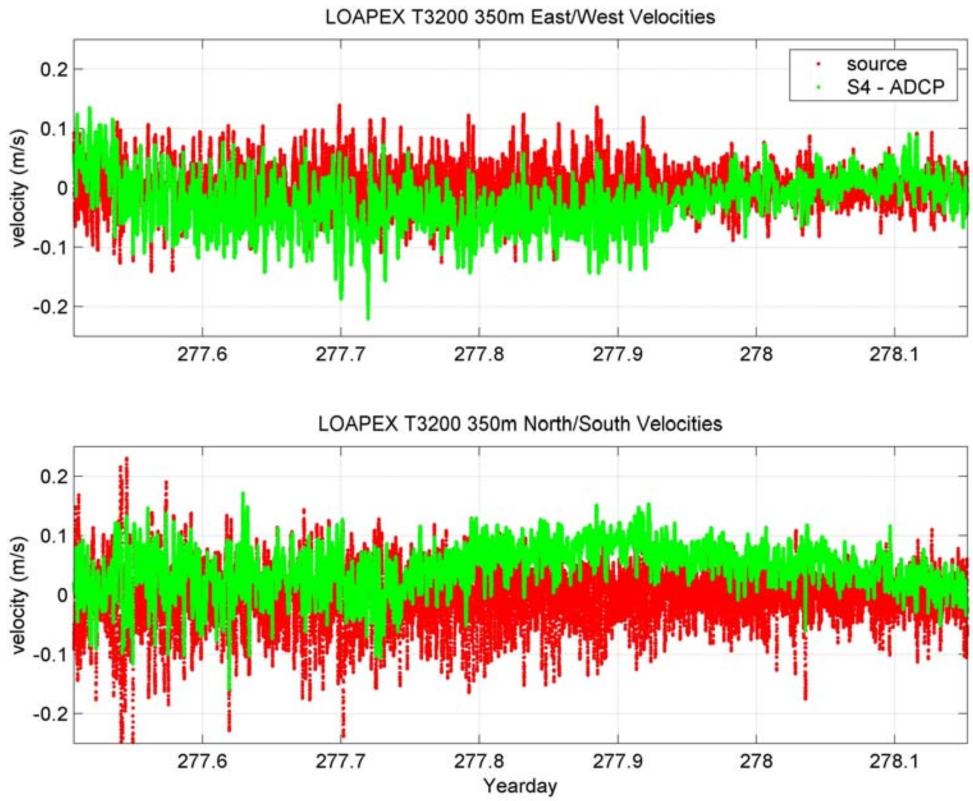

Figure A8.13. Station T3200 350 m source deployment S4-ADCP and source prediction velocity comparison. The high excursions shown at the beginning of the time series relate to source position predictions based on less reliable C-Nav data.

Appendix 9: LOAPEX stations to 'r' path sound velocity profiles

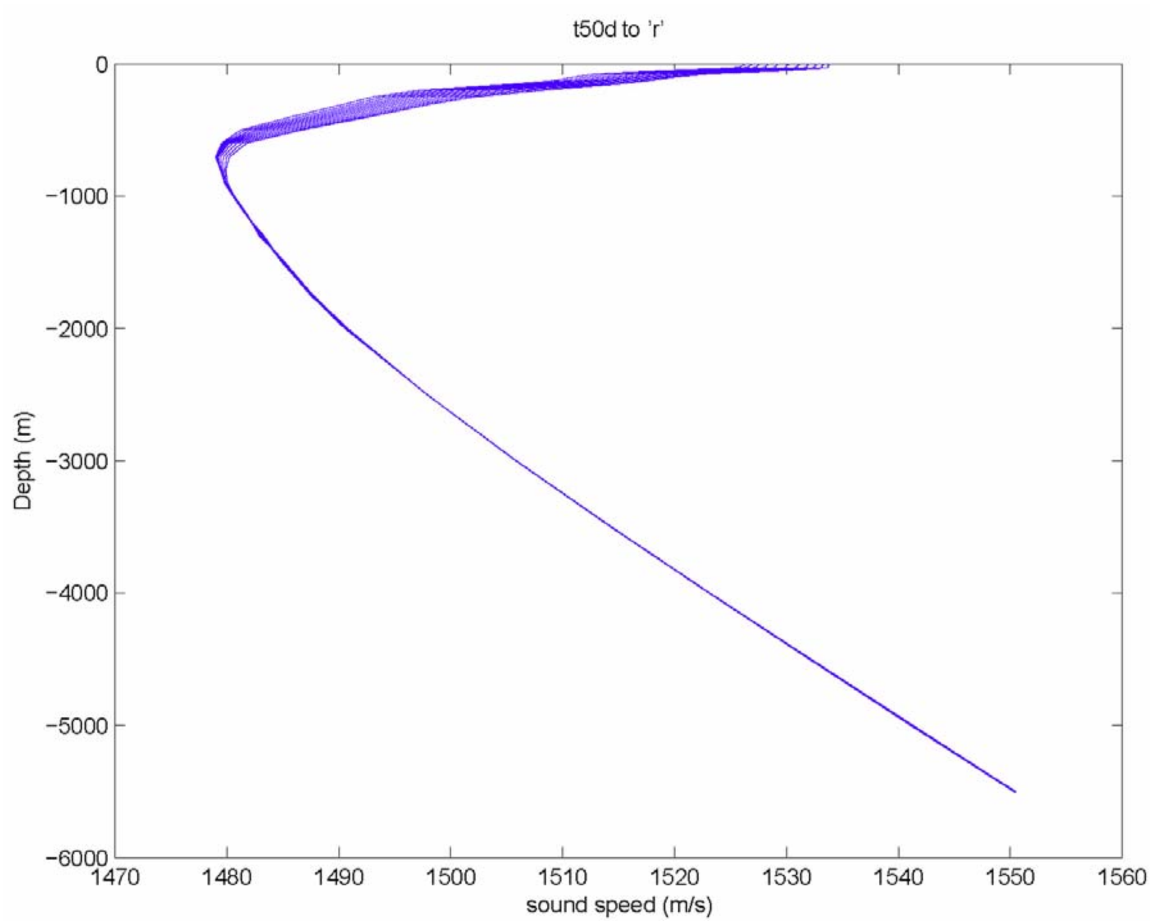

Figure A9.1. Station T50 to 'r' sound speed profiles

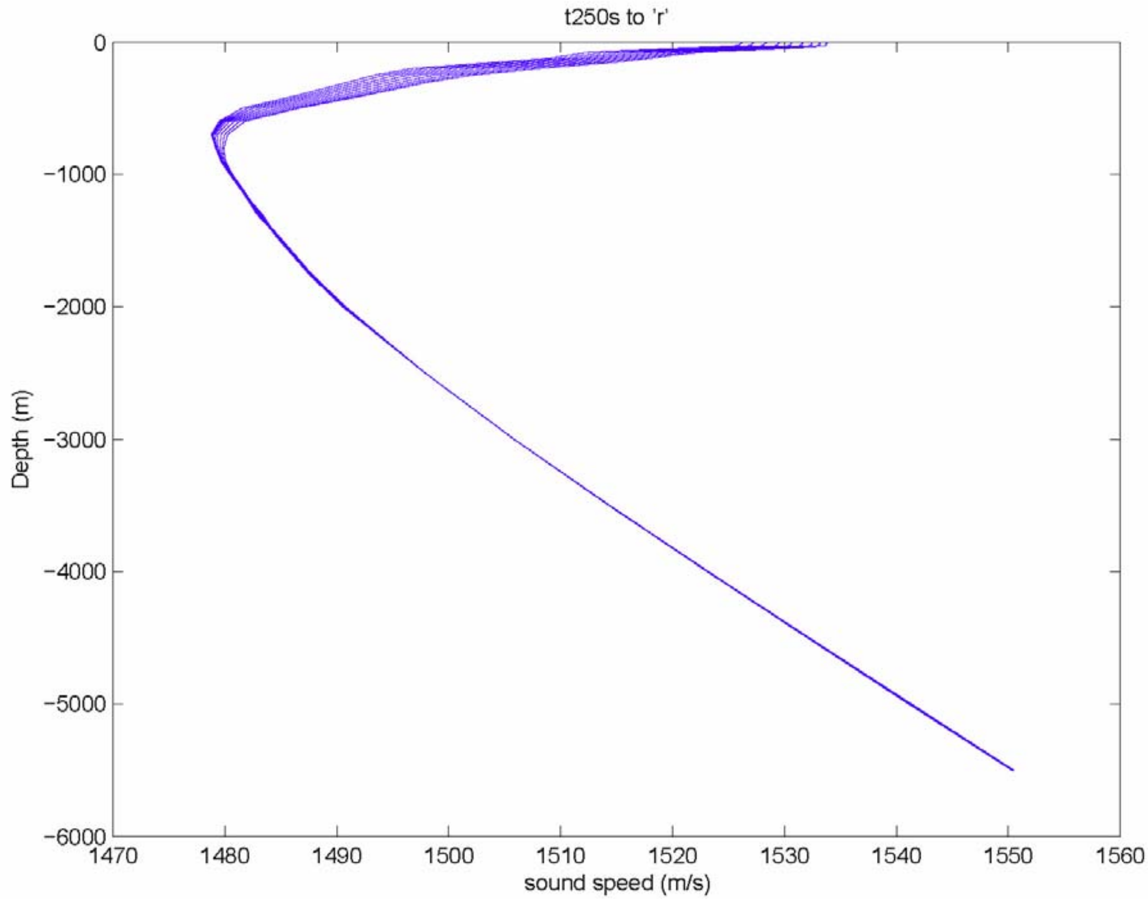

Figure A9.2. Station T250 to ‘r’ sound speed profiles

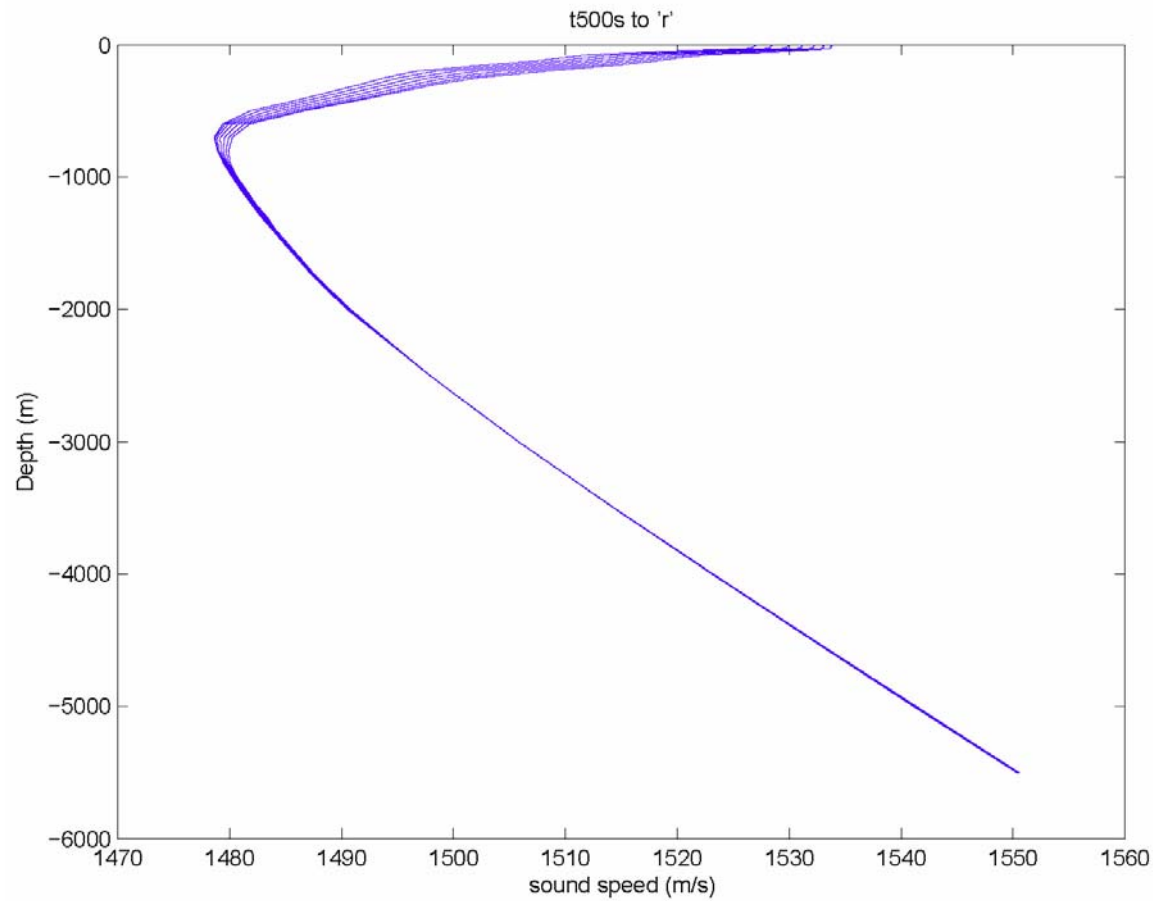

Figure A9.3. Station T500 to 'r' sound speed profiles

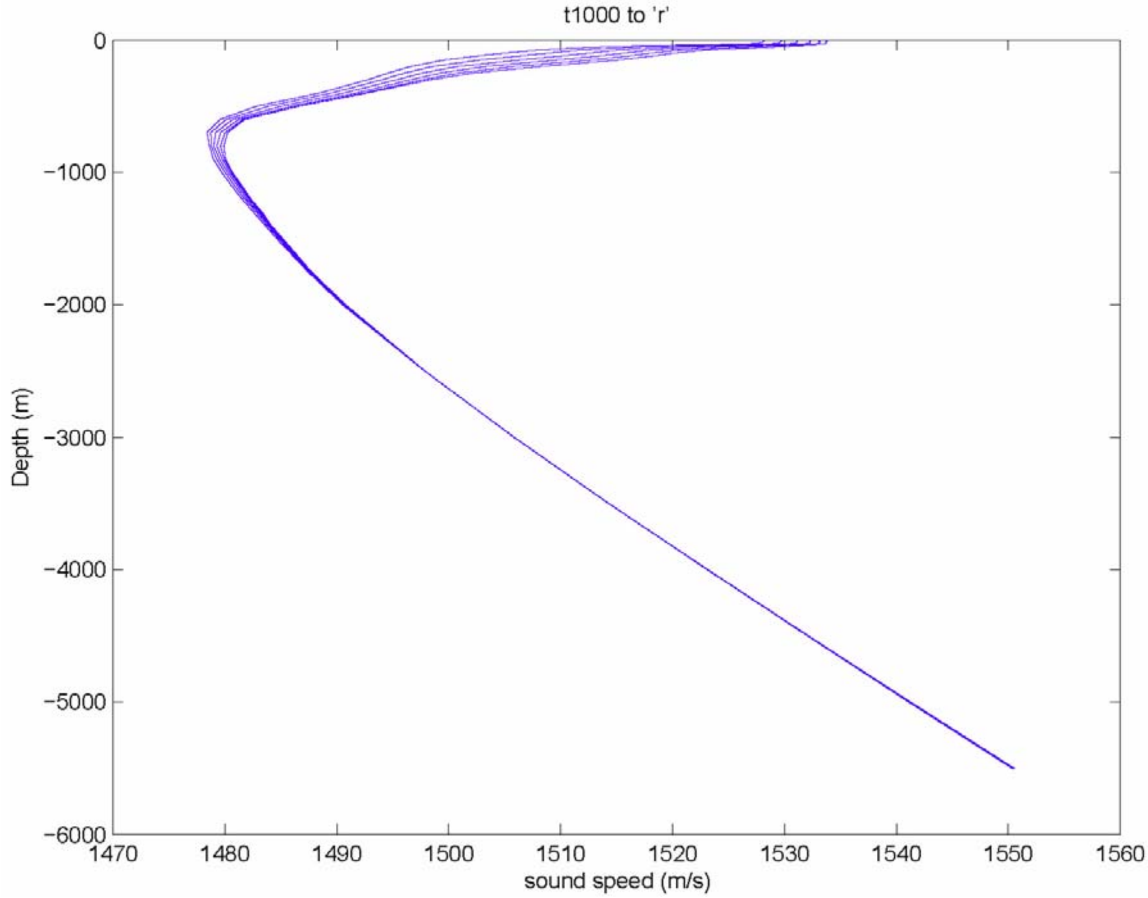

Figure A9.4. Station T1000 to ‘r’ sound speed profiles

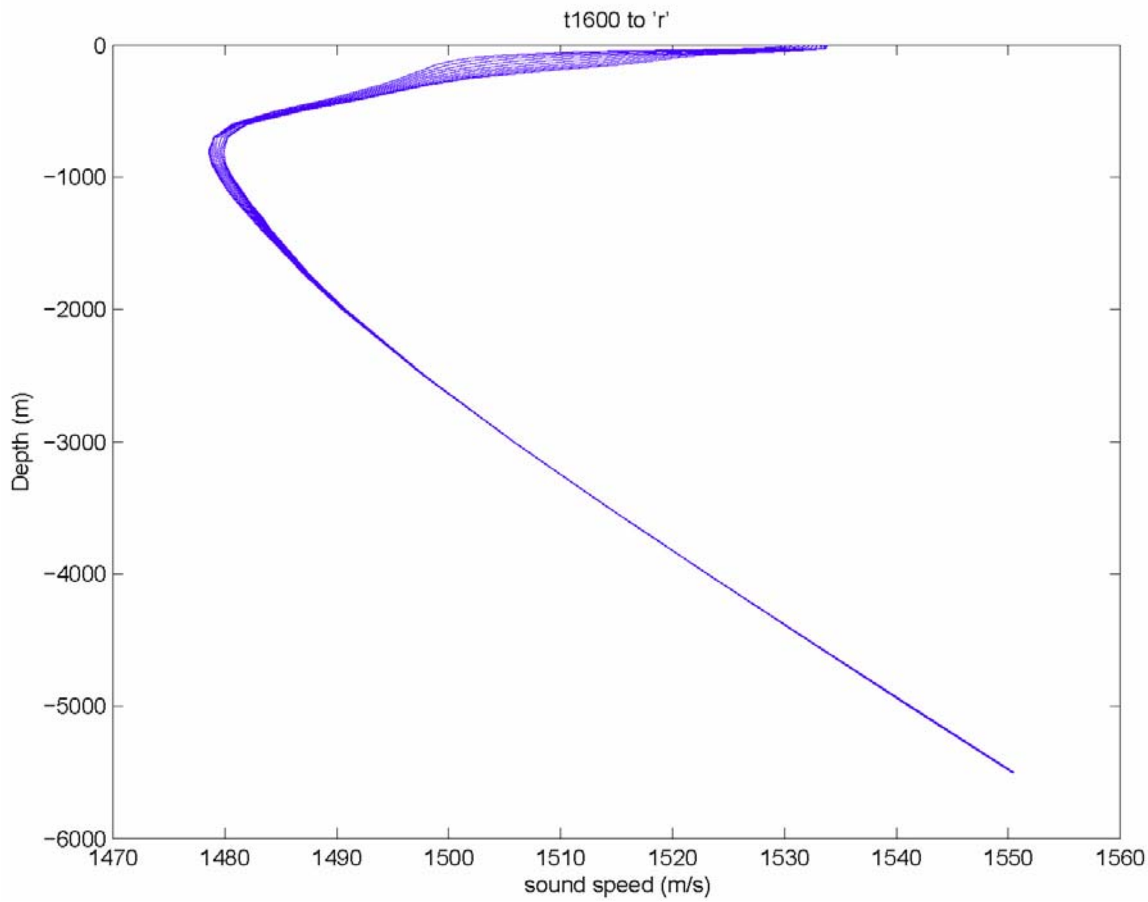

Figure A9.5. Station T1600 to ‘r’ sound speed profiles

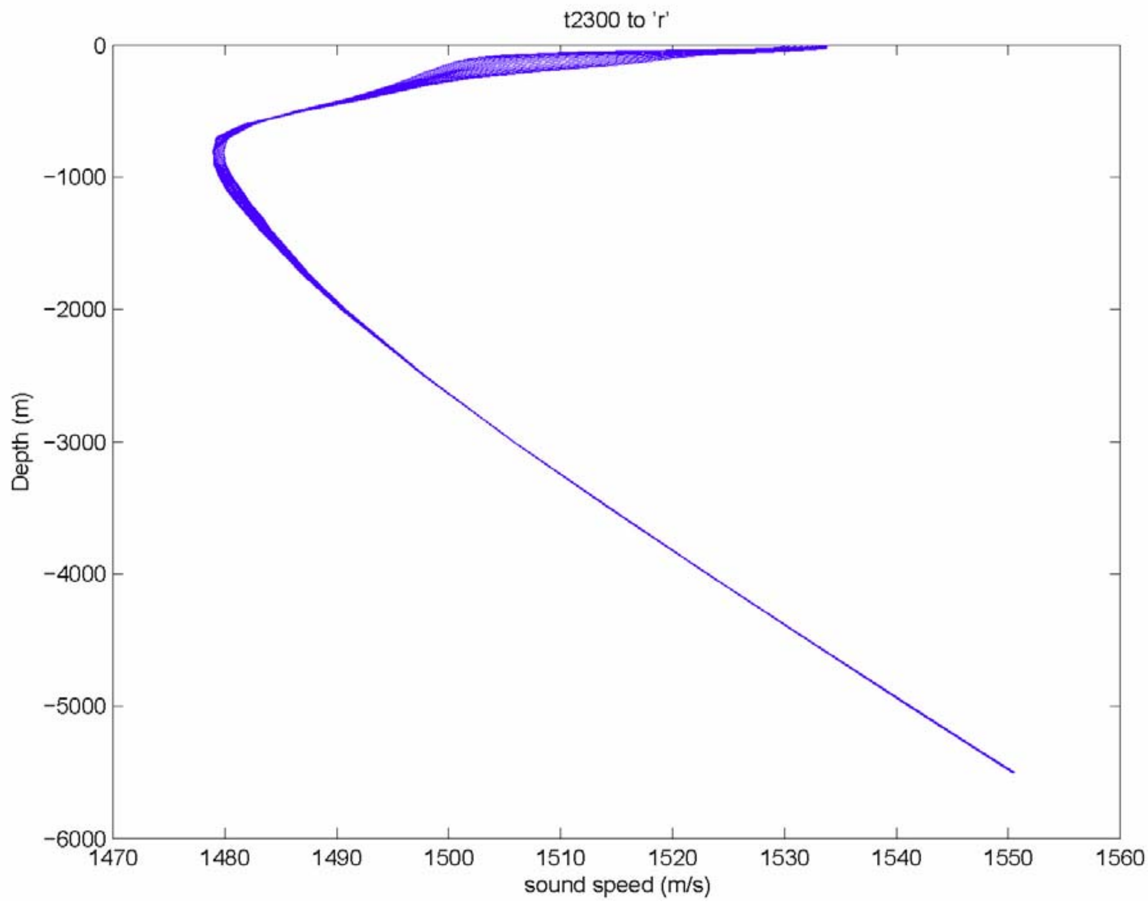

Figure A9.6. Station T2300 to ‘r’ sound speed profiles

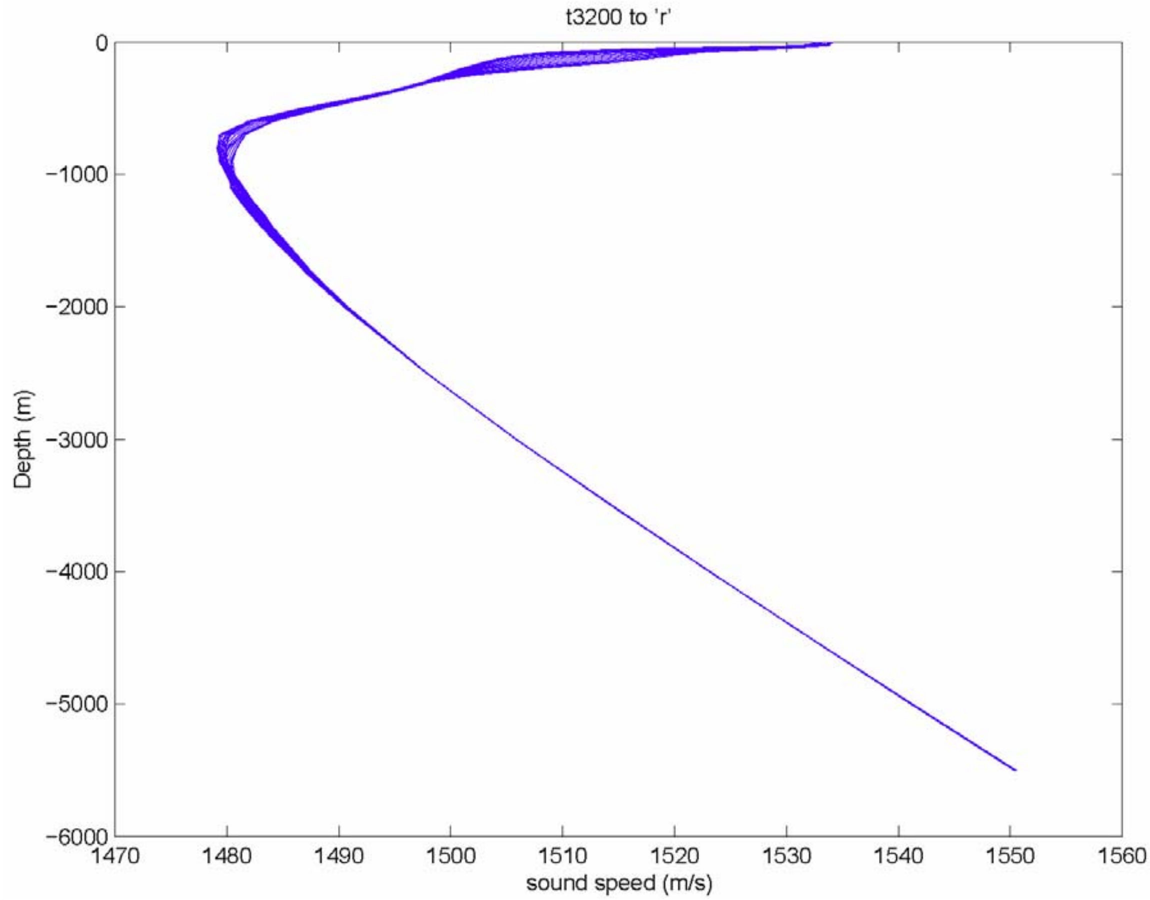

Figure A9.7. Station T3200 to ‘r’ sound speed profiles

Appendix 10: Predicted eigenrays, time fronts and arrival angles for the paths between all LOAPEX stations and 'r'.

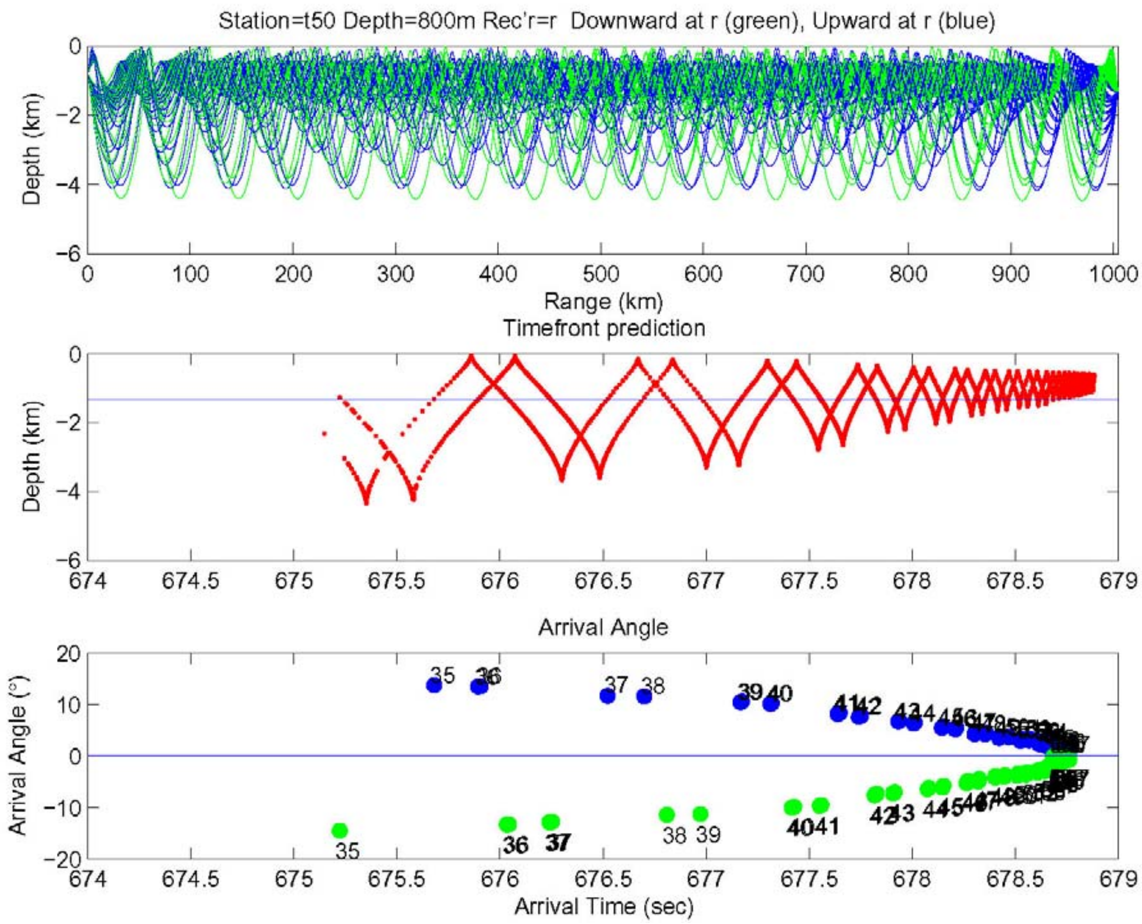

Figure A10.1. Station T50 800 m source deployment to 'r' propagation predictions

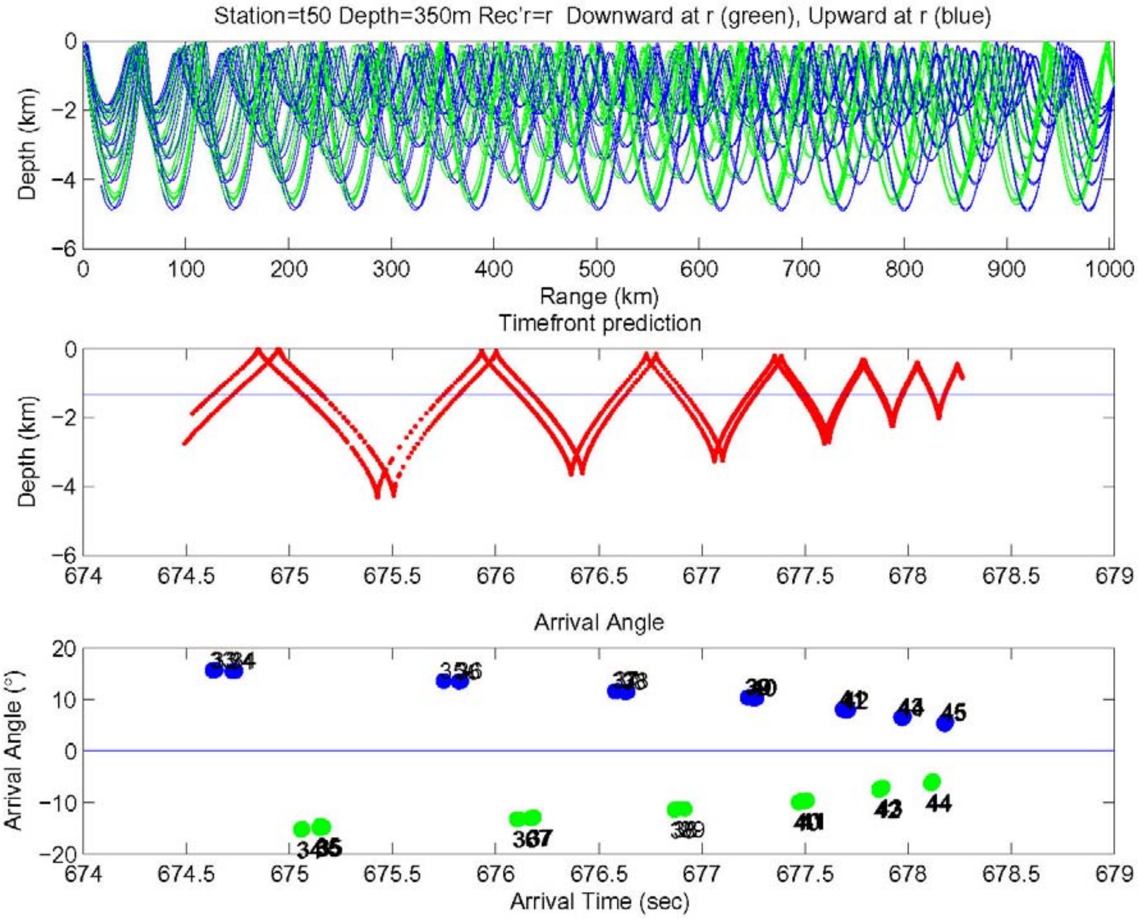

Figure A10.2. Station T50 350 m source deployment to ‘r’ propagation predictions

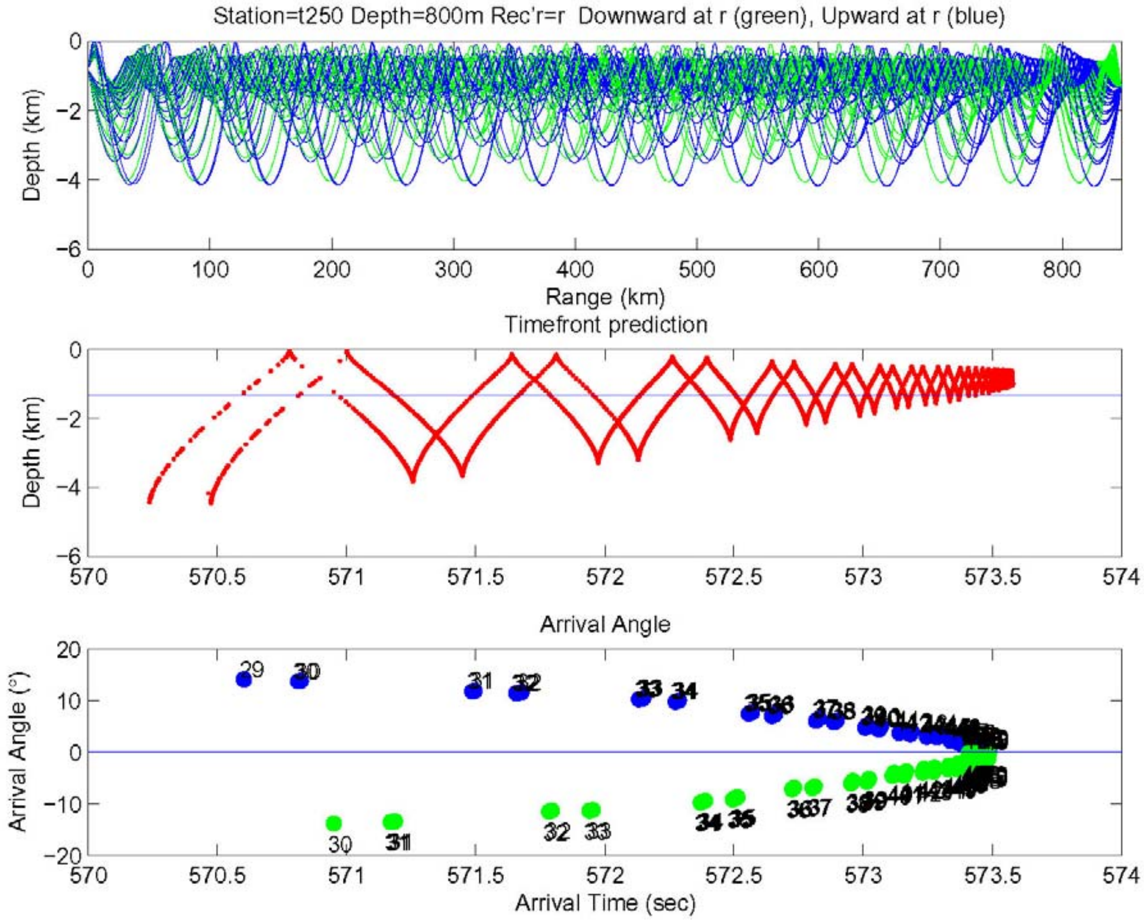

Figure A10.3. Station T250 800 m source deployment to ‘r’ propagation predictions

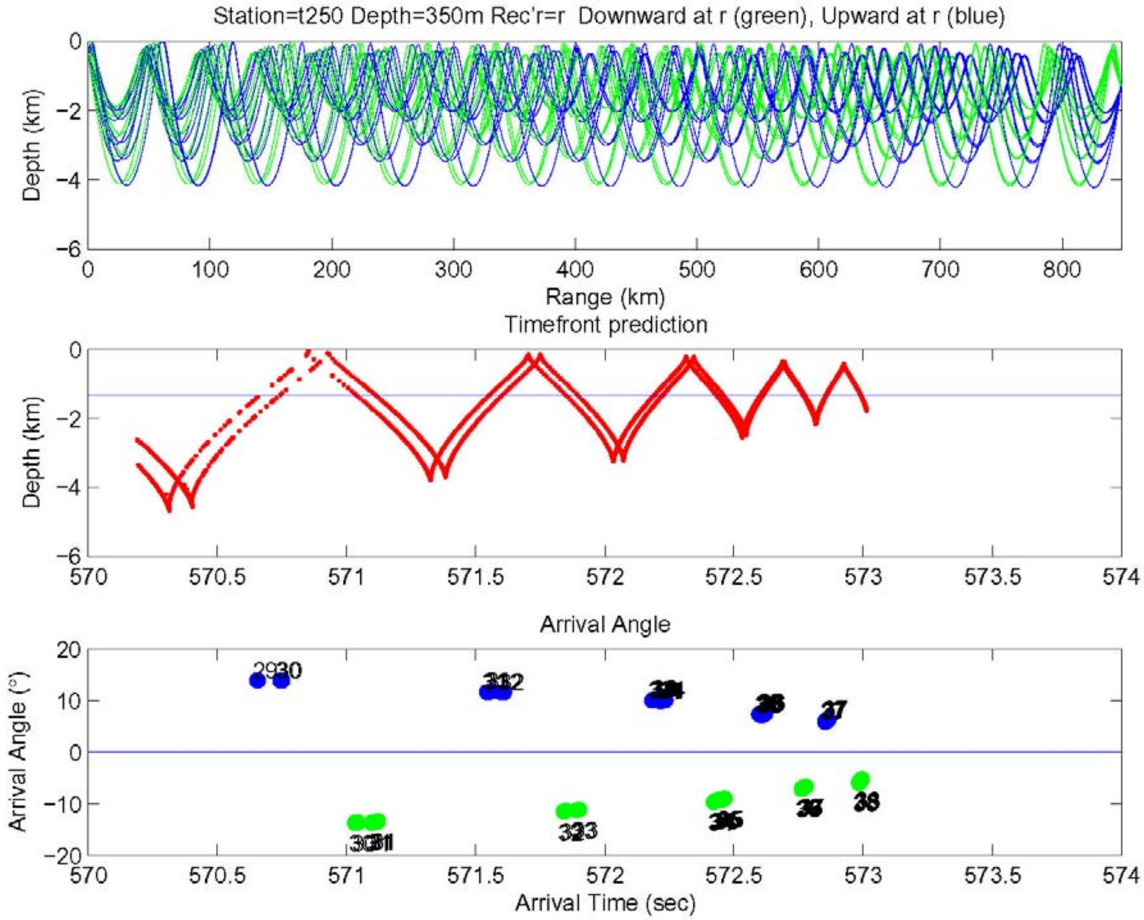

Figure A10.4. Station T250 350 m source deployment to 'r' propagation predictions

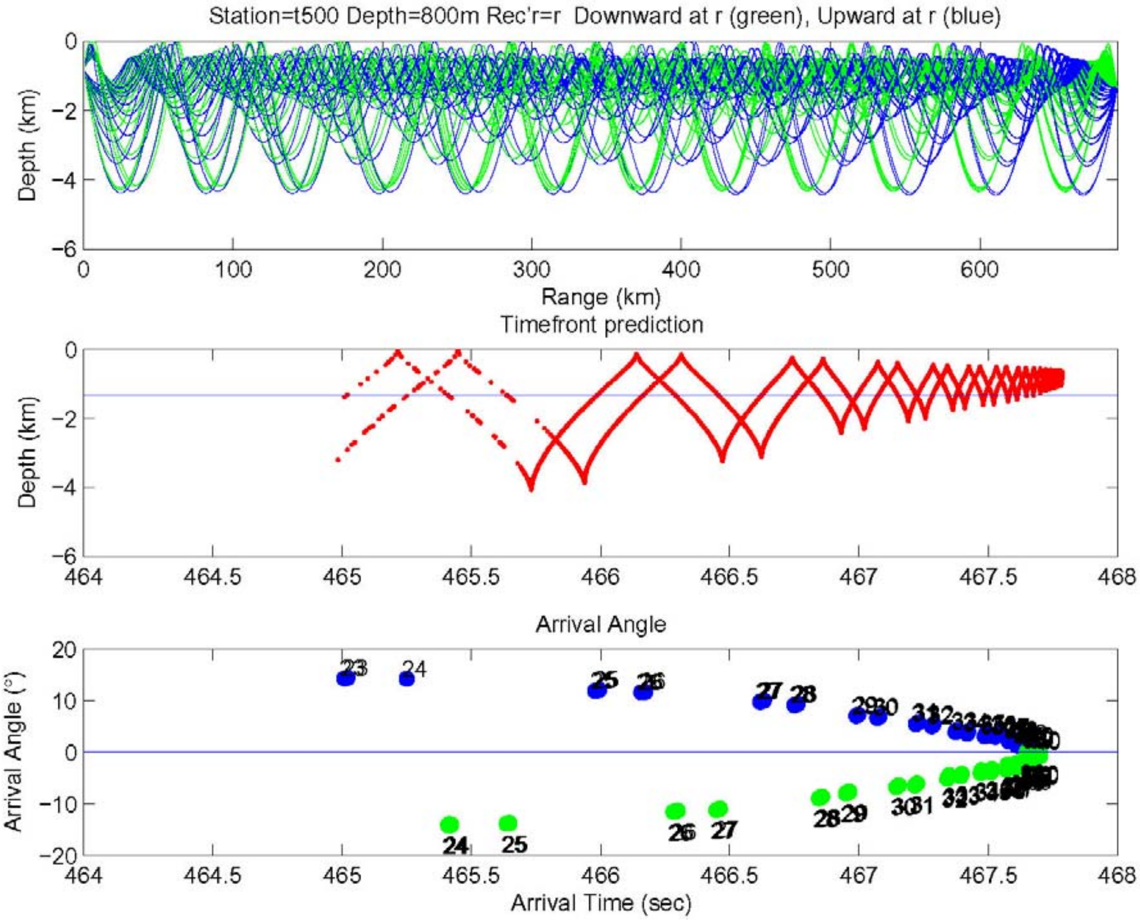

Figure A10.5. Station T500 800 m source deployment to ‘r’ propagation predictions

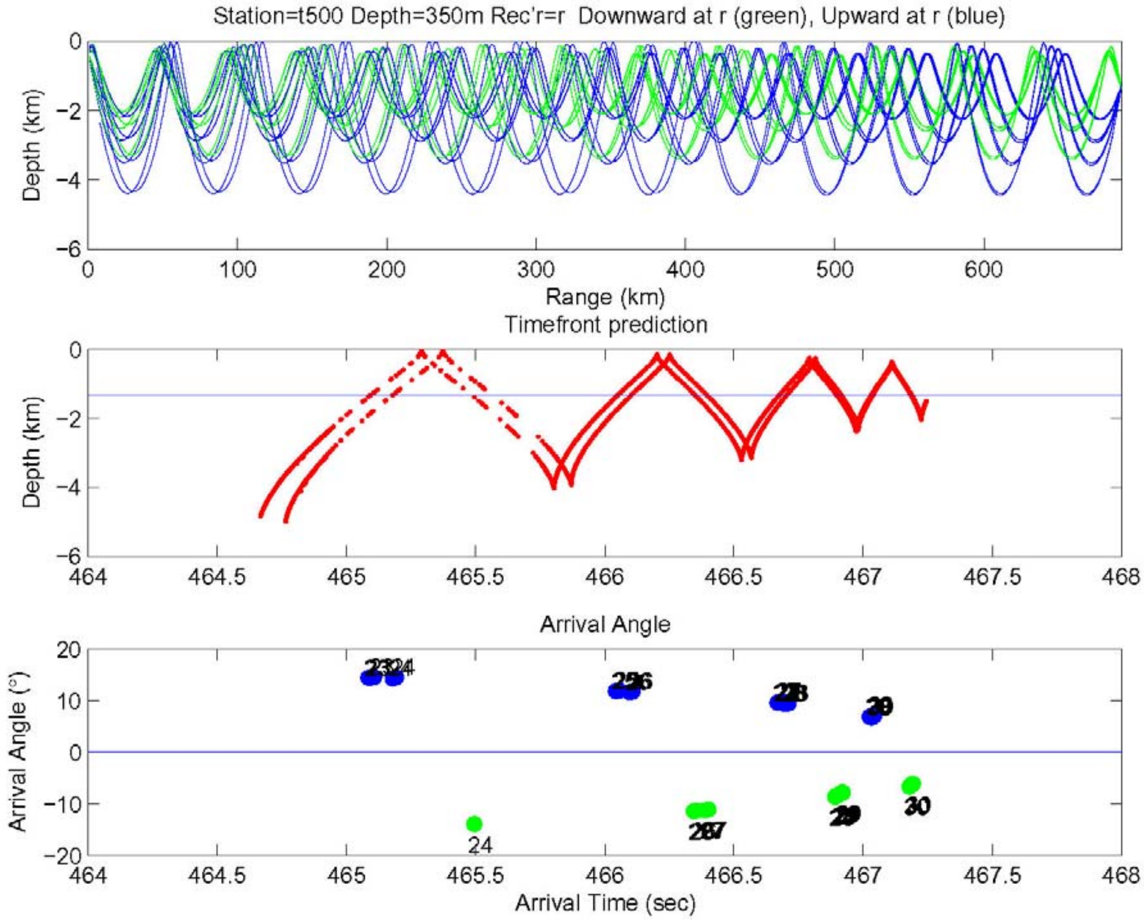

Figure A10.6. Station T500 350 m source deployment to ‘r’ propagation predictions

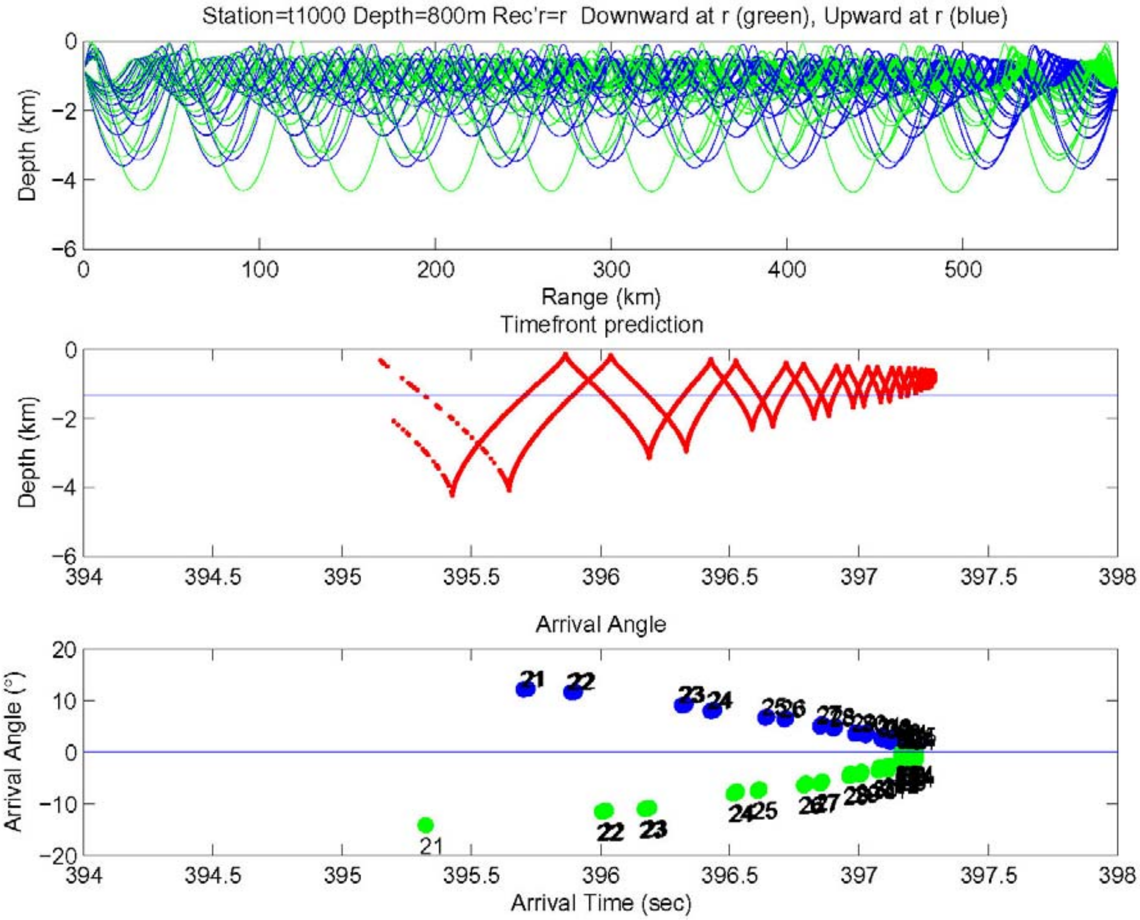

Figure A10.7. Station T1000 800 m source deployment to ‘r’ propagation predictions

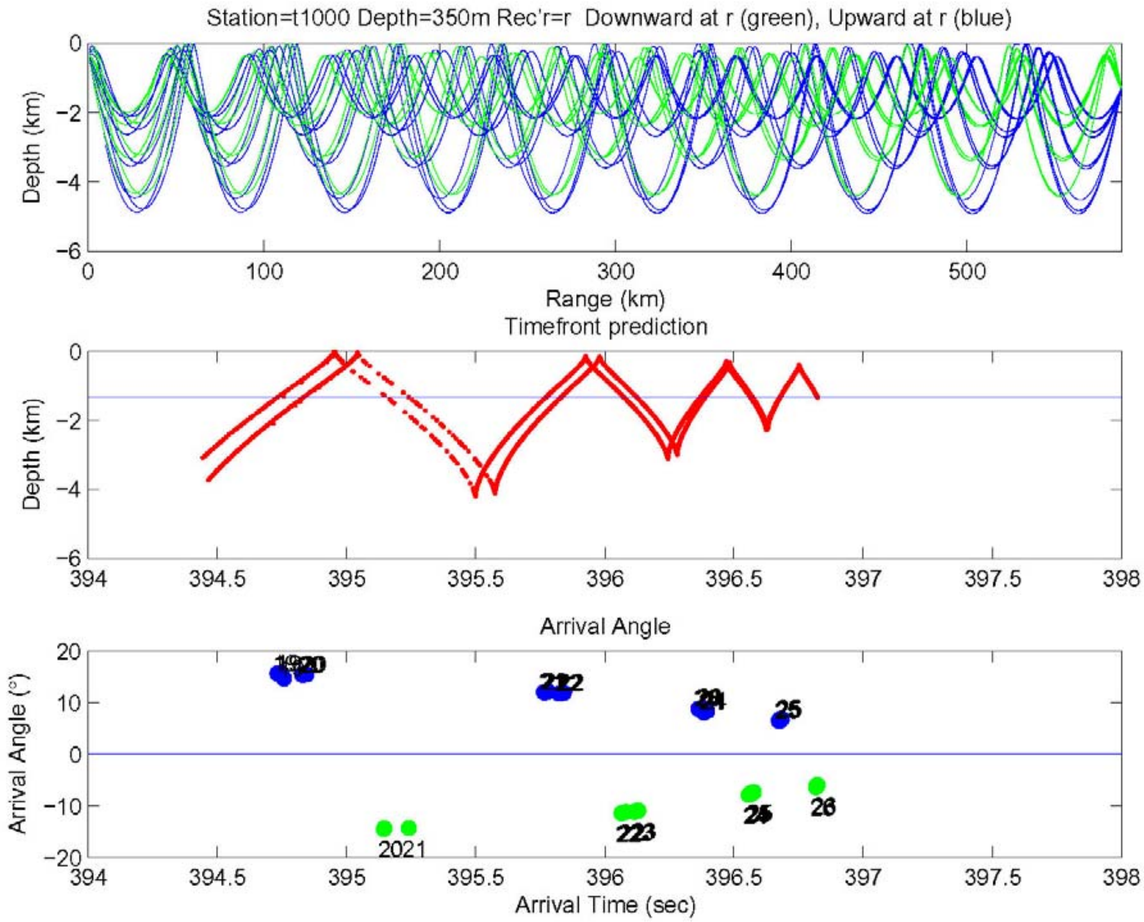

Figure A10.8. Station T1000 350 m source deployment to ‘r’ propagation predictions

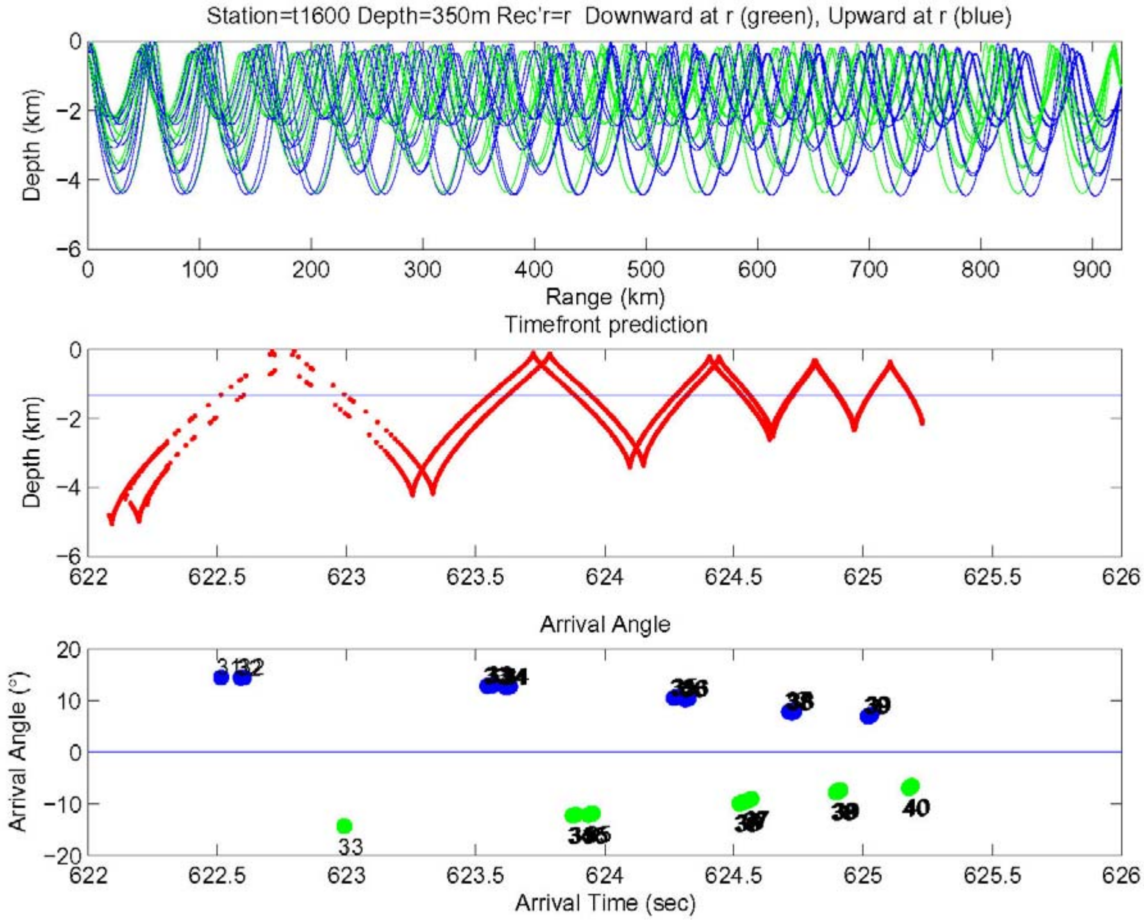

Figure A10.9. Station T1600 350 m source deployment to ‘r’ propagation predictions

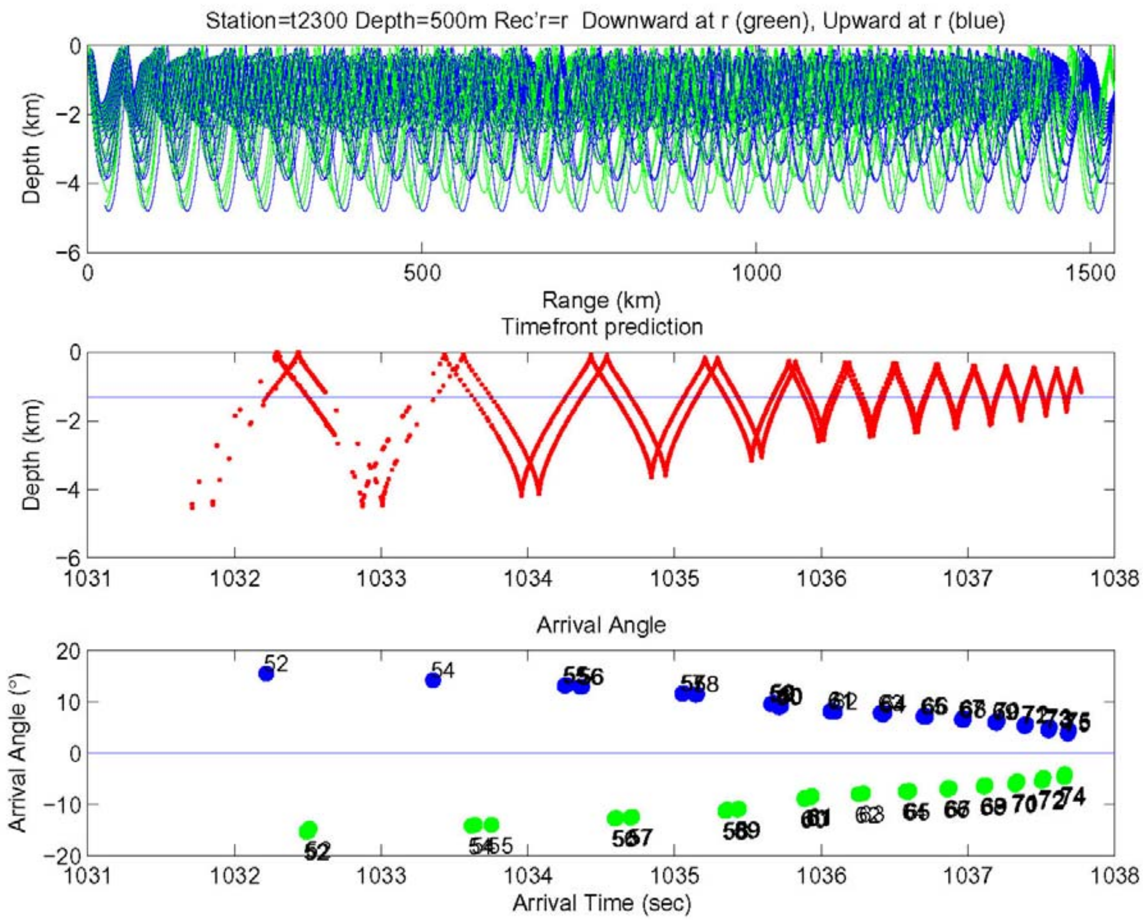

Figure A10.10. Station T2300 500 m source deployment to ‘r’ propagation predictions

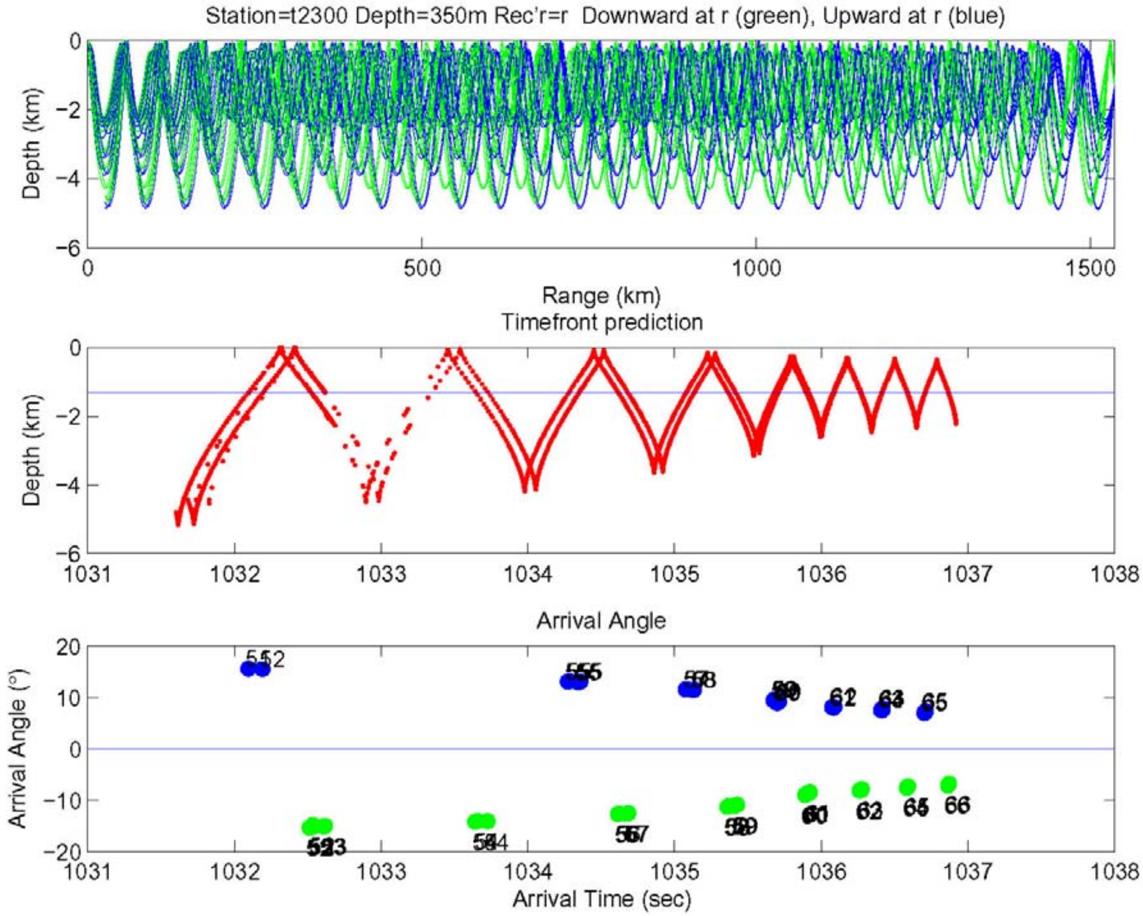

Figure A10.11. Station T2300 350 m source deployment to ‘r’ propagation predictions

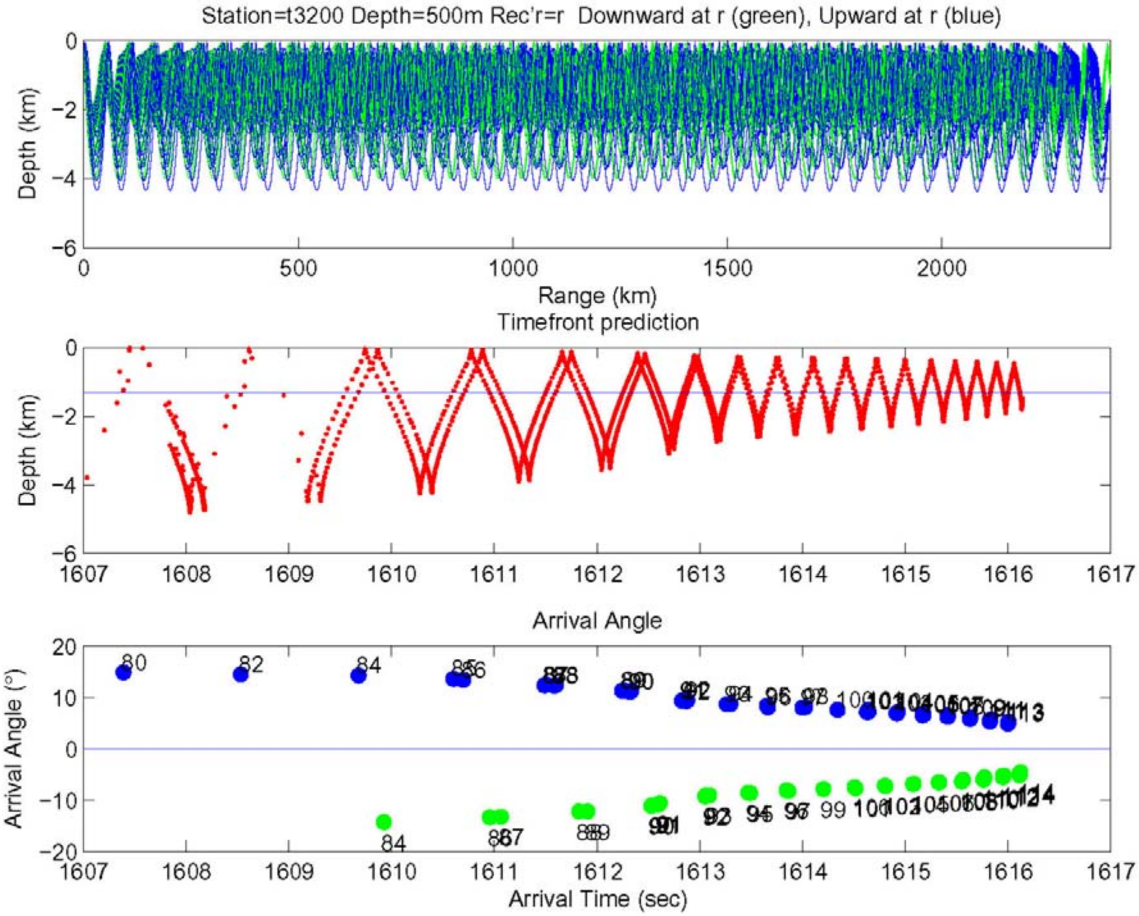

Figure A10.12. Station T3200 500 m source deployment to ‘r’ propagation predictions

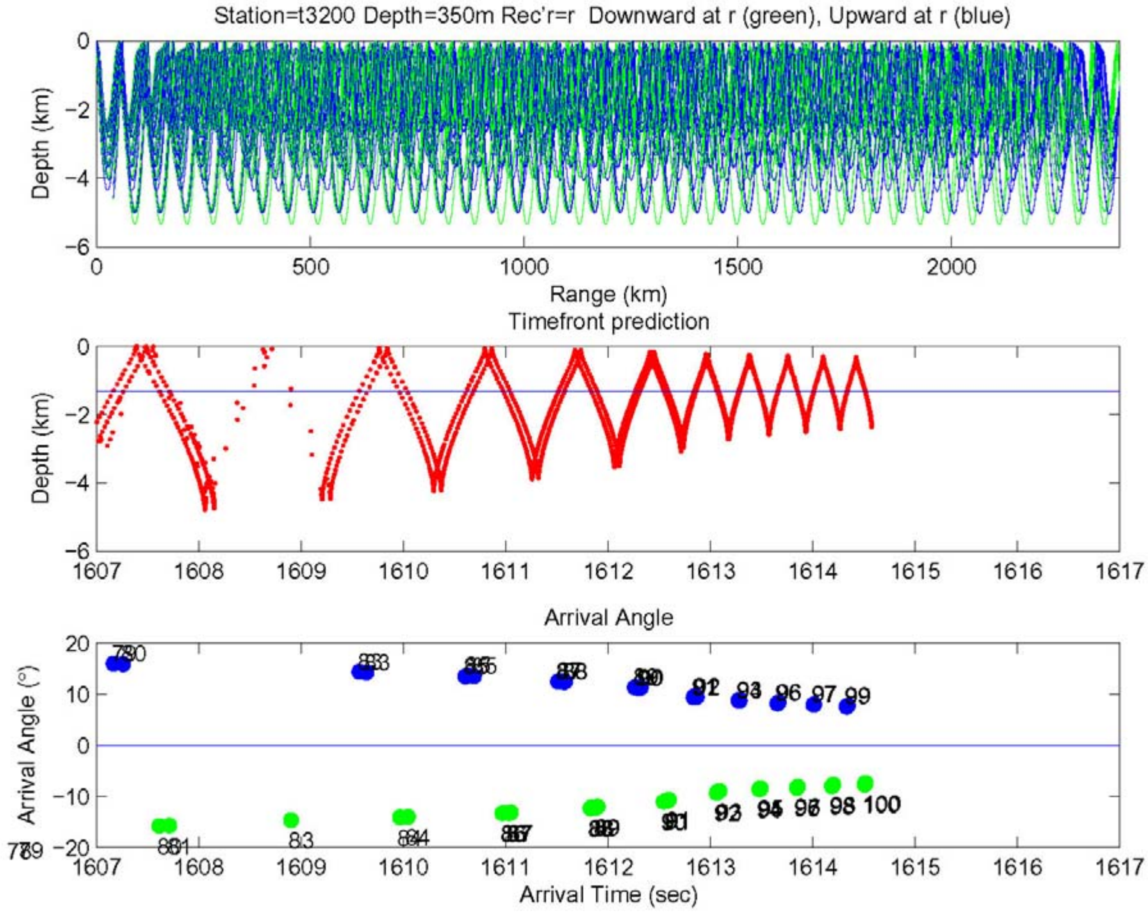

Figure A10.13. Station T3200 350 m source deployment to ‘r’ propagation predictions

Appendix 11: Predicted time front and measured reception alignments for all receptions at 'r' from the LOAPEX stations

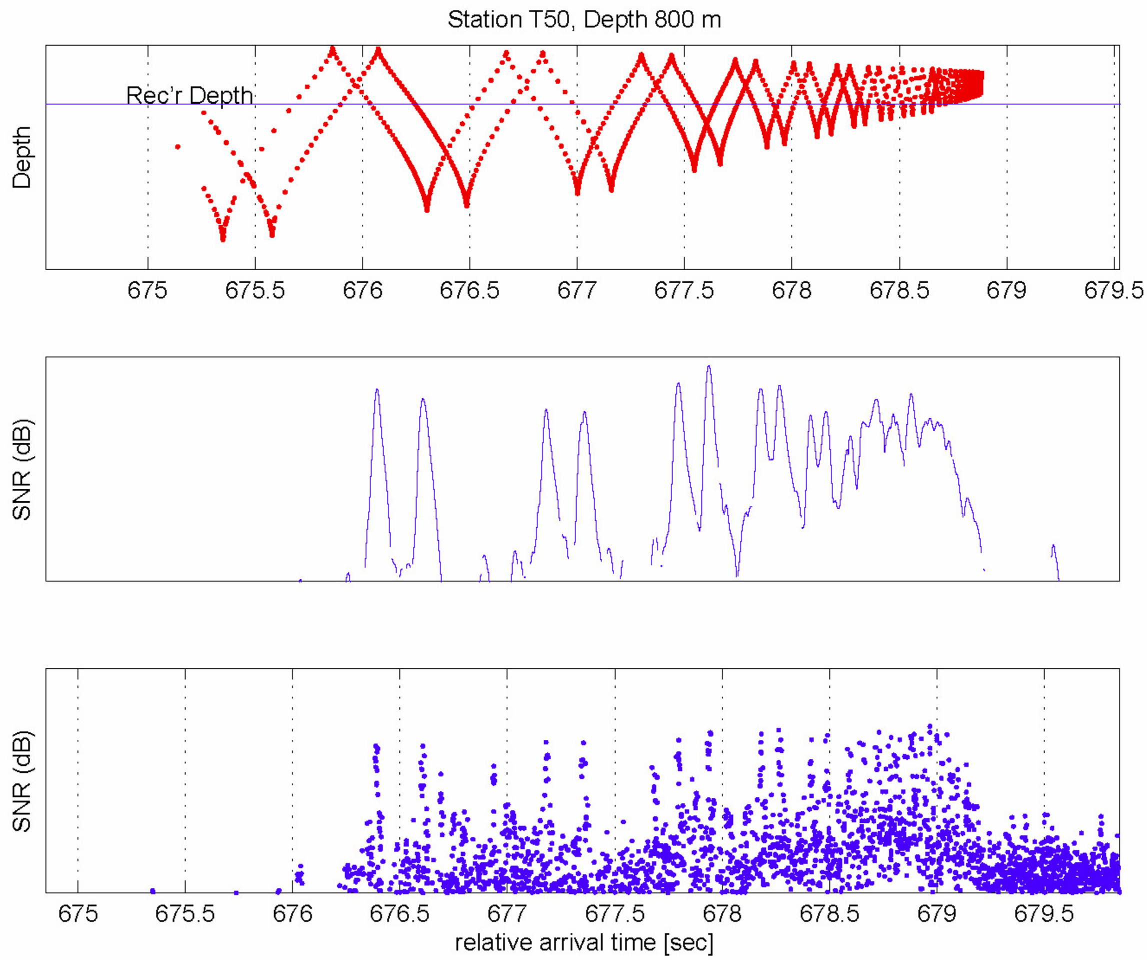

Figure A11-1. Station T50 800 m source deployment to 'r' predicted time front aligned with measured receptions. The middle and bottom panels lie on the same time axis.

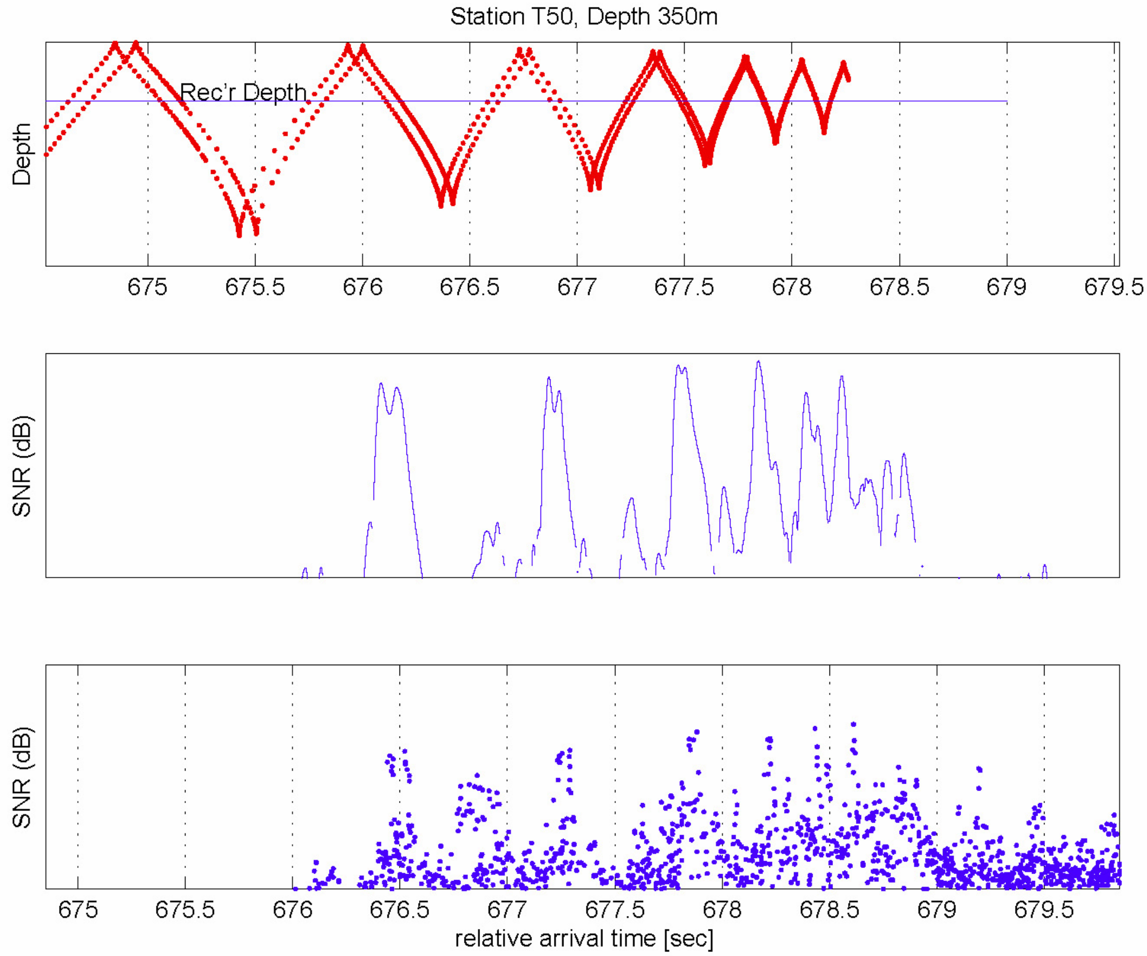

Figure A11-2. Station T50 350 m source deployment to ‘r’ predicted time front aligned with measured receptions. The middle and bottom panels lie on the same time axis.

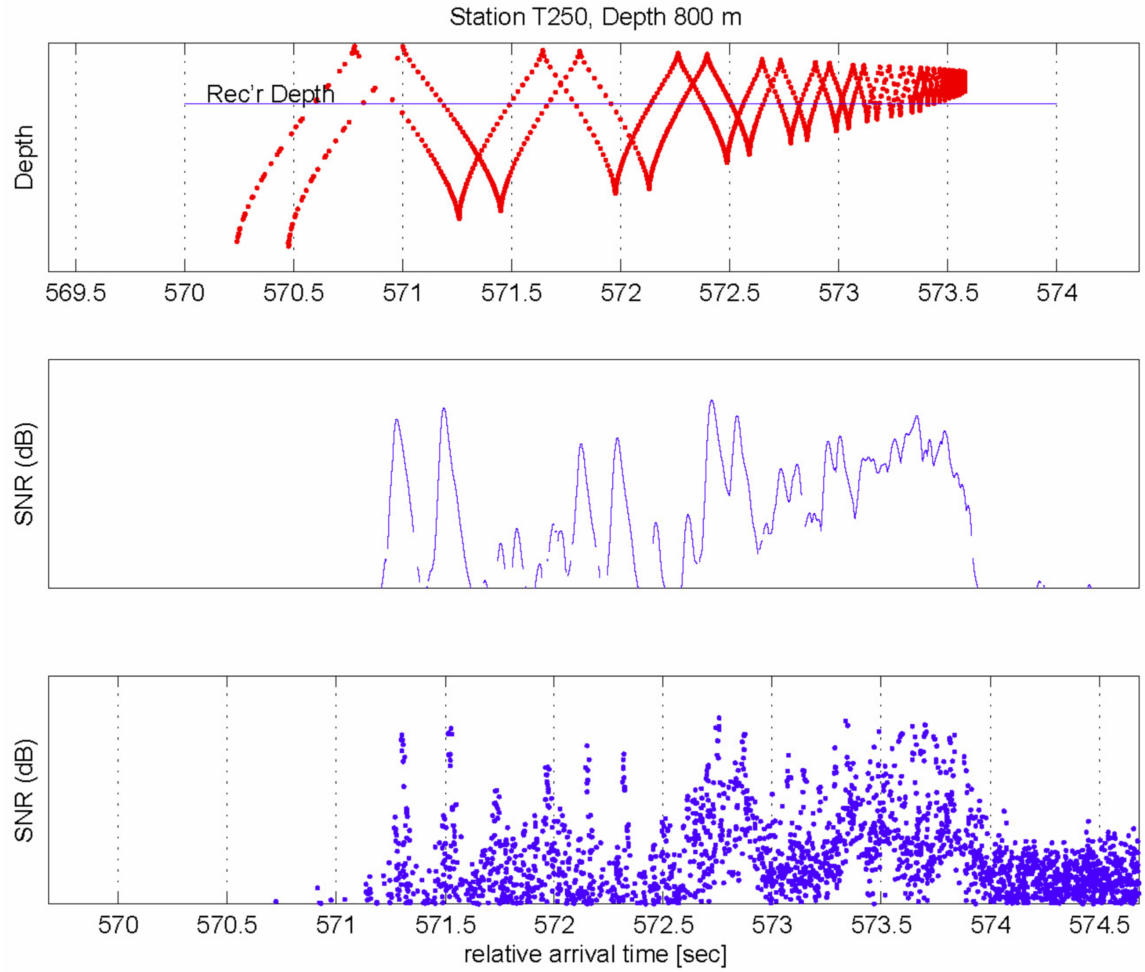

Figure A11-3. Station T250 800 m source deployment to 'r' predicted time front aligned with measured receptions. The middle and bottom panels lie on the same time axis.

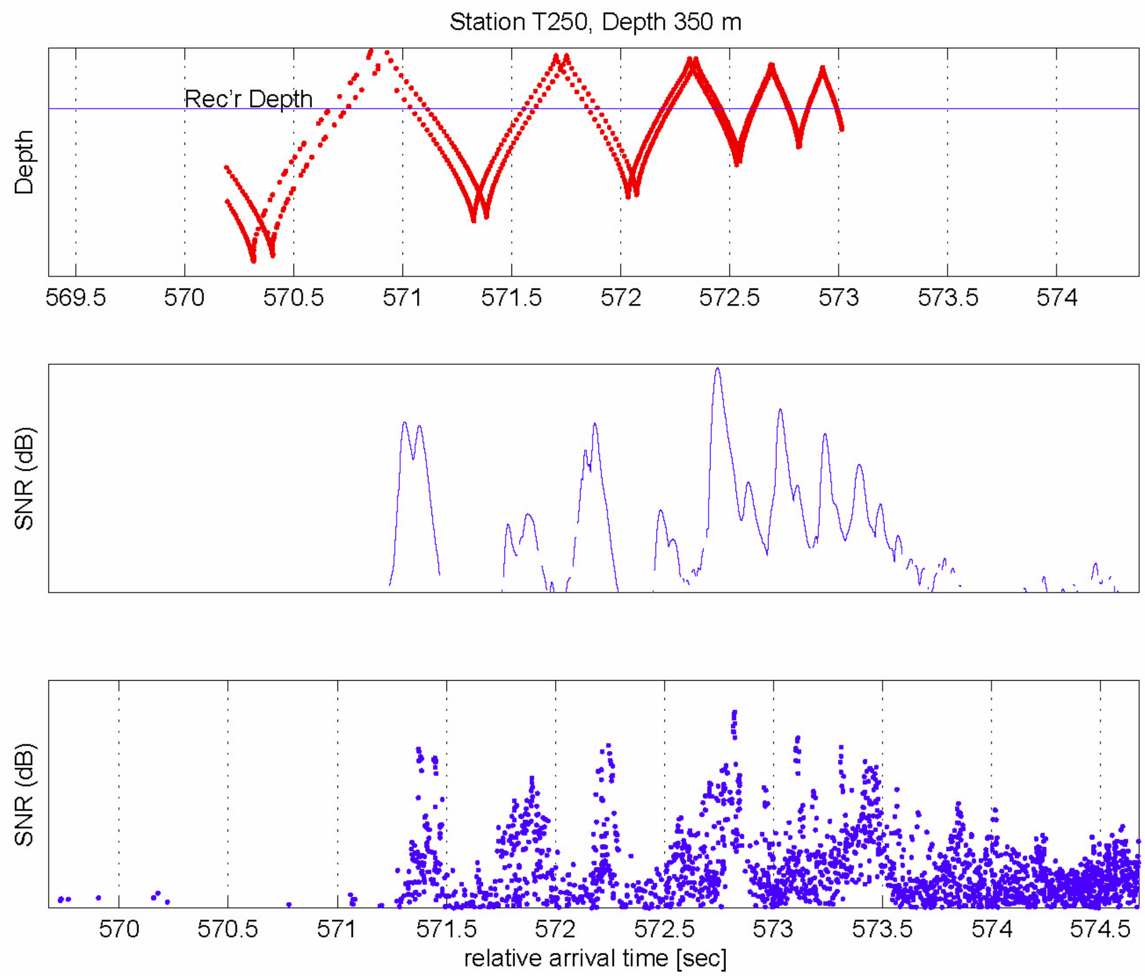

Figure A11-4. Station T250 350 m source deployment to ‘r’ predicted time front aligned with measured receptions. The middle and bottom panels lie on the same time axis.

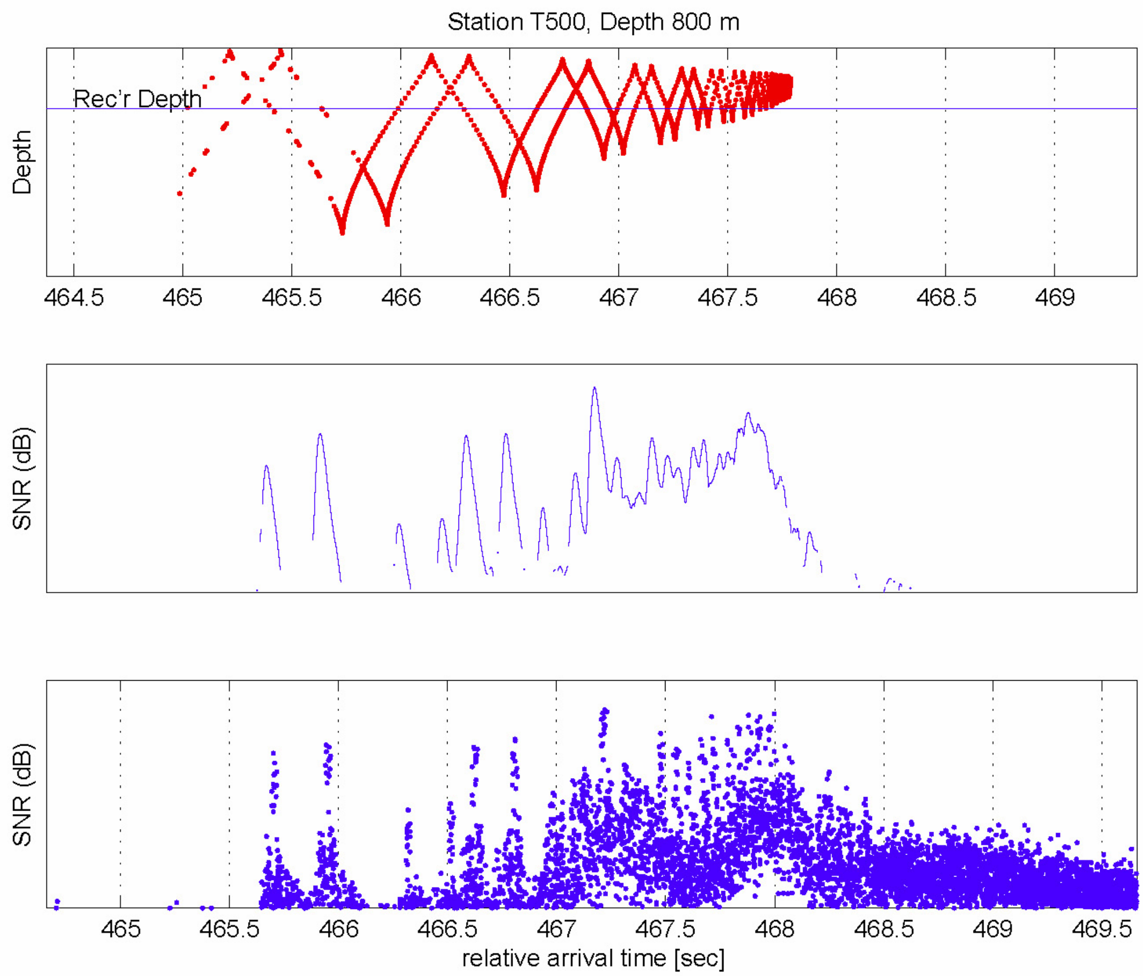

Figure A11-5. Station T500 800 m source deployment to 'r' predicted time front aligned with measured receptions. The middle and bottom panels lie on the same time axis.

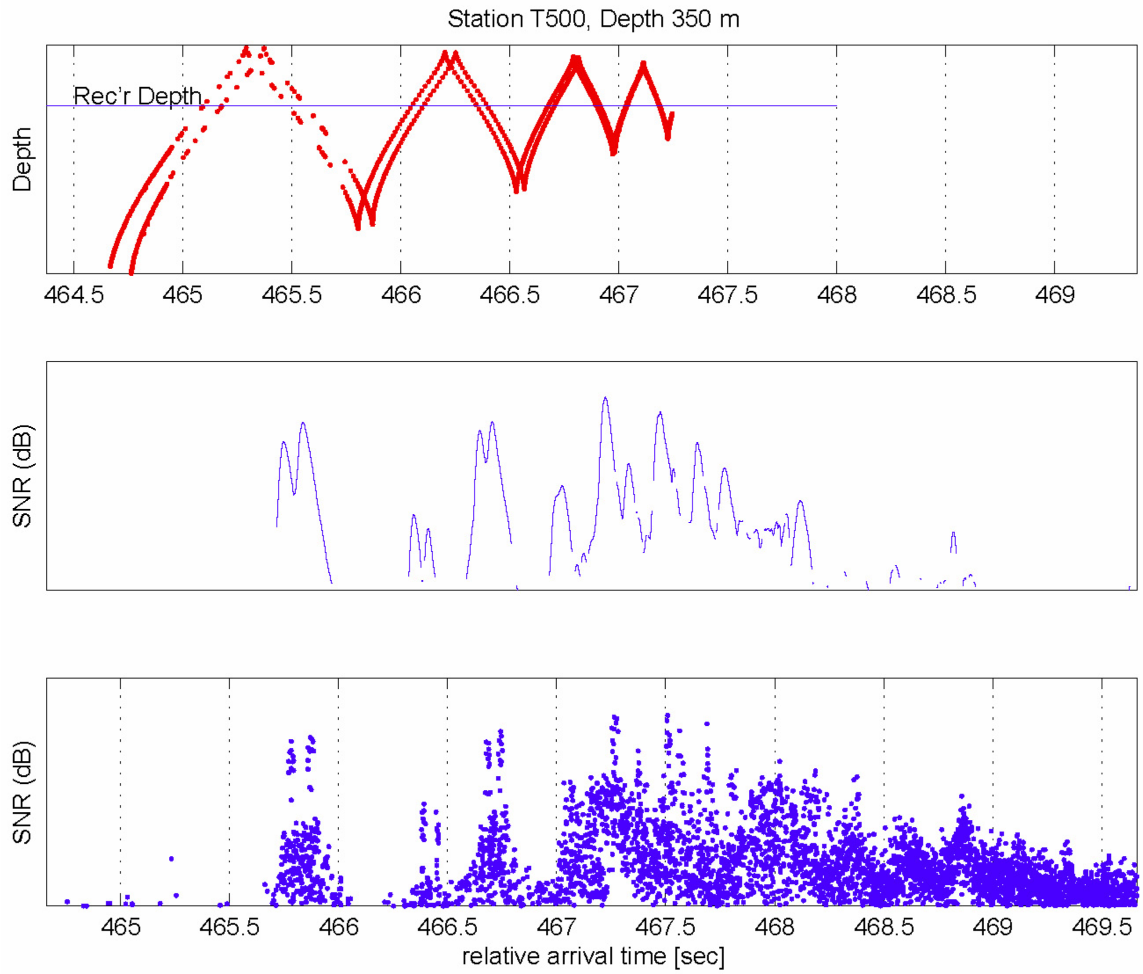

Figure A11-6. Station T500 350 m source deployment to 'r' predicted time front aligned with measured receptions. The middle and bottom panels lie on the same time axis.

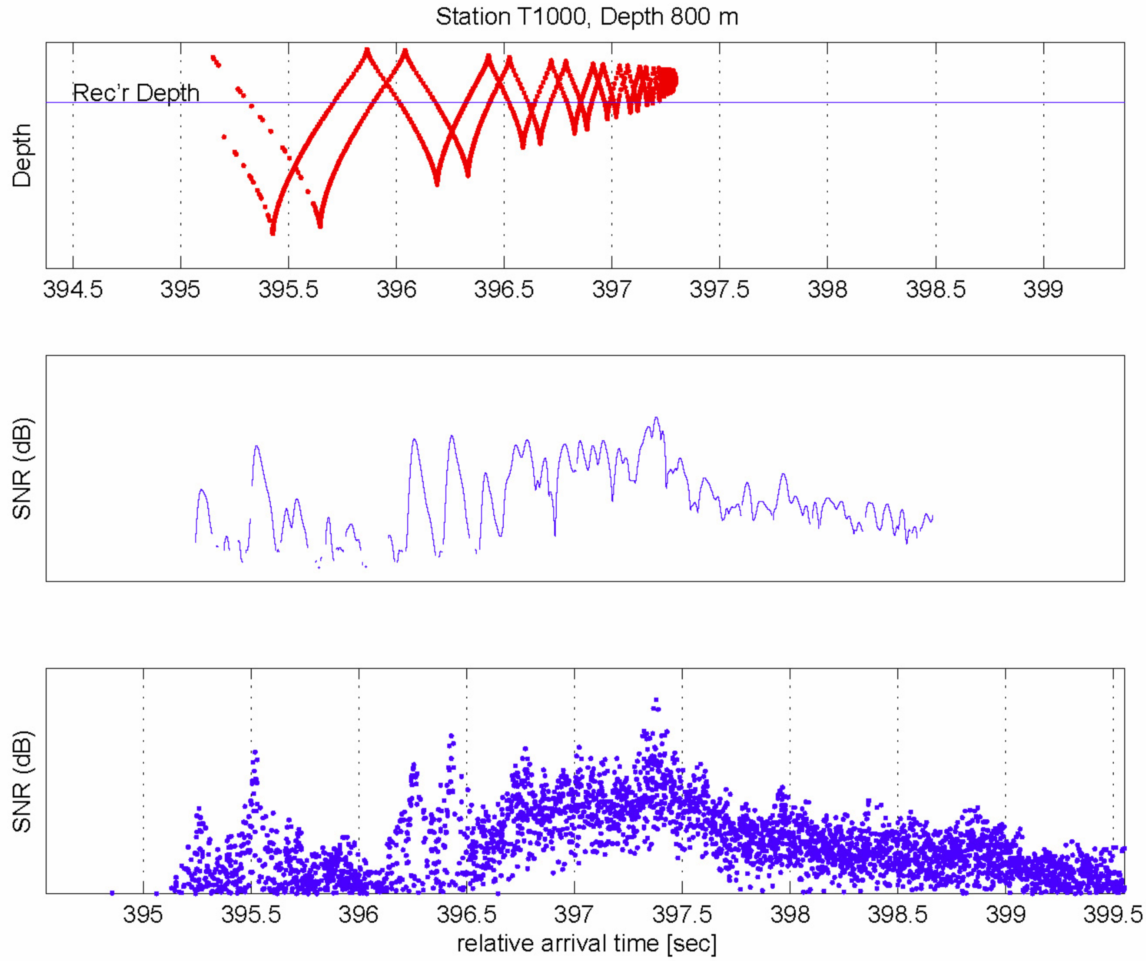

Figure A11-7. Station T1000 800 m source deployment to 'r' predicted time front aligned with measured receptions. The middle and bottom panels lie on the same time axis.

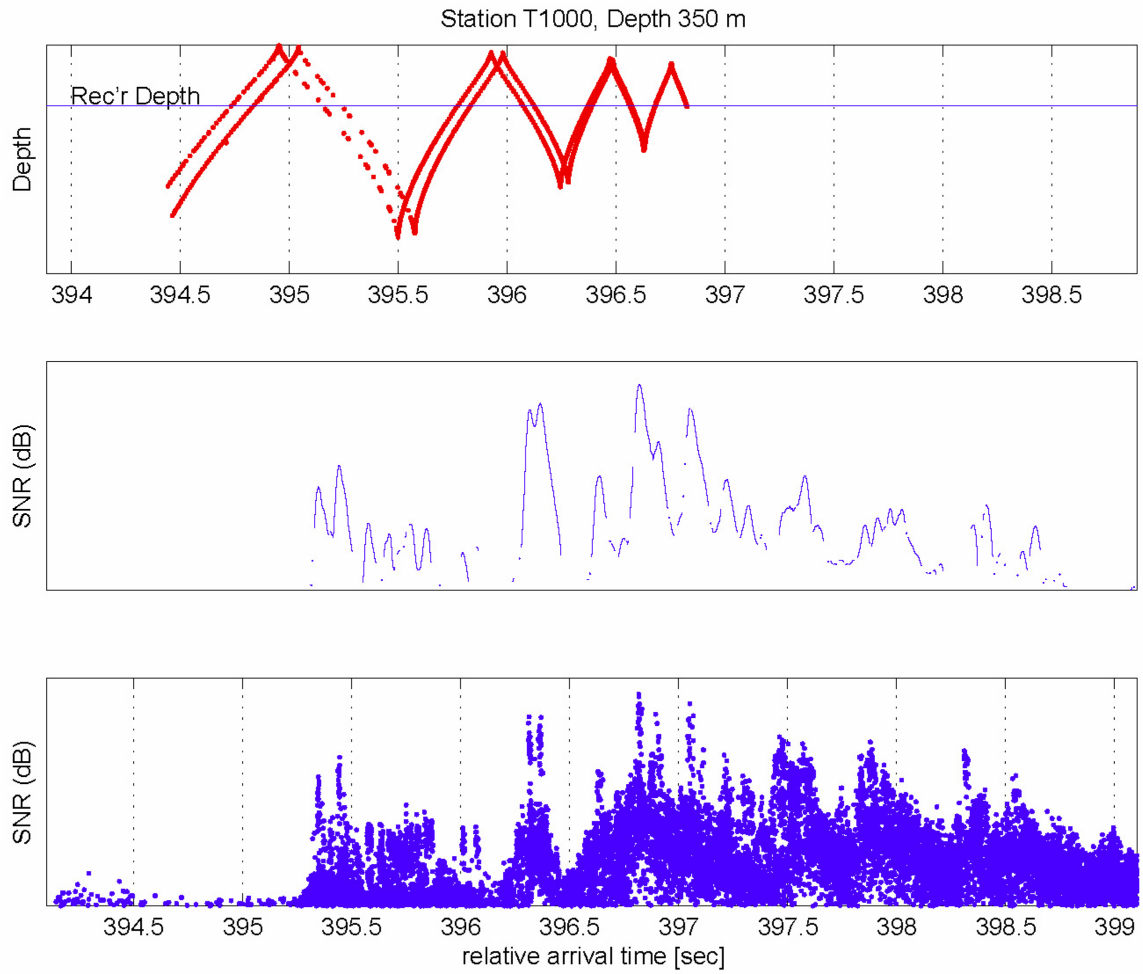

Figure A11-8. Station T1000 350 m source deployment to 'r' predicted time front aligned with measured receptions. The middle and bottom panels lie on the same time axis.

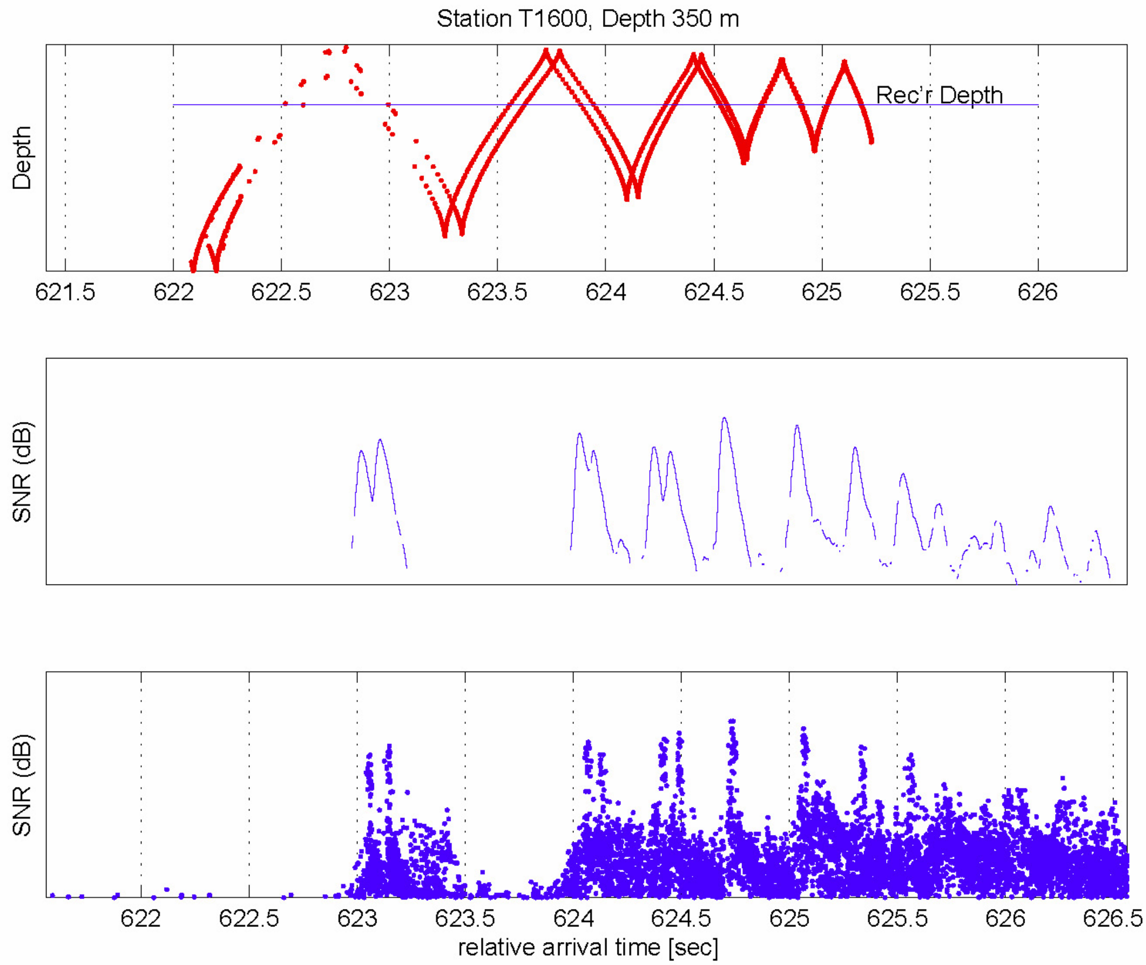

Figure A11-9. Station T1600 350 m source deployment to ‘r’ predicted time front aligned with measured receptions. The middle and bottom panels lie on the same time axis.

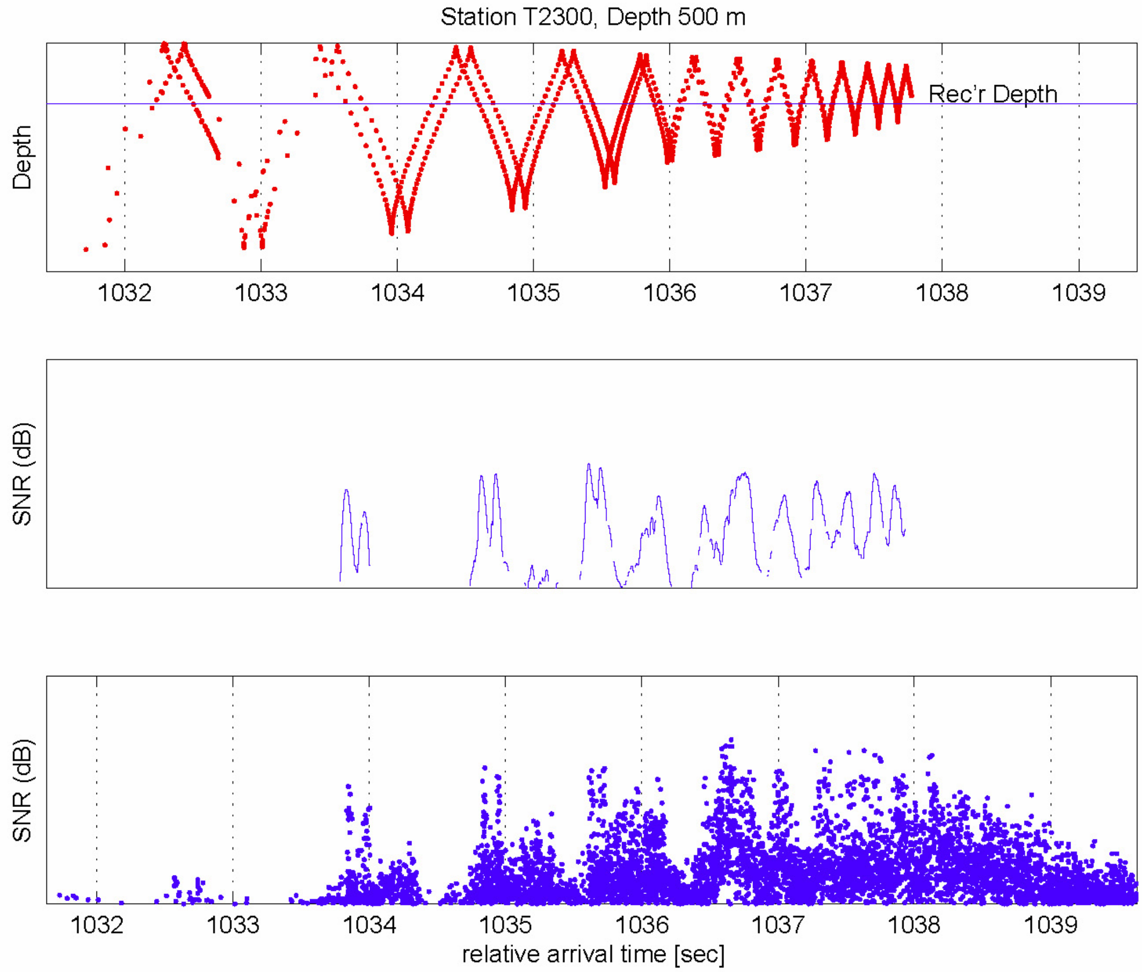

Figure A11-10. Station T2300 500 m source deployment to ‘r’ predicted time front aligned with measured receptions. The middle and bottom panels lie on the same time axis.

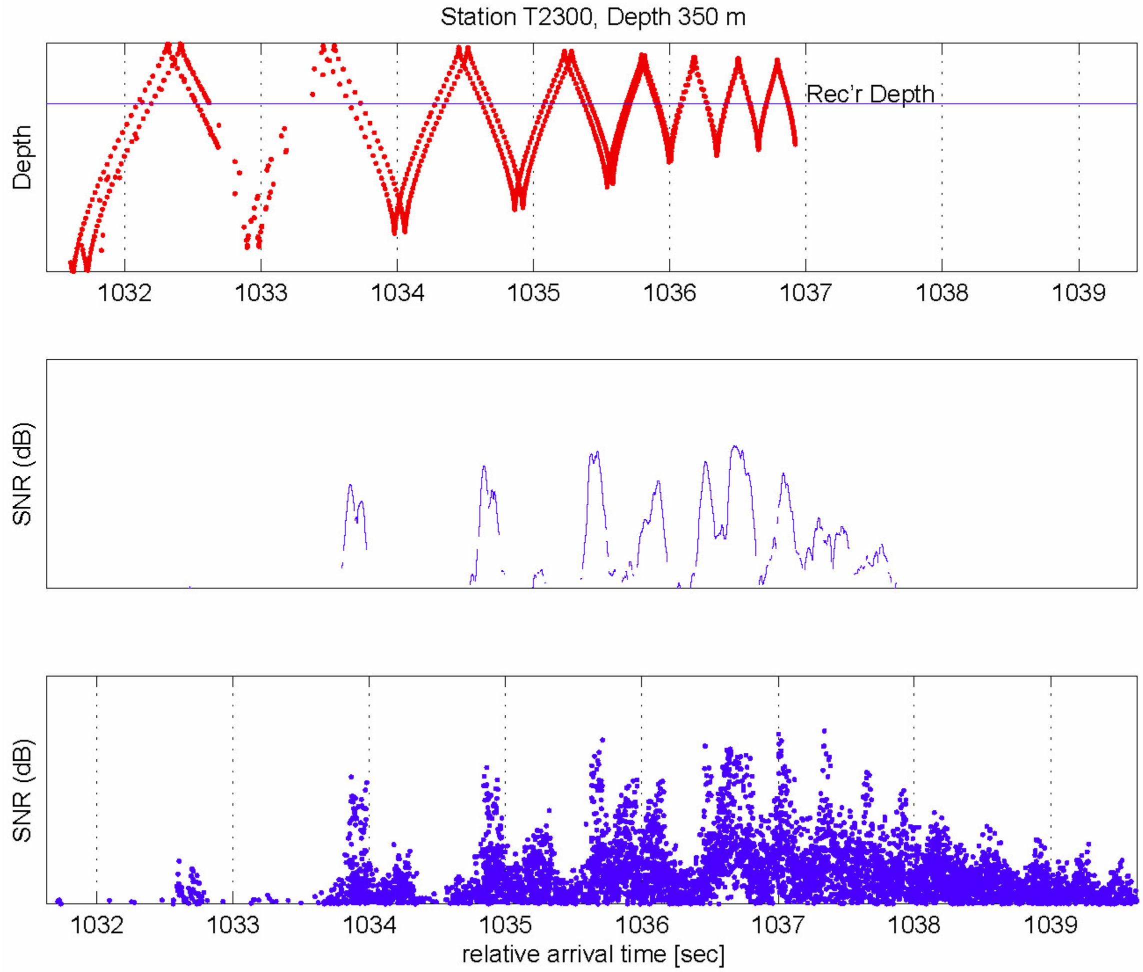

Figure A11-11. Station T2300 350 m source deployment to 'r' predicted time front aligned with measured receptions. The middle and bottom panels lie on the same time axis.

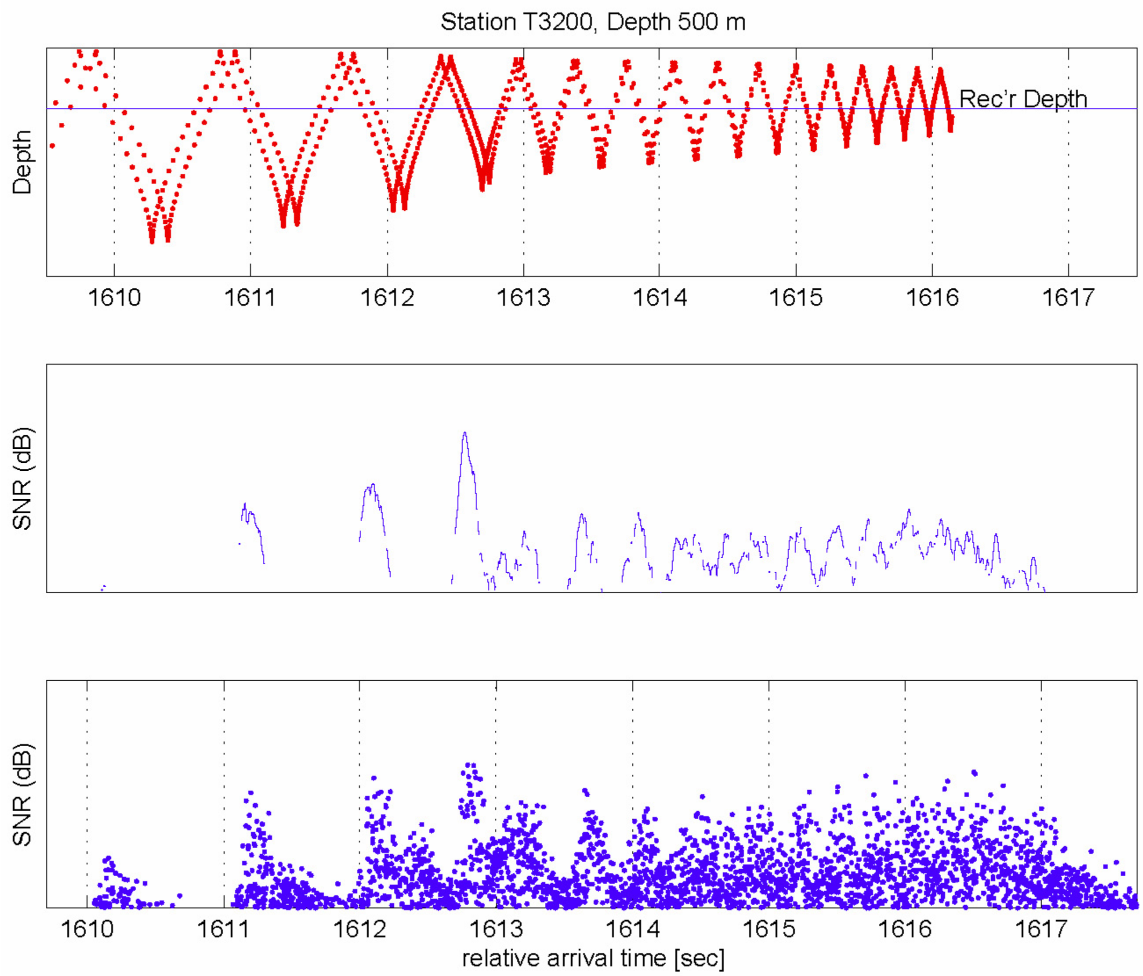

Figure A11-12. Station T3200 500 m source deployment to 'r' predicted time front aligned with measured receptions. The middle and bottom panels lie on the same time axis.

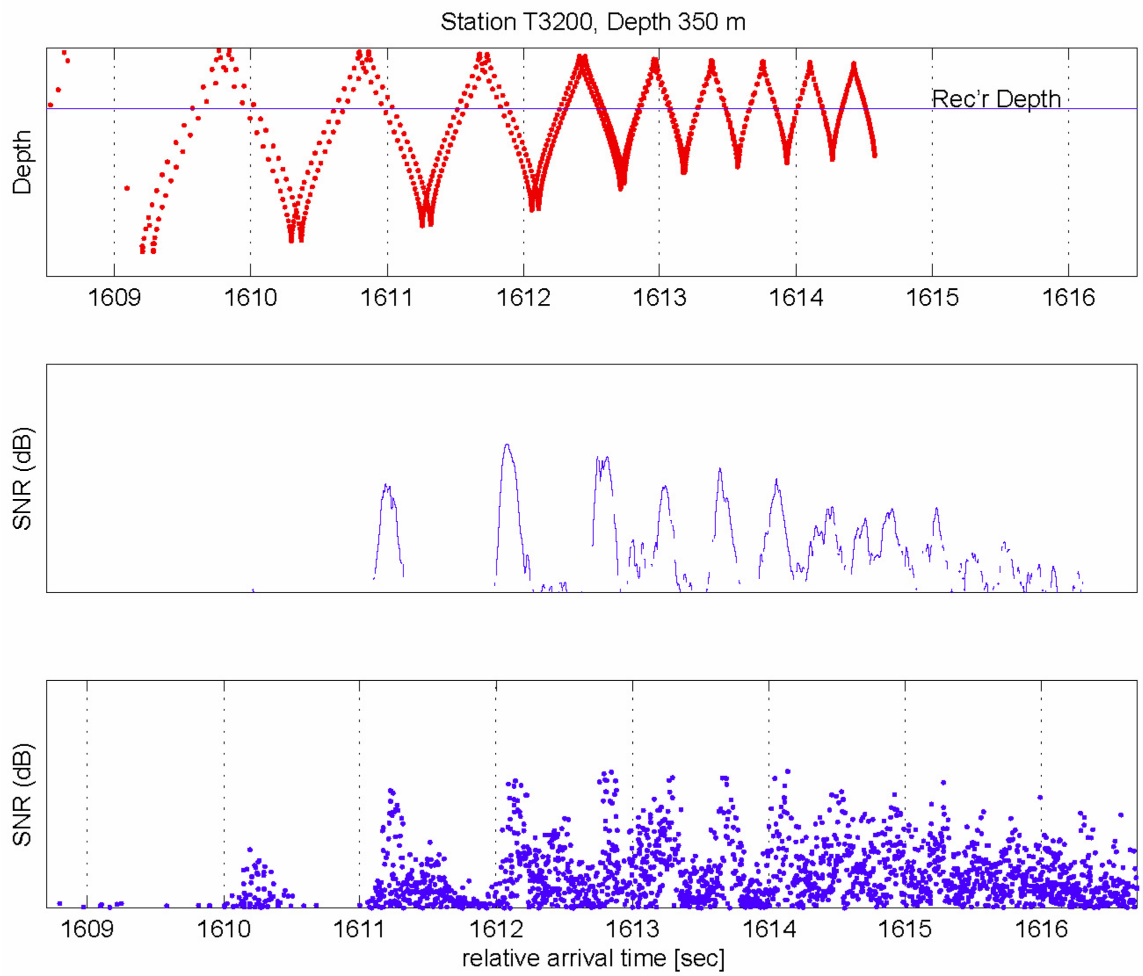

Figure A11-13. Station T3200 350 m source deployment to ‘r’ predicted time front aligned with measured receptions. The middle and bottom panels lie on the same time axis.

Appendix 12. Receptions at 'r' for all LOAPEX transmissions shown in a waterfall format

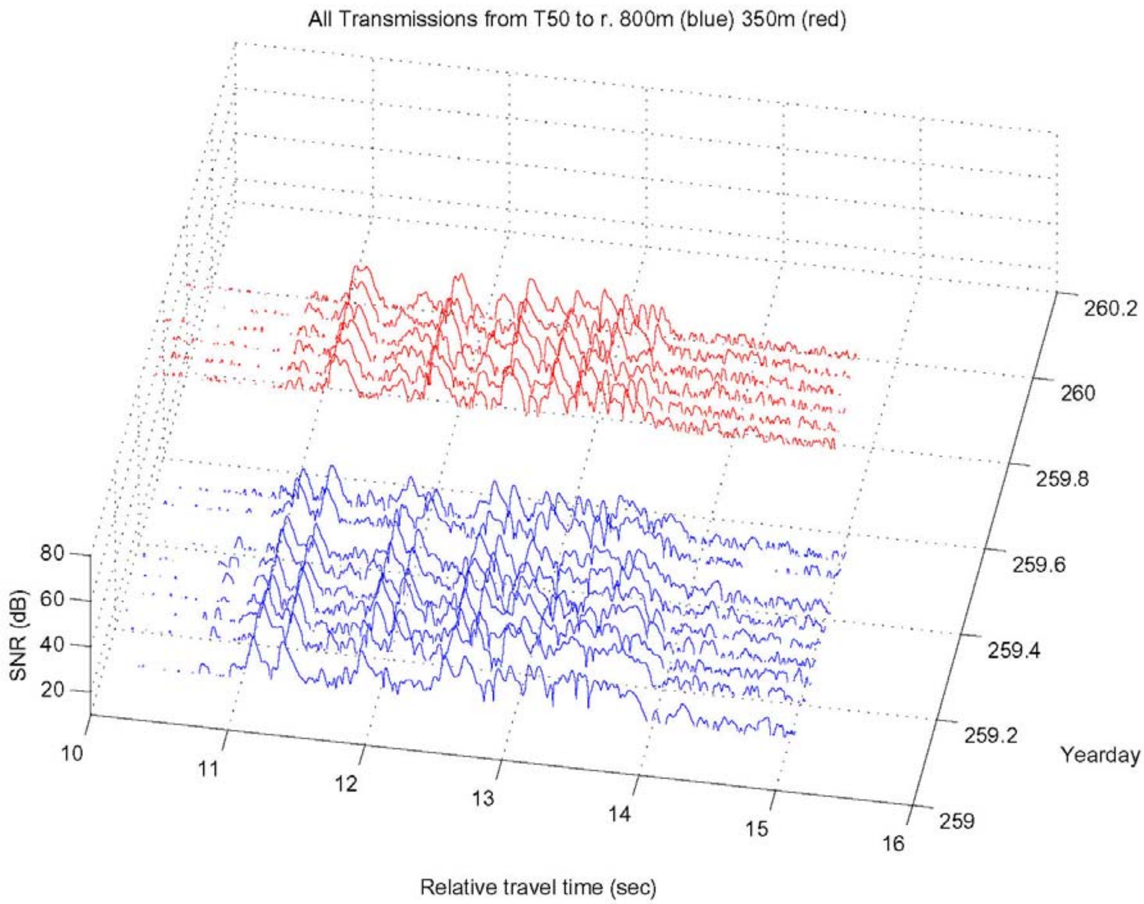

Figure A12-1. Station T50 to 'r' measured reception waterfall

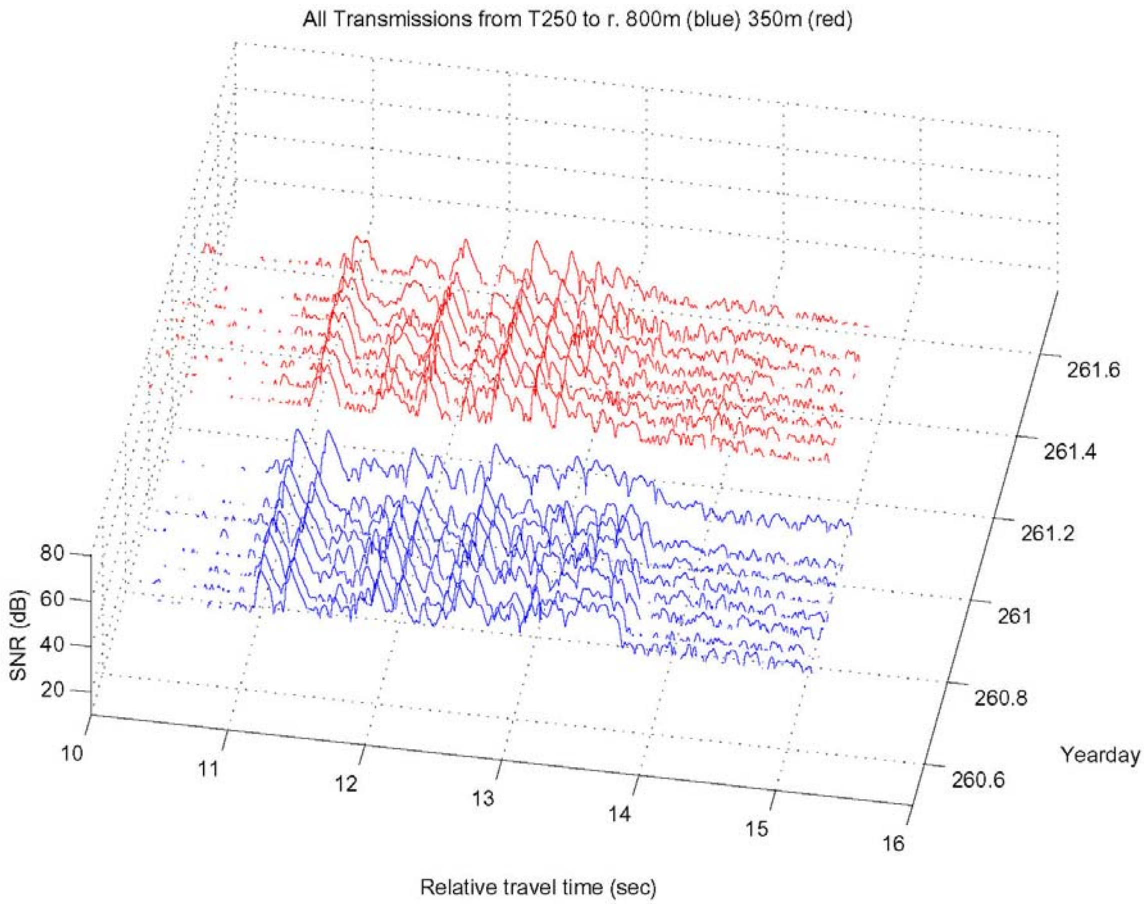

Figure A12-2. Station T250 to ‘r’ measured reception waterfall

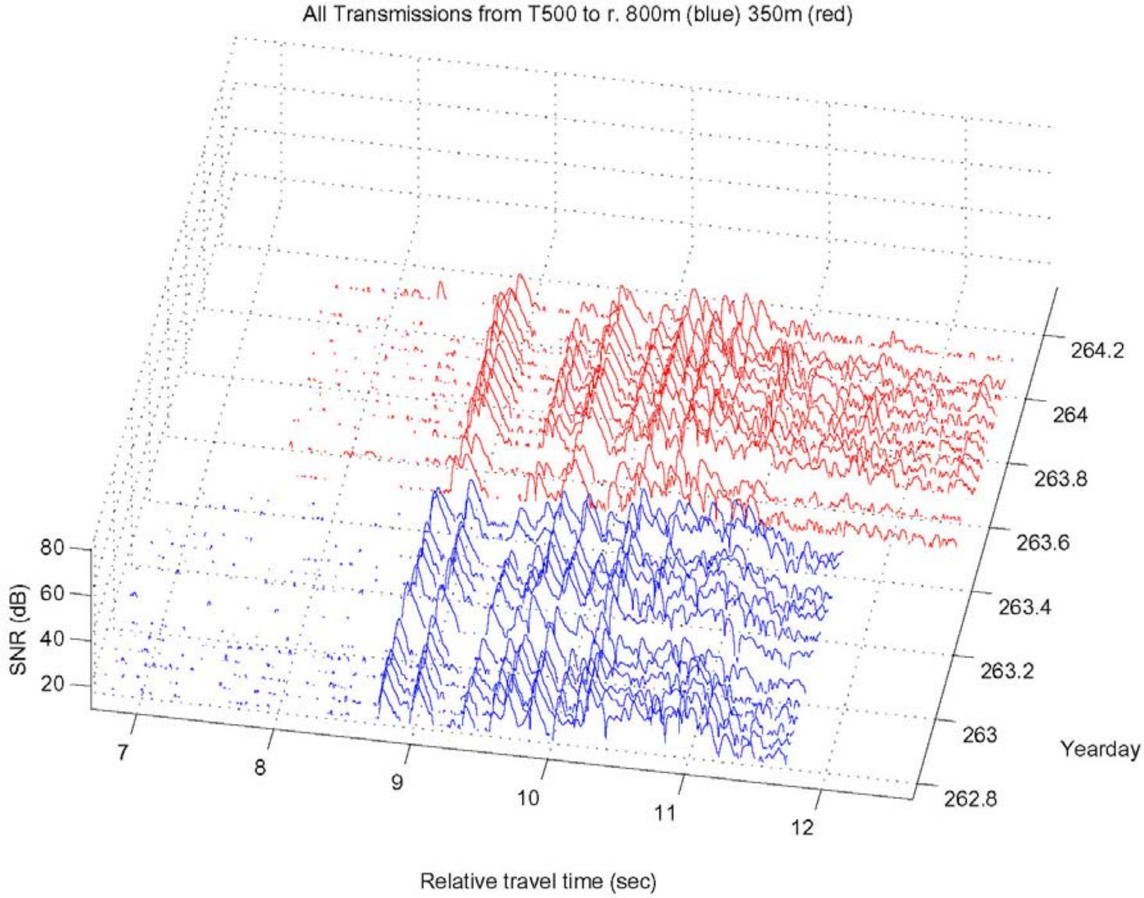

Figure A12-3. Station T500 to ‘r’ measured reception waterfall

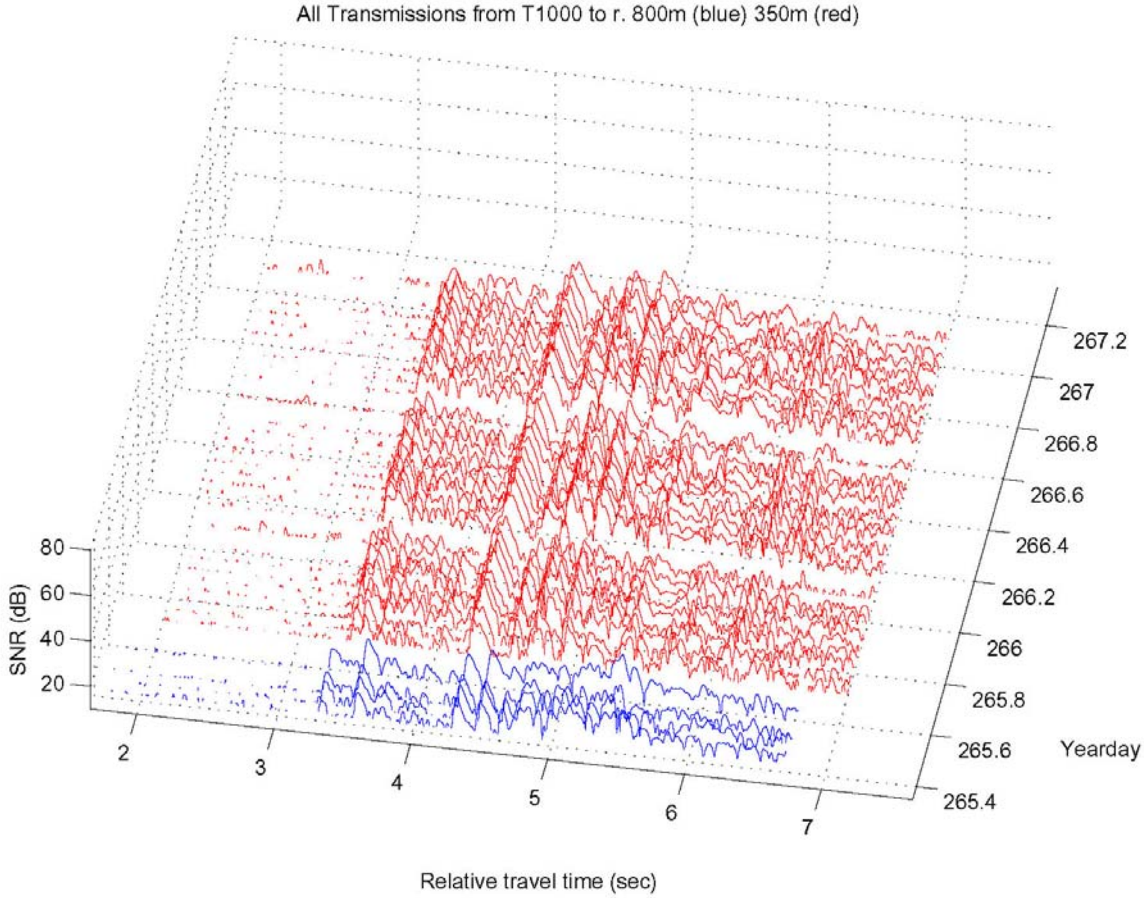

Figure A12-4. Station T1000 to ‘r’ measured reception waterfall

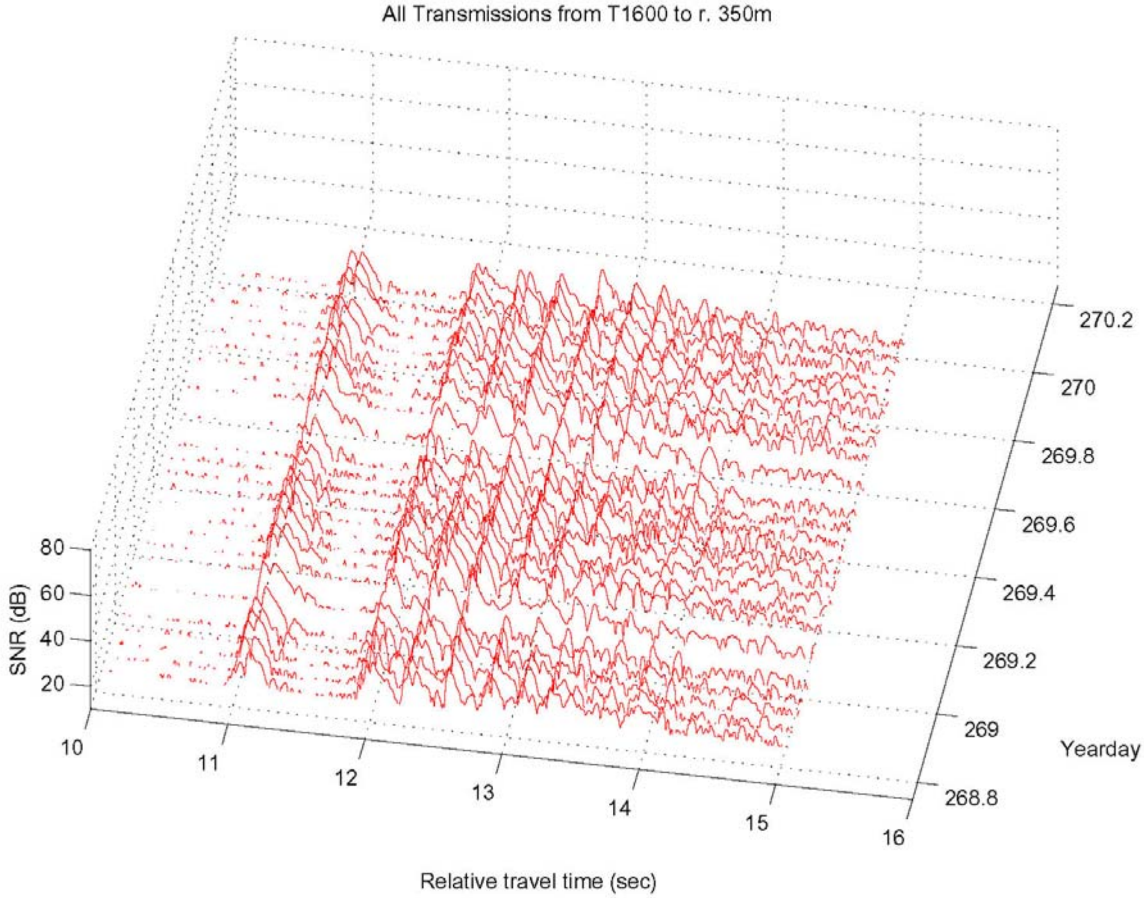

Figure A12-5. Station T1600 to ‘r’ measured reception waterfall

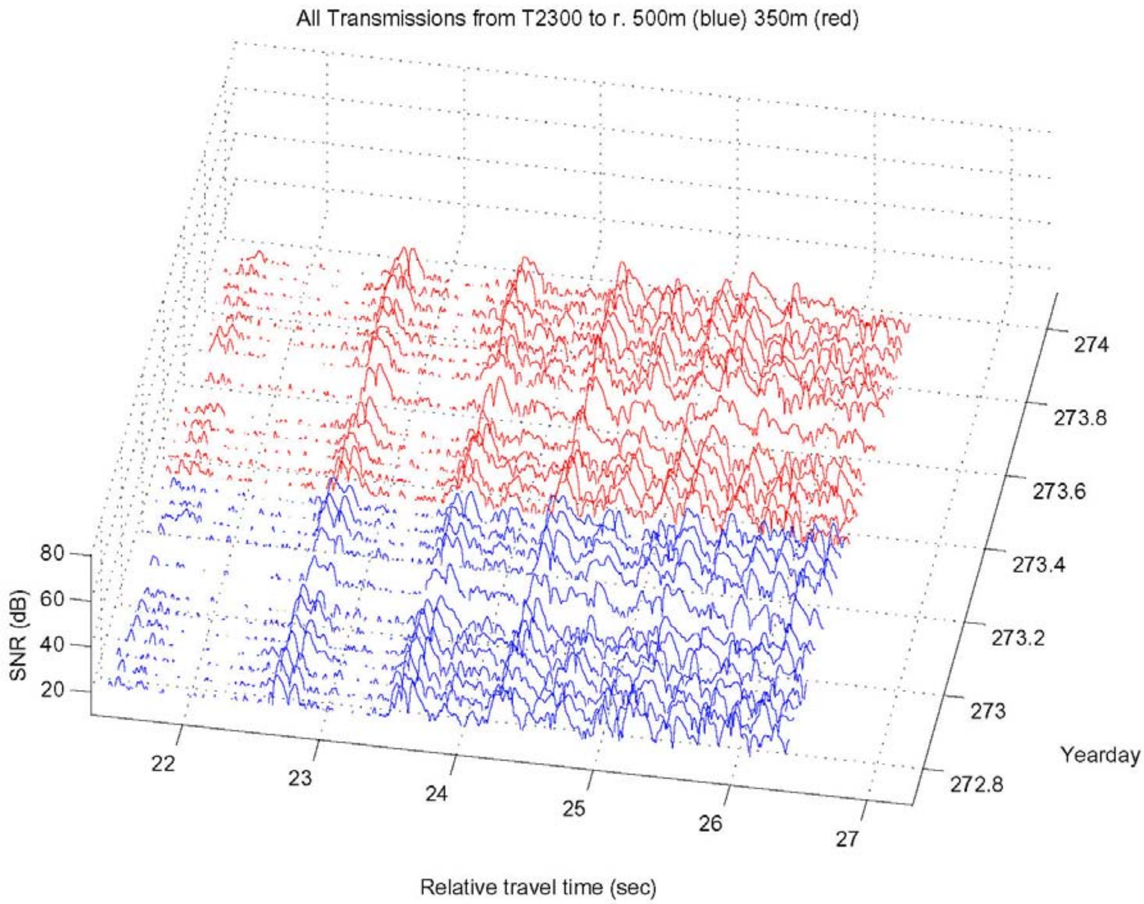

Figure A12-6. Station T2300 to 'r' measured reception waterfall

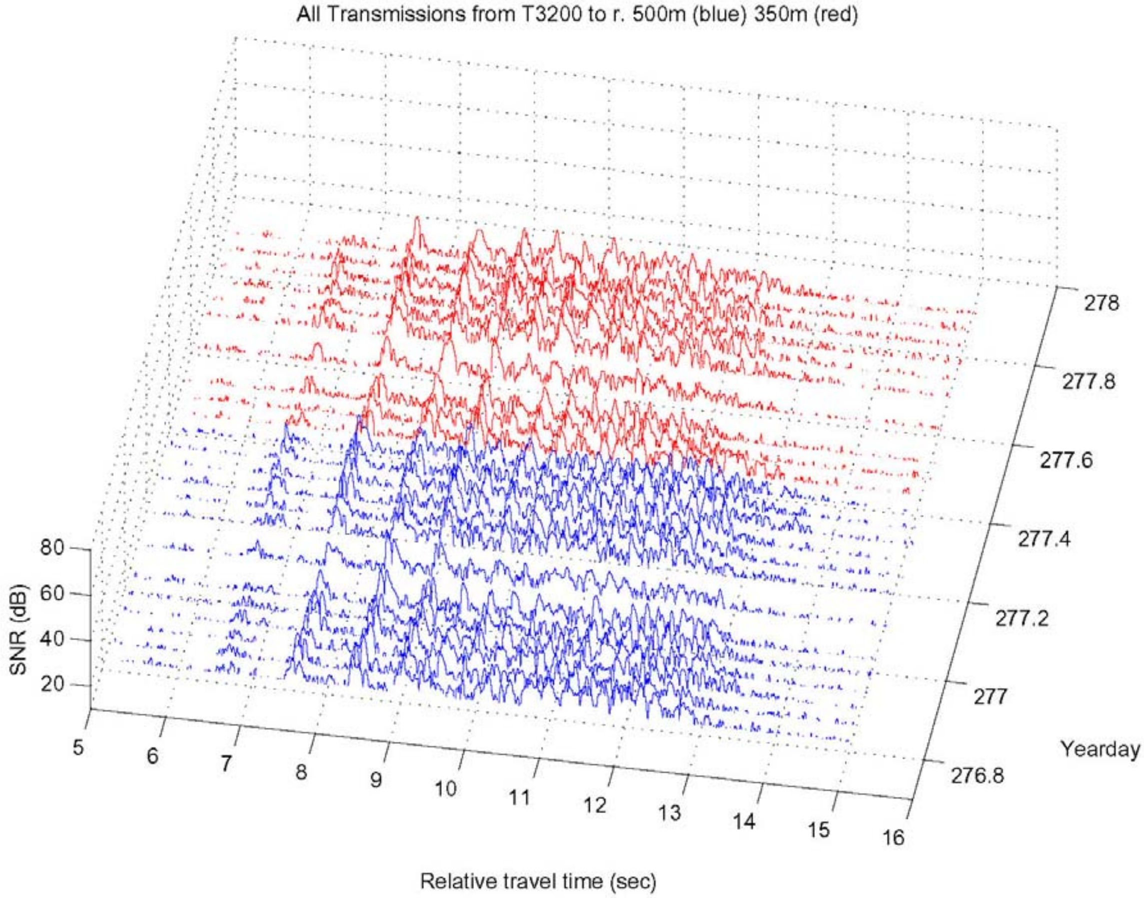

Figure A12-7. Station T3200 to ‘r’ measured reception waterfall

Appendix 13: Comparison of first four tracked raw acoustic arrivals and test tidal travel time offsets

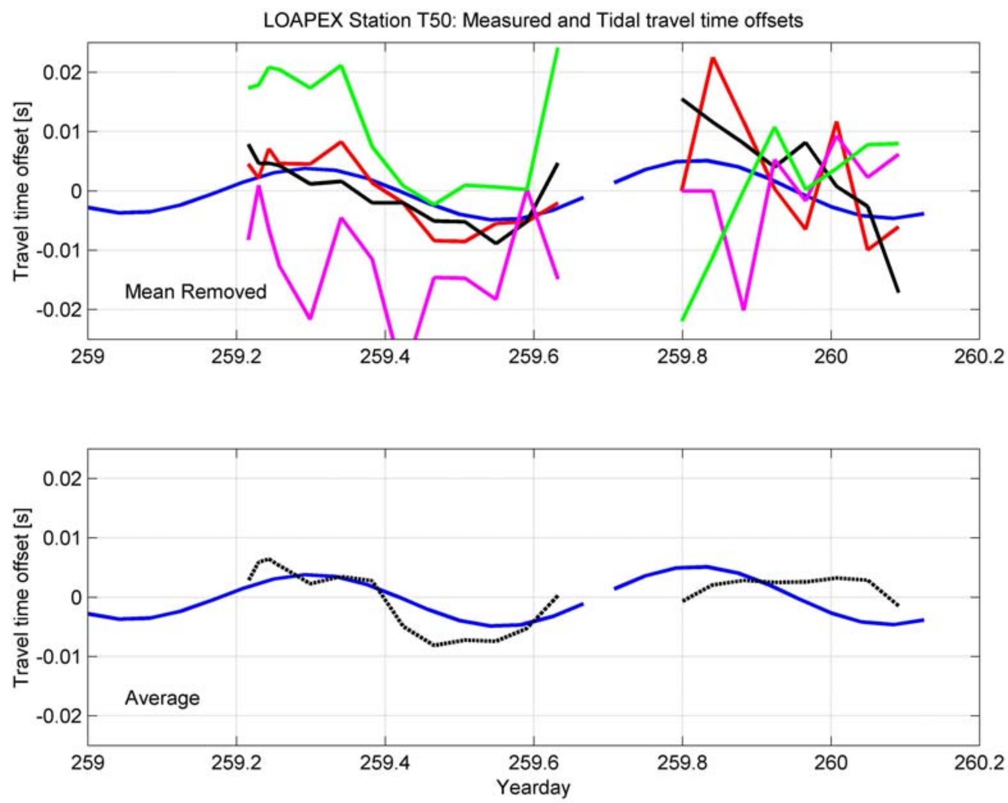

Figure A13-1. Station T50 to 'r' tracked raw receptions with their mean removed (colored), the average of the tracked receptions (dotted) and the tidal prediction (blue)

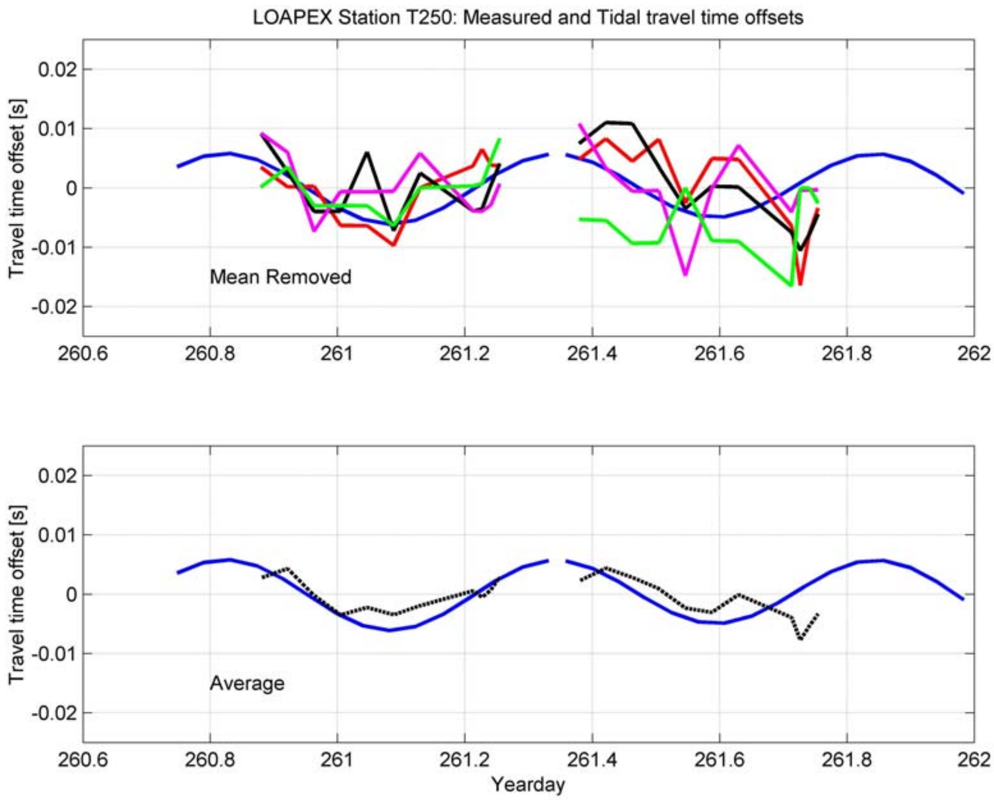

Figure A13-2. Station T250 to ‘r’ tracked raw receptions with their mean removed (colored), the average of the tracked receptions (dotted) and the tidal prediction (blue)

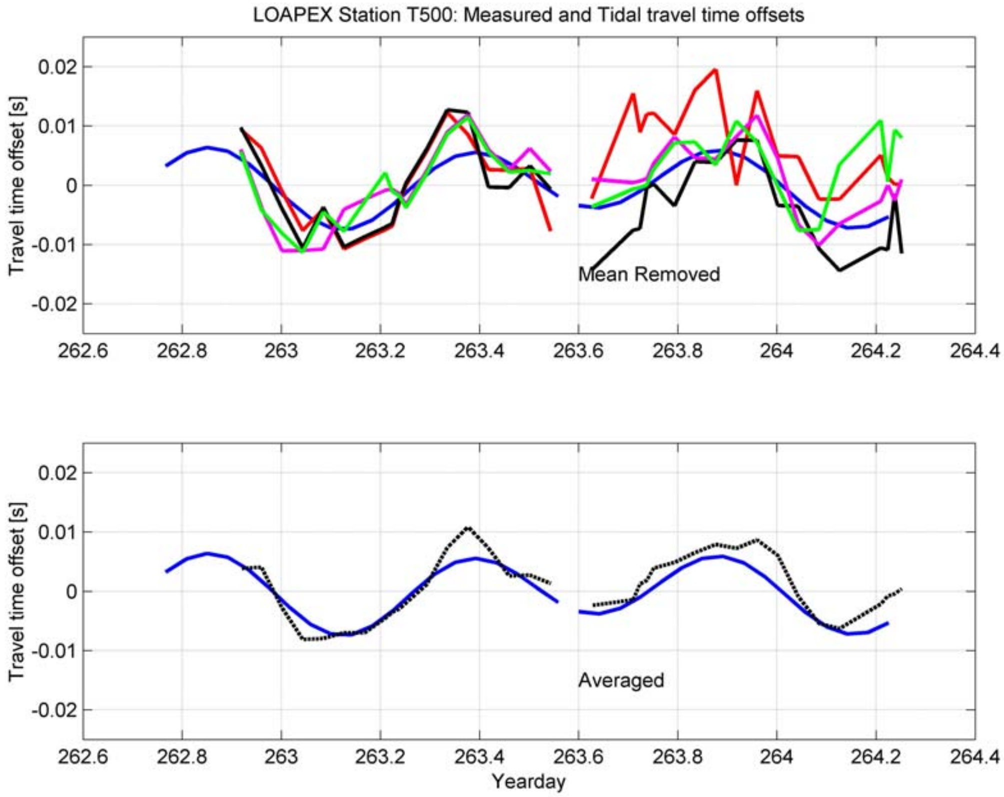

Figure A13-3. Station T500 to ‘r’ tracked raw receptions with their mean removed (colored), the average of the tracked receptions (dotted) and the tidal prediction (blue)

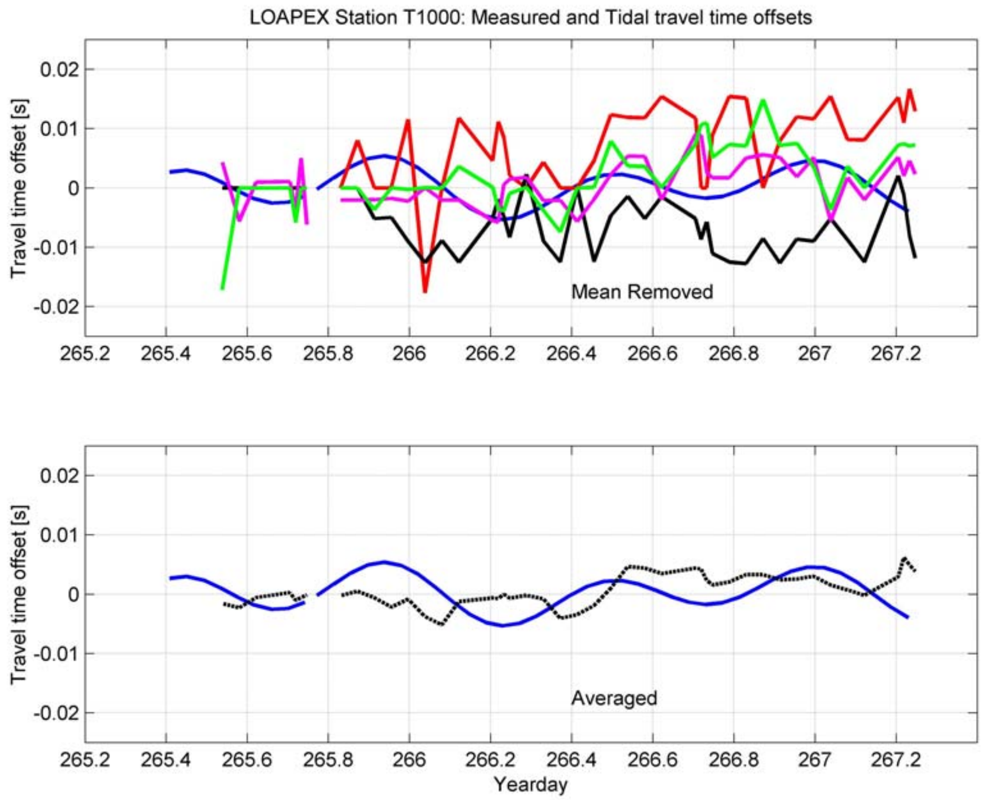

Figure A13-4. Station T1000 to ‘r’ tracked raw receptions with their mean removed (colored), the average of the tracked receptions (dotted) and the tidal prediction (blue)

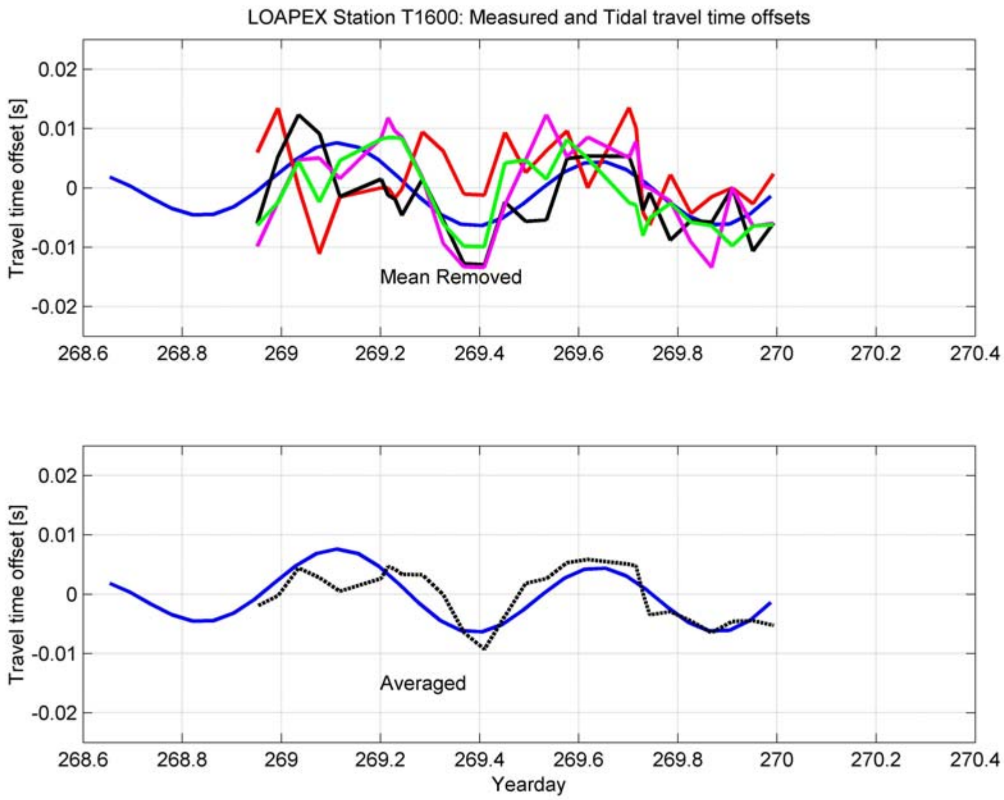

Figure A13-5. Station T1600 to 'r' tracked raw receptions with their mean removed (colored), the average of the tracked receptions (dotted) and the tidal prediction (blue)

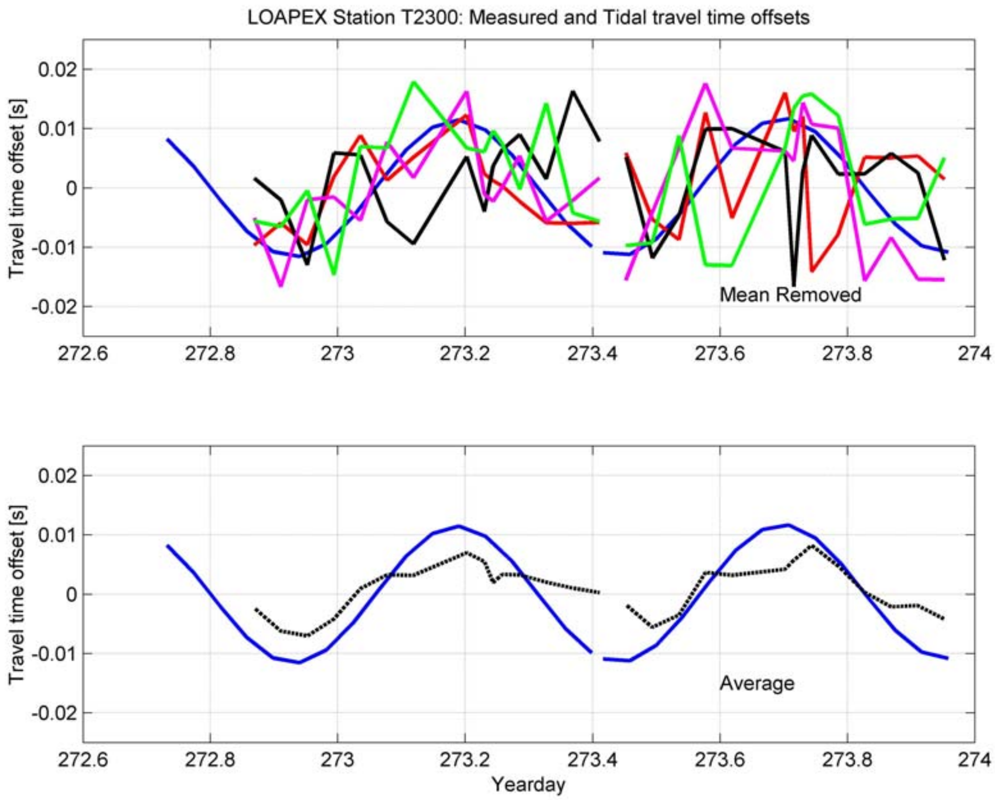

Figure A13-6. Station T2300 to ‘r’ tracked raw receptions with their mean removed (colored), the average of the tracked receptions (dotted) and the tidal prediction (blue)

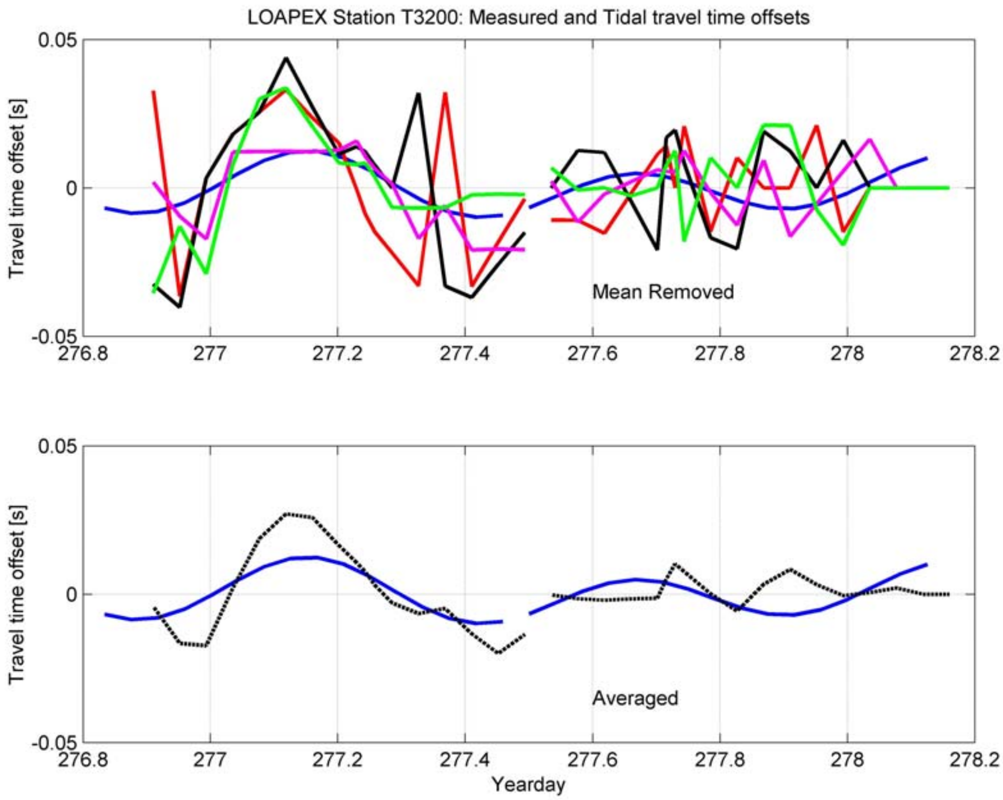

Figure A13-7. Station T3200 to ‘r’ tracked raw receptions with their mean removed (colored), the average of the tracked receptions (dotted) and the tidal prediction (blue)

Appendix 14: Comparison of first four tracked and corrected acoustic arrivals and test tidal travel time offsets

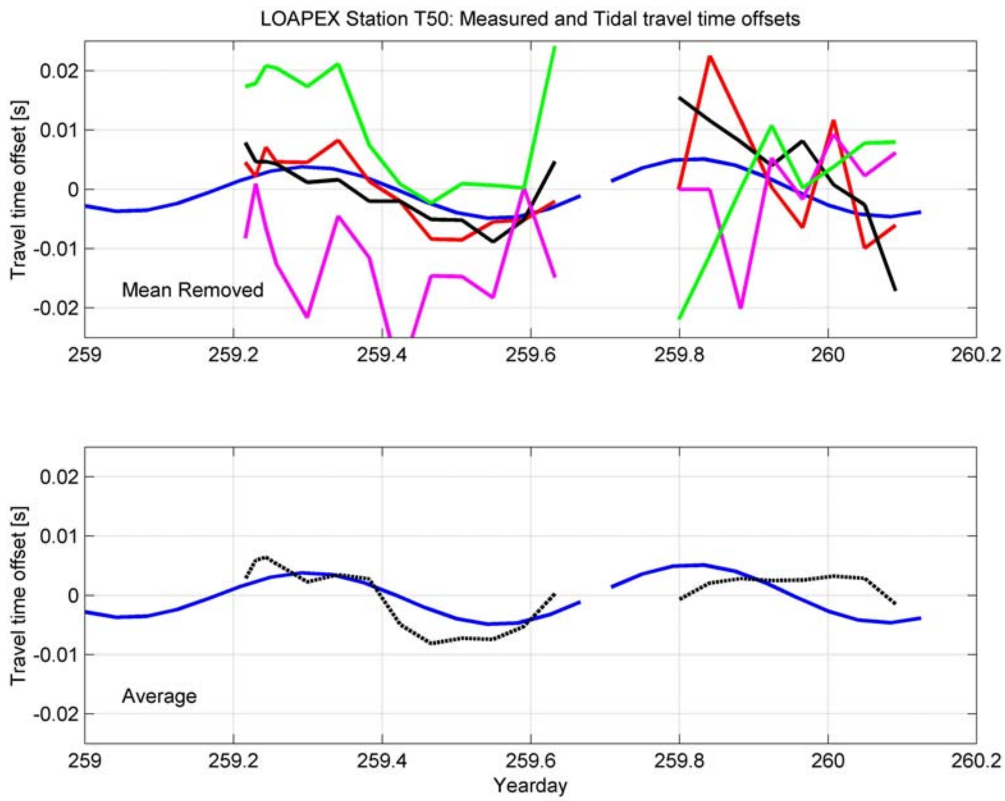

Figure A14-1. Station T50 to ‘r’ tracked receptions with their mean removed and corrected for source motion (colored), the average of the tracked receptions (dotted) and the tidal prediction (blue)

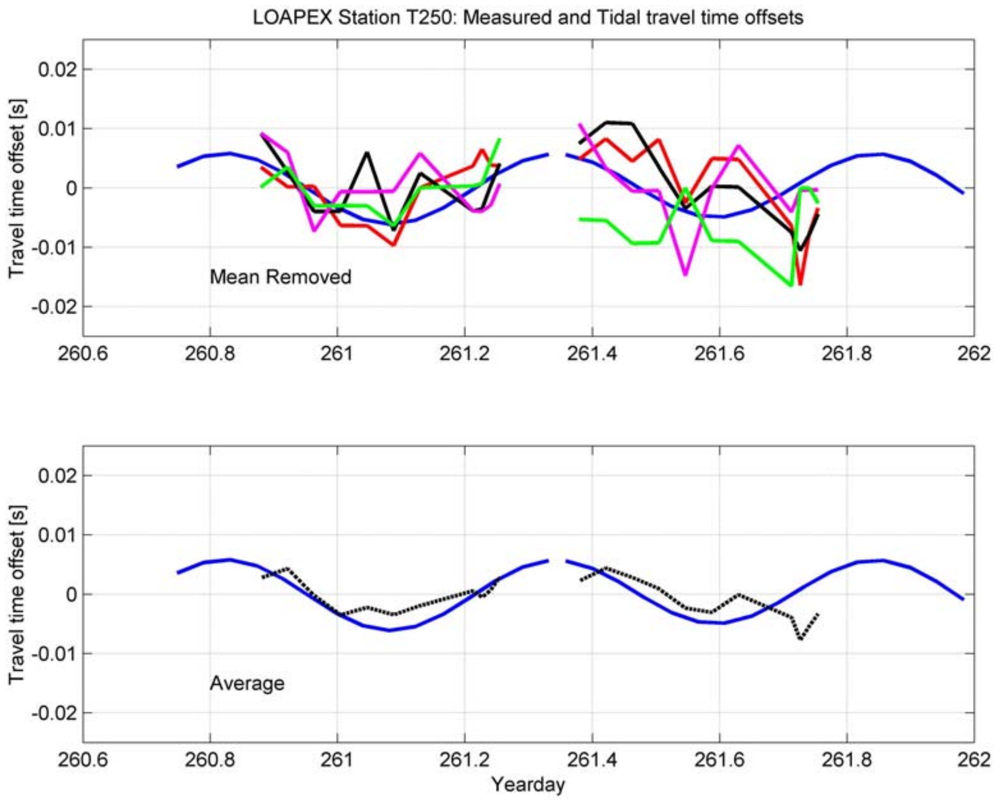

Figure A14-2. Station T250 to ‘r’ tracked receptions with their mean removed and corrected for source motion (colored), the average of the tracked receptions (dotted) and the tidal prediction (blue)

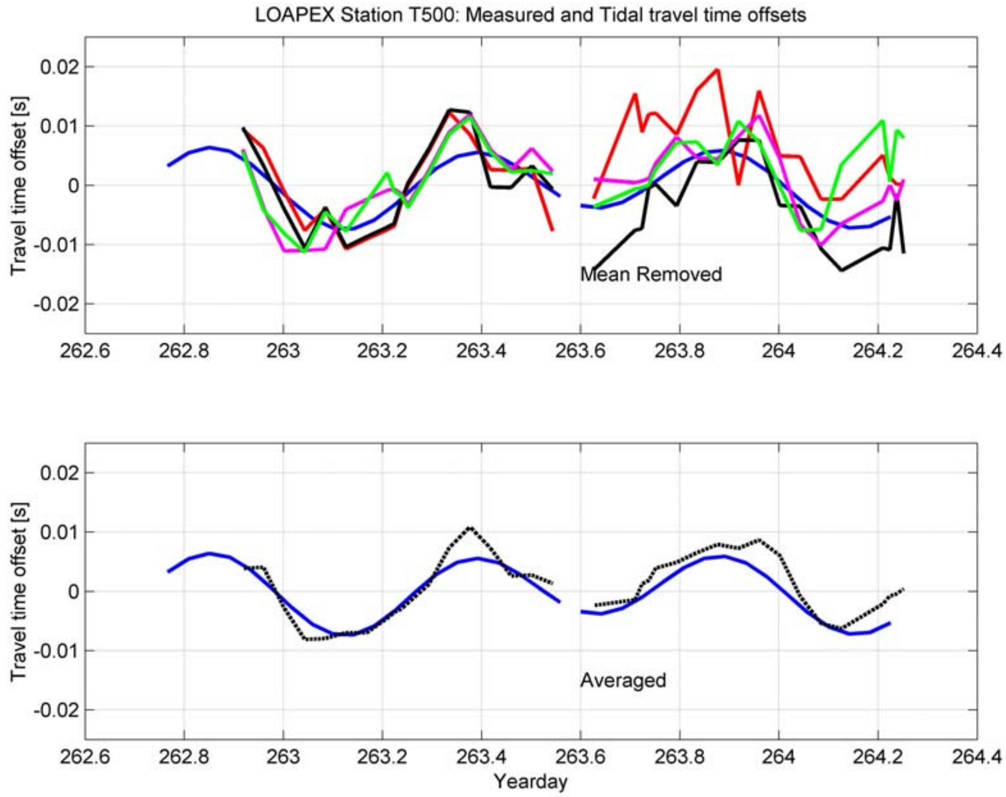

Figure A14-3. Station T500 to ‘r’ tracked receptions with their mean removed and corrected for source motion (colored), the average of the tracked receptions (dotted) and the tidal prediction (blue)

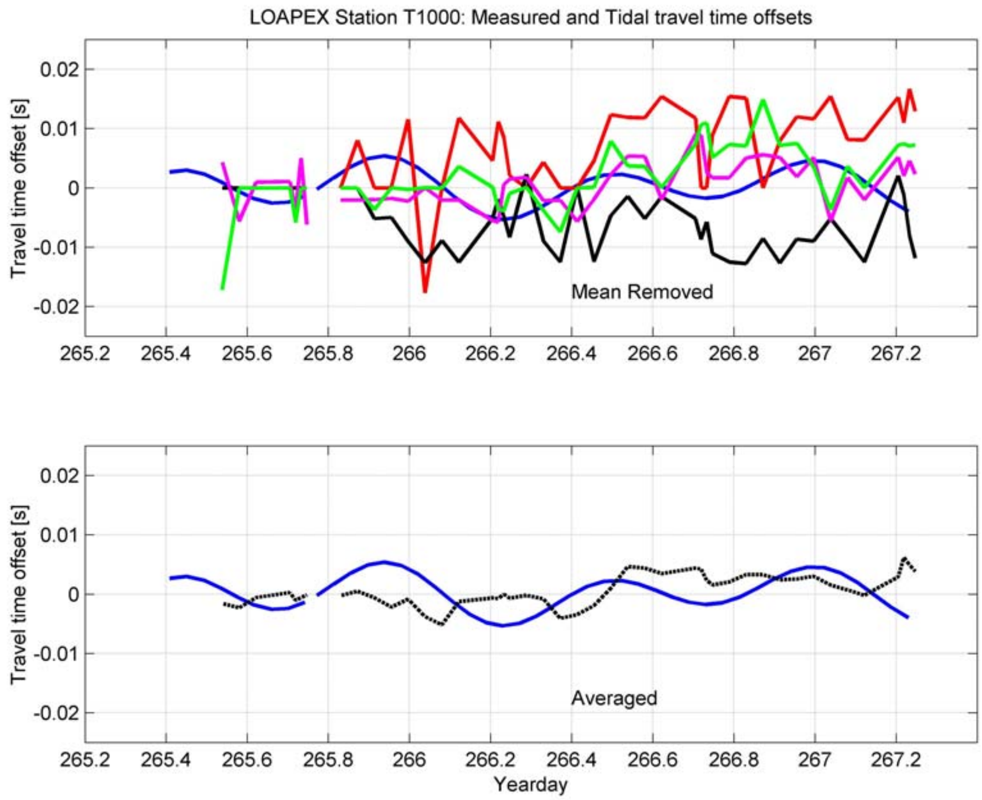

Figure A14-4. Station T1000 to ‘r’ tracked receptions with their mean removed and corrected for source motion (colored), the average of the tracked receptions (dotted) and the tidal prediction (blue)

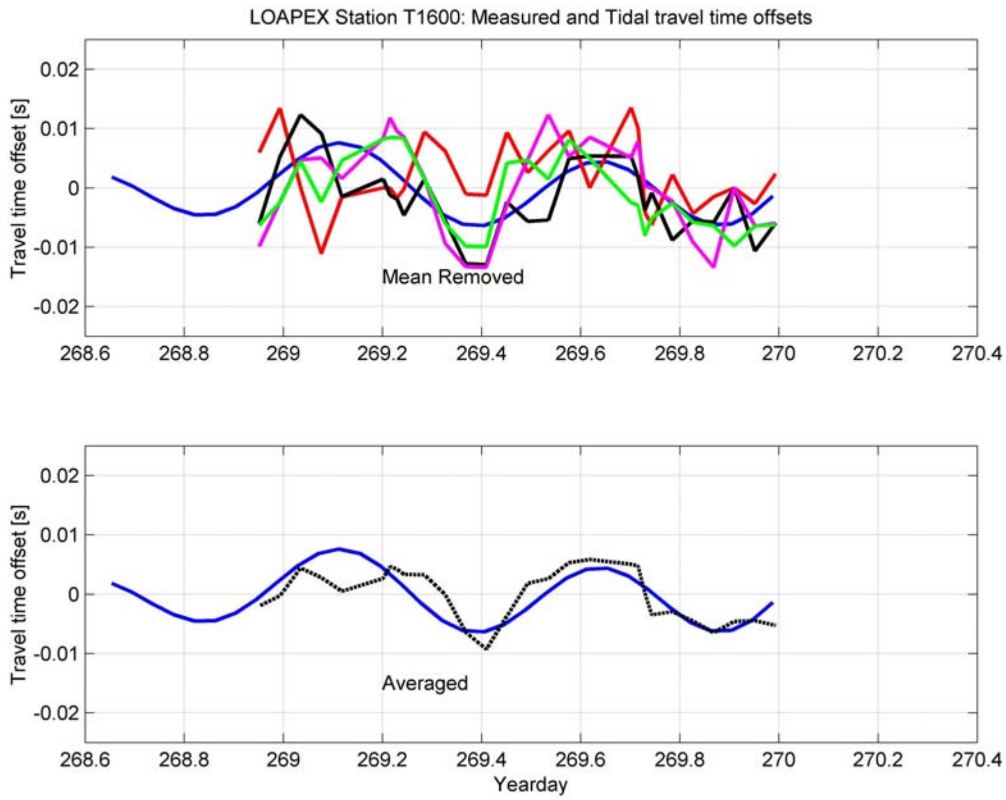

Figure A14-5. Station T1600 to ‘r’ tracked receptions with their mean removed and corrected for source motion (colored), the average of the tracked receptions (dotted) and the tidal prediction (blue)

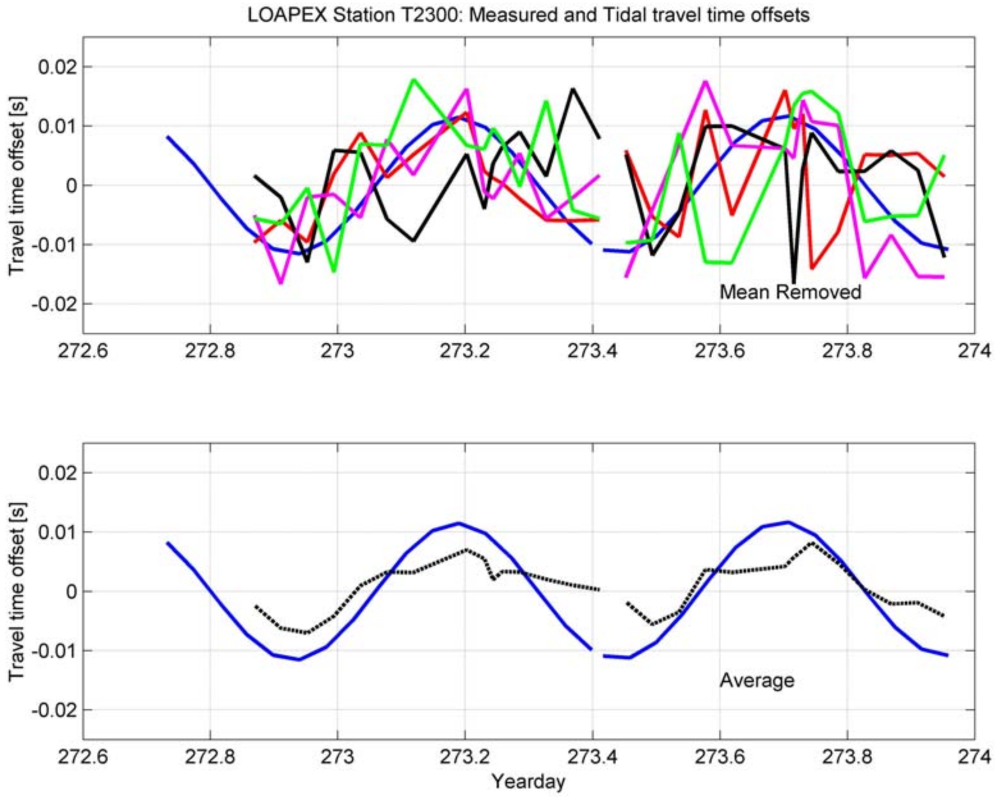

Figure A14-6. Station T2300 to ‘r’ tracked receptions with their mean removed and corrected for source motion (colored), the average of the tracked receptions (dotted) and the tidal prediction (blue)

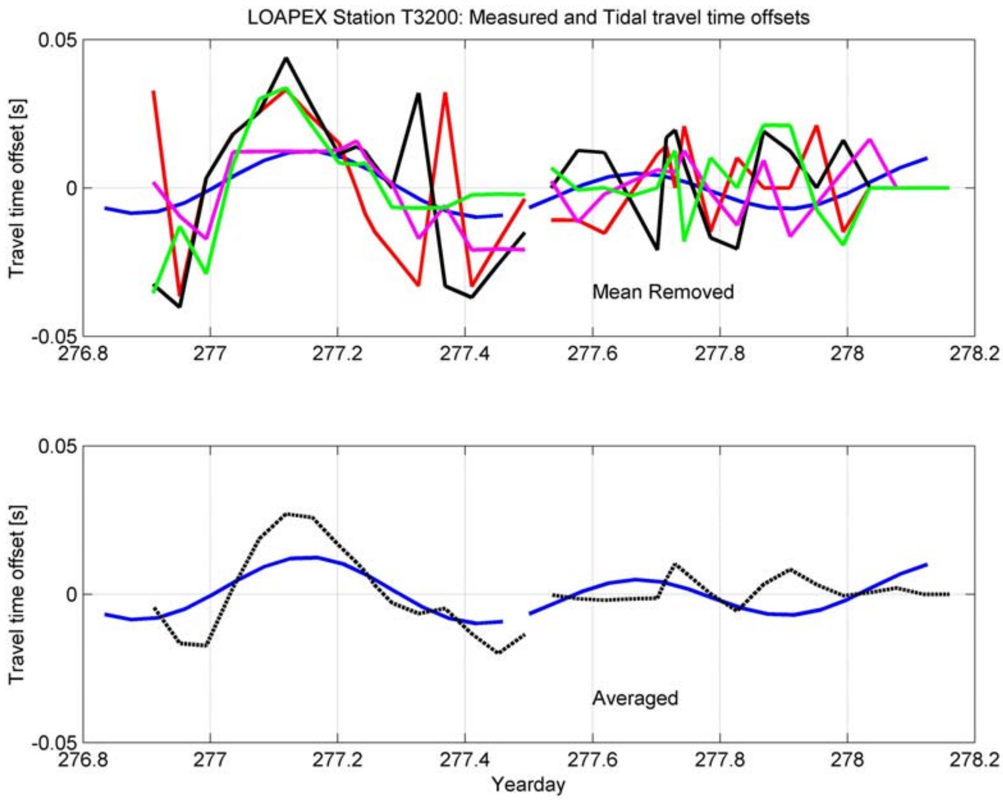

Figure A14-7. Station T3200 to ‘r’ tracked receptions with their mean removed and corrected for source motion (colored), the average of the tracked receptions (dotted) and the tidal prediction (blue)